

High shear granulation: A study of blade-granule bed interactions

by

Ei Leen Chan

*A thesis submitted in partial fulfillment of the requirements for the degree of
Doctor of Philosophy*

December 2012



The University of Sheffield

Department of Chemical and Biological Engineering

Thesis abstract

Wet granulation, a common unit operation in multiple industries, involves the production of "granules" which are assemblies of primary particles held together by interparticle bonds. Depending on the application, granules with the required attributes such as enhanced strength, flowability, dissolution properties or uniform composition, can be manufactured. It is widely accepted in granulation research that the wet granulation process is comprised of several competing rate processes that dictate the granule growth behaviour and ultimately the granule attributes. In the micro-scale models developed for these rate processes (granule coalescence, consolidation and breakage) and further mapping studies to link formulation, processing and equipment variables to the granule growth behaviour, where the most significant of such work being the "Granulation growth regime map" (Iveson and Litster, 1998b; Iveson et al., 2001b), a fundamental parameter is the external stress exerted on the granules during granulation. The external stress is exerted by the main agitator in the granulator and subsequently transmitted via inter-granule or granule-wall collisions in the system. This thesis studies and characterises the external stress in a high shear granulator, more specifically the impeller blade-granule bed stress. The reserach was divided into the following main parts:

A novel, custom-built telemetric impeller stress sensor in the studied granulator was first developed for direct measurements of the instantaneous blade-bed stress. With this system, the steady-state blade-bed stresses were studied for a range of parameters including bed load, granule sieve size and granule/particle density for dry beds and liquid addition for wet beds. The bed surface velocity, measured using high speed recording and analysed with Particle Imaging Velocimetry (PIV), was used to represent the characteristic velocity of the dynamic bed. A correction factor was applied to the theoretical blade-bed stress equation derived based on the imparted inertial stress on continuous bed, which accounted for the increasing bed "fluidisation" with increasing impeller speed. This enabled much improved predictions of the time-averaged blade-bed stress for the studied parameters, especially at high impeller speeds. The blade-bed stress behaviour during the granulation process was also studied while looking at the evolution of granule attributes.

Further characterisation of the steady-state blade-bed stress was carried out by simulating the dynamic dry particle beds in the high shear granulator using the Discrete Element Method

(DEM), a widely used simulation method for granular systems. Following the validation of the DEM simulation with the experiments, additional impeller speeds, particle/particle bed properties, impeller geometries and granulator scales were studied from the simulations. A modified correction factor was also applied in the blade-bed stress equation to account for different granulator scales and blade widths. Additionally for the bed characteristic velocity, it was also shown that the bed surface velocity is not the dominant factor for the stress over-prediction from theory with increasing impeller speeds, i.e. the increasing bed “fluidisation” is the dominant factor.

Finally, the temporal values of the steady-state blade-bed stress, bed surface velocity and bed height were studied in terms of the variability/fluctuations, for the different parameters/conditions studied in the experiments and simulations as previously mentioned. More importantly, the results were also related to the identified flow regimes of the granule/particle bed when the impeller speed or Froude number was varied.

Acknowledgements

Firstly, I would like to extend my greatest appreciation to my academic supervisors, Professor Agba Salman and Professor Mike Hounslow for their continuous support and guidance throughout my PhD studies. Their support has been extremely helpful for me to cope with the challenges of research. I would also like to thank AstraZeneca for funding this work and not forgetting my industrial supervisors, Dr Gavin Reynolds and Dr Bindhu Gururajan for their helpful suggestions and industrial insight in this field of study.

I am also particularly grateful for the assistance given by the departmental technicians, notably Oz Macfarlene, Stuart Richards and Usman Younis in building, improving (and repairing!) the central piece of equipment for this research.

My fondest thanks to the members of the Particle Products Group (past and present alike) for all their help, support, encouragement and also in making my PhD life a thoroughly memorable and enjoyable one. Thanks to Kate for your meticulous reviews and general help; to Jinsheng for your technical insight on the research; to Washino for supplying your DEM code, imparting your coding and simulation knowledge and for putting up with my incessant questions; to Ranjit for your support and sharing of our PhD "pains"; to Vikram, Xavier, James, Michal, Christine, Ale and Robert for your various help, company and in making PPG as great and special as it is!); and to Vishal, Vikrant, Heledd, Chi, Selassie, Bart, Waleed, Bob, Riyadh, William, Menan, Chalak, Syed and Mohammed- it has been truly great to know you all.

For their eternal love and support, I reserve my special gratitude to God, Mom, Dad and William. The constant encouragement, prayers and our "Skyping" sessions are some of the biggest motivations to me in pursuing this work.

Publications

Listed below are the publications resulting from this thesis.

Journal papers:

- Chan, E.L., Reynolds, G.K., Gururajan, B., Hounslow, M.J., and Salman, A.D., 2013. *Blade-granule bed stress in cylindrical high shear granulator: I-online measurement and characterisation*. Chemical Engineering Science, 86, 38-49.
- Chan, E.L., Reynolds, G.K., Gururajan, B., Salman, A.D., and Hounslow, M.J., 2012. *Blade-granule bed stress in cylindrical high-shear granulator: variability studies*. Chemical Engineering and Technology, 35, 1435-1447.
- Chan, E.L., Reynolds, G.K., Gururajan, B., Hounslow, M.J., and Salman, A.D., 2010. *Granule stress characterisation for high shear granulation: model validation*. Journal of Pharmacy and Pharmacology, 62, 1335-1336 (Extended abstract).

Conference papers:

- Chan, E.L., Reynolds, G.K., Gururajan, B., Hounslow, M.J., and Salman, A.D., 2012. *Blade-granule bed stress in a cylindrical high shear granulator: wet bed study*. 7th International Conference for Conveying and Handling of Particulate Solids, Friedrichshafen, Germany.
- Chan, E.L., Reynolds, G.K., Gururajan, B., Hounslow, M.J., and Salman, A.D., 2011. *Blade-granular bed stress in cylindrical high shear granulator: online measurement*. 5th International Granulation Workshop, Lausanne, Switzerland, Paper 108.

Thesis content

Thesis abstract	i
Acknowledgements	iii
Publications	iv
Thesis content	v
List of figures	x
List of tables	xx
Nomenclature	xxii
Chapter 1 Introduction	1
1.1 Granulation: What, why and how?.....	1
1.2 Research motivation and objectives	5
1.3 Thesis structure.....	6
Chapter 2 Literature review	7
2.1 Introduction	7
2.2 Wet agitation granulation: the three main rate processes	7
2.2.1 Wetting and nucleation	8
2.2.2 Coalescence and consolidation	9
2.2.3 Breakage and attrition	10
2.3 Granule growth and growth behaviour.....	11
2.3.1 Micro-scale modelling	12
2.3.1.1 Granule consolidation	12
2.3.1.2 Granule coalescence models	16
2.3.1.3 Growth limiting/breakage models.....	20
2.3.1.4 Wet granule strength	21
2.3.2 Macro-scale characterisation.....	24
2.3.2.1 Granule growth behaviours	24
2.3.2.2 Mapping in granulation.....	25
2.4 External stress on granules	29
2.4.1 Stress characterisation in granulation.....	31
2.4.2 Stress measurement and granulation monitoring methods.....	32
2.4.3 Outlook and thesis objectives revisited.....	35

Chapter 3 Telemetric impeller stress sensor system and other methodology	37
3.1 Introduction	37
3.2 Blade-granule bed stress measurement	37
3.2.1 High shear granulator and pressure colouring films method	37
3.2.2 Telemetric impeller stress sensor system	39
3.2.2.1 Sensor description	39
3.2.2.2 Sensor calibration.....	42
3.2.2.3 Measurement and analysis	46
3.3 Granule bed surface velocity and height	48
3.3.1 High speed camera recording.....	48
3.3.2 Bed surface velocity and height analysis	49
3.4 Dry granule/particle and liquid properties.....	51
3.4.1 Granule/particle size.....	51
3.4.2 Granule/particle apparent density	53
3.4.3 Strength and Young's modulus.....	54
3.4.3.1 Single granule diametric compression	55
3.4.3.2 Uniaxial confined multiple granules compression.....	57
3.4.4 Liquid viscosity	58
3.4.5 Liquid surface tension.....	60
Chapter 4 Dry granule/particle bed characterisation: experimental.....	61
4.1 Introduction	61
4.2 Blade-granule bed stress: theory	61
4.2.1 Force of a blade moving linearly through a cohesionless granule bed	61
4.2.2 Force and stress of a rotating blade through a cohesionless granule bed.....	64
4.3 Materials and methodology	67
4.3.1 Granule preparation and granule/particle properties.....	67
4.3.2 Blade-bed stress, bed surface velocity and bed height measurements	71
4.4 Bed-granule bed stress, bed surface velocity and bed height results	72
4.4.1 Bed load	72
4.4.2 Granule size.....	76
4.4.3 Granule/particle materials	78
4.5 Blade-bed stress prediction from theory.....	80
4.6 Chapter summary and conclusions.....	87

Chapter 5 Wet granule/particle bed characterisation: experimental	89
5.1 Introduction	89
5.2 Steady-state stress for wet beds.....	89
5.2.1 Materials and methodology.....	89
5.2.2 Blade-bed stress, bed surface velocity and bed height results	92
5.2.3 Blade-bed stress prediction from theory	98
5.3 Unsteady-state stress for wet beds.....	100
5.3.1 Materials and methodology.....	100
5.3.2 Results and discussion.....	102
5.4 Chapter summary and conclusions.....	108
Chapter 6 Dry particle bed characterisation: simulation	110
6.1 Introduction	110
6.2 Principle of Discrete Element Method (DEM).....	111
6.2.1 Description and equations of motion	111
6.2.2 Soft-sphere DEM model	112
6.2.2.1 Stiffness and damping coefficients	115
6.3 Simulation geometries and parameters.....	117
6.3.1 Main description.....	117
6.3.2 Particle bed/particle properties.....	118
6.3.3 Impeller geometries.....	121
6.3.4 Granulator scale	123
6.4 Simulation and analysis method of the blade-bed stress, bed velocities and bed height	124
6.5 DEM validation: experimental comparison.....	126
6.6 Simulation results: impeller speed and radial position.....	135
6.7 Simulated blade-bed stress, bed surface velocity and bed height results	145
6.7.1 Particle/particle bed properties.....	145
6.7.2 Impeller geometries.....	156
6.7.3 Granulator scale	162
6.8 Blade-bed stress prediction from theory.....	166
6.8.1 Predictions using different bed heights	166
6.8.2 Fittings for different parameters.....	169
6.8.3 Predictions using different bed velocities	175
6.9 Chapter summary and conclusions.....	178

Chapter 7 Further insight: variability studies across flow regimes	181
7.1 Introduction	181
7.2 Flow studies.....	181
7.3 Materials and methodology	182
7.4 Granule/particle bed flow regimes	183
7.4.1 Dry beds	183
7.4.2 Wet beds.....	185
7.5 Behaviour of the bed surface.....	188
7.5.1 Experimental bed surface velocity and bed height.....	188
7.5.1.1 Dry beds	188
7.5.1.2 Wet beds.....	196
7.6 Behaviour of blade-bed region	202
7.6.1 Experimental blade-bed stress.....	202
7.6.2 Simulated bed-blade stress.....	204
7.7 Chapter summary and conclusions.....	209
Chapter 8 Overall conclusions and future work.....	211
8.1 Thesis conclusions.....	211
8.1.1 Dry granule/particle bed characterisation (Chapter 4)	211
8.1.2 Wet granule/particle bed characterisation (Chapter 5).....	212
8.1.3 Further dry bed characterisation using DEM simulations (Chapter 6)	213
8.1.4 Variability studies across flow regimes (Chapter 7)	214
8.2 Future work	215
References	217
Appendix A Blade-bed stress measurements using pressure colouring films	227
A.1 Film description.....	227
A.2 Film calibration	228
A.3 Application for blade-granule bed stress measurements	231
A.4 Comparison with impeller stress sensor and time effect	236
Appendix B Particle Imaging Velocimetry (PIV): further details	239
B.1 Overview of PIV algorithms.....	239
B.1.1 Auto-correlation algorithm.....	239
B.1.2 Cross-correlation (COR) algorithm.....	240
B.1.3 Minimum quadratic difference (MQD) algorithm	240

B.2 Pixel-distance calibration.....	241
B.3 Size of interrogation area.....	242
Appendix C Granulation: binder spray system calibration	246
Appendix D DEM simulations: particle bed flow images and further details	247
D.1 Particle bed/particle properties	247
D.1.1 Bed load.....	247
D.1.2 Particle size	249
D.1.3 Particle density	251
D.1.4 Interparticle sliding friction coefficient.....	253
D.1.5 Restitution coefficient	257
D.1.6 Young's modulus	258
D.2 Impeller geometries	260
D.2.1 Blade width	260
D.2.2 Blade angle.....	263
D.2.3 Number of blades	266
D.3 Granulator scale.....	269
D.3.1 Same particle diameter ($D/d_p = 20-160$).....	269
D.3.2 Same particle diameter to granulator diameter ratio ($D/d_p = 80$).....	271

List of figures

Chapter figures:

Figure 1.1: Schematic of the general wet agitation granulation process.	3
Figure 2.1: Competing rate processes or mechanisms in wet agitation granulation processes (modified from Ennis & Litster, 1997).....	8
Figure 2.2: Distribution and immersion mechanisms in the formation of nuclei (modified from Schaefer and Mathiesen, 1996)	9
Figure 2.3: Granule breakage and attrition.	10
Figure 2.4: Development of granule consolidation models.....	12
Figure 2.5: Development of granule coalescence models.	16
Figure 2.6: Two colliding particles covered in a viscous layer of liquid of thickness h (modified from Ennis et al., 1991).	17
Figure 2.7: Collision & separation stages: (a) approach stage; (b) deformation stage; (c) initial separation stage; (d) final separation stage (modified from Liu & Litster, 2001).	18
Figure 2.8: Boundaries for type I, II coalescence and rebound for surface-wet granules (taken from Liu & Litster, 2001).	20
Figure 2.9: Dimensionless strength, Str^* versus Capillary number, Ca (taken from Iveson et al, 2002).....	23
Figure 2.10: Modified "Granulation growth regime map" (taken from Iveson & Litster, 1998b).	26
Figure 2.11: Effect of processing and formulation variables on granule growth behaviour (taken from Iveson & Litster, 1998b).....	27
Figure 2.12: Experimental validation of growth regime map (Iveson et al, 2001b).	28
Figure 2.13: Factors affecting granule growth behaviour in the wet agitation granulation process.	29
Figure 2.14: Mixer granulator configurations: (a) horizontal mixer and (b) vertical, bottom-driven mixer (taken from Reynolds et al., 2007).....	31
Figure 3.1: ~10 L Roto Junior high shear granulator.	38
Figure 3.2: Sensor plate on the impeller blade.	40
Figure 3.3: Schematic of the telemetric impeller stress sensor system in the Roto Junior.....	40
Figure 3.4: Flow diagram of the telemetric impeller stress sensor system.....	42
Figure 3.5: Output flow in the telemetric impeller stress sensor system.	43
Figure 3.6: Customised sensor plate holder for calibration. Right: position of the strain gauge on the underside of the plate.....	43
Figure 3.7: Setup for the sensor plate calibration.....	44

Figure 3.8: Calibration curve for a 0.25 mm stainless steel plate using continuous compression and deadweights and the fitted polynomial expression. R^2 is the coefficient of determination showing the goodness of fit, where 1 indicates perfect fit.	45
Figure 3.9: Plate average vertical height displacement, w_{avg} , from continuous compression. ...	45
Figure 3.10: Loading and unloading results (weights) for 0.25 mm thick stainless steel plate..	46
Figure 3.11: Example sensor output: readings for dry mannitol bed (1.5kg load, 0.5-1.0 mm sieve size) at impeller speed of 150 rpm.	47
Figure 3.12: Time-averaged blade-bed stress for dry mannitol granules bed (1.5 kg load, 0.5-1.0 mm sieve size) and empty runs at different impeller speeds.	47
Figure 3.13: Schematic of the high speed camera setup with the Roto Junior.	48
Figure 3.14: Example high speed camera image (top view of granule bed) for bed surface velocity analysis.	49
Figure 3.15: Example high speed camera image for bed height evaluation.	51
Figure 3.16: Schematic of the dynamic image analysis method for size measurement in the Camsizer.	52
Figure 3.17: Zwick/Roell Z0.5 compression machine and schematic (left) of the punch and die.	55
Figure 3.18: Force-displacement curve for single granule crushing tests (dry mannitol granules, 0.5-1.0 mm sieve size produced in Chapter 4).	56
Figure 3.19: Force-displacement curve for uniaxial confined multiple granules compression (dry mannitol granules, 0.5-1.0 mm sieve size produced in Chapter 4).	57
Figure 3.20: Plot of $\ln P$ (pressure) versus $\ln \varepsilon'$ (natural strain) and fitted Adam's equation (Equation 3.8) (dry mannitol granules, 0.5-1.0 mm sieve size produced in Chapter 4).	58
Figure 3.21: proRheo R180 Rheomat “tube and bob” rotational viscometer with the 32.54 mm diameter tube and 30 mm diameter bob attached. Left: Schematic of the tube and bob.	59
Figure 3.22: Viscosity of paraffin oil at different shear rates.	59
Figure 3.23: FTA 32 drop shape analyser for liquid surface tension measurements.	60
Figure 4.1: Blade moving through a granule bed (modified from Bagster and Bridgwater, 1967 and Bagster and Bridgwater, 1969).	62
Figure 4.2: Vertical axis cylindrical granulator.	64
Figure 4.3: Granule bed and impeller blade profile in the $z-r$ plane (front view).	65
Figure 4.4: Granule bed and impeller blade profile in $z-\alpha$ plane (side view).	65
Figure 4.5: Microscopic images of (a) lactose granules, 0.1-2.0 mm (b) mannitol granules, 0.1-2.0 mm.	70
Figure 4.6: Granule bed images at different impeller speeds (mannitol granules, 1.0-2.0 mm sieve size, 1.5 kg load).	73
Figure 4.7: Time-averaged data for different bed loads (mannitol granules, 0.5-1.0 mm) (a) blade-granule bed stress (b) bed surface velocity (circumferential) and (c) bed height.	75

Figure 4.8: Time-averaged data for different sieve sizes (mannitol granules, 1.5 kg) (a) blade–granule bed stress (b) bed surface velocity (circumferential) and (c) bed height.....	77
Figure 4.9: Time-averaged blade–granule bed stress, bed surface velocity (circumferential) and bed height of different granule types and polypropylene balls at different bed loads.....	79
Figure 4.10: Experimental and calculated (Equation 4.8) blade–bed stress (mannitol granules, 0.5-1.0 mm) at bed loads of (a) 1.0 kg (b) 1.5 kg (c) 2.0 kg.	81
Figure 4.11: Variation of the normalised bed velocity (circumferential) with the normalised bed height from DEM simulations (3.5mm monosized particles, 1.5 kg bed load). The top most value for each series indicates the average surface velocities and the respective arrows indicate the surface height fluctuation range.....	83
Figure 4.12: Plot of B_I and $1/v_{rel}$ for all materials. Dashed lines represent $x = y$	84
Figure 4.13: Comparison of the calculated blade–bed stress without (Equation 4.8) and with the correction parameter B_I (Equation 4.12) with the experimental results (mannitol granules, 0.5-1.0 mm) at bed loads of (a) 1.0 kg (b) 1.5 kg (c) 2.0 kg.....	85
Figure 4.14: Plotted measured stress with the predicted values with the correction parameter B_I (Equation 4.12) for (a) mannitol granules of all sieve sizes and bed loads and (b) different granule types and polypropylene balls. Dashed lines represent $x = y$	86
Figure 5.1: Microscopic images of polypropylene balls wetted with different water content. Scale bar represent 2000 μm	91
Figure 5.2: Saturation states of liquid-bound particles (modified from Newitt and Conway-Jones, 1958).....	91
Figure 5.3: Time-averaged blade-bed stress and bed surface velocity for different water content: large fluctuations at 25%w/w water.	93
Figure 5.4: Bed flow images for different water content at 350 rpm.	93
Figure 5.5: Time-averaged data for different water content (a) blade-bed stress (b) bed surface velocity (circumferential) and (c) bed height.	95
Figure 5.6: Time-averaged data for different 8% HPC solution content (a) blade-bed stress (b) bed surface velocity (circumferential) and (c) bed height.	97
Figure 5.7: Plots of B_I and $1/v_{rel}$ for (a) different water content and (b) different 8% HPC solution content. Dashed lines represent $x = y$	99
Figure 5.8: Plotted measured stress with the predicted values with the correction parameter B_I (Equation 4.9) for dry and wet polypropylene beds. Dashed lines represent $x = y$	100
Figure 5.9: Results for continuous water adding (a) blade-bed stress during granulation (b) size of dried granules and (c) bulk strength of dried granules.....	103
Figure 5.10: Granule images with granulation time for continuous water adding.	103
Figure 5.11: Results for L/S : 0.21 (a) blade-bed stress during granulation (b) size of dried granules and (c) bulk strength of dried granules.	105
Figure 5.12: Granule images with granulation time for L/S : 0.21	105
Figure 5.13: Results for L/S : 0.28 (a) blade-bed stress during granulation (b) size of dried granules and (b) bulk strength of dried granules.	106

Figure 5.14: Granule images with granulation time for L/S : 0.28.....	106
Figure 5.15: Impeller torque and power consumption in a Fielder PMA 10 (10 liter) high shear granulator (modified from Levin, 2007).....	108
Figure 6.1: Contact between two spherical particles of radius r_p . A is the area of deformation and δ is depth of the contact deformation (taken from Campbell, 2006).	112
Figure 6.2: Soft-sphere DEM model for (a) normal force (b) tangential force (modified from Tsuji et al., 1992).....	113
Figure 6.3: Forces and torque of two spherical particles (i and j) in contact.	114
Figure 6.4: Relationship between parameter β and restitution coefficient, e (taken from Tsuji et al., 1992).....	117
Figure 6.5: Experimental and simulated geometry (~10 L mixer, three-bladed impeller with 32° inclined blades).....	118
Figure 6.6: Simulated blade geometries.	122
Figure 6.7: Experimental impeller stress sensor plate and analysed contact region for the simulations.....	125
Figure 6.8: Top view of the granulator and the bed surface velocities analysis region. Inset: High speed camera recorded image. The colour bar indicates the particle total velocity in m/s.	126
Figure 6.9: Images of the granule/particle bed at three different impeller speeds for 1.5 kg bed load. Top row: 1.0-2.0 mm mannitol granules; Middle row: simulated 2.0 mm particles; Bottom row: simulated 3.5 mm particles. The colour bar indicates the particle total velocity in m/s.	127
Figure 6.10: Temporal blade-bed stress for the 1.5 kg bed load of (a) 1.0-2.0 mm mannitol granules and (b) simulated 2.0 mm particles.	128
Figure 6.11: Temporal blade-bed stress for the 1.5 kg bed load of (a) 2.0-4.75 mm mannitol granules and (b) simulated 3.5 mm particles. * No measurement data for the 2.0-4.75 mm mannitol granules at 350 rpm.	129
Figure 6.12: Time-averaged blade-bed stress for the 1.5 kg bed load of (a) 1.0-2.0 mm mannitol granules and simulated 2.0 mm particles and (b) 2.0-4.75 mm mannitol granules and simulated 3.5 mm particles.	130
Figure 6.13: Temporal bed surface velocity for the 1.5 kg bed load of (a) 1.0-2.0 mm mannitol granules and (b) simulated 2.0 mm particles. Top and bottom rows show the circumferential and radial components respectively.....	131
Figure 6.14: Temporal bed surface velocity for the 1.5 kg bed load of (a) 2.0-4.75 mm mannitol granules and (b) simulated 3.5 mm particles. Top and bottom rows show the circumferential and radial components respectively.....	132
Figure 6.15: Time-averaged bed surface velocities for the 1.5 kg bed load of (a) 1.0-2.0 mm mannitol granules and simulated 2.0 mm particles and (b) 2.0-4.75 mannitol granules and simulated 3.5 mm particles.....	133
Figure 6.16: Temporal bed height at the wall for 1.5 kg bed load of (a) 1.0-2.0 mm mannitol granules and (b) simulated 2.0 mm particles.....	133

Figure 6.17: Temporal bed height at the wall for 1.5 kg bed load of (a) 2.0-4.75 mm mannitol granules and (b) simulated 3.5 mm particles.	134
Figure 6.18: Time-averaged bed height at the wall for the 1.5 kg bed load of (a) 1.0-2.0 mm mannitol granules and simulated 2.0 mm particles and (b) 2.0-4.75 mannitol granules and simulated 3.5 mm particles.	134
Figure 6.19: Simulated time-averaged blade-bed stress along the radial position (normalised with the blade radius) for the 1.5 kg, 3.5 mm particle beds.	136
Figure 6.20: Simulated time-averaged bed height along the radial position (normalised with the blade radius) for the 1.5 kg, 3.5 mm particle beds.	137
Figure 6.21: Simulated time-averaged bed surface velocity (circumferential) along the radial position (normalised with the blade radius) for the 1.5 kg, 3.5 mm particle beds. *The top graph for the 50 rpm case is plotted additionally on an adjusted y-axis.	139
Figure 6.22: Simulated time-averaged particle bed velocities (circumferential) and blade linear velocity along the radial position at different impeller speeds for the 1.5 kg, 3.5 mm particle beds.	140
Figure 6.23: Simulated time-averaged blade-bed normal stress at the sensor and blade tip regions for the 1.5 kg, 3.5 mm particle beds.	141
Figure 6.24: Simulated time-averaged blade-bed normal and shear stress at the sensor regions for the 1.5 kg, 3.5 mm particle beds.	142
Figure 6.25: Simulated time-averaged bed surface and bed height-averaged velocities (circumferential component) for the 1.5 kg, 3.5 mm particle beds.	143
Figure 6.26: Simulated time-averaged bed height at the sensor region and at the wall for the 1.5 kg, 3.5 mm particle beds.	143
Figure 6.27: Simulated time-averaged data for different bed loads (a) blade-bed stress (b) bed surface velocity (circumferential) and (c) bed height.	146
Figure 6.28: Simulated time-averaged blade-bed stress (left column) and bed height (right column) along the radial position at different bed loads.	147
Figure 6.29: Simulated time-averaged data for different particle sizes (a) blade-bed stress (b) bed surface velocity (circumferential) and (c) bed height.	149
Figure 6.30: Simulated time-averaged data for different particle densities (a) blade-bed stress (b) bed surface velocity (circumferential) and (c) bed height. *Numbers in brackets are the bed bulk density.	150
Figure 6.31: Simulated time-averaged data for different interparticle sliding friction coefficients (a) blade-bed stress (b) bed surface velocity (circumferential) and (c) bed height.	152
Figure 6.32: Simulated time-averaged blade-bed stress (shear component) for different interparticle sliding friction coefficients.	153
Figure 6.33: Simulated time-averaged data for different restitution coefficients (a) blade-bed stress (b) bed surface velocity (circumferential) and (c) bed height.	154
Figure 6.34: Simulated time-averaged data for different Young's modulus (a) blade-bed stress (b) bed surface velocity (circumferential) and (c) bed height.	155

Figure 6.35: Simulated time-averaged total blade-bed force for different blade widths *Legends indicate the blade width, h_w , and blade inclined height, h_l in brackets.....	157
Figure 6.36: Simulated time-averaged data for different blade widths (a) blade–bed stress (b) bed surface velocity (circumferential) and (c) bed height. *Legends indicate the blade width, h_w , and blade inclined height, h_l in brackets.....	158
Figure 6.37: Simulated time-averaged data for different blade angles (a) blade–bed stress (b) bed surface velocity (circumferential) and (c) bed height.	159
Figure 6.38: Simulated time-averaged total blade-bed force (at the sensor region for all blades) for different number of blades.....	160
Figure 6.39: Simulated time-averaged data for different number of blades (a) blade–bed stress (b) bed surface velocity (circumferential) and (c) bed height.	161
Figure 6.40: Bed flow images from simulation for different granulator scales at a Froude number of 0.18 for the same particle size (3.5 mm) and different D/d_p . The colour bar indicates the particle total velocity in m/s.	162
Figure 6.41: Simulated time-averaged data for different granulator scales (a) blade–bed stress (b) bed surface velocity (circumferential) and (c) bed height. Left column: constant D/d_p , right column: constant d_p	164
Figure 6.42: Scaled parameters for different simulated granulator scales (a) normalised blade-bed stress (b) bed surface velocity (circumferential) to impeller linear velocity ratio (c) bed height to blade inclined height ratio. Left column: constant D/d_p , right column: constant d_p ..	165
Figure 6.43: Comparison of the calculated blade–bed stress with no correction factor (Equation 4.8) using either the simulated bed height at the wall or sensor region-averaged bed height, with the simulated blade-bed stress for the 3.5 mm particles, 1.5 kg bed. The measured blade-bed stresses for the 1-2 mm sieve size mannitol granule are also included in the plot.	167
Figure 6.44: Plot of B_1 versus $1/v_{rel}$ for different simulated bed loads using the (a) bed height at the wall and the (b) sensor region-averaged bed height.	167
Figure 6.45: Comparison of the calculated blade–bed stress with correction factor B_1 (Equation 4.9) with the simulated blade-bed stress at different bed loads.....	168
Figure 6.46: Plot of B_1 versus $1/v_{rel}$ for different simulated particle bed/particle properties (a) bed load (b) particle size (c) particle density (bed bulk density in brackets) and (d) interparticle sliding friction coefficient.	169
Figure 6.47: Plot of B_1 versus $1/v_{rel}$ for different simulated impeller geometries and granulator scales (a) number of blades (b) blade width (blade inclined height in brackets) (c) blade angle and (d) granulator scales.....	170
Figure 6.48: Results of (a) relative velocity, v_{rel} , and (b) relative Froude number, $Fr_{rel}^{0.5}$, for different granulator scales.	171
Figure 6.49: Plot of B_2 versus $(2h_w/D)^{0.3}/Fr_{rel}^{0.5}$ for different simulated particle bed/particle properties (a) bed load (b) particle size (c) particle density (bed bulk density in brackets) and (d) interparticle sliding friction coefficient.	173
Figure 6.50: Plot of B_2 versus $(2h_w/D)^{0.3}/Fr_{rel}^{0.5}$ for different simulated impeller geometries and granulator scales (a) number of blades (b) blade width (blade inclined height in brackets) (c) blade angle and (d) granulator scales.	174

Figure 6.51: Variation of K_2 values with blade angle.....	174
Figure 6.52: Comparison of the calculated blade–bed stress with no correction factor (Equation 4.8) using either the simulated bed surface velocity or bed height-averaged velocity, with the simulated blade-bed stress for the 3.5 mm particles, 1.5 kg bed.....	175
Figure 6.53: Plot of B_2 versus $(2h_w/D)^{0.3}/Fr_{rel}^{0.5}$ using the simulated bed height-averaged velocities for different simulated particle bed/particle properties (a) bed load (b) particle size (c) particle density (bed bulk density in brackets) and (d) interparticle sliding friction coefficient.....	176
Figure 6.54: Plot of B_2 versus $(2h_w/D)^{0.3}/Fr_{rel}^{0.5}$ using the simulated bed height-averaged velocities for different simulated impeller geometries and granulator scales (a) number of blades (b) blade width (blade inclined height in brackets) (c) blade angle and (d) granulator scales.....	177
Figure 7.1: Granule bed flow regimes for 1.0-2.0 mm, 1.5 kg dry mannitol bed at different speeds/Froude number: (a) slow/frictional (b) toroidal and (c) fluidised.....	184
Figure 7.2: Bed flow images for 1.5 kg bed of dry and wet (2% w/w and 5% w/w water) polypropylene balls.....	186
Figure 7.3: Bed flow images for 1.5 kg bed of wet (5% w/w, 15% w/w, and 25% w/w water) polypropylene balls.....	187
Figure 7.4: Total bed surface velocity ($v_{surf,t}$) results: (a) temporal values and RSD (relative standard deviation) for 0.5-1.0 mm, 1.5 kg granule bed (b) time-averaged values for different sieve sizes (i) actual values (ii) normalised values (c) time-averaged values for different bed loads (i) actual values (ii) normalised values.....	190
Figure 7.5: Circumferential ($v_{surf,c}$) and radial ($v_{surf,r}$) velocity results: (a) time-averaged values for different sieve sizes (b) time-averaged values for different bed loads.....	191
Figure 7.6: Total bed surface velocity ($v_{surf,t}$) with impeller rotation and FFT analysis for 0.5-1.0 mm, 1.5 kg granule bed.....	193
Figure 7.7: Bed height at the wall ($H_{g,R}$) results: (a) temporal values and RSD (relative standard deviation) for 0.5-1.0 mm, 1.5 kg granule bed (b) time-averaged values for different sieve sizes (c) time-averaged values for different bed loads.....	194
Figure 7.8: Bed height at the wall ($H_{g,R}$) with impeller rotation for 0.5-1.0 mm, 1.5 kg granule bed.....	195
Figure 7.9: Time-averaged total bed surface velocity ($v_{surf,t}$) results for dry and wet beds of polypropylene balls (a) actual values (b) normalised values and (c) RSD (relative standard deviation).....	196
Figure 7.10: Total bed surface velocity ($v_{surf,t}$) with impeller rotation for dry and wet (2% w/w water) bed of polypropylene balls.....	198
Figure 7.11: Total bed surface velocity ($v_{surf,t}$) with impeller rotation for wet (5% w/w and 10% w/w water) bed of polypropylene balls.....	199
Figure 7.12: Total bed surface velocity ($v_{surf,t}$) with impeller rotation for wet (15% w/w and 25% w/w water) bed of polypropylene balls.....	200

Figure 7.13: Experimental blade–granule bed stress results: (a) temporal values and RSD (relative standard deviation) for 0.5-1.0 mm, 1.5 kg granule bed (b) time-averaged values for different sieve sizes (c) time-averaged values for different bed loads.	203
Figure 7.14: Simulated blade-bed stress results for 3.5 mm, 1.5 kg bed of particles (a) temporal blade–bed stress and (b) FFT analysis.....	205
Figure 7.15: Simulated temporal blade–bed stress at 350 rpm (Fr : 0.97) for (a) different particle sizes and (b) different bed loads.	206

Appendix figures:

Figure A.1: Schematic diagram of the pressure colouring film.	227
Figure A.2: Pressure chart for LW (low pressure) film (Fujifilm Corporation, 2012b).....	229
Figure A.3: Calibration image for a 4LW film: coloured patches from six compressions.	230
Figure A.4: Pressure calibration plots for 3LW and 4LW films.	230
Figure A.5: Measurement using pressure films in the high shear granulator (a) film strip on the blade (b) film strip (C-film) after measurement.	231
Figure A.6: Segmented areas (indicated by the bright red patches) of the film for area determination (x37.5 magnification - 2.3 mm x 1.6 mm).	232
Figure A.7: Results for varying impeller speed, angle and bed load cases (pressure film method).....	233
Figure A.8: Plotted measured blade-bed stress using the pressure films with (a) blade-bed stress equation (no correction factor, Equation 4.8) and (b) blade-bed stress model with correction factor $B_I = K_I/v_{rel}$ (Equation 4.12).	235
Figure A.9: Comparison with the impeller stress sensor (a) pressure film affixed onto the blade (b) pressure film (C-film) after measurement.....	236
Figure A.10: Measured blade-bed stress using the impeller stress sensor and pressure film for 0.5-1.0 sieve size dry mannitol granules, 1.5kg bed load. Dashed lines represent the time-averaged values from the sensor measurements.	237
Figure A.11: Micro-capsules containing colour-forming material on the A-film (4LW grade).	238
Figure B.1: Schematic of a multiple exposure image (arrow indicates the displacement vector).	239
Figure B.2: Pixel-distance values at different mixer heights.....	241
Figure B.3: Temporal bed surface velocity (circumferential+radial components), $v_{surf,t}$, for 0.1-0.5 mm mannitol granules at 150 rpm impeller speed for different interrogation area sizes. ...	243
Figure B.4: Temporal bed surface velocity (circumferential+radial components), $v_{surf,t}$, for 0.5-1.0 mm mannitol granules at 150 rpm impeller speed for different interrogation area sizes. ...	243
Figure B.5: Temporal bed surface velocity (circumferential+radial components), $v_{surf,t}$, for 1.0-2.0 mm mannitol granules at 150 rpm impeller speed for different interrogation area sizes. ...	244

Figure B.6: Temporal bed surface velocity (circumferential+radial components), $v_{surf,t}$, for 2.0-4.75 mm mannitol granules at 150 rpm impeller speed for different interrogation area sizes.	244
Figure B.7: Time-averaged bed surface velocity (circumferential+radial components), $v_{surf,t}$, at different interrogation area sizes for different mannitol granule sieve sizes.	245
Figure C.1: Spray rate calibration with different nozzle sizes for water.	246
Figure D.1: Particle bed image for 1.0 kg (left column) and 1.5 kg (right column) bed loads. The colour bar indicates the particle total velocity in m/s (and also for subsequent figures in Appendix D).	247
Figure D.2: Particle bed images for 2.0 kg (left column) and 3.0 kg (right column) bed loads.	248
Figure D.3: Particle bed images for 2.0 mm (left column) and 3.5 mm (right column) particles.	249
Figure D.4: Particle bed images for 5.0 mm (left column) and 10.0 mm (right column) particles.	250
Figure D.5: Particle bed images for 600 kg/m ³ (left column) and 1230 kg/m ³ (right column) particles.	251
Figure D.6: Particle bed images for 2500 kg/m ³ particles.	252
Figure D.7: Particle bed images for $\mu_f = 0.02$ (left column) and $\mu_f = 0.1$ (right column).	253
Figure D.8: Particle bed images for $\mu_f = 0.3$ (left column) and $\mu_f = 0.5$ (right column).	254
Figure D.9: Particle bed images for $\mu_f = 0.9$ (left column) and $\mu_f = 1.5$ (right column).	255
Figure D.10: Simulated time-averaged blade-bed stress, bed surface circumferential velocity and bed height along the radial position for $\mu_f = 0.02$ (left column) and $\mu_f = 0.3$ (right column).	256
Figure D.11: Particle bed images for different restitution coefficients. Left: 150 rpm, Right: 350 rpm.	257
Figure D.12: Particle bed images for different Young's modulus. Left: 150 rpm, Right: 350 rpm.	258
Figure D.13: Simulated time-averaged number of particles in contact with the blade at the sensor region, N_p , for different Young's modulus.	259
Figure D.14: Particle bed images for $h_w = 20$ mm (left column) and $h_w = 35$ mm (right column).	260
Figure D.15: Particle bed images for $h_w = 50$ mm (left column) and $h_w = 65$ mm (right column).	261
Figure D.16: Plot of $\log(B_2 Fr_{rel}^{0.5})$ against $\log(2h_w/D)$ for different blade width cases from simulation.	262
Figure D.17: Particle bed images for 20° (left column) and 32° (right column) inclined blades.	263
Figure D.18: Particle bed images for 45° (left column) and 65° (right column) inclined blades.	264

Figure D.19: Particle bed images for 90° inclined blades.	265
Figure D.20: Particle bed images for the 2-bladed (left column) and 3-bladed (right column) impellers.	266
Figure D.21: Particle bed images for the 4-bladed impellers.	267
Figure D.22: Simulated time-averaged blade-bed stress (left column) and bed height (right column) along the radial position for different number of blades.	268
Figure D.23: Particle bed images for the 0.173 L, $D/d_p = 20$ (left column) and 1.39 L, $D/d_p = 40$ (right column) granulators.	269
Figure D.24: Particle bed images for the 11.1 L, $D/d_p = 80$ (left column) and 88.7 L, $D/d_p = 160$ (right column) granulators.	270
Figure D.25: Particle bed images for the 0.173 L (left column) and 1.39 L (right column) granulators ($D/d_p = 80$).	271
Figure D.26: Particle bed images for the 11.1 L (left column) and 88.7 L (right column) granulators ($D/d_p = 80$).	272

List of tables

Chapter tables:

Table 1.1: Wet agitation granulation equipment (summarised from Snow et al., 1997).....	4
Table 2.1: Effect of powder, binder properties and agitation intensity on consolidation behaviour.	15
Table 2.2: Effect of powder, binder properties and agitation intensity on wet granule strength.	23
Table 2.3: Dimensionless parameters in "Granulation growth regime map".	25
Table 2.4: Regimes in the "Granulation growth regime map".	26
Table 2.5: Qualitative prediction of the effect of processing and formulation variables on granule growth behaviour (summarised from Iveson & Litster, 1998b).....	27
Table 2.6: Stress and monitoring measurements in granulators.	33
Table 3.1: Properties of paraffin oil.....	53
Table 4.1: Powder grades and properties.....	67
Table 4.2: Formulation for the different granules.	68
Table 4.3: Size and density properties of different formulation granules and polypropylene balls.....	69
Table 4.4: Single and bulk granule/particle strength.	71
Table 5.1: Bed bulk density and bed porosity of the dry and wet beds.	96
Table 5.2: Granulation formulation and operating conditions for unsteady-state measurements.	101
Table 6.1: Stiffness and damping coefficients models used for the DEM soft sphere model in this thesis.	116
Table 6.2: Measured Young's modulus of dry mannitol granules.	119
Table 6.3: Simulation parameters for different particle bed/particle properties.....	120
Table 6.4: Simulation parameters for different impeller geometries.....	121
Table 6.5: Simulation parameters for different granulator scales.	123
Table 6.6: Froude numbers in commercial high shear granulators.	144
Table 6.7: Summary of the fitted constants for the correction factors.	179
Table 7.1: Summary of the fluctuation periodicity of the bed surface velocity and bed height for dry mannitol granule beds.	201
Table 7.2: Summary of the fluctuation periodicity of the bed surface velocity and bed height for dry and wet beds of polypropylene balls.	202
Table 7.3: Summary of the blade-bed stress fluctuation properties for different particle/particle bed properties at Fr : 0.97 (350 rpm in the 11.1 L granulator) from simulation.	207

Table 7.4: Summary of the blade-bed stress fluctuation properties for different impeller geometries and granulator scale at Fr : 0.97 from simulation.....	208
--	-----

Appendix tables:

Table A.1: Grades of the pressure films (FujiFilm Corporation, 2009a)	228
Table A.2: Formulation and granulation conditions for pressure film measurements.	232

Nomenclature

a_p	acceleration of particle/granule
$a_{I,tip}$	acceleration of the impeller tip
A_p	contact area of impeller stress sensor
B_1	correction parameter 1 for the blade-bed stress equation ($\sigma_{i(r)cor}$)
B_2	correction parameter 2 for the blade-bed stress equation ($\sigma_{i(r)cor}$)
C	particle shape constant
Ca	Capillary number
Co	correlation number (for PIV)
D	impeller diameter
$dF_{i(r)}$	inertial blade-particle/granule bed force at a particular radial position
D_l	distance between loading points (for single particle/granule compression)
d_p	particle/granule diameter
dr	radial displacement of the particle/granule bed
$d_{v,10}$	10 th percentile of the particle size volume-based distribution
$d_{v,50}$	50 th percentile (median) of the particle size volume-based distribution
$d_{v,90}$	90 th percentile of the particle size volume-based distribution
$d\alpha$	angular displacement of the particle/granule bed
e	restitution coefficient
E^*	effective Young's modulus
E_p	particle/granule Young's modulus
E_w	Young's modulus of the wall
f_1, f_2	pixel values of first and second images respectively (for PIV)
F_{Ci}	total interparticle and particle-wall contact force for particle i (for DEM simulation)
$F_{Cl,n}$	normal component of blade-particle force (for DEM simulation)
$F_{Cn,ij}$	normal contact force between particle i and particle j (for DEM simulation)
$F_{Ct,ij}$	tangential contact force between particle i and particle j (for DEM simulation)
F_f	load during fracture (for single particle/granule compression)
F_H	horizontal force on a linear blade
Fr	Froude number
$Fr_{rel}^{0.5}$	relative Froude number (square root)

g	gravitational acceleration
G_p	particle/granule shear modulus
h_0	thickness of liquid binder layer on particle/granule
H_0	initial granule bed height (for bulk granule compression)
h_a	length of particle/granule surface asperities
$H_{g,R}$	particle/granule bed height at the wall
$H_{g,r}$	particle/granule bed height at a particular radial position
H_{g0}	undisturbed particle/granule bed height
h_I	impeller blade inclined height
H_{max}	maximum falling distance (for a tumbling drum)
H_S	height of surcharge
h_w	impeller blade width
I_i	moment of inertia of particle i (for DEM simulation)
K_1	fitted constant 1 for the corrected blade-bed stress equation ($\sigma_{i(r)cor}$)
K_2	fitted constant 2 for the corrected blade-bed stress equation ($\sigma_{i(r)cor}$)
K_c	dimensionless particle/granule consolidation rate
k_n	normal stiffness (for DEM simulation)
K_p	coefficient of passive failure
k_t	tangential stiffness (for DEM simulation)
L_I	blade length (linear blades)
$m_{b,r}$	mass of the particle/granule bed at a particular radial position
M_{Ci}	total torque of particle i (for DEM simulation)
m_i	mass of particle i (for DEM simulation)
m_p	particle/granule mass
N_D	number of drum revolutions
n_I	number of impeller blades
\mathbf{n}_{ij}	unit vector of the centre of particle i to the centre of particle j (for DEM simulation)
N_x, N_y	sizes of the interrogation area (for PIV)
$/Output/$	normalised output of the impeller stress sensor
P	sum of the pixel value differences (for PIV)
R	impeller radius
r	radial position in the cylindrical granulator
r_p	particle/granule radius

s	granule liquid saturation
s_{max}	maximum granule liquid saturation
St_{def}	Stokes deformation number
Str^*	dimensionless strength
St_v	Stokes viscous number
St_v^*	critical Stokes viscous number
$t_{contact,H}$	Hertzian particle contact time
\mathbf{t}_{ij}	unit vector in the tangential direction between particle i and particle j (for DEM simulation)
u_0	particle/granule initial or characteristic velocity
v_g	particle/granule bed linear velocity
\mathbf{v}_i	translational velocity of particle i (for DEM simulation)
v_I	impeller blade linear velocity
V_p	particle volume
$\mathbf{v}_{r,ij}$	relative velocity between particle i and particle j (for DEM simulation)
v_{rel}	relative velocity between the blade and the particle/granule bed
$\mathbf{v}_{rt,ij}$	relative tangential velocity (slip velocity) at the contact surface between particle i and particle j (for DEM simulation)
$v_{surf,c}$	bed surface velocity (circumferential component)
$v_{surf,r}$	bed surface velocity (radial component)
$v_{surf,t}$	bed surface velocity (circumferential+radial component)
v_{tip}	impeller tip velocity
w	binder content, i.e. liquid to solid weight ratio
W_f	gap height between the bottom of blade to the undisturbed particle bed surface
x	interparticle gap
x_i, y_j	x and y coordinates in the image (for PIV)
Y_p	wet particle/granule yield strength
Z	immersion of the blade

Greek characters:

α'	parameter proportional to the friction coefficient (for bulk granule compression)
β	parameter function of the restitution coefficient (for DEM simulation)
γ_l	liquid surface tension
Δ	displacement of particle/granule or particle/granule bed (for single or bulk granule compression)
$\delta_{n,ij}$	depth of the particle deformation or displacement due to normal force between particle i and particle j (for DEM simulation)
$\delta_{t,ij}$	depth of the particle deformation or displacement due to tangential force between particle i and particle j (for DEM simulation)
ϵ'	natural strain (for bulk granule compression)
$\dot{\epsilon}$	strain rate
ϵ_b	particle/granule bed porosity
ϵ_p	intra-particle/granule porosity
η_n	normal damping coefficient (for DEM simulation)
η_t	tangential damping coefficient (for DEM simulation)
θ_I	impeller blade inclination angle
θ_{lf}	liquid-solid interfacial contact angle
μ_l	liquid viscosity
μ_f	sliding friction coefficient (for DEM simulation)
μ_p	coefficient of interparticle friction
μ_r	rolling friction coefficient (for DEM simulation)
ρ_a	particle/granule apparent density
ρ_b	particle/granule bed bulk density
ρ_L	liquid density
ρ_p	particle/granule density
ρ_s	solid density
ρ_t	particle/granule true density
$\sigma_{i(r)}$	impeller blade-bed normal stress at a particular radial position
$\sigma_{i(r)cor}$	impeller blade-bed normal stress at a particular radial position with correction parameter
σ_n	normal component of the blade-particle contact stress (for DEM simulation)
τ_o'	bulk agglomerate strength parameter (for bulk granule compression)
τ_s	particle/granule tensile strength

ν_p	particle/granule Poisson's ratio
ν_w	Poisson's ratio of the wall
Φ	granule packing coefficient
ϕ_f	dynamic angle of friction between between the granules and the floor
ϕ_p	angle of internal friction
ϕ_l	liquid fraction
ϕ_s	solid fraction
ϕ_w	angle of wall friction
ψ_c	degree of particle/granule consolidation
ω_g	particle/granule bed rotational velocity
ω_i	rotational velocity of particle i (for DEM simulation)
ω_I	impeller rotational speed

Abbreviations:

CCD	charge-coupled device
CFD	Computational Fluid Dynamics
COR	Cross-Correlation Algorithm (for PIV)
DAQ	data acquisition
DEM	Discrete Element Method
FFT	Fast Fourier Transform
HPC	Hydroxypropylcellulose
L/S	liquid to solid weight ratio
MCC	Microcrystalline cellulose
MQD	Minimum Quadratic Difference (for PIV)
PEPT	Particle Emission Positron Tracking
PIV	Particle Imaging Velocimetry
RSD	relative standard deviation

Chapter 1

Introduction

This chapter starts with a general background to the research area, i.e. granulation, followed by the motivation behind this thesis, the main objectives to achieve and finally a description on how this thesis is structured.

1.1 Granulation: What, why and how?

What?

Granulation, a unit operation in chemical engineering processes specifically for particle processing, is the process of producing granules from primary particles. By definition, *granulation* is a particle size enlargement process which involves several competing rate processes or mechanisms (Iveson, 2001) and a *granule* is an assemblage of primary particles held together by one or a combination of interparticle bonding forces or mechanisms. These include:

- Attractive forces between solid particles, such Van der Waals and electrostatic forces;
- Adhesion, cohesion and interfacial forces due to the presence of liquid;
- Solid bridges from hardening of binder, partial melting or crystallisation of dissolved materials; and
- Mechanical interlocking between pores or irregularities of particle surfaces.

The granular products are sometime classified as either granules or pellets. Granules are agglomerates which are irregular in shape with a wider size distribution while pellets are more spherical agglomerates with a narrow size distribution (Seo and Schaefer, 2001).

Why?

Granulation is carried out extensively in a broad range of industries such as pharmaceutical, food, agricultural, homecare and fine chemicals, to produce granular products for end-users (consumers) or intermediate products for subsequent processing. Some examples of granular products include instant drink or soup granules, food flavouring cubes, granules for pharmaceutical tablets, fertilizers, detergent powders and catalysts. There are numerous reasons for granulation depending on the application, for instance to:

- Improve strength of the particles to withstand handling or transportation conditions;
- Prevent segregation of the constituents of a powder mix;
- Ensure uniform distribution of the constituents of a powder mix, such as the active drug components for pharmaceutical tablets;
- Reduce dustiness of the product and therefore human hazard or explosion risks;
- Improve flowability of the product for storage and transportation. Fine powders are cohesive and difficult to flow;
- Increase bulk density, such as for storage and transportation where the volume of material is reduced;
- Improve compressibility of granules, such as for drug or food tablets;
- Reduce caking and lumping for hygroscopic material since granules can absorb more moisture and retain their flowability due to their larger size;
- Improve product appearance, e.g. smooth, spherical granules with uniform size distributions;
- Control the dissolution characteristics, such as for food granules; and
- Control the surface area per volume and porosity, such as for catalysts.

How?

In general, there are several types of granulation which could be categorised as either:

- Wet agitation granulation, which is the type of granulation studied in this thesis and is described further below;
- Compression-type or pressure granulation where pressure is applied on the primary particles to promote the interparticle bonds without the addition of liquid (although solid binder may or may not be used). Examples of this type of agglomeration are dry extrusion, roller compaction, tablet pressing and pellet milling (Litster and Ennis, 2004); and
- Heat bonding granulation such as sintering where the powders are heated below their melting point until they adhere to each other (Sherrington, 1981).

In wet agitation granulation, liquid binder is added to the solid primary particles (Figure 1.1). Interparticle bonds are created from the presence of liquid and subsequently from solid bridges after drying. During the process, the granulating mixture is also continuously subjected to agitation that is induced mechanically or by other means. This is important to mix the granulating mixture, disperse the binder uniformly and impart forces onto the granulating mixture for size enlargement. The solid primary particles and liquid binder are commonly known as the granulation formulation, and the solid ingredients can include active material (e.g. active drug ingredients for pharmaceutical formulations), excipients or fillers, additional binders, diluents, flow aids, surfactants, wetting agents, lubricants, or end use aids (Green and Perry, 2008). Common equipment used for wet agitation granulation is summarised in Table 1.1.

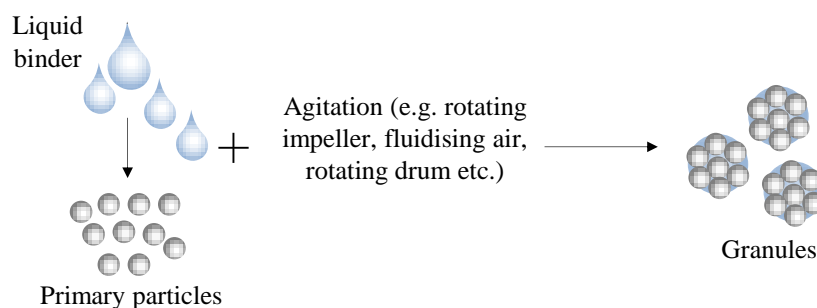


Figure 1.1: Schematic of the general wet agitation granulation process.

Table 1.1: Wet agitation granulation equipment (summarised from Snow et al., 1997).

<i>Equipment</i>	<i>Agitation method</i>
Mixer granulator (batch or continuous high shear mixers) e.g.: horizontal (plough mixer, paddle mixer, ribbon mixer), vertical (cylindrical mixer, conical mixer, pan mixer)	Impeller (vertical axis cylindrical mixer), ploughshare (plough mixer), paddle (paddle mixer)
Tumbling granulator e.g.: Rolling drum, discs granulators	Rotating/rolling motion of drum
Fluidised bed granulator	Fluidising gas
Twin screw granulator	Rotating screws

Ultimately, granulation is carried out to obtain granular products that achieve or meet specific attributes depending on the application. For instance, granules for instant drinking powders should readily dissolve (influenced by granule porosity) while granules intended for tableting should have high compressibility (influenced by granule size, shape, surface area, density and strength). For this, characterisation and analysis of final product properties is a crucial step following the granulation process and can be divided into the following categories:

- Granule size/size distribution and specific surface area.
- Granule outer morphology such as surface properties and shape.
- Granule inner morphology such porosity, composition, binder content and homogeneity.
- Granule mechanical properties such compressive strength, impact strength, Young's modulus and friability.
- Dissolution characteristics.
- Flow properties such bulk density and frictional properties.

These attributes are dictated by the granulation rate processes, which are in turn affected by a variety of factors during processing, such as those listed below for the wet agitation granulation process:

- Formulation variables such as the amount and properties of primary particles (physical properties) and binder (rheological properties).
- Processing variables such agitation intensity, temperature, binder addition method, binder addition rate and processing time.

- Equipment variables such as granulator geometry, configuration and granulator scale/size.

In granulation, structured experiments are often carried out to investigate the effect of the aforementioned variables on the granular product attributes, which is of interest to generate an ideal “working space” of the process that gives the desired granules attributes. This is however heavily based on empirical knowledge rather than sound scientific principles and more often than not, a large number of “trial and error” experiments are required to achieve the ideal granulation conditions.

1.2 Research motivation and objectives

As elucidated in the previous section, in order to achieve better scientific control of granulation it is important to understand how formulation, processing and equipment variables influence the underlying granulation rate processes. Micro-scale models have been developed to describe some of the rate processes or mechanisms, for instance granule coalescence (i.e. the sticking of two granules or particles). A more recent development involves the macro-scale approach of linking formulation, processing and equipment variables to the granule growth behaviour based on understanding and application of the rate processes, also known as the “Granulation growth regime map” (Iveson and Litster, 1998b; Iveson et al., 2001b). One of the fundamental parameters in both the micro-scale models and the “Granulation regime map” is the external stress exerted on the granules. The stress affects the rate processes and thus plays a role in dictating the granule growth behaviour and ultimately the granule attributes.

Therefore, the primary objective of this thesis is to improve the understanding of the external stress exerted on the granules in high shear granulation, specifically in a vertical axis, cylindrical high shear granulator. For the high shear granulator, the stress of interest is the impeller blade-granule bed stress. To achieve this, the research is divided into the following main parts:

- Development of a novel, direct impeller blade-granule bed stress measurement method in the high shear granulator; measurement and theoretical prediction of the impeller blade-bed

stresses in the granulator for different processing conditions (impeller speed, particle or particle bed properties and liquid addition).

- Application of simulations (DEM) for further characterisation of the blade-bed stress for different particle/particle bed properties, impeller blade geometries and granulator scales.
- Further insight on the blade-bed stress and bed flow across different flow regimes in the granulator.

1.3 Thesis structure

This thesis is structured in the following order:

- Chapter 2 presents a comprehensive review of the relevant literature and highlights the gaps in knowledge that this research work aims to fill;
- Chapter 3 explains the measurements and analysis methods employed, particularly highlighting the development of a novel, direct impeller blade-granule bed stress measurement method in a high shear granulator;
- Chapter 4-7 presents the core results and achievements: Chapter 4 focuses on experiments of dry granule/particle beds in the high shear granulator; Chapter 5 studies wet granule/particles beds; Chapter 6 presents further characterisation of the blade-bed stress using Discrete Element Method (DEM) simulations; and Chapter 7 presents additional insight of the granule bed behaviour across flow regimes;
- Chapter 8 summarises the overall conclusions and achievements of this research work and discusses the scope for future work stemming from this study; and
- The appendix provides supplementary information and material.

Each chapter also commences with a brief introduction section presenting the chapter's structure and content.

Chapter 2

Literature review

2.1 Introduction

The content of this chapter is presented in the following order:

- Following the brief introduction of granulation in Chapter 1: Section 1.1, further review on the wet agitation granulation process, with emphasis on the main rate processes, is presented;
- Review of granule growth and growth behaviours: (a) micro-scale models and (b) macro-scale characterisation of the granule growth behaviour, followed by the development of the granulation regime maps;
- Review of granule stresses in high shear granulators; the importance, characterisation work and measurement methods; and
- Outlook from the literature review.

2.2 Wet agitation granulation: the three main rate processes

As previously described, in the wet agitation granulation process, binder is introduced in liquid form into the granulating mixture while being continuously agitated. The process often involves the following main steps:

- Dry mixing of the powder;
- Addition of binder; common methods for mixer granulators are via spraying (Holm et al., 1985b; Ohno et al., 2007; Realpe and Velazquez, 2008), pouring (Hoornaert et al., 1998; Knight et al., 2000; Tu, 2008), or drip in (Ohno et al., 2007);
- Wet massing, i.e. agitation of the granulating mixture after the completion of binder addition; and
- Drying of granules, e.g. with an oven or fluidised bed.

Another common wet granulation method is melt granulation, also known as a single step process (Schaefer, 2001; Tan et al., 2006; Theis and Kleinebudde, 1999; Walker et al., 2006). Powdered or flaked binder is mixed together with the initial powder mixture and melted with the application of heat. The wet agitation granulation process is generally divided into three main and competing rate processes which have been widely accepted in modern granulation: wetting and nucleation; consolidation and growth; and breakage and attrition (Ennis and Litster, 1997) (Figure 2.1). The final granule attributes such as size, strength, porosity and morphology ultimately depends on the balance of these rate processes.

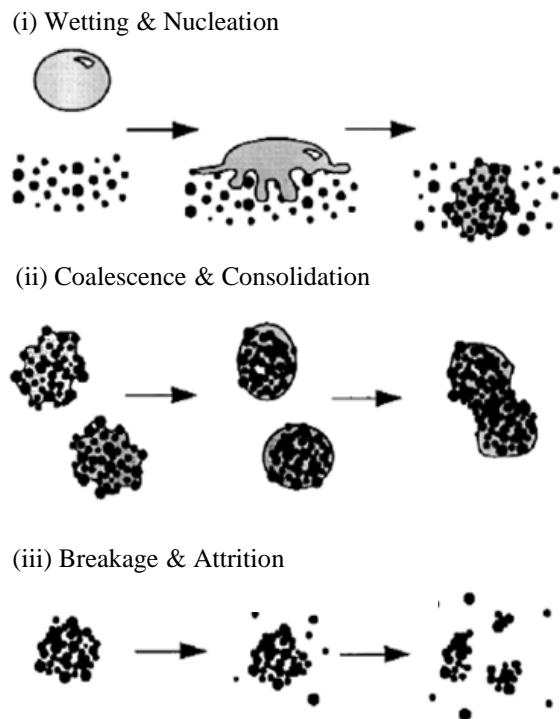


Figure 2.1: Competing rate processes or mechanisms in wet agitation granulation processes (modified from Ennis & Litster, 1997).

2.2.1 Wetting and nucleation

Wetting and nucleation is the first stage of the granulation process where liquid is brought into contact with the powder, imbibes into the bed to a certain degree and is then dispersed throughout the system. This stage is important as poor wetting produces nuclei with broad size distributions or a mixture of overwet and ungranulated material. Preferential wetting of the binder also leads to inhomogeneous composition in the granules (Hapgood et al., 2007). Two

key processes take place in this stage (Iveson et al., 2001a). The first is the formation of ‘nuclei’, which occurs as the liquid droplet penetrates into the powder bed and forms an initial weak, loose particle assembly. The process is governed by wetting thermodynamics (i.e. if the process is energetically favourable) and wetting kinetics (i.e. rate of droplet penetration into the solid pores or spreading across the surfaces). The second process is the binder dispersion which is promoted by mechanical agitation. Effective binder dispersion more often results in granules with more uniform properties and a narrower size distribution (Holm et al., 1984; Holm et al., 1983).

It was also proposed that two different nuclei formation mechanisms exist depending on the relative size of the droplet and primary particles (Schaefer and Mathiesen, 1996) (Figure 2.2). If the drop size is relatively small, the distribution mechanism is likely to take place; the binder droplets are distributed on the primary particles surfaces followed by the coated particles sticking to each other. This mechanism typically yields nuclei with air voids. Conversely, if the binder droplet size is relatively large compared to the powder size, the immersion mechanism occurs where the small particles are immersed in the drop, which usually produces nuclei with saturated pores.

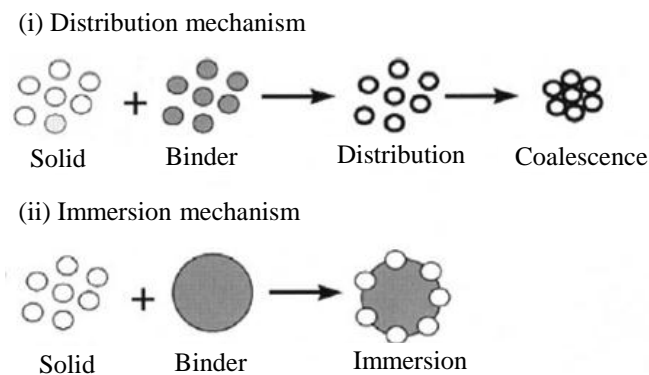


Figure 2.2: Distribution and immersion mechanisms in the formation of nuclei (modified from Schaefer and Mathiesen, 1996)

2.2.2 Coalescence and consolidation

The second rate process during wet agitation granulation is coalescence and consolidation. Consolidation is defined as the compaction of the initial nuclei and granules by impact with the agitator, vessel wall and collision with the other granules. The extent of consolidation will

ultimately determine the porosity and strength of the final product. More consolidated granules will be less porous and hence, stronger and vice versa. Granule coalescence is described as the enlargement of granules as more particles come together and stick with each other through formation of interparticle bonds which are strong enough to resist the separating forces in the system. Consolidation is also closely related to granule coalescence since a higher degree of consolidation typically causes more interstitial liquid to be squeezed out onto the granule surface thus promoting coalescence and growth. Several coalescence and consolidation models have been developed for different types of particles (i.e. elastic, plastic, surface-dry or surface-wet) and these models are reviewed in Section 2.3.1.1 and 0 which also discusses the granule growth phenomena in more detail.

2.2.3 Breakage and attrition

The final rate process which can affect the final granule attributes can be divided into two phenomena as shown in Figure 2.3 (Iveson et al., 2001a).

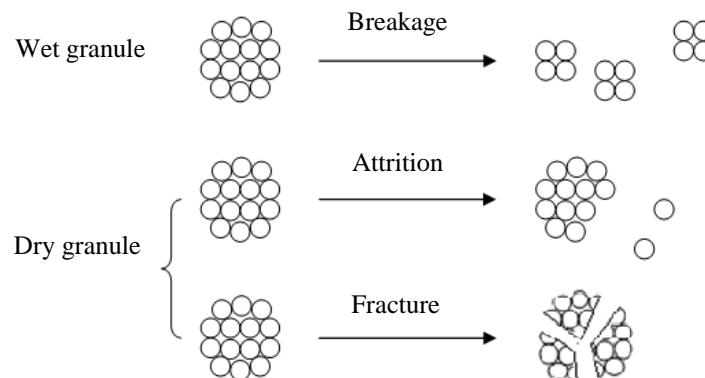


Figure 2.3: Granule breakage and attrition.

If bonds formed in the granules are not strong enough to resist the separating forces in the granulator after a certain time, breakage of the wet granules will take place. Attrition or fracture of the dry granules may also occur due to binder solidification inside the granulator or during subsequent drying and handling stages. The breakage and attrition phenomena depend largely on the fracture mechanics and mechanical properties of the granules (such as elastic modulus, hardness, fracture toughness etc) as well as the types and magnitudes of stress

application. Several models to predict the conditions under which wet granule breakage will occur have been developed and are presented in Section 2.3.1.3.

2.3 Granule growth and growth behaviour

Granule growth is generally described as the increase granule size with the granulation time, and for wet agitation granulation these occur during the liquid addition and wet massing steps. There are several modes of granule growth (Sastry and Fuerstenau, 1973), as follows:

- Nucleation: formation of an initial 'nuclei' of loosely held primary particles by the liquid binder either by the distribution or immersion mechanism as shown previously in Figure 2.2.
- Coalescence: (a) random, i.e. two similar size particles colliding and sticking together or rebounding, or (b) preferential, i.e. sticking of multiple small particles on the surface of a larger agglomerate, also typically known as "layering", "snow-balling" or "onion-layering".
- Crushing and layering and abrasion transfer for weaker, brittle granules.

In the micro-level (single particles) scale, several coalescence models have been developed to describe the sticking of two equi-sized spherical particles. These models differ in the material properties of the particles and surface conditions such as elastic, plastic or elastoplastic and surface wet or surface dry. There are several factors contributing to the coalescence phenomena such as the wet granule strength, force exerted on the particles and amount of liquid binder at the particle surface. Granule consolidation leads to transfer of liquid to the granule surface, thus altering the liquid amount and ultimately affects the coalescence process. Breakage of granules is another phenomenon that limits granule growth, ultimately affecting the growth behaviour. Therefore, micro-scale models to describe the following rate processes are presented in Section 2.3.1: consolidation, coalescence and breakage.

In the macro-scale or processing level, granule growth is typically classified in terms of the growth behaviour during processing, i.e. change of granule size with granulation time. Based on these growth behaviours, regime maps to link formulation, processing and equipment

variables to the growth behaviours are built with the most significant development being the "Granulation regime map" by Iveson and co-workers (Iveson and Litster, 1998b; Iveson et al., 2001b).

2.3.1 Micro-scale modelling

2.3.1.1 Granule consolidation

The consolidation process is described as the compaction of granules through interparticle, particle-agitator and/or particle-wall collisions, which leads to the reduction of granule porosity. For wet granules, the extent and rate of consolidation depends on the interaction of three forces: friction from interparticle contact, capillary and viscous forces from the interparticle liquid bridges, the same forces which contribute to the strength of granules (Iveson et al., 2002; Iveson and Litster, 1998a; Iveson et al., 1996). Logically, granules that are stronger will be harder to consolidate and vice versa. The reduction of granule porosity is commonly used to describe the consolidation process (Iveson and Litster, 1998a; Iveson et al., 1996; Ouchiyama and Tanaka, 1980). Ennis et al and Tardos et al, on the other hand, modelled the granule consolidation in terms of reduction of interparticle gap (Ennis et al., 1991; Tardos et al., 1997). Figure 2.4 displays the milestones in the development of consolidation models.

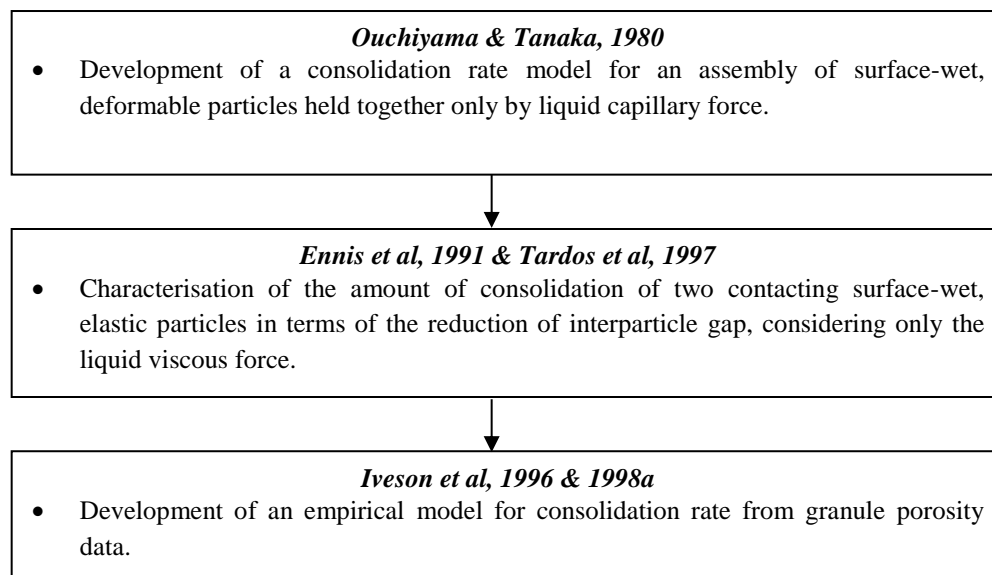


Figure 2.4: Development of granule consolidation models.

Ouchiyama and Tanaka considered a granular matrix held together by the liquid capillary force which generates a normal resistive force at the interparticle contacts (Ouchiyama and Tanaka, 1980). Taking into account the packing coordination number of spherical granules, i.e. the number of neighbouring particles that are in contact with the central particle, consolidation is described as the increase of the coordination number as the external applied force is increased. The coordination number is then related to the granule porosity. The detachment of the granules due to dilation was not considered in this case. From force balance of the external applied force and resisting force of the granule assembly, the rate of consolidation, i.e. change of porosity with time, $d\varepsilon_p/d\tau$, is given by Equation 2.1. τ is the dimensionless consolidation time, K_c is the dimensionless consolidation rate, n_i is the parameter describing the distribution of granule impact energies, q is the collision frequency, t is the granulation time, ρ_p is the particle density, g is the gravitational acceleration, H_{max} is the maximum falling distance (for a tumbling drum), $f(\mu_p)$ is a function of the coefficient of interparticle friction, $\Phi(s)$ is a function of granule saturation and particle assembly, d_p is the particle diameter, γ_l the liquid surface tension and θ_{lf} is the liquid-solid interfacial contact angle.

$$\frac{d\varepsilon_p}{d\tau} = - \left\{ 1 - \frac{(1 - \varepsilon_p)^3}{\varepsilon_p \cdot K_c} \right\}^n$$

$$\tau = \left(\frac{13}{256} \right) q \cdot t; K_c = \frac{16}{3} \frac{\rho_p g H_{max}}{f(\mu_p) \Phi(s) \gamma_l \cos \theta_{lf}} \frac{d_p}{\rho_p g H_{max}}$$

Equation 2.1

In Ennis and co-workers' work, for non-rebound cases of two contacting particles, when the initial kinetic energy is fully dissipated, subsequent collisional forces results only in the reduction of the interparticle gap (Ennis et al., 1991). This reduction of the interparticle gap, Δx , is the amount of consolidation, which is given in Equation 2.2, where only the liquid viscous force is considered. h_0 is the thickness of the binder layer which is also assumed to be half the initial gap distance and St_v is the Stokes viscous number (Equation 2.4). Tardos and co-workers also rewrote Equation 2.2 in terms of the degree of consolidation, ψ_c (Equation 2.3) (Tardos et al., 1997).

$$\Delta x = 2h_0(1 - e^{-St_v})$$

Equation 2.2

$$\psi_c = \frac{\Delta x}{2h_0} = (1 - e^{-St_v})$$

Equation 2.3

$$St_v = \frac{2m_p u_0}{3\pi\mu_l r_p^2} = \frac{8\rho_p u_0 r_p}{9\mu_l}$$

Equation 2.4

In Equation 2.4, m_p is the particle mass, u_0 is the particle initial velocity, r_p is the particle radius, ρ_p is the particle density and μ_l is the liquid viscosity. The Stokes viscous number gives the ratio of the initial kinetic energy of the colliding granules to the energy dissipation by the viscous liquid layer, first defined by Ennis and co-workers, and is an important dimensionless parameter in granule coalescence studies.

An empirical equation to describe the consolidation rate (Equation 2.5) is proposed by Iveson and co-workers from granule porosity data using glass ballotini as powder and water and aqueous glycerol solutions as binder granulated in a drum granulator (Iveson and Litster, 1998a; Iveson et al., 1996). Exponential decay of the porosities were observed. $\varepsilon_{p,min}$ is the minimum porosity reached, $\varepsilon_{p,0}$ is the granule initial porosity, k_c is the consolidation rate constant and N_D is the number of drum revolutions.

$$\frac{\varepsilon_p - \varepsilon_{p,min}}{\varepsilon_{p,0} - \varepsilon_{p,min}} = \exp(-k_c N_D)$$

Equation 2.5

From literature, various experiments have been conducted to investigate the consolidation behaviour at different formulation and processing variables. Table 2.1 summarises the results for studies of changing the powder, binder properties and agitation intensity.

Table 2.1: Effect of powder, binder properties and agitation intensity on consolidation behaviour.

<i>Powder/binder Properties</i>	<i>Effect of consolidation behaviour</i>		<i>Mechanistic explanation</i>
	<i>Consolidation rate ($d\varepsilon_p/dt$)</i>	<i>Extent of consolidation ($\varepsilon_{p,min}$)</i>	
Primary particle size, d_p	Increase as d_p increase (Iveson and Litster, 1998a; Schaefer et al., 1990)	Increase as d_p increase (Gabbott, 2007; Ganderton and Hunter, 1971; Iveson and Litster, 1998a; Schaefer and Mathiesen, 1996)	The interparticle force decreases as d_p increases (number of interparticle contact decrease); the viscous force decreases as d_p increases (due to increasing average gap distance) and capillary force also decreases as d_p increase (liquid bridge curvature decrease). All these forces contribute to the strength of the granules. Hence, reduction of these forces will promote consolidation.
Binder viscosity, μ_l	Decrease as μ_l increase (Iveson and Litster, 1998a; Keningley et al., 1997; Schaefer and Mathiesen, 1996)	At low binder content, increase as μ_l increase; at high binder content, decrease as μ_l increase (Iveson and Litster, 1998a)	The consolidation behaviour of granules for varying binder viscosity depends on the balance between the interparticle friction and viscous force. The interparticle friction could decrease as μ_l increases due to better lubricating effect and conversely, the viscous force increases with increasing μ_l . At high binder content, the particles are more lubricated and granules are compacted more easily, while at lower binder content, the viscous force dominates which hinders consolidation.
Binder content, w	Does not change significantly with w (Iveson and Litster, 1998a)	At low viscosity, increase as w increase; At high viscosity, decrease as w increase (Iveson and Litster, 1998a; Schaefer et al., 1990)	Similar to the viscosity effect, the consolidation behaviour for varying binder content depends on both the friction and viscous force. The interparticle friction decreases as w increases (better lubricating effect) and conversely, the viscous force increases with increasing w (more binder between particles). At low viscosity, the lubrication effect is more pronounced while at high viscosity the viscous force dominates.
Agitation intensity (impeller speed, fluidising air velocity etc)	Increase as agitation intensity increases (Gabbott, 2007; Ohno et al., 2007; Ritala et al., 1988; Schaefer et al., 1986)	Increase as agitation intensity increases (Gabbott, 2007; Ohno et al., 2007; Ritala et al., 1988; Schaefer et al., 1986)	As agitation intensity increases, the force to deform and consolidate the granule increases.
	Decrease as agitation intensity increases (Eliassen et al., 1999; Ganderton and Hunter, 1971)	Decrease as agitation intensity increases (Eliassen et al., 1999; Ganderton and Hunter, 1971)	If the system is weak (such as low binder content), increasing the agitation intensity promotes breakage of granules which delays the consolidation process.

2.3.1.2 Granule coalescence models

Modelling of granule coalescence is usually carried out for two equi-sized spherical particles. Successful coalescence or sticking of particles is deemed to occur if the binding forces are dominant over the separating forces. Figure 2.5 shows the development of coalescence models.

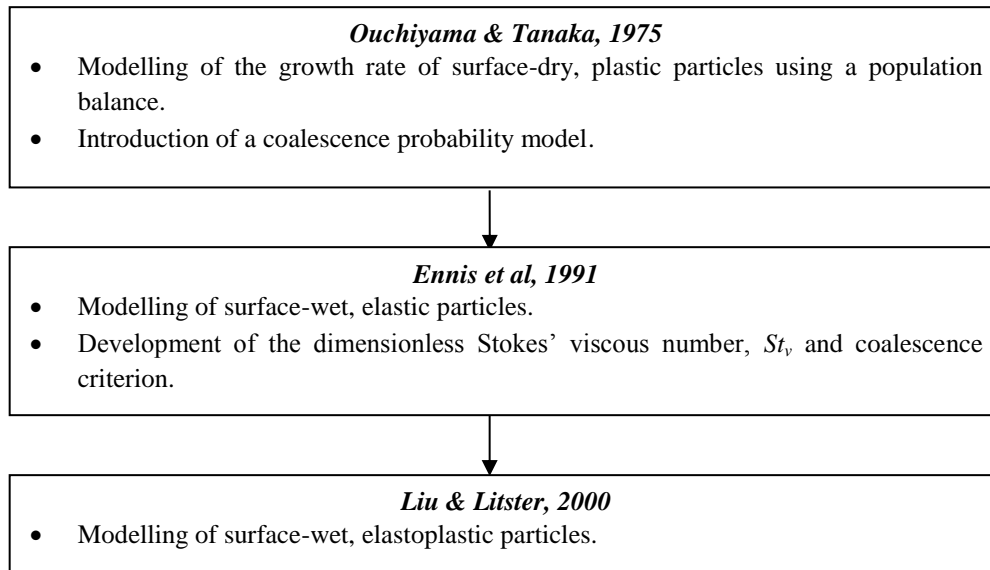


Figure 2.5: Development of granule coalescence models.

From one of the earliest works of particle coalescence models, Ouchiyama and Tanaka deduced that particle coalescence depends strongly on the cohesion force developed at the point of deformation of two colliding particles (Ouchiyama and Tanaka, 1975). The particles will stick together should this cohesion force be strong enough to resist the subsequent separating forces. A coalescence probability model is then introduced for dry, spherical, deformable particles.

In Ennis and co-workers's work, they asserted that successful coalescence of two colliding particles will occur if they do not possess sufficient kinetic energy to overcome the strength of a dynamic pendular liquid bridge between the particles (Ennis et al., 1991). Force balance conducted on two surface-wet, elastic particles coming into contact (Figure 2.6) yields Equation 2.6 to describe the motion of the particle upon collision, considering only the liquid viscous forces. St_v is the Stokes viscous number which is the ratio of the initial kinetic energy

of the colliding particles to the energy dissipative by the viscous liquid layer as previously explained, x is the interparticle gap and h_0 is the binder layer thickness.

$$u = u_0 \left[1 - \frac{1}{St_v} \ln \left(\frac{h_0}{x} \right) \right]$$

Equation 2.6

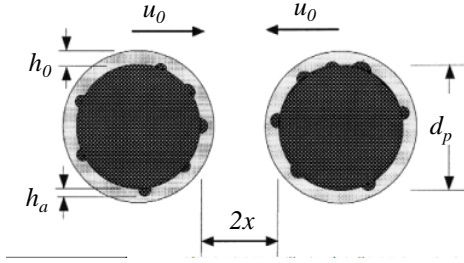


Figure 2.6: Two colliding particles covered in a viscous layer of liquid of thickness h (modified from Ennis et al., 1991).

A critical value of the Stokes coalescence number, St_v^* which rebound of the colliding particles will occur is given in Equation 2.7. e is the particle's restitution coefficient and h_a is the length of the surface asperities. For successful coalescence, the viscous force of the liquid bridge has to fully dissipate the initial kinetic energy of the colliding particles. This gives the criterion for successful coalescence, as shown in Equation 2.8.

$$St_v^* = \left(1 - \frac{1}{e} \right) \ln \left(\frac{h_0}{h_a} \right)$$

Equation 2.7

$$St_v < St_v^*$$

Equation 2.8

To model elastoplastic particles, Liu and Litster characterised the particle mechanical behaviour by both the elastic or Young's modulus and the wet particle yield strength (Liu et al., 2000). Like Ennis and co-worker's work, only the liquid viscous force was considered. Plastic deformation is taken to commence upon solid contact of the colliding granules. The approach and separation process of two surface-wet, colliding particles are divided into a few stages (Figure 2.7). Coalescence of particles occurs for either of the following situations: The velocity of the colliding particle decreases to zero during the approach stage before the solid surfaces come into contact and prior to any deformation of the particle taking place (Figure 2.7a) which

is referred to as type I coalescence; or the particle velocity decreases to zero during the separation stage (Figure 2.7c-d), referred to as type II coalescence. The criterion for type I coalescence is given in Equation 2.9.

$$St_v^* < \ln\left(\frac{h_0}{h_a}\right)$$

Equation 2.9

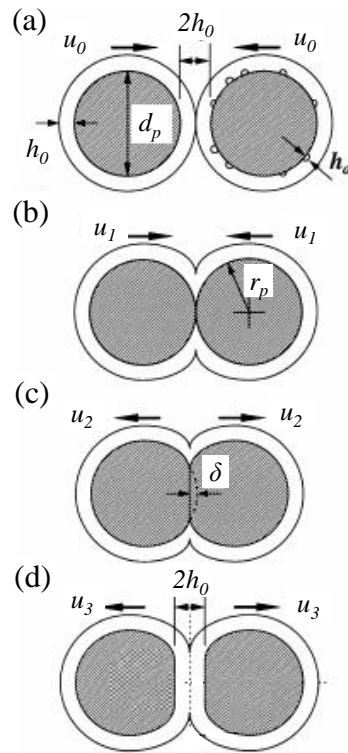


Figure 2.7: Collision & separation stages: (a) approach stage; (b) deformation stage; (c) initial separation stage; (d) final separation stage (modified from Liu & Litster, 2001).

Further theory development by Liu and Litster incorporating the plastic deformation of the particles upon contact during the deformation and separation stages yield the condition for type II coalescence (Equation 2.10) where the initial collision kinetic energy is completely dissipated after the particles collide, deform to a certain extent and start to move away from each other. Y_p is the wet particle yield strength, E^* is the particle Young's modulus, \tilde{D} is the

particle harmonic mean diameter, δ'' is the permanent plastic deformation and St_{def} is the dimensionless Stokes deformation number.

$$\begin{aligned} & \left(\frac{Y_p}{E^*}\right)^{\frac{1}{2}} (St_{def})^{-9/8} \\ & < \frac{0.172}{St_v} \left(\frac{\tilde{D}}{h_0}\right)^2 \left[1 - \frac{1}{St_v} \ln\left(\frac{h_0}{h_a}\right)\right]^{\frac{5}{4}} \left[\left(\frac{h_0^2}{h_a^2} - 1\right) + \frac{2h_0}{\delta''} \left(\frac{h_0}{h_a} - 1\right) \right. \\ & \left. + \frac{2h_0^2}{(\delta'')^2} \left(\frac{h_0}{h_a}\right)\right] \left\{1 - 7.36 \left(\frac{Y_p}{E^*}\right) (St_{def})^{-1/4} \left[1 - \frac{1}{St_v} \ln\left(\frac{h_0}{h_a}\right)\right]^{-1/2}\right\}^2 \end{aligned}$$

Equation 2.10

The Stokes deformation number, St_{def} (Equation 2.11) was first defined by Tardos and co-workers to characterise the deformation of liquid-bounded particles (Tardos et al., 1997). V_p is the particle volume and τ_y is the particle characteristic strength. Equation 2.11 can be rewritten to Equation 2.12 in terms of density, and the wet particle or granule yield strength, Y_p is used in place of the characteristic strength. The Stokes deformation number is defined as the ratio of the external energy to the energy required for deformation and is a measure of the particle's deformability. The external energy is taken as the initial kinetic energy of the colliding granules.

$$St_{def} = \frac{m_p u_0^2}{2V_p \tau_y}$$

Equation 2.11

$$St_{def} = \frac{\rho_p u_0^2}{2Y_p}$$

Equation 2.12

Regimes for both coalescence types are mapped in Figure 2.8. As expected, type I coalescence occurs if St_v is small enough, or in other words, the liquid is viscous enough to impede and stop the approaching particles before contact of the surfaces. This is regardless of the deformation number as non-contact of the particles indicates that the mechanical properties of the solids are not considered. Type II coalescence, on the other hand, depends on both St_v and St_{def} . Increasing particle deformation enhances the probability of coalescence even when

the viscous number is high. This can be accounted for by the contribution of the plastic deformation in absorbing the impact kinetic energy and increasing viscous dissipation as the particle contact area increases. At small deformation numbers, there is a limiting viscous number that will result in coalescence, in which the criterion is the same as that proposed by Ennis and co-worker for non-plastic deformable particles (Equation 2.7 and Equation 2.8).

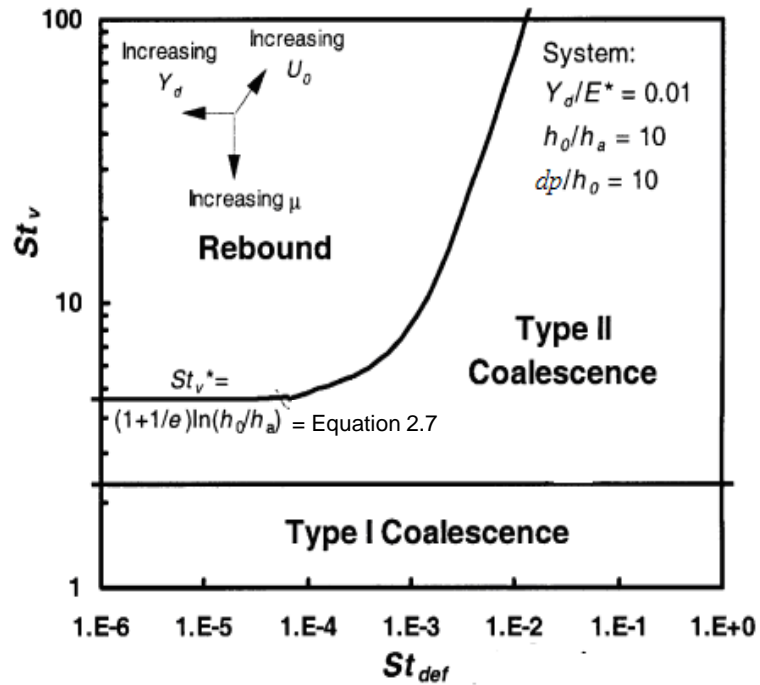


Figure 2.8: Boundaries for type I, II coalescence and rebound for surface-wet granules (taken from Liu & Litster, 2001).

2.3.1.3 Growth limiting/breakage models

In wet agitation granulation, granules undergo continuous impact and collisions throughout the granulation process. These impact forces lead to deformation of granules which contributes to coalescence but could also lead to breakage of granules. Tardos and co-workers who introduced the Stokes deformation number also deduced that granules will deform and break if there is enough externally applied mechanical energy (Tardos et al., 1997). Breakage will occur if St_{def} exceeds a critical deformation number (Equation 2.13). Below the critical number, granules will only deform and perhaps coalesce. There are no existing models for this critical number, although Tardos and co-workers found that that the breakage of granules in a fluidised bed occurs at St_{def} of approximately 0.2.

$$St_{def} > St_{def}^*$$

Equation 2.13

Keningley and co-workers proposed an equation describing that granules will be formed if they are strong enough to resist the impact forces (Keningley et al., 1997). The granules will deform from the impact forces and eventually fracture and break at a critical strain. Force balance of the kinetic energy from the impact and energy absorbed by granule deformation gives Equation 2.14. ϵ_{max} is the maximum strain above which fracture and breakage of the granule will occur. The critical strain value is found to be 0.1 by Keningley and co-workers for calcium carbonate granules in a food processor.

$$\epsilon_{max}^2 = \frac{1}{540} \frac{\epsilon_p^3}{1 - \epsilon_p^2} \frac{\rho_p u_0 d_p}{\mu_l}$$

Equation 2.14

2.3.1.4 Wet granule strength

Modelling of granule coalescence and breakage in the previous sections shows that the granule deformability, reflected by the Stokes deformation number, is also dependent on the yield strength of the wet granules (Y_p in Equation 2.12). The strength of wet granules itself depends on many factors, and studies to characterise the strength have been attempted by several authors. One of the earliest works was carried out by Rumpf where a model for the static tensile strength of liquid-bounded granules, τ_s , is proposed (Equation 2.15) (Rumpf, 1962), where the mode of failure is the abrupt rupture between an assembly of equi-sized spheres. Only the liquid capillary force is considered. s is granule liquid saturation and C is the particle shape constant. Subsequent works started to highlight the contribution of frictional and viscous effects on the granule strength at high strain rates, also sometimes known as the "dynamic yield strength" (Adams and Edmondson, 1987; Iveson et al., 2002; Liu et al., 2009; Pepin et al., 2001; Simons and Pepin, 2003; Van Den Dries and Vromans, 2002). For instance, Van den Dries and Vromans modified Rumpf's equation to consider the liquid viscous force instead of the capillary force (Equation 2.16). v_{rel} is the relative velocity of moving particles.

$$\tau_s = sC \frac{1 - \varepsilon_p \gamma \cos \theta_{lf}}{\varepsilon_p d_p}$$

Equation 2.15

$$Y_p = \frac{9}{8} \left(\frac{1 - \varepsilon_p}{\varepsilon_p} \right)^2 \frac{9\pi\mu_l v_{rel}}{16d_p}$$

Equation 2.16

Iveson and co-workers performed dimensional analysis on the granule strength, taking into account a wide range of parameters that would affect the wet granule yield strength (including the coefficient of inter-particle friction, μ_p , granule packing coefficient, Φ , and strain rate, $\dot{\varepsilon}$) (Equation 2.17) (Iveson et al., 2002). The left hand dimensionless term is the dimensionless strength while the first right hand term is called the "Capillary number". Experimental validation of the model using different powder and binder combinations gave a relationship between the dimensionless strength, Str^* and the capillary number, Ca (Equation 2.18) where k_1 , k_2 and p are empirical parameters. Figure 2.9 presents the experimentally fitted Equation 2.18 by Iveson and co-workers. It can be seen that at low strain rates, frictional force dominates (i.e. Ca number does not change) while at higher strain rates the contribution of viscous effects towards granule strength becomes significant.

$$\frac{Y_p d_p}{\gamma \cos \theta_{lf}} = f \left(\frac{\mu_l d_p \dot{\varepsilon}}{\gamma_l \cos \theta_{lf}}, \mu_p, s, \Phi \right)$$

Equation 2.17

$$Str^* = k_1 + k_2 Ca^p$$

Equation 2.18

Table 2.2 summarises the literature on studies of the effect of particle properties, binder properties and agitation intensity on the wet granule strength. Existing experimental measurements of the wet granule yield strength from literature can be divided into two types: granule compression or impact tests, with the latter producing much higher strain rates (Iveson et al., 2002; Iveson and Litster, 1998c).

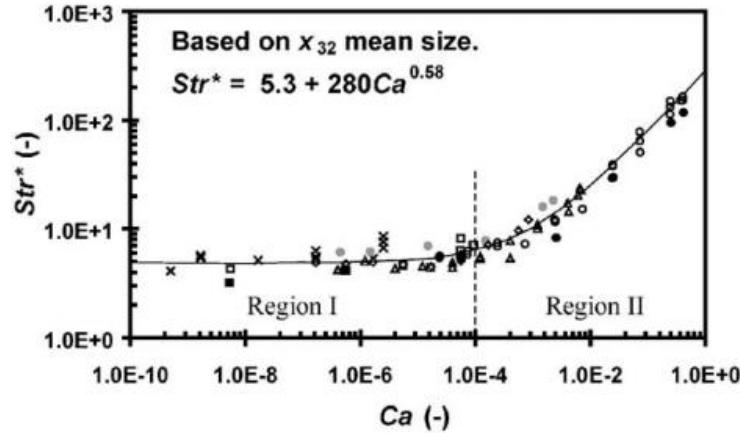


Figure 2.9: Dimensionless strength, Str^* versus Capillary number, Ca (taken from Iveson et al, 2002).

Table 2.2: Effect of powder, binder properties and agitation intensity on wet granule strength.

<i>Powder/binder Properties</i>	<i>Prediction from models (Equation 2.16 & Equation 2.18)</i>	<i>Experimental results</i>	<i>Mechanistic explanation</i>
Primary particle size, d_p	Increasing d_p decreases strength	Increasing d_p decreases strength (Iveson and Litster, 1998c; Van Den Dries et al., 2003)	Increasing d_p decreases the inter-particle friction (number of inter-particle contacts decrease), decreases the capillary force (liquid bridge curvature decreases) and decreases the viscous force (bigger average gap distance) \rightarrow all contributing to the decrease of strength.
Binder viscosity, μ_l	Increasing μ_l increases strength	Increasing μ_l increases strength (Eliassen et al., 1998; Iveson and Litster, 1998c)	Viscous force increases with increasing viscosity. Viscous effect, however is negligible at low strain rates (Iveson et al, 2002).
Binder content, w (which affects granule saturation level, s)	Increasing w increases strength	Variable effect (Iveson and Litster, 1998c; Schubert, 1975)	Increasing binder reduces friction (lubrication), increases the viscous force and increases the capillary force. Net effect on strength will depend on the balance of these forces. Again, at low strain rates, the capillary and viscous effects are negligible. Strength also changes according to saturation states (Newitt and Conway-Jones, 1958; Schubert, 1975).
Binder surface tension, γ	Increasing γ increases strength	Increasing γ increases strength (Iveson and Litster, 1998c)	Increasing γ increases the capillary force but for viscous binder, viscous force dominates and effect of γ is negligible.

2.3.2 Macro-scale characterisation

The rate processes described in the previous section: granule consolidation, coalescence, and breakage, occur simultaneously during granulation and affect the granule growth mechanism or behaviour during the process. Several granule growth behaviours can also be characterised based on the evolution of granule size with granulation time.

2.3.2.1 Granule growth behaviours

Nucleation only behaviour occurs when granules do not grow significantly, i.e. formation of nuclei or small, weak granules only. This is most commonly due to insufficient liquid for coalescence, as found by Realpe and Velazquez when using small amounts of binder (Realpe and Velazquez, 2008) or when weak binder is used. *Steady-state growth* is characterised by a steady increase in the granule mean size with time and is usually observed for granules that are relatively easy to deform and consolidate and when adequate binder liquid is added to promote coalescence (Knight, 1993). Provided that the impact forces are not too high, granule growth will dominate over breakage resulting in a net increase in size. *Unconstrained growth* can occur when granule growth is much more dominant than breakage and usually occurs for systems with high liquid content and easily deformable and consolidated granules (Scott et al., 2000). This usually ends in the formation of a large amount of lumps and is also known as balling. The *induction behaviour* is described as an initial period of little or no growth (the duration of this period is called the induction time), followed by a rapid increase of the granule size. Induction behaviour is commonly observed for hard, non-deformable granules which result in slow consolidation and growth during the induction time. When sufficient liquid is squeezed out onto the granule surface to trigger coalescence, rapid growth is observed. Schaefer observed this behaviour when granulating fine primary particles and high viscosity binder which led to initially strong, poorly deformable and consolidated agglomerates (Schaefer, 1995). Finally, *crumbling or breakage* behaviour is characterised by no change in the granule size or a decrease in the granule size with time. If breakage of granules is balanced by growth, there is zero net growth while reduction of granule mean size is observed if breakage is dominant. This behaviour usually occurs when the impact forces are high and granules are relatively weak. Breakage can also be detected via granule size distribution, i.e. an increase in the smaller size fractions and a decrease in the large size fractions during breakage gives a bimodal granule size distribution (Realpe and Velazquez, 2008).

2.3.2.2 Mapping in granulation

From literature, a widely used approach in granulation is the study of the effect of formulation, processing and equipment variables to the granule growth behaviour and granule attributes. More often, the results obtained are only limited to the studied variables. Hence, mapping in granulation is another approach to gain a more generalised understanding of the granulation process. These works typically explore the combined effect of two or more variables to obtain a map with different granule growth regimes (Keningley et al., 1997; Tu et al., 2009). An earlier example of such work was carried out by Keningley and co-workers, who produced an experimental map with regimes of granule growth behaviour at different binder liquid content and viscosity for calcium carbonate granules in a food processor (Keningley et al., 1997). These maps provide a better understanding in the growth behaviour prediction but are still limited to a particular system, i.e. formulation and equipment. A milestone in granulation is the development of the "Granulation growth regime map" for generalised systems by Iveson and co-workers (Iveson and Litster, 1998b; Iveson et al., 2001b). The aim of the map is to link the formulation, processing and equipment variables to the granule growth behaviours. Iveson and Litster proposed the following two dimensionless parameters for the map which affects the granule growth behaviour: the maximum granule pore saturation, s_{max} (Equation 2.19) and the Stokes deformation number, St_{def} (Equation 2.12). Table 2.3 presents the definition and description of these two parameters.

Table 2.3: Dimensionless parameters in "Granulation growth regime map".

<i>Term</i>	<i>Description</i>	<i>Effect on granule growth</i>	<i>Symbols</i>
$s_{max} = \frac{w\rho_s(1 - \varepsilon_{p,min})}{\rho_l\varepsilon_{p,min}}$ <p>Equation 2.19 (Eliassen et al., 1998)</p>	<p>The maximum granule pore liquid saturation (a measure of the amount of binder liquid occupying the granule pores). Pore saturation varies with granulation time; hence the maximum saturation value is taken to represent a particular system.</p>	<p>The liquid saturation reflects the binder liquid content added to the system. Generally, increasing the binder content increases the growth until its saturation point.</p>	<p>w: liquid to solid mass ratio ρ_s: density of solid ρ_l: density of liquid ε_{min}: minimum granule porosity</p>
$St_{def} = \frac{\rho_p u_0^2}{2Y_p}$ <p>(Equation 2.12)</p>	<p>The extent of deformation experienced by the granule based on the process agitation intensity and granule strength.</p>	<p>The deformability affects the consolidation and coalescence of granules; higher deformability promotes consolidation and coalescence but if the deformation is too high, breakage occurs.</p>	<p>ρ_p: granule density u_0: characteristic velocity (impeller tip velocity for high shear granulator) Y_p: granule dynamic yield strength</p>

In the proposed map, different regimes of growth behaviours are established for the varying maximum pore saturation and amount of deformation (Figure 2.10). Table 2.4 summarises the different regimes or growth behaviours in the map, most of which have also been described previously in Section 2.3.2.1. From the regime map, the effects of various operating parameters and formulation properties on the granule growth behaviour were also predicted qualitatively by the authors (Figure 2.11 and summarised in Table 2.5).

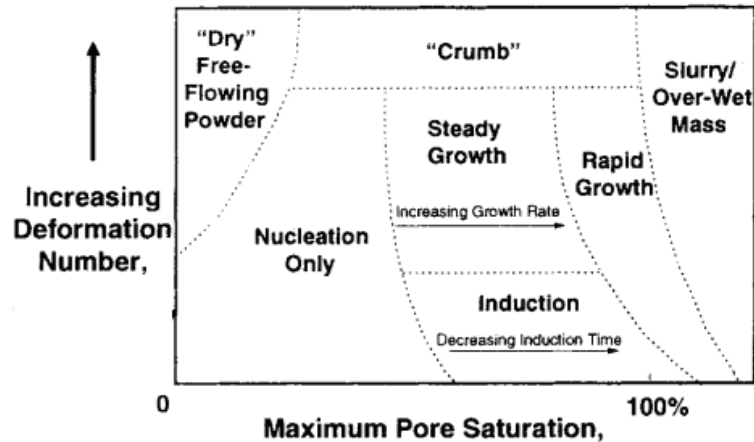


Figure 2.10: Modified "Granulation growth regime map" (taken from Iveson & Litster, 1998b).

Table 2.4: Regimes in the "Granulation growth regime map".

Regimes	Description	Conditions
Nucleation only	Only formation of nuclei takes place. There is insufficient liquid content to promote coalescence and granule growth.	Low liquid content (low s_{max}), low and intermediate St_{def} .
Steady growth	Sufficient liquid at the surface of the granule promotes coalescence and steady granule growth.	Sufficient liquid content (medium to high s_{max}), intermediate St_{def} .
Rapid growth	Rapid increase of granule size with granulation time.	High liquid content (high s_{max}), low and intermediate St_{def} .
Induction	Poor deformability leads to an initial period of little or no growth followed by rapid growth once sufficient liquid is squeezed out onto the granule surface.	Sufficient liquid content (medium to high s_{max}), low deformability (low St_{def}).
Dry powder	At very little liquid content, the powder remains dry.	Very low s_{max} .
Crumb	Granules could not be formed in this regime due to weak system/high agitation intensity and remain as particle fragments.	High process agitation intensity; weak granules (high St_{def}).
Slurry	Excessive liquid added leads to the formation of an over-wetted mass.	Excessive liquid content (very high s_{max}).

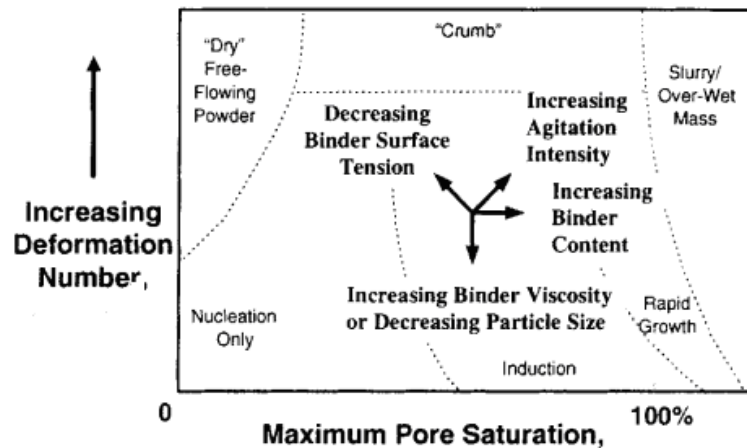


Figure 2.11: Effect of processing and formulation variables on granule growth behaviour (taken from Iveson & Litster, 1998b).

Table 2.5: Qualitative prediction of the effect of processing and formulation variables on granule growth behaviour (summarised from Iveson & Litster, 1998b)

Process Variables	Effect on:		Granule growth behaviour
	St_{def}	S_{max}	
Process agitation intensity (impeller speed for high shear granulator)	Increasing agitation intensity increases the impact velocity and hence, St_{def} .	Increasing agitation intensity promotes granule consolidation, hence producing more compact granules (smaller ϵ_{min}) and hence, higher s_{max} .	Shifts from the nucleation to crumb, steady/induction growth; induction to steady/rapid growth; steady to crumb/rapid growth; and rapid growth to over-wetted mass.
Binder viscosity	Increasing viscosity generally increases granule strength and hence, reduces deformability and St_{def} .	Variable effect.	Shifts from crumb to steady growth; and steady to induction growth.
Primary particle size	Decreasing primary particle size generally increases granule strength and hence, reduces deformability and St_{def} .	Variable effect.	Shifts from crumb to steady growth; and steady to induction growth.
Binder content	Variable effect	Increasing binder content increases s_{max} .	Shifts from dry powder to nucleation only; nucleation to steady/induction growth; steady/induction rapid growth; and rapid growth to over-wetted mass.
Binder surface tension	Decreasing surface tension generally decreases granule strength and hence, increases St_{def} .	Decreasing surface tension reduces the extent of consolidation (larger ϵ_{min}) and hence, smaller s_{max} .	Shifts from induction to steady growth; and steady growth to crumb/nucleation only.

To validate the regime map, Iveson and co-workers collected granulation data from available literature for different types of granulators, e.g. food processors, horizontal plough (Lodige) mixer and drum granulators (Iveson et al., 2001b). Additional granulation experiments were also carried out in a drum granulator and a vertical axis, high shear granulator. The wet granule yield strength, Y_p , was determined by compressing hand-made cylindrical compacts of the studied formulation (Iveson et al., 2002). Data for most granulators fitted into the map except for the high shear granulator where St_{def} is much higher than the rest (Figure 2.12). A reason postulated is the choice of the characteristic velocity, u_0 for the high shear granulator. The speed of the chopper was chosen instead of the impeller speed and could be an overestimate of the externally applied stress. Another reason is the characterisation of the granule dynamic yield strength. Strength is affected by strain rate (Iveson et al, 2002) but since the strength was determined via compression, the strain rates were not comparable to the high strain rates in the high shear granulator.

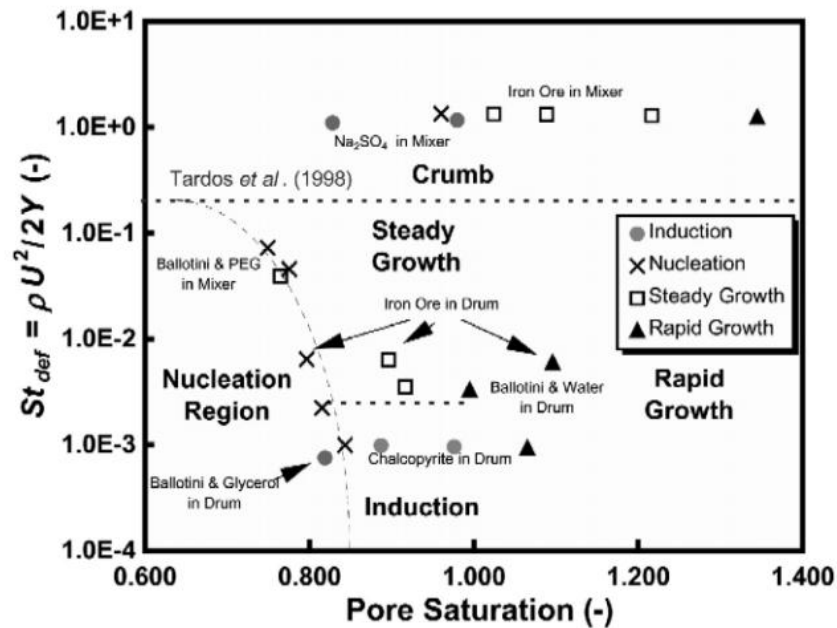


Figure 2.12: Experimental validation of growth regime map (Iveson et al, 2001b).

2.4 External stress on granules

From the review in previous sections on the micro-scale models of granule growth and macro-scale characterisation of granule growth behaviour followed by the development of the "Granulation regime map" which links formulation, operating and equipment variables with the granule growth behaviour, it can be summarised that the extent of granule growth, and hence granule growth behaviour depends ultimately on the balance of the binding and separating forces acting on the granule. Figure 2.13 provides a summary of the factors that contribute to the binding and separating forces in the wet agitation granulation process.

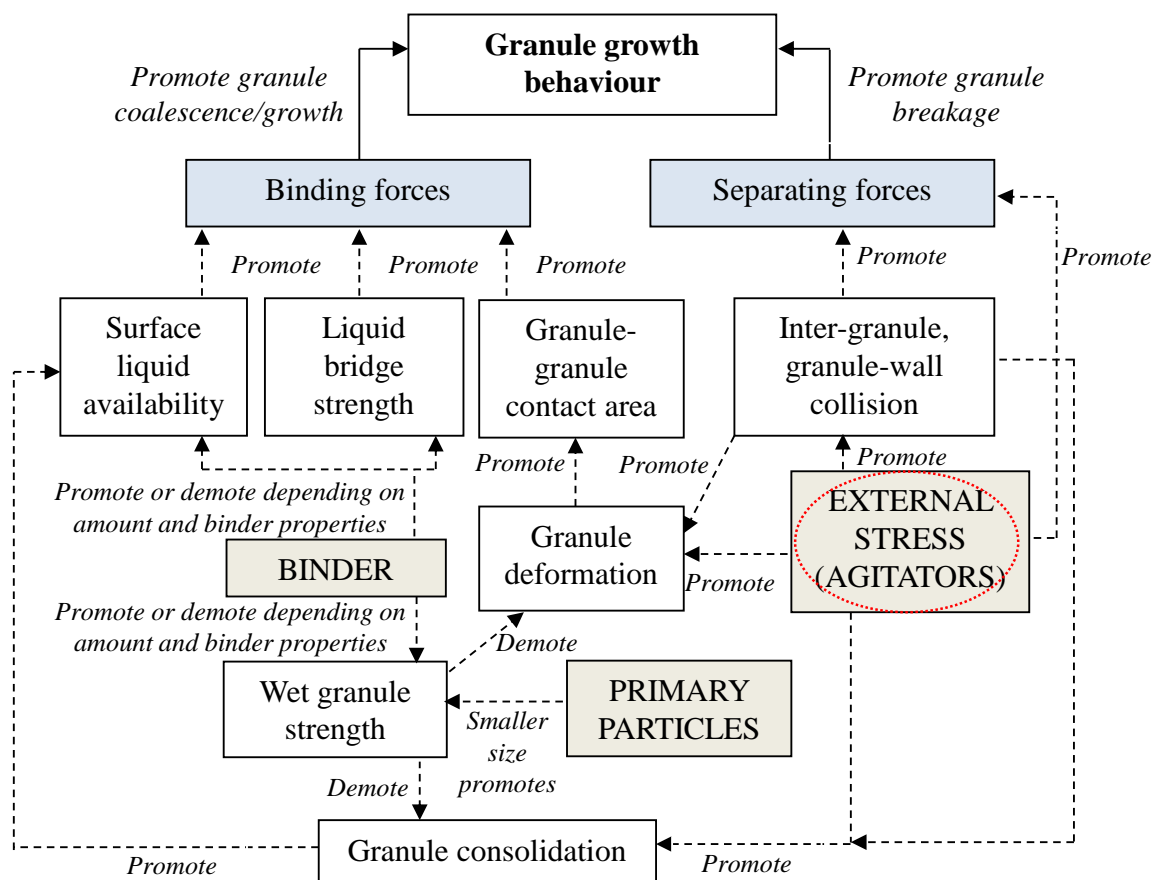


Figure 2.13: Factors affecting granule growth behaviour in the wet agitation granulation process.

The boxes shaded in light brown indicate the primary factors (i.e. formulation and external stress exerted on the granules) that affect the secondary factors (i.e. wet granule strength, consolidation, deformation behaviour etc.) which help to promote either the binding or separating forces. The formulation can be controlled by the binder and powder properties,

however proper characterisation of the external stresses remains an interesting and useful area for granulation research. In wet agitation granulation processes, this external stress is exerted by the agitation source in the granulator and is transmitted throughout the granule bed through intergranule collisions. The effect of the external stress, which initiates the intergranule and granule-wall collisions, on granule growth is varied since the collisions could either deform, consolidate and/or break the granules. At low forces, insufficient deformation and consolidation hinders granule growth while at a critical stress, granules will break or fracture, thereby limiting growth. The optimal granule growth condition would be between these two critical points.

The agitation method that applies the external stress differs with granulator types. In mixer granulators, these are the agitators rotating at high speed depending on the granulator configuration. There are several mixer granulator configurations which can be continuously or batch operated, namely the horizontal and vertical shaft mixers, and the latter can be either top- or bottom-driven (Figure 2.14). Also previously summarised in Table 1.1 of Chapter 1, examples of horizontal mixers include the plough mixer, paddle mixer and ribbon mixer while the bottom-driven cylindrical mixer and top-driven conical mixers are examples of a vertical axis mixer (Snow et al., 1997). In these mixers, the agitator (e.g. impeller, plough, paddles etc.) rotates at high speeds, i.e. ~100-1500 rpm depending on the scale (Reynolds et al., 2007), to disperse the binder and continuously mix the granulating mixture in addition to exerting normal and shear stresses on the granule bed to promote granule growth. The rotating agitator also initiates the intergranule contacts/collisions, thus generating a continuous network of forces throughout the granule bed (Campbell, 2006). Aside from the main agitator, a chopper is also typically mounted at the top or side of the granulator and rotates at a much high speed (~1500 rpm) to disperse the binder and break up the larger granules.

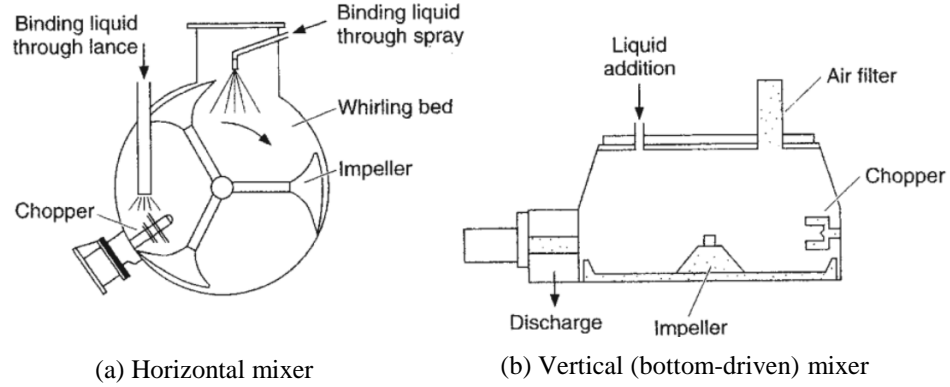


Figure 2.14: Mixer granulator configurations: (a) horizontal mixer and (b) vertical, bottom-driven mixer (taken from Reynolds et al., 2007).

2.4.1 Stress characterisation in granulation

There is little characterisation work on the stress in mixer granulators found in the literature. The impact stress was often used to predict the stress experienced by granules based on the acceleration imparted by the agitator (Oulahna et al., 2003; Van Den Dries and Vromans, 2002; Vonk et al., 1997; Vromans et al., 1999), given by Equation 2.20. F is the impact force, A_p is the granule projected surface area, m_p is the granule mass and d_p is the granule diameter. a_p is the acceleration that the granules gained from collision with the mixer agitator. This was taken as the acceleration of the impeller tip by the authors which is estimated from Equation 2.21, where v_{tip} is the impeller tip velocity. Substituting Equation 2.21 into Equation 2.20 gives the impact stress in Equation 2.22.

$$\sigma_{impact} = \frac{F}{A_p} = \frac{m_p a_p}{\pi \left(\frac{d_p}{2}\right)^2}$$

Equation 2.20

$$a_p = a_{l,tip} = \frac{\Delta v}{\Delta t} \approx v_{tip} \frac{v_{tip}}{d_p}$$

Equation 2.21

$$\sigma_{impact} = \frac{2}{3} \rho_p v_{tip}^2$$

Equation 2.22

The impact stress is given as a product of the granule density and the square of the impeller tip speed. This is in fact similar in form as the numerator in the Stokes deformation number (Equation 2.12, rewritten below) if u_0 , the characteristic velocity, is taken as the impeller tip speed. For mixer granulators however, the impact stress is logically affected by the agitator geometry such as the blade width/height, angle and other granule bed properties such as bed load or filling level. The effects of these are not explicitly known from Equation 2.22 since it is not a direct correlation of the agitator to granule bed stress.

$$St_{def} = \frac{\rho_p u_0^2}{2Y_p}$$

From: Equation 2.12

2.4.2 Stress measurement and granulation monitoring methods

Measurements of stresses in mixer granulators from the literature were scarce, particularly for direct evaluation of the agitator–granule bed stress, i.e. measurement of the stress at the agitator-granule bed contact region.

Table 2.6 summarises the stress and other monitoring measurement methods from the literature. Amongst the methods, the direct agitator torque and power draw or consumption measurements are widely used as an indication of the agitator-granule bed load due to the relatively inexpensive and simple measurement since most commercial granulators are equipped with torque or power measurement devices. The power draw or consumption of the agitator motor is measured using a power or watt transducer while direct agitator torque, i.e. the force required to rotate the agitator, is measured using strain gauge sensors attached on the agitator shaft. Agitator torque and power draw measurements were used in most of these works for granulation monitoring, i.e. to monitor the torque or power and relate them to the change of targeted granule attributes, typically mean size or size distribution, the cohesiveness or "wetness" of the granulating mixture and granule density or granule strength. From the monitoring, a granulation "end-point" is then determined when the target granule attributes are obtained. Besides granulation monitoring, the power draw is also used in granulation scale-up studies, i.e. keeping the Power Number constant across scales (Horsthuis et al., 1993; Mort, 2005; Mort, 2009).

Table 2.6: Stress and monitoring measurements in granulators.

<i>Type of measurement</i>		<i>Granulator type</i>	<i>Method</i>	<i>Reference</i>
Stress	Granule bed internal stress (shear and normal)	Vertical axis, cylindrical mixer	Stress sensor probe (strain gauge) inserted into the granule bed	(Watano et al., 2005)
	Granule bed internal stress (normal)	Vertical axis, cylindrical mixer	Pressure colouring films attached on a probe inserted into the granule bed	(Fu et al., 2009)
	Granule bed internal stress (shear)	Vertical axis, cylindrical mixer	Breakage count of calibrated "test" particles added to the granule bed.	(Tardos et al., 2004)
	Wall-granule bed stress (shear and normal)	Fluidised Couette Device	Stress sensor (hydraulic piston force transducer) at the wall	(Talu et al., 2001)
	Wall-granule bed stress (shear and normal)	Horizontal axis, plough mixer	Piezoelectric stress sensor at the wall	(Fu et al., 2011)
Internal vibration of granule bed		Vertical axis, cylindrical mixer	Sensor probe (strain gauge or piezoesensors) inserted into the granule bed	(Ohike et al., 1999; Staniforth et al., 1986)
		Planetary mixer	Sensor probe (strain gauge) inserted into the granule bed	(Staniforth and Quincey, 1986)
Direct agitator torque		Vertical axis, cylindrical mixer	Strain gauge sensors on impeller shaft	(Cavinato et al., 2010; Chitu et al., 2011; Corvari et al., 1992; Ghanta et al., 1984; Kopcha et al., 1992; Leuenberger et al., 1990; Mackaplow et al., 2000)
		Planetary mixer	Strain gauge sensors on impeller shaft	(Lindberg et al., 1977)
Power draw/consumption		Vertical axis, cylindrical mixer	Watt transducer or power cell at the mixer motor	(Cliff, 1990; Holm et al., 1985a, b; Kopcha et al., 1992; Mackaplow et al., 2000; Ritala et al., 1988; Rondet et al., 2012; Schaefer et al., 1992; Terashita et al., 1990a; Terashita et al., 1990b)

However, the torque and power draw often involve other influences as they reflect the total resistance of the bed while being rotated by the agitator or in other words, the total load exerted on the agitator by the bed. Factors such as the granule-wall friction and the bed cohesiveness will affect the torque and power draw readings (Darelius et al., 2007; Knight et al., 2001). These measurements are, therefore, not directly correlated to the actual agitator-granule bed interactions or impacts. In addition, power draw is also influenced by the bearing wear and other changes on the efficiency of the motor system, and is thus less sensitive to change in the granulating mixture than the torque (Cliff, 1990; Corvari et al., 1992; Kristensen and Schaefer, 1987).

Direct measurements of the stresses in agitator granulator have focused on either the granule bed internal stress or the granulator wall-granule bed stresses. For the granule bed internal stress, this was carried out by inserting a stress sensor probe with attached strain gauge, into a specific location in the granule bed which measures both the normal and shear stresses (Watano et al., 2005). In another work, Fu and co-workers introduced a probe with affixed pressure colouring films into the granule bed to measure the normal stress on the probe (Fu et al., 2009). The pressure colouring films consist of micro-bubbles containing colour forming material which burst upon pressure application and the resulting colour density is related to the pressure or normal stress. After a certain measurement time, the probe was removed to detach the films for analysis of the colour density. However, this method gives a built-up stress over the measurement time. In Tardos and co-worker's work, they measured the granule shear stresses indirectly by using cylindrical “test” particles made from Play-Doh® with known yield strength (Tardos et al., 2004). Specific amount of the “test” particles were added to the granulating mixture and the average shear stress was assumed to be equal to the measured yield strength if approximately 50% of the “test” particles were broken upon inspection. In the above works, the measured granule stresses were applied for scaling-up of the granulators. Maintaining the same stresses of the granule bed is also a method to control the same granulation conditions in different granulator scales (Mort, 2009).

For the granulator wall-granule bed stresses, Fu and co-workers introduced piezoelectric stress sensor probes at the wall of a horizontal axis Lodige plough mixer with rotating “pin tools” (Fu et al., 2011). Two probes in different orientations enabled both the normal and shear components of the stress to be measured. The authors then applied the stresses to predict

material caking on the mixer wall, also known as “wall make-up” from balance of the applied shear stress on the material and the resistance stress of the material at the wall. In another work by Talu and co-workers, hydraulic piston force transducers were attached onto the wall of a Fluidised Couette Device, which consists of two concentric cylinders and granules in the annulus was sheared by the rotating inner cylinder (Talu et al., 2001). Both shear and normal components were measured and the authors concluded that the normal stresses could be applied to monitor the granulation process. The fluctuations of the normal stresses were affected by the granule size, density and strength.

Other probe methods have also been employed which measure the vibration of the strain gauge sensor probes instead of the stress (Ohike et al., 1999; Staniforth et al., 1986). The vibration amplitudes and frequencies were also used to monitor the granulation process and for the "end-point" determination. For instance, Ohike and co-workers carried out Fast Fourier Transform on the vibration fluctuations and related the intensity or amplitude of the main frequency peak to the mean size of the granules. The authors found that the intensity or amplitude increased with the granule mean size.

2.4.3 Outlook and thesis objectives revisited

A recent development in granulation involved the introduction of the "Granulation growth regime map" which aims to link processing, formulation and equipment to the granule growth behaviour through understanding and application of micro-scale models of granulation rate processes. The authors have validated the map using granulation data from different types of granulators although several limitations still exist; one being the proper characterisation of the external force or stress on the granules which influences the granule deformability from the Stokes deformation number. From the summary in Figure 2.13, the external stress from the agitator which initiates the intergranule collisions throughout the granule bed can affect the granule behaviour in several ways. For mixer granulators, the main source of external stress comes from the main agitator which rotates at high speeds. Previous granulation work estimates the impact stress based on the impeller tip speed which is not directly correlated to blade geometry and granule bed properties. There are also currently no direct measurements of the force and hence stress exerted by the agitator to the granule bed, where most stress

measurements were carried out either at a specific location in the granule bed or at the granulator wall. Therefore, in this thesis, a novel direct measurement method for the stress exerted by the agitator to the granule (i.e. the impeller blade-granule bed stress) in a vertical axis, cylindrical high shear granulator, is developed. This is detailed in the next chapter. Subsequently in Chapter 4, an impeller blade-granule bed stress equation is proposed from theory which directly correlates the stress with blade geometries and granule bed properties, followed by characterisation of the blade-bed stress from both experiments and Discrete Element Method (DEM) simulations (Chapter 4, Chapter 5 and Chapter 6). Description of the DEM is given in Chapter 6 itself.

Chapter 3

Telemetric impeller stress sensor system and other methodology

3.1 Introduction

In this chapter, the measurement and analysis methods for the experimental work carried out in this thesis are detailed. For clarity, the methods are presented in the following order:

- Description of the high shear granulator and the development of a novel direct blade-granule bed stress measurement method in the studied granulator;
- Description of secondary measurements of the granule bed in the granulator, necessary for the impeller blade-bed stress equation, which theoretical development is highlighted in Chapter 4. These are the granule or particle bed surface velocity and bed height measurements; and
- Description of methods to ascertain the properties of dry granules or particles used or produced in the experiments (size, apparent density, strength and Young's modulus), as well as some properties of liquids used in the experiments (viscosity and surface tension).

The types of materials used and granulation steps are explained in the individual chapters, as appropriate.

3.2 Blade-granule bed stress measurement

3.2.1 High shear granulator and pressure colouring films method

The studied high shear granulator was a lab scale, ~10 litre vertical axis, cylindrical commercial granulator from Zanchetta & C. s.r.l., Italy (model name: Roto Junior) (Figure 3.1). The mixer bowl had a constant diameter of 0.28 m and a height of 0.18 m. The impeller in the mixer bowl can be rotated from ~5 to 700 rpm, corresponding to tip speeds of 0.07-10.3 m/s or Froude numbers (see Equation 6.19 in Chapter 6) of 0.0002-3.88. Also shown in Figure 3.1 is the binder spraying system for wet granulation and the control panel of the granulator for control settings and temperature monitoring.

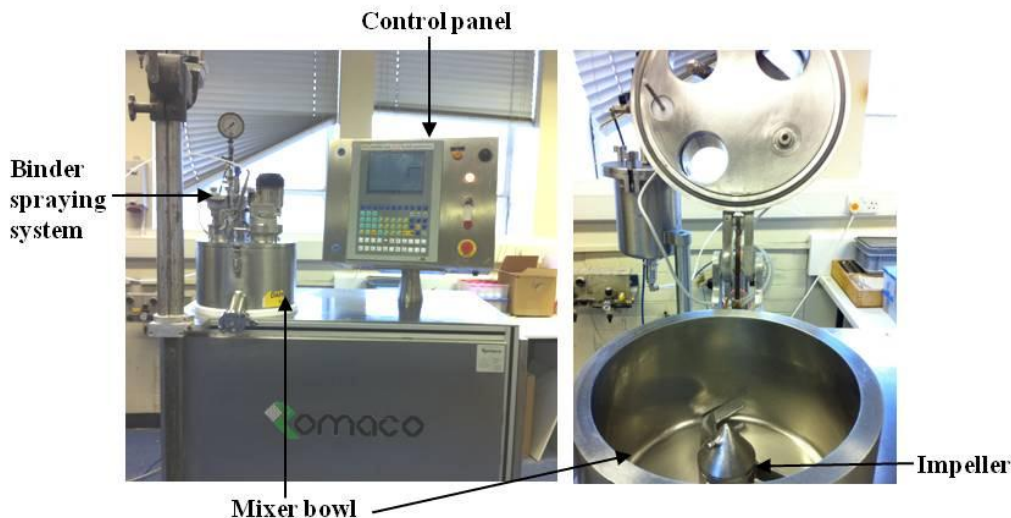


Figure 3.1: ~10 L Roto Junior high shear granulator.

From the literature review, Fu and co-workers measured the granule bed stress by using pressure colouring films attached onto a probe inserted into a particular location of the granule bed (Fu et al., 2009). As a first attempt to evaluate the impeller blade-granule bed stresses for this research, the films were used and affixed onto the impeller blades for the measurements. The measured stress indicates the normal stress on the plane of the inclined blade. Appendix A details the working principle of the films (manufactured by FujiFilm), the measurement steps and results obtained from this method. With the films method, several three-bladed impellers with single pitch blades at different inclination angles (27° , 32° , 38° and 45°) were tested. Following these experiments, there are several limitations of using the pressure films, summarised as follows:

The films were incapable of measuring the instantaneous, real-time blade-bed stresses in the granulator. The results indicate a built-up stress over the measurement time. Initial experiments in the Roto Junior show that the stress obtained with the films are at least a magnitude higher than the expected values. Experiments to evaluate effect of the measurement time for a steady-state bed shows a near linear increase of the blade-bed stress measured using the film with the measurement time. This is attributed to more micro-bubbles on the films which contain the colour-forming materials being burst upon continuous, repeated impacts with the granules with time.

The films were quite difficult to handle in the high shear granulator. Special care has to be taken to ensure that the micro-bubbles are not broken before the measurements, particularly for the low pressure grade films which are suited for the blade-bed stress range in the Roto Junior. At the same time, the results can also be affected if there are trapped air bubbles between the adhesive tape and the pressure film if the layers are not affixed properly. Furthermore, to obtain measurements especially for different granulation times, the process has to be stopped, followed by removal of the bed mixture and impeller to remove the used films and to attach fresh ones for the subsequent measurements.

To overcome the said limitations, a stress sensor method was proposed and custom-built for the blade-bed stress measurements in the Roto Junior, detailed in the following section.

3.2.2 Telemetric impeller stress sensor system

3.2.2.1 Sensor description

For measurements of the instantaneous, real-time blade-bed stress, a telemetric impeller stress sensor system was designed in the ~10 L Roto Junior by modifying one of the single pitch impellers. This measures the normal stress on the blade's inclined surface. A stainless steel plate of 27×27 mm on which a foil resistance strain gauge is adhered to, was attached onto one of the blades of the 32° impeller (Figure 3.2). The blade was drilled to create an internal chamber so that the plate could be attached on without any protruding surface which would otherwise affect the inclination angle of the measured area. The plate was secured onto the blade using screws at each corner and with sealant applied along the edges. This gave a deformable measurement area of ~22×22 mm as indicated in Figure 3.2. For wet granule beds, the plate was coated with a Teflon layer to avoid material build-up on the plate. Figure 3.3 shows a schematic of the system setup in the Roto Junior. Other main parts of the system located in the granulator are an output controller plus transmitter box and a battery box attached to the central support of the impeller. Both boxes have dimensions of 7×5×3 cm. A receiver installed to a DAQ (Data Acquisition) software on a computer enables the transmitted output to be relayed and read telemetrically. From the sensor plate, an internal channel in the blade towards to the central impeller area connects the wires from the plate to the control box. Very importantly, this allows all wires to be safely concealed in the impeller. During

measurements, the entire system including the control and battery boxes rotates together with the impeller.

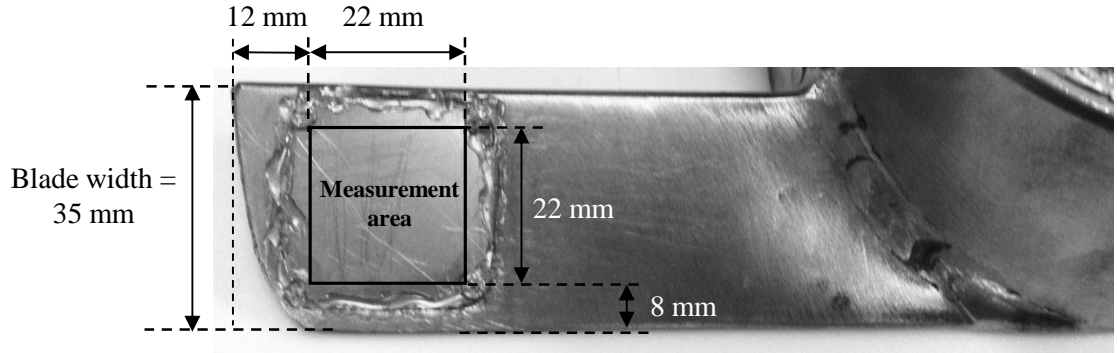


Figure 3.2: Sensor plate on the impeller blade.

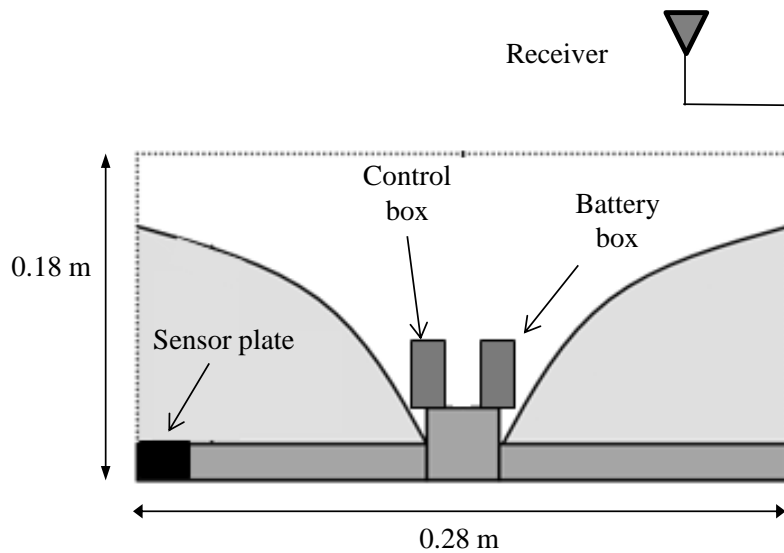


Figure 3.3: Schematic of the telemetric impeller stress sensor system in the Roto Junior.

Figure 3.4 shows the flow diagram of the telemetric impeller stress sensor system. The outputs of different components are also indicated in the figure. A single strain gauge was attached onto the underside of the sensor plate (see Figure 3.6 for the location of the gauge on the plate). This was a 9.8×5.2 mm foil resistance strain gauge (Omega UK, model number: SGD-5/350-LY11, nominal resistance of 350 Ω, maximum strain of 3%, operating temperature range of -75 to 95 °C) which consisted of the strain sensitive resistance element (Constantan), attached onto a backing material or carrier (Polyimide). When pressure or normal stress is

applied on the sensor plate, this deforms the plate, the attached strain gauge and the strain sensitive resistance element on it. The strain of the resistive element results in a change of resistance, ΔR , between the two ends of the element. The change in resistance is related to the strain by its Gauge factor which is $\approx 2.0 \pm 5\%$ for the used gauge type. To obtain a useful output from the strain gauge, a resistance bridge circuit (or more commonly known as the Wheatstone bridge) was built. For this setup, the quarter bridge configuration was employed, which is made up of one active gauge (connected to the sensor plate) and three dummy resistors which are located in the controller box. These are resistors with variable resistances and set to the nominal resistance of the strain gauge. Connected to the resistance bridge circuit was a power or DC (direct current) voltage supply to provide the excitation voltage for the circuit. For the system, a 9 V battery located in the battery box provided the voltage supply and a 5 V voltage regulator was added to reduce and maintain the excitation voltage at 5 V. When the Wheatstone bridge is unbalanced due to the deformation and change in resistance of the strain gauge, a difference in the voltage output results. The voltage output from the Wheatstone bridge then goes through a voltage offset which adjusts the amount of offset required (i.e. 2.5 V in the system), followed by an amplifier located in the controller box to amplify the voltage output by ~ 100 times. This is necessary since the maximum voltage difference from the Wheatstone bridge is ~ 0.0375 V without amplification, which would be difficult to detect in the output readings. A micro-controller in the controller box then converts the voltage output to bits (maximum 1024 bits which corresponds to 2.5 V) and a transmitter (LPRS Radio Ltd) collects the bit data and transmits them telemetrically to the receiver in selected time intervals. For this system, the data was relayed every 0.5 seconds and this gave a sampling rate of 2 Hz without any data buffer. The receiver board was connected to the computer where the LPRS Radio software reads and displays the relayed output. In addition to the above parts, resistor-capacitor network filters were also used to filter noise from the signals.

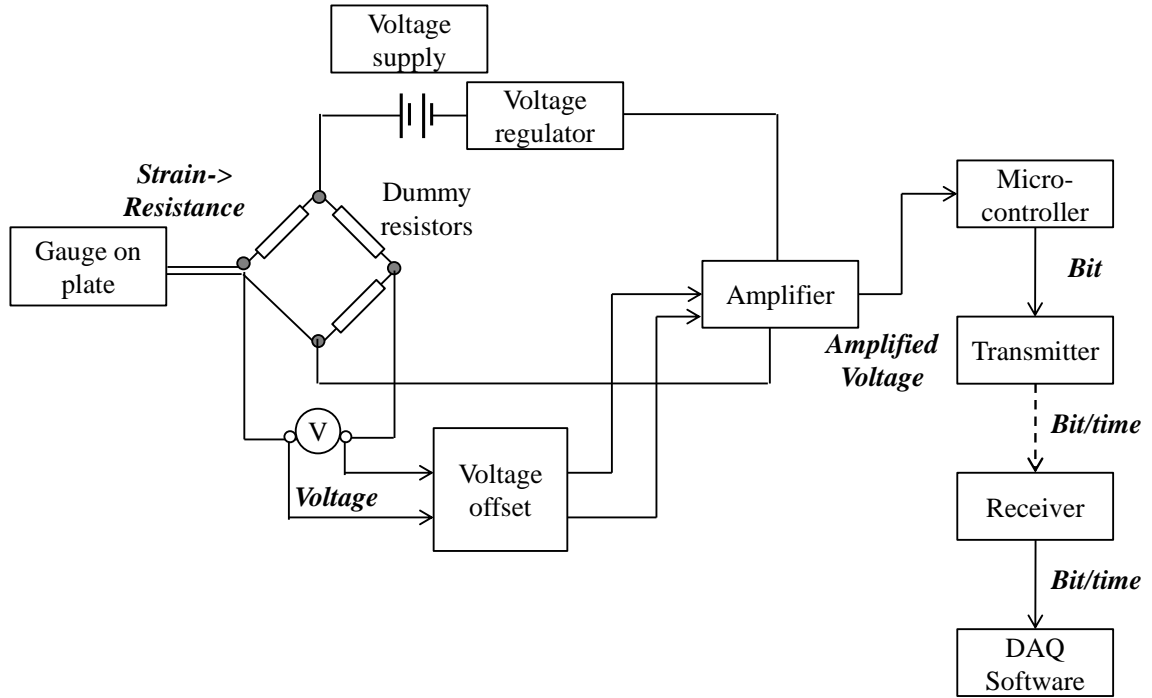


Figure 3.4: Flow diagram of the telemetric impeller stress sensor system.

3.2.2.2 Sensor calibration

The previous section describes the integral parts of the telemetric impeller stress system. To summarise, when a force is applied over the deformable area of the sensor plate, the sensor plate deforms. This leads to a strain of the strain gauge causing a change in resistance and, therefore, a change of the voltage output of the Wheatstone bridge which is then amplified and converted into bits (Figure 3.5). Also included in Figure 3.5 are the factors affecting the conversions of the outputs in each step. Since the gauge factor, excitation voltage, amplifier gain and voltage to bit conversions are fixed for this system, the final output change depends ultimately on the deformation behaviour of the sensor plate which is clamped onto the blade. The deformation behaviour of the plate is dependent on its clamping condition, thickness and material.

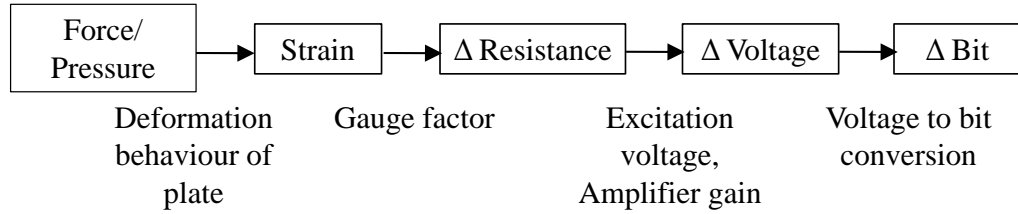


Figure 3.5: Output flow in the telemetric impeller stress sensor system.

To relate the bit or output change of the sensor to the averaged applied pressure over the plate's deformable area, calibrations of sensor plates were carried out using two methods: continuous compression of the plate using the compression machine (Zwick/Roell Z0.5) and by placing weights on the plate. Figure 3.6 shows the customised plate sensor holder which was designed for the calibrations. The sensor plate was attached on the customised holder, screwed and sealed at the edges, similar to the fixing conditions on the impeller blade. For calibration using continuous compression, a thin piece of rubber with the same dimensions as the plate deformable area was first placed on the plate deformable area before the punch of the compression machine was lowered onto it (Figure 3.7). Similarly for the calibration with weights, the weights were placed onto the rubber piece. The placement of the rubber piece was to ensure a continuous contact of the entire deformable area of the plate while being deformed. In both methods, the sensor output was first read prior to any load. This is the reference reading of the sensor. For the weights method, the sensor output was recorded after each weight increment (0.65-6.3 N weights or 0.0013-0.013 MPa). It was also observed that the sensor readings do not fluctuate when the weights were placed on the sensor plate and rubber. With the compression machine, a continuous load up to 40 N or 0.08 MPa from the punch was applied onto the sensor and rubber and the sensor readings were continuously read.

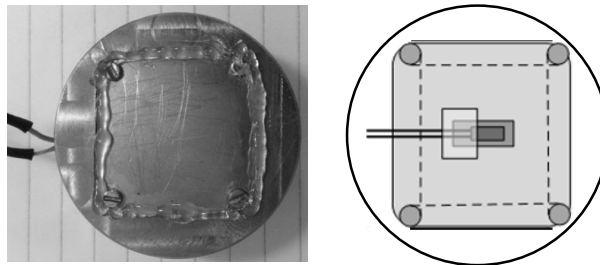


Figure 3.6: Customised sensor plate holder for calibration. Right: position of the strain gauge on the underside of the plate.

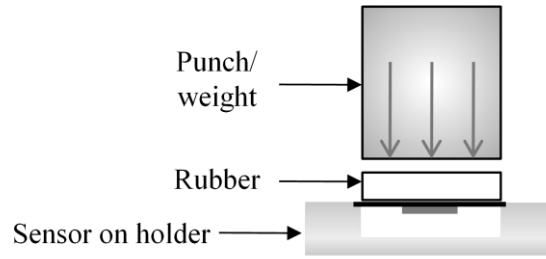


Figure 3.7: Setup for the sensor plate calibration.

Results of both calibration methods on a 0.25 thick mm stainless steel plate are presented in Figure 3.8. Both methods are in good agreement despite the difference in force range. For the continuous compression of the sensor plate, the curve presented is the combined curve of 5 repetitions and the weights results are averaged values of 5 repetitions. The output indicated in the figure (y-axis) denotes the output change normalised with the maximum available output change. The output change is the difference between the reference reading (no load) and the reading with applied load, and the maximum available output change is 1024. A non-linear variation of the output with the applied pressure is observed and the polynomial expression for the pressure is reported in Figure 3.8. At lower loads, the *Output* increases linearly with the applied pressure and starts to converge at high pressure ranges. Since the inherent linearity of the gauge deformation and resistance is given by the manufacturer, this non-linearity could be largely attributed to the plate deflection behaviour due to the clamping condition of the plate which is sealed along all edges. The plate average vertical displacement variation with the applied pressure from the compression machine (Figure 3.9), which reflects the plate deflection, also substantiated the observed non-linearity. After a certain loading force, there is limited vertical displacement or deflection of the plate, and hence lateral deformation of the strain gauge. Ramirez and co-workers, who calibrated similar plate-type normal pressure cells for silo storage studies, also noted this occurrence (Ramirez et al., 2010).

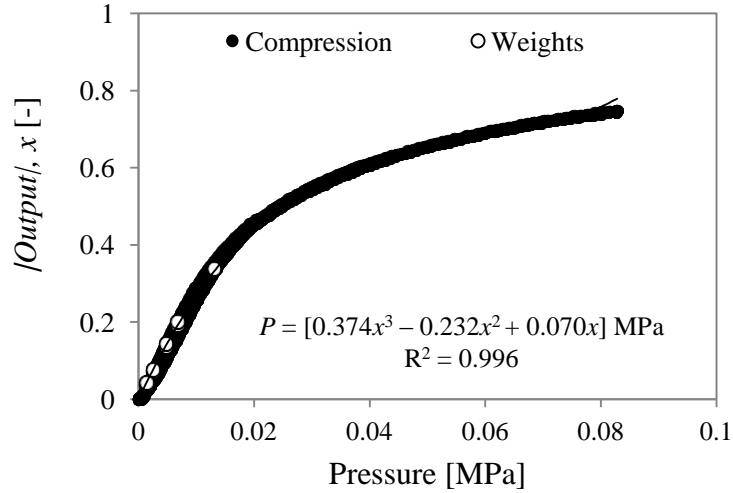


Figure 3.8: Calibration curve for a 0.25 mm stainless steel plate using continuous compression and deadweights and the fitted polynomial expression. R^2 is the coefficient of determination showing the goodness of fit, where 1 indicates perfect fit.

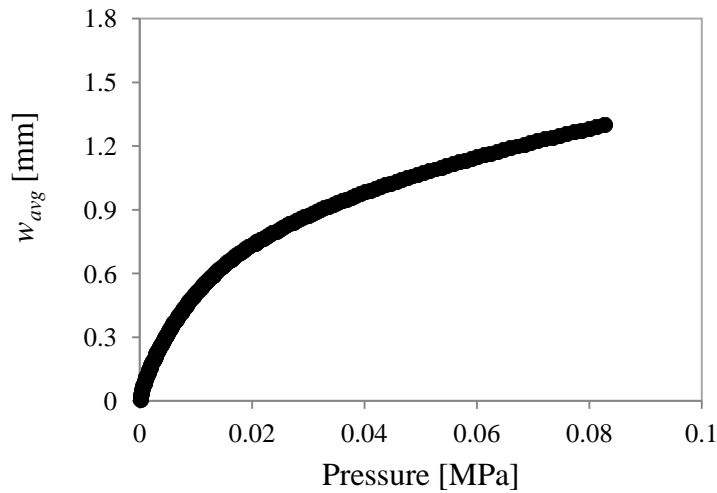


Figure 3.9: Plate average vertical height displacement, w_{avg} , from continuous compression.

Loading and unloading tests were also conducted using the weights to detect any hysteresis, i.e. memory retaining of the system, a common occurrence in strain gauge sensor systems (Chalmers, 1982). This was, however, not possible with the compression machine which had no gradual unloading/force release capabilities. Figure 3.10 shows the results of this analysis. At the tested pressure range, the difference between the loading and unloading cycles is negligible. Relaxation of the plate also occurred almost instantly, i.e. within the output

frequency of 2 Hz. This is also important as the measurements obtained from the Roto Junior experiments reported in this thesis are all within this pressure range. From the calibration model, the sensitivity of the 0.25 mm stainless steel sensor plate is also evaluated and is ~ 70 Pa, since the minimum output change is 1 bit.

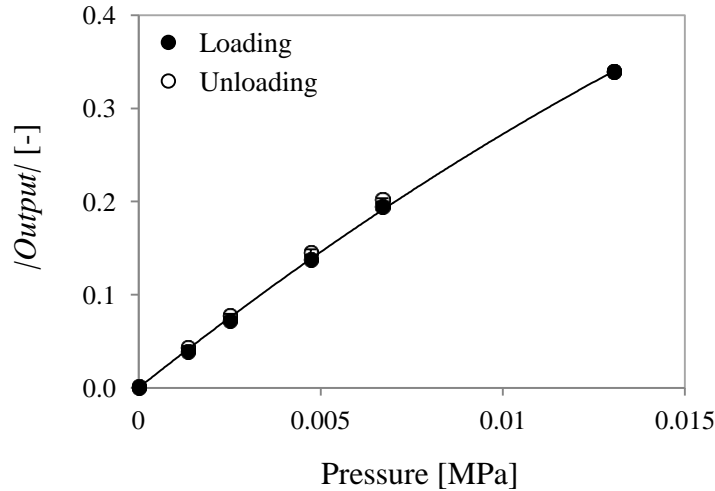


Figure 3.10: Loading and unloading results (weights) for 0.25 mm thick stainless steel plate.

3.2.2.3 Measurement and analysis

For the actual blade-bed stress measurements in the Roto Junior, Figure 3.11 displays an example of the sensor output for a steady-state dry granule bed (production and properties of the bed and measurement steps are detailed in Chapter 4: Section 4.3), where the points when the impeller rotation is started and stopped are indicated in the figure. From the raw readings, the output change is computed using the reference values and converted to normal stress or pressure values from the calibration data. Figure 3.12 presents these time-averaged blade-bed stress values for steady-state measurements of a dry granule bed at different impeller speeds up to 350 rpm. The measurements were conducted at least three times at each impeller speed and Figure 3.12 shows good repeatability of the measurements. Runs at different impeller speeds without any granules were also carried out to determine if the mechanical rotation and vibration of the impeller and Roto Junior affects the readings. The time-averaged results of these empty runs are also presented in Figure 3.12. For all impeller speeds, the output fluctuates between the reference reading (output change of 0) and 1 or 2 bits above the reference reading (output

change of -1 or -2) when there are no granules in the granulator, instead of the expected decrease in reading when pressure is applied onto the sensor plate. Therefore, minute negative pressure values for the empty runs are reported in Figure 3.12 and from this, it can be seen that the mechanical vibrations do not cause significant noise or increase in the blade-bed stress measurements.

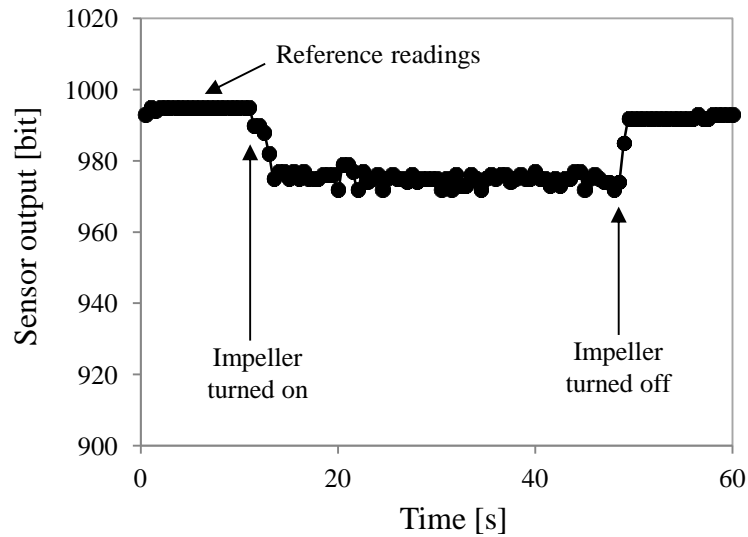


Figure 3.11: Example sensor output: readings for dry mannitol bed (1.5kg load, 0.5-1.0 mm sieve size) at impeller speed of 150 rpm.

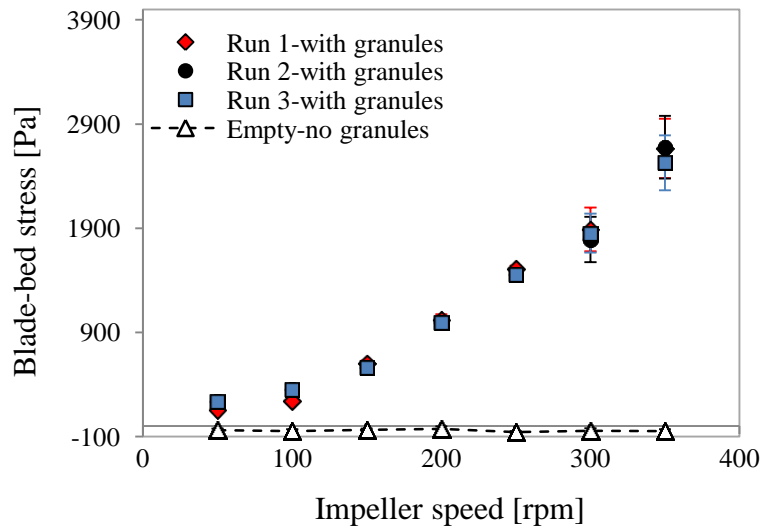


Figure 3.12: Time-averaged blade-bed stress for dry mannitol granules bed (1.5 kg load, 0.5-1.0 mm sieve size) and empty runs at different impeller speeds.

3.3 Granule bed surface velocity and height

3.3.1 High speed camera recording

The granule or particle bed surface velocities were obtained by Particle Imaging Velocimetry (PIV), a method to track and measure the motion of a bulk particle bed surface. Images of the moving bed was first recorded using a high speed camera (Photron Fastcam 1024-PCI with a Nikon 24-85mm f/2.8-4 AF-D macro lens) directed vertically downwards towards the bed. The camera was located above the bed near to the granulator wall (Figure 3.13) in order to capture the bed surface above the location the sensor plate, which is of interest. In this thesis, the top view of the bed (Conway et al., 2005; Lekhal et al., 2006; Plank et al., 2003; Remy et al., 2010) instead of the perpendicular view (Dorvlo, 2009; Litster et al., 2002; Nilpawar et al., 2006) towards the inclined bed surface was recorded to avoid inconsistencies in the changing planes of the bed surface at different conditions. Additionally, the circumferential motion, also the dominant motion of the agitated granule bed, could be adequately captured from this top view. The images were recorded at frame rates of 1000 or 1500 frames per second (1000 fps for low impeller speeds and 1500 fps for higher speeds). Recording was carried out for particular time frames depending on the impeller speed, i.e. the time taken for at least two impeller rotations for each impeller speed. Figure 3.14 shows an example image of the recorded bed surface in the Roto Junior with the analysed region also indicated in the figure.

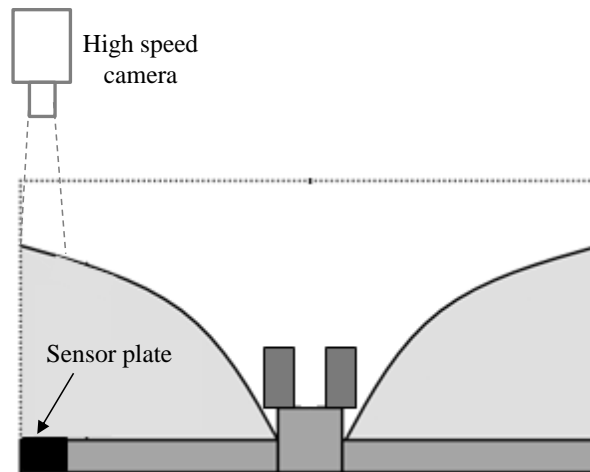


Figure 3.13: Schematic of the high speed camera setup with the Roto Junior.

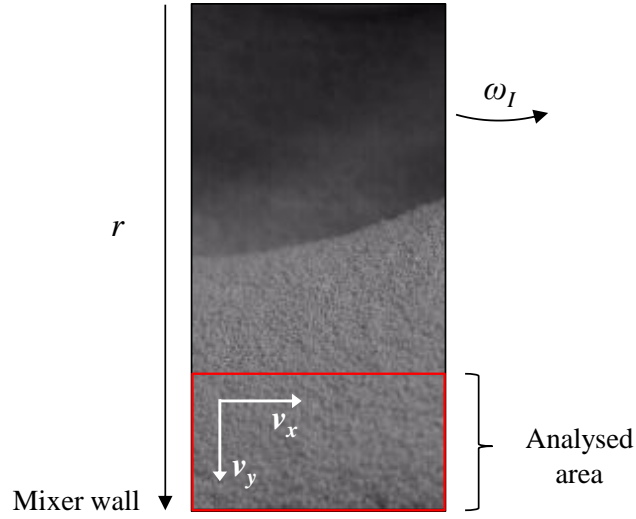


Figure 3.14: Example high speed camera image (top view of granule bed) for bed surface velocity analysis.

3.3.2 Bed surface velocity and height analysis

The 2-D velocities at the observed area above where the sensor was located (Figure 3.14), an area of $\sim 45 \times 30$ mm above the impeller stress sensor and adjacent to the wall, were computed using the Minimum Quadratic Difference (MQD) algorithm package available in Matlab (Mori and Chang, 2009). Each image was divided into sufficiently small calculation areas, called the interrogation areas. With the algorithm, the displacement and velocity vectors between successive images in an interrogation area were computed by evaluating the minimum in the sum of pixel value (or grey value for binary images) difference between the search area in the second image and the interrogation area in the first. Equation 3.1 shows the MQD algorithm equation, first introduced by Gui and Merzkirch (Gui and Merzkirch, 1996).

$$P(\Delta x, \Delta y) = \min \left[\sum_{i=1}^{N_x} \sum_{j=1}^{N_y} |f_1(x_i, y_j) - f_2(x_i + \Delta x, y_j + \Delta y)| \right]$$

Equation 3.1

P is the sum of the pixel value differences, Δx and Δy are the x and y displacements between the search areas in the second image and investigated interrogation area in the first image, f_1 and f_2 are the pixel values (or gray values for the grayscale images in this work) where the

subscripts "1" and "2" denote the first and second image respectively, x_i and y_j are the x and y coordinates in the image, and N_x and N_y are the sizes of the interrogation area. P is evaluated over a range of search areas where Δx and Δy are selected when P has a minimum value. The displacements and, consequently, velocities were determined from the time interval between successive images. This was repeated for all the interrogation areas in the image. Despite being generally more computationally exhaustive, particularly for larger search areas, this algorithm was chosen over others due to the minimal error and its robustness (Mori and Chang, 2009). Descriptions of other algorithms are also given in Appendix B.1.

For the calculations, there are several definable parameters; the interrogation area size and the search area range. The interrogation area size denotes the size of each processing area and the number of velocity vectors obtained; a smaller interrogation area results in more velocity vectors but increases the processing time. The interrogation area is typically selected based on the total resolution of the image and the size of the particles, in order to obtain a good texture or pattern of the bulk motion. For standard image resolutions, the interrogation areas are set at multiples of 8 pixels, i.e. 8×8 pixels, 16×16 pixels and so forth. Appendix B.3 shows the surface velocity results of different interrogation areas at several conditions and, based on those results, an interrogation area of 64×64 pixels was found to be adequate for accuracy and to reduce the processing times. The search area, also in terms of pixels, is set depending on how fast the particles move between images, although an excessively large search area will significantly increase the processing time. For all the conditions studied in this thesis, a maximum search area of 20 pixels was sufficient to capture the motion of the particles between images.

The computed x and y velocities represent the circumferential/tangential, $v_{surf,c}$, and radial velocities, $v_{surf,r}$, respectively for the moving bed in a cylindrical granulator. In Chapter 7, the total bed surface velocity, $v_{surf,t}$, in each interrogation area was also computed from the circumferential, and radial components ($v_{surf,t} = \sqrt{v_{surf,c}^2 + v_{surf,r}^2}$). Note that this total bed surface velocity does not include the vertical motion of the bed. The bed height was determined from a second set of recorded images from the high speed camera directed towards the inner surface of the mixer wall on which a scale was affixed (Figure 3.15).

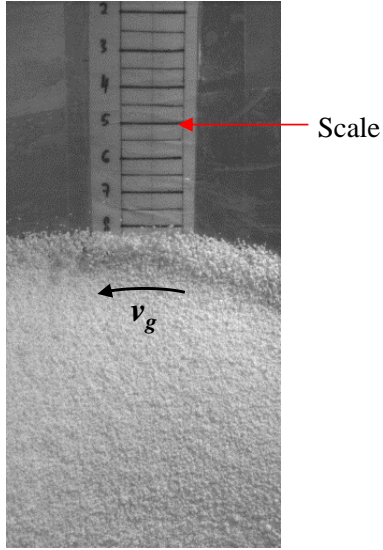


Figure 3.15: Example high speed camera image for bed height evaluation.

To obtain the velocities, the image pixels have to be correlated with the actual distance of the recorded image. This was usually done by capturing an image with an inserted scale. Since the top view of the granulator was recorded, the pixel-distance correlation was carried out for different heights in the granulator. Refer to Appendix B.2 for a pixel-distance correlation plot at different heights. For the velocity computations, the appropriate pixel-distance value was used depending on the measured bed height.

3.4 Dry granule/particle and liquid properties

3.4.1 Granule/particle size

Granule or particle sizes can be measured in several ways; the most common techniques are sieve analysis, laser diffraction and static or dynamic image analysis. The dynamic image analysis method with a Camsizer S by Retsch was used for the size measurements of granules produced by the Roto Junior or larger particles used in the experiments due to the suitable measurable size range, i.e. 30 μm to 30 mm. In the Camsizer, the granules or particles were placed on an in-built vibratory feeder where they were transported and dropped between a light source and two CCD (charge-coupled device) digital cameras (Figure 3.16). The projected shadows of the falling particles were recorded by the cameras at frame rates of at least 60 fps.

In this manner, every single particle in the bulk material flow can be recorded and analysed. The two camera system; a zoom and a basic camera enables maximum resolution across the size ranges. The zoom camera ensures good resolution of the finer particles while the basic camera captures the larger ones and also provides a large sampling size for good statistical certainty. Each particle size was then evaluated directly from the images, i.e. the equivalent diameter based on the particle's surface area was calculated. The size distributions are, therefore, primarily number-based and can be converted to volume-based distributions. The granule or particle size data reported in this thesis are the median, 10th percentile and 90th percentile of the volume-based distributions, i.e. $d_{v,10}$, $d_{v,50}$, $d_{v,90}$.

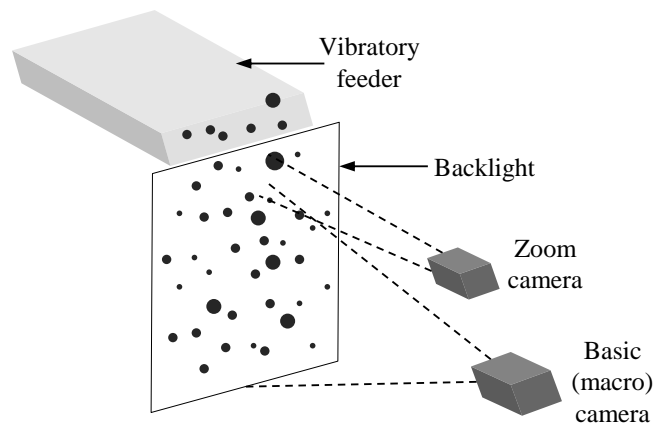


Figure 3.16: Schematic of the dynamic image analysis method for size measurement in the Camsizer.

The laser diffraction method with a Mastersizer S Series – Long Bench by Malvern was used for size analysis of some of the fine raw materials or powders used in this thesis. The measurable size range using the selected lens was 0.5-900 μm . Using a compressed air supply, the powder was dispersed and fed to the measurement field where collimated laser beams were directed to. The particles scatter the beam, which are deflected at different angles thus producing a scatter pattern measured by a series of detector. The angles of observation produces unique light intensity characteristics and the angles at which peak energies are registered are related to the diameter. Large particles have peak energies in small scatter angles, i.e. scatter at narrower angles, and vice versa. The particle size distribution is obtained from comparison of the scattering pattern with an appropriate optical model using a mathematical inversion process (Mie scattering theory) where the optical properties of the sample and surrounding medium (i.e. air for dry powder measurements) also have to be known. The

particle size distribution generated with this method is the volume-based distribution, and from the distribution data, the $d_{v,50}$ value is reported for the powders.

3.4.2 Granule/particle apparent density

The two most common methods of determining the particle or granule apparent density, i.e. density of the granule including the internal pores, are the submersion or liquid displacement (Fu, 2006; Gabbott, 2007; Iveson et al., 1996) and liquid pycnometer (Blake and Hartge, 1986; Heiskanen, 1992; Redding et al., 2005) methods. In the liquid displacement method with non-polar liquids such as kerosene, benzene or non-aromatic hydrocarbons, a certain mass of granules is added into a precision burette with a known volume of liquid. From the volume of liquid displaced, the apparent density of the sample of granules can be calculated.

In this thesis, the apparent densities were measured using the pycnometer method using paraffin oil as the displacing liquid. Properties of the paraffin or mineral oil at ambient conditions are given in Table 3.1. The viscosity and surface tension were measured using the methods described in Section 3.4.4 and 3.4.5 of this chapter. It is important that the liquid's density is lower than that of the granules so that the granules do not float. Additionally, the surface tension should also be reasonably low so that the liquid envelops the surfaces of the granules well and does not penetrate into the granule pores. The granules were first soaked with the paraffin oil coloured with an oil-soluble dye for several minutes, removed and dissected. It was confirmed visually that there were no traces of dye and hence, liquid penetration into the granule pores.

Table 3.1: Properties of paraffin oil

Density	864 kg/m ³ (~1000)
Viscosity	0.27 Pa.s (0.001)
Surface tension	33.5 mN/m (72)

*values in brackets are for water

For the measurements, a 25 ml liquid pycnometer was first weighed and paraffin oil was added to the brim. The stopper was inserted after allowing all air bubbles to rise to the top. The paraffin oil filled pycnometer was then weighed. Next, half of the oil was removed from the pycnometer and a portion of weighed granules (~2 g) were added. Finally, the pycnometer was

topped with paraffin oil and weighed again. After each sample, the pycnometer was emptied, cleaned and dried thoroughly using compressed air. Following the measurements, the volume of liquid displaced from the pycnometer when the granules were added is given by Equation 3.2.

$$V_l = \frac{m_{pl} - (m_{plg} - m_g)}{\rho_l}$$

Equation 3.2

m_{pl} is the mass of the pycnometer filled with liquid, m_{plg} is the mass of the pycnometer with the liquid and added granules, m_g is the mass of the added granules and ρ_l is the density of the liquid. From the volume of the liquid displaced, the apparent density of the granules, ρ_a , is thereby given in Equation 3.3.

$$\rho_a = \frac{m_g}{V_l}$$

Equation 3.3

3.4.3 Strength and Young's modulus

The strength of dry granules was evaluated using two methods: the conventional quasi-static single granule diametric compression (Bika et al., 2001; Coury and Aguiar, 1995; Wynnyckyj, 1985) and uni-axial confined compression (Adams et al., 1994; Samimi et al., 2005) for a bed of granules. In the single granule diametric compression, granules were crushed individually by a platen while the force-displacement data was recorded to determine the load during fracture. For the uniaxial confined compression of a bed of granules, a bed of granules in a confined volume was compressed by a punch. From the force-displacement behaviour of the entire bed, compression models notably by Heckel, Kawakita and Ludde and Adams and co-worker are commonly used to approximate the average granule bed strength (Adams et al., 1994; Heckel, 1961; Kawakita and Ludde, 1971). While the single granule crushing test provides direct information of the individual granule strength, a sufficiently large sample number is often required due to the inevitable variation of each granule's internal structure and composition. In addition, crushing of granules with sizes $< \sim 0.5$ mm individually is impracticable. Multiple granule compression, on the other hand, enables a bulk granule sample to be tested, thus

reducing individual granule variations and is also suited for finer granules. However, the bulk behaviour of the bed does not always agree to the single granule behaviour, as discovered by several authors (Bashaiwoldu et al., 2004; Gabbott, 2007; Samimi et al., 2005). Therefore in this thesis, data from both tests are reported, where appropriate. Both compression tests were carried out using a Zwick/Roell Z0.5 compression machine (Figure 3.17) connected to a computer for data logging and analysis. A 500 N load cell for the force application, with an accuracy of 0.001 N was used. For the displacement data, a crosshead travel moved the punch or platen vertically with an accuracy of $\sim 0.2 \mu\text{m}$.

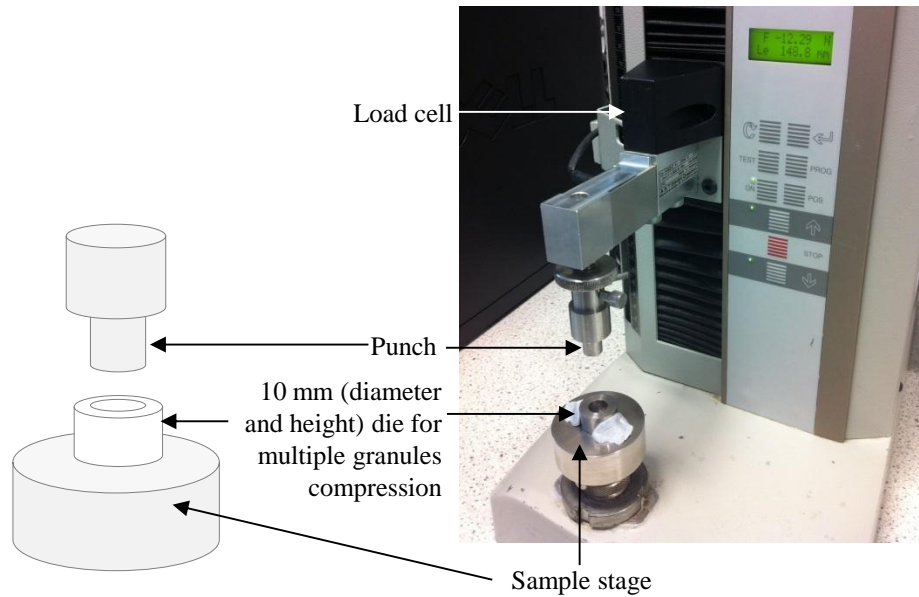


Figure 3.17: Zwick/Roell Z0.5 compression machine and schematic (left) of the punch and die.

3.4.3.1 Single granule diametric compression

A single granule was placed on the stationary sample stage shown in Figure 3.17 while the punch was slowly driven downwards at a crosshead speed of 5 mm/min to apply an increasing load on the granule until it fractured. The force-displacement behaviour of the granules, exhibited in Figure 3.18 conforms to the characteristic of semi-brittle failure of materials, where there is a sudden drop in load during granule fracture. This was observed by several authors when studying different types of granules (Cheong et al., 2005; Gabbott, 2007; Pitchumani et al., 2004). Based on this semi-brittle characteristic of the granules, the tensile strength of the granule is given by Equation 3.4, derived by (Hiramatsu and Oka, 1966). F_f is the load during fracture and D_f is the distance between loading points. For simplification, D_f is

often estimated as the representative granule size, which is the granule diameter. The tensile strength is also known as the strength of single granules reported in this thesis.

$$\tau_s = \frac{2.8F_f}{\pi D_t^2}$$

Equation 3.4

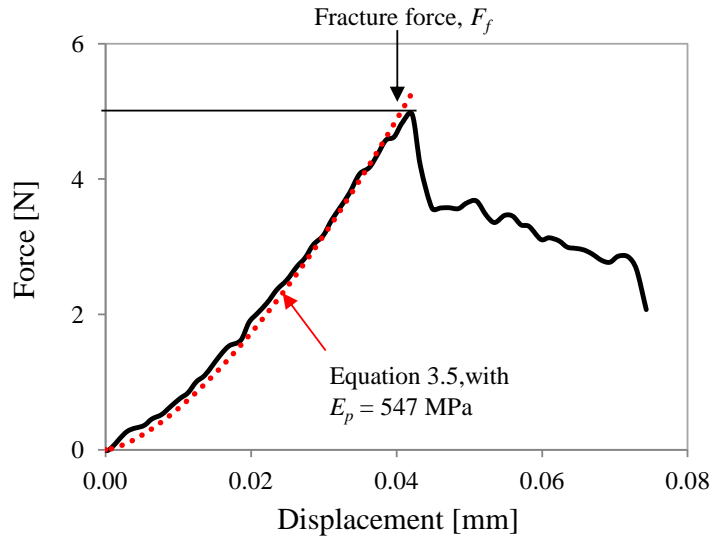


Figure 3.18: Force-displacement curve for single granule crushing tests (dry mannitol granules, 0.5-1.0 mm sieve size produced in Chapter 4).

To obtain the Young's modulus of the single granules, the Hertzian equation to describe the power law relationship between the load applied on a spherical body and the elastic deformation can be applied (Equation 3.5) (Johnson, 1985). r_p is the granule radius, E^* is the effective Young's modulus and Δ is the displacement. According to the theory, the load is proportional to the displacement to the power of 3/2. The granule Young's modulus, E_p , is related to the effective Young's modulus, E^* , by Equation 3.6. The value of the granule Poisson's ratio, ν_p , is typically taken as 0.25. Figure 3.18 includes the force-displacement curve fitted into Equation 3.5 to obtain E_p .

$$F = \frac{\sqrt{2}}{3} r_p^{3/2} E^* \Delta^{3/2}$$

Equation 3.5

$$E_p = E^* (1 - \nu_p^2)$$

Equation 3.6

3.4.3.2 Uniaxial confined multiple granules compression

In the confined multiple granules strength test, granules were filled into a 10 mm high, 10 mm diameter cylindrical die, also shown in Figure 3.17. The granule bed was tapped gently multiple times during filling to ensure proper packing. The punch was lowered onto the die and applied a force of up to 450 N on the granule bed with the same crosshead speed as that of the single strength tests. Figure 3.19 shows a typical applied force versus displacement curve for the multiple granules compression.

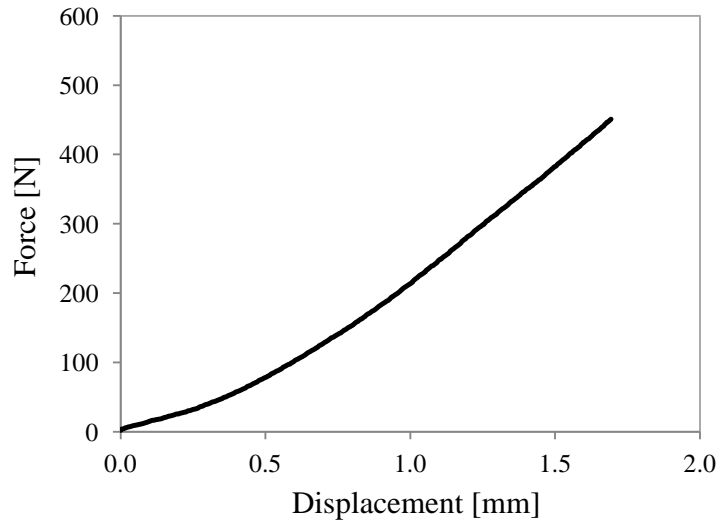


Figure 3.19: Force-displacement curve for uniaxial confined multiple granules compression (dry mannitol granules, 0.5-1.0 mm sieve size produced in Chapter 4).

In this work, the compression model proposed by Adams and co-workers is applied (Adams et al., 1994). The authors modelled the bed as a series of parallel columns to bear the applied load and applied the Mohr-Coulomb macroscopic failure criterion (Equation 3.7).

$$\tau = \tau_0 + \alpha P'$$

Equation 3.7

τ is the shear failure stress, τ_0 is the cohesive strength, α is the friction coefficient and P' is the lateral stress. $\alpha P'$ represents the frictional stress acting at the failure planes. Based on the failure criterion and the parallel-column model, the authors related the applied nominal pressure on the bed, P , to the natural strain, ϵ' , by Equation 3.8. τ_0' and α' are proportional to the τ_0 and α in Equation 3.7 respectively and τ_0' is used to represent the strength of the bulk

granules, the 'bulk agglomerate cohesive strength parameter'. The natural strain, ϵ' , is given in Equation 3.9 where H_0 is the initial bed height and Δ is the displacement.

$$\ln P = \ln\left(\frac{\tau'_0}{\alpha'}\right) + \alpha' \epsilon' + \ln[1 - \exp(-\alpha' \epsilon')]$$

Equation 3.8

$$\epsilon' = \ln\left(\frac{H_0}{H_0 - \Delta}\right)$$

Equation 3.9

To obtain the bulk agglomerate strength parameter, τ'_0 , the applied force and displacement are first converted into pressure, P , (from the bed's cross-sectional area) and natural strain, ϵ' , respectively. The plot of $\ln P$ versus $\ln \epsilon'$ is then fitted into Equation 3.8 (Figure 3.20). The bulk granule strength reported in this thesis is the τ'_0 obtained using this method.

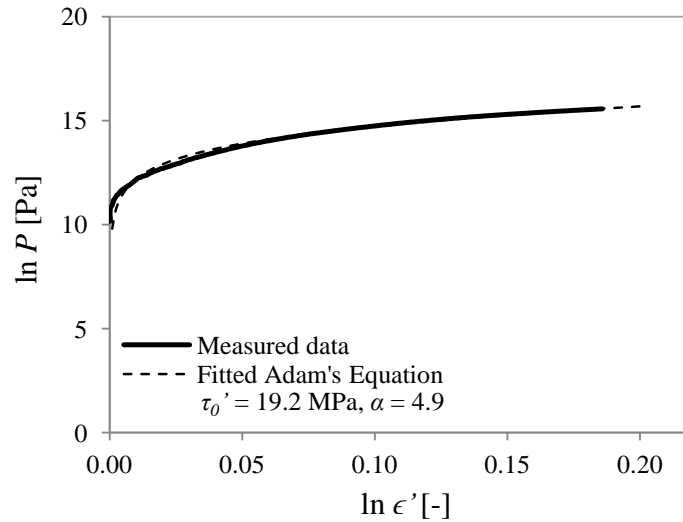


Figure 3.20: Plot of $\ln P$ (pressure) versus $\ln \epsilon'$ (natural strain) and fitted Adam's equation (Equation 3.8) (dry mannitol granules, 0.5-1.0 mm sieve size produced in Chapter 4).

3.4.4 Liquid viscosity

The viscosity of liquids was measured using a proRheo R180 Rheomat "tube and bob" rotational viscometer by Rheometric Scientific. The instrument consists of a motor driven bob rotating in a tube filled with the measured liquid (Figure 3.21). The rotational torque was measured and converted to shear stress from the known volume of sheared liquid and the liquid viscosity was computed by the shear stress and shear rate ratio. Several tube and bob

combinations with different diameters enable viscosities from 0.003-150 Pa.s to be measured. Shear rates can also be varied from 6.5 to 1291 s⁻¹.

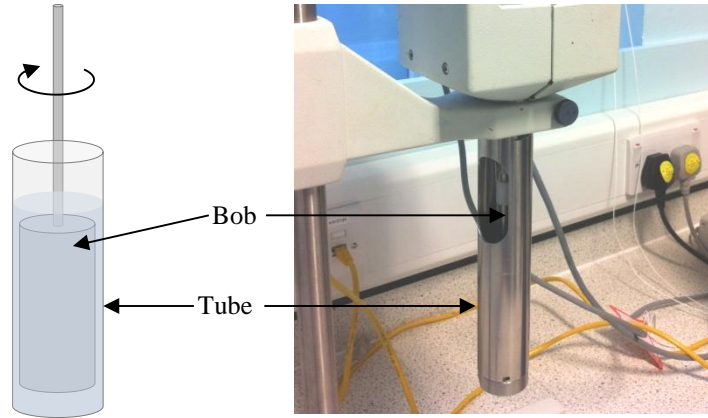


Figure 3.21: proRheo R180 Rheomat “tube and bob” rotational viscometer with the 32.54 mm diameter tube and 30 mm diameter bob attached. Left: Schematic of the tube and bob.

Figure 3.22 shows an example plot of the viscosity of paraffin oil used as the displacing liquid for the granule/particle apparent density measurements in Section 3.4.2, across the full range of shear rates in the instrument. It can be seen that the paraffin oil exhibits slight pseudoplastic properties, i.e. reduced viscosity at high shear rates. The viscosity value reported in Table 3.1 is taken as the y-intercept of a fitted linear line to the viscosity data across the shear rates.

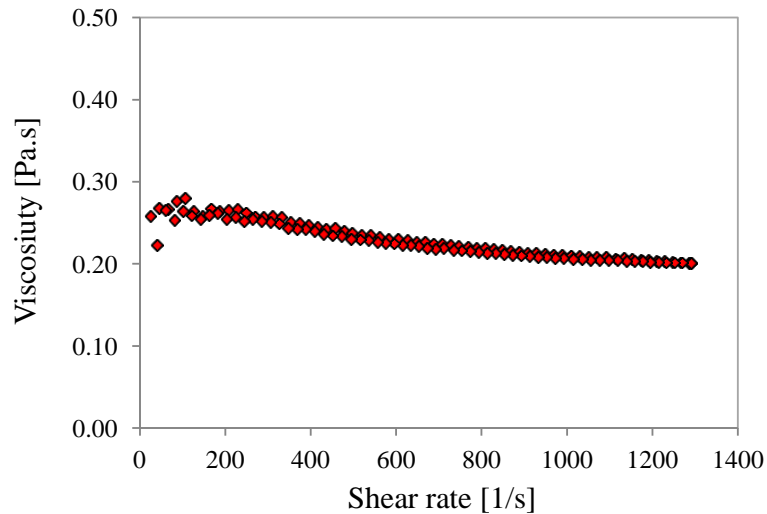


Figure 3.22: Viscosity of paraffin oil at different shear rates.

3.4.5 Liquid surface tension

The surface tension of liquids was measured using the FTA 32 drop shape analyser by First Ten Angstrom Inc (Figure 3.23), with the widely used "pendant drop" test. Using a manual dispensing syringe and needle, a suspended droplet of the studied liquid in air was produced and an in-built high speed camera recorded the images at 60 fps for analysis, as shown in Figure 3.23. The surface tension was calculated by fitting the droplet shape to the Laplace-Young equation which describes the capillary pressure difference across the interface of two fluids (i.e. air and the analysed liquid for this thesis). The liquid density, necessary for the calculations was determined prior to the measurements using a liquid pycnometer.

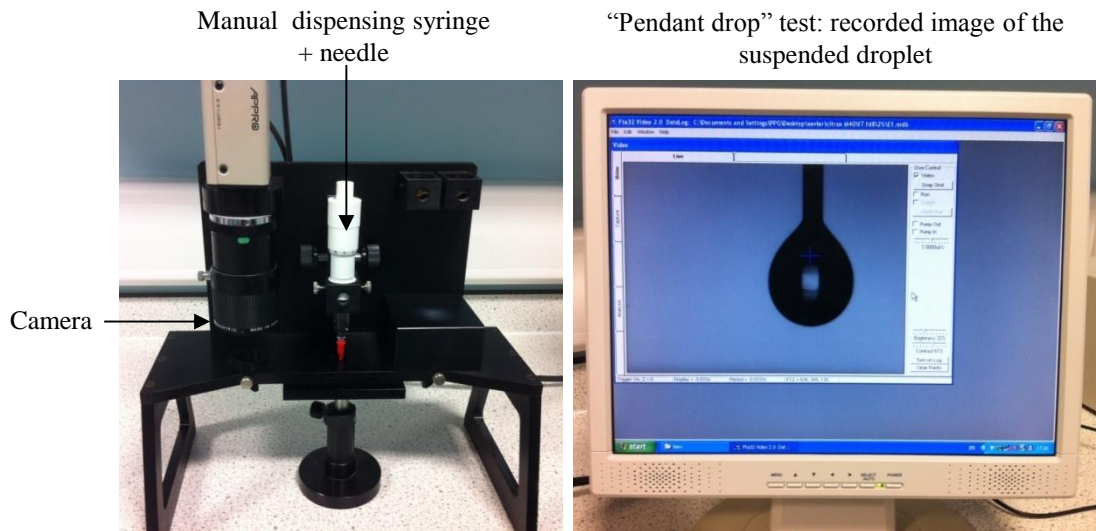


Figure 3.23: FTA 32 drop shape analyser for liquid surface tension measurements.

Chapter 4

Dry granule/particle bed characterisation: experimental

4.1 Introduction

In this chapter, the impeller blade-granule bed stress is characterised and measured using the custom-built impeller stress sensor described in the previous chapter for dry granule beds in the ~10 L Roto Junior high shear granulator. Contents of this chapter are presented in the following order:

- Explanation of the theory for direct correlation of the impeller blade-granule bed force, and the impeller blade-bed stress equation for a cohesionless, continuous granule bed in the studied granulator system;
- Description of the materials for the dry granule beds used for the measurements, production method and characterisation of the granule/particle properties;
- Measurement results for several important operating conditions and granule bed properties, i.e. impeller speed, bed load, granule sieve size and granule materials/density; and
- Prediction of the blade-bed stress from the proposed theoretical equation.

4.2 Blade-granule bed stress: theory

4.2.1 Force of a blade moving linearly through a cohesionless granule bed

For direct correlation of the blade–granule bed interaction with the blade and granule bed properties, characterisation of the force imparted by a linear blade moving through a cohesionless, continuous granule bed has been carried out by a number of authors (Bagster and Bridgwater, 1967, 1969; Makishima and Shirai, 1968), where the force is dependent on the following factors: weight of the bed, velocity of the blade through the bed, blade geometries (height and angle), frictional properties of the bed and the blade gap and floor effects. Bagster and Bridgwater carried out dimensional analysis on the total horizontal force, F_H to move a blade through a bed of cohesionless granular particles (Figure 4.1) (Equation 4.1):

$$\frac{F_H}{\rho_p(1-\varepsilon_b)gh_I^2L_I} = f\left(\frac{Z}{h_I} \cdot \frac{L}{h_I} \cdot \frac{W_f}{h_I} \cdot \Phi_f \cdot \frac{v_I^2}{gh_I} \cdot \theta_I \cdot \Phi_p \cdot \Phi_w \cdot \varepsilon_b\right)$$

Equation 4.1

ρ_p is the density of the constituent granules of the bed, ε_b is the bed porosity, g is the gravitational acceleration, h_I is the blade inclined height, L_I is the blade length, Z is the immersion of the blade (defined as the vertical distance from the bottom of the blade to the undisturbed particle bed surface), W_f is the gap height between the bottom of the blade and the floor, Φ_f is the dynamic angle of friction between the granules and the floor, v_I is the blade linear velocity, θ_I is the blade inclination angle, Φ_p is the angle of internal friction (granule-granule) and Φ_w is the angle of wall friction (granule-blade).

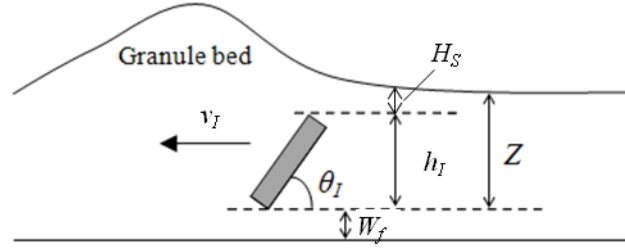


Figure 4.1: Blade moving through a granule bed (modified from Bagster and Bridgwater, 1967 and Bagster and Bridgwater, 1969).

From the analysis, the dimensionless horizontal force, $\frac{F_H}{\rho_p(1-\varepsilon_b)gh_I^2L}$ depends on the following dimensionless groups:

- $\left(\frac{Z}{h_I}\right)$ and (ε_b) which reflect the effect of the weight of a static granular bed supported by the blade.
- $\left(\frac{W_f}{h_I}\right)$ and (Φ_f) for the blade gap and floor effects.
- $\left(\frac{v_I^2}{gh_I}\right)$ for the effect of the movement (inertial contribution) of the bed through the granular bed.
- (Φ_p) and (Φ_w) for the effect of the frictional properties of the bed.

- (θ_l) for the effect of the blade's inclination angle.

The static weight and frictional effects have been modelled by Nedderman using Coulomb's method of wedges for the static force of a cohesionless material on a vertical wall (Nedderman, 1992). For passive failure analysis of the wall, i.e. force vector directed outwards from the wall to the bed, and taking into account the effect of a uniform surcharge, i.e. stress applied by additional material to the top surface of fill/wall, Equation 4.2 was obtained for a horizontal force per unit length of the blade:

$$\frac{F_H}{L_I} = \frac{1}{2} K_p \rho_p (1 - \varepsilon_b) g (h_I^2 + 2H_S h_I)$$

Equation 4.2

H_S is the height of the surcharge and K_p is the coefficient of passive failure. The coefficient of passive failure, or more specifically the ratio between the horizontal force and the vertical force on the retaining wall, is a function of the angles of internal and wall frictions and also the inclination angle of the wall (Jumikis, 1962; Terzaghi, 1966).

The inertial component of the horizontal force per unit blade length from the dimensional analysis is given in Equation 4.3.

$$\frac{F_H}{L_I} = \alpha_1 \rho_p (1 - \varepsilon_b) h_I v_I^2$$

Equation 4.3

α_1 is the proportionality constant determined experimentally as obtained by Bagster and Bridgwater (Bagster and Bridgwater, 1969). Experimental measurement of the force vector on a vertical blade moving through a granular bed by the authors using a customised force measuring apparatus showed that the force due to the blade movement (above ~ 0.25 m/s) is found to be almost independent of the values of ϕ_p and ϕ_w , hence the frictional properties of the granular bed. On the other hand, at low velocities (up to ~ 0.25 m/s), they found that the force is independent of speed and therefore the inertial group. In this velocity range, the static weight and frictional effects on the force are dominant. Bagster and Bridgwater also used Equation 4.2 (without the effect of surcharge) to obtain a semi-empirical correlation between the dimensionless force and the frictional properties.

4.2.2 Force and stress of a rotating blade through a cohesionless granule bed

The previous section described the force of a blade moving linearly through a granular bed. In high shear granulators, the impeller blades rotate about the axis of rotation. For a vertical axis, cylindrical high shear granulator (Figure 4.2), the impeller is mounted and rotates (in the azimuthal, α direction) about a central, vertical shaft (z -axis).

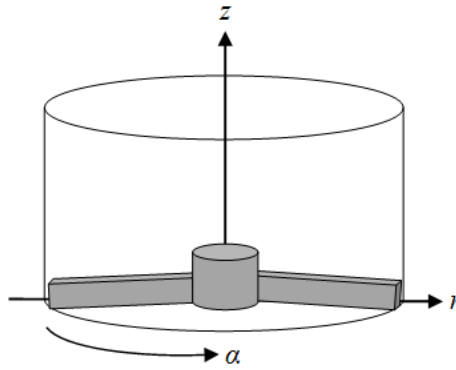


Figure 4.2: Vertical axis cylindrical granulator

Figure 4.3 and Figure 4.4 display the granule bed and impeller blade profiles in the z - r and z - α planes respectively. The granule bed is typically pushed towards the granulator's periphery due to centrifugal effects from the impeller rotation and, therefore, the granule bed height varies along the radial position, r . Unlike the blade of length, L_I , moving linearly through the granule bed in Figure 4.1 which gives a constant force across its length, the impeller-granule force varies along the blade radius, r , due to the variation of linear speed ($v_I = 2\pi r\omega_I$) and granule bed mass (from the bed height) along the radius. ω_I is the impeller rotational speed. The inertial force, dF_i , which accounts for the acceleration imparted by the blade to the bed is simply given as the rate of change of momentum (Knight et al., 2001). This is assumed to be the dominant force for the blade-granule bed interactions in the high shear granulator, since the impeller is usually rotated at high speeds. Therefore, frictional effects are not considered. For simplicity, the floor effects are also disregarded and since the impeller blade-floor gap in the Roto Junior is ~ 1 mm.

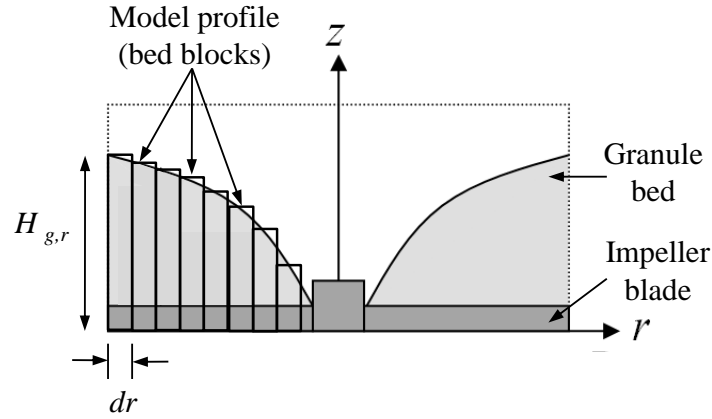


Figure 4.3: Granule bed and impeller blade profile in the $z-r$ plane (front view).

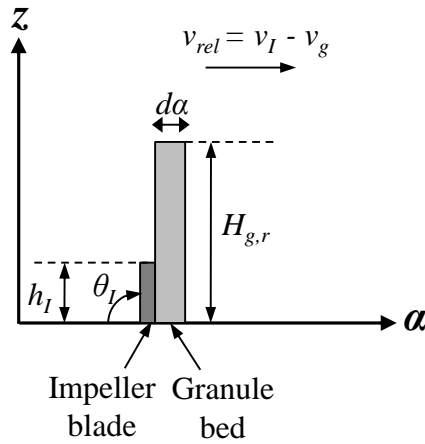


Figure 4.4: Granule bed and impeller blade profile in $z-\alpha$ plane (side view).

The inertial force of a particular bed block, $dF_{i(r)}$, acting in the circumferential direction, is derived from Equation 4.4, i.e. the rate of change of momentum of a block of granule bed with dimensions $H_{g,r} \times d\alpha \times dr$ (Figure 4.3 and Figure 4.4) which is pushed by the impeller blade. $H_{g,r}$ is the bed height at a particular radial position or for a particular granule bed block, $d\alpha$ and dr are the angular and radial displacements respectively. A particular block of bed is assumed to have similar physical properties and velocity throughout.

$$dF_{i(r)} = \frac{d(m_{b,r}v_{rel})}{dt}$$

Equation 4.4

$m_{b,r}$ is the mass of a granule bed block and v_{rel} is the relative velocity between the blade and granule bed. The angular displacement is given in Equation 4.5. Also, the inclination angle of the blade affects the force imparted to the granules and the deformation of the granule bed. Knight and co-workers suggested the inclusion of a $(1 - \cos \theta_I)$ term to the force, where θ_I is the blade inclination angle from the horizontal. Substituting the granule bed bulk density, ρ_b , the bed block dimensions ($H_{g,r} \times d\alpha \times dr$), Equation 4.5 for the angular displacement and the inclusion of the blade angle term into Equation 4.4 consequently gives Equation 4.6 for the inertial force. The bed bulk density, ρ_b , is equal to the $\rho_p(1 - \varepsilon_b)$ term used by Bagster and Bridgwater in the previous section.

$$d\alpha = v_{rel} dt$$

Equation 4.5

$$dF_{i(r)} = \rho_b H_{g,r} v_{rel}^2 (1 - \cos \theta_I) dr$$

Equation 4.6

The blade–granule bed normal stress, $\sigma_{i(r)}$, is then derived assuming that the force varies only along the blade radial length and is constant across the blade height, h_I (Equation 4.7), thus giving Equation 4.8 (Equation 4.8a in terms of linear velocities, v_{rel} , and Equation 4.8b in terms rotational speeds, ω_{rel}). $v_{rel} = v_I - v_g$ and $\omega_{rel} = \omega_I - \omega_g$ where subscripts "I" and "g" denote the impeller and granule bed respectively.

$$\sigma_{i(r)} = \frac{1}{h_I} \frac{dF_{i(r)}}{dr}$$

Equation 4.7

$$\sigma_{i(r)} = \frac{\rho_b H_{g,r} v_{rel}^2 (1 - \cos \theta_I)}{h_I}$$

Equation 4.8a

$$\sigma_{i(r)} = \frac{4\pi^2 \rho_b H_{g,r} \omega_{rel}^2 r^2 (1 - \cos \theta_I)}{h_I}$$

Equation 4.8b

From Equation 4.8, the blade–granule bed stress is dependent on the blade geometries (blade inclined height, h_I , blade inclined angle, θ_I), granule bed properties (bed height, $H_{g,r}$, bed bulk density, ρ_b) and blade and bed velocities (v_I , v_g). Also, there are several dependent,

measurable parameters of the moving bed: the bed velocity, v_g , and the bed height, $H_{g,r}$, which need to be determined for the stress prediction. Logically, the characteristic bed velocity should be taken as the average bed velocity across its height. In this work however, the bed surface velocity is assumed as the characteristic velocity. Since the blade-bed stress is measured using the custom-built impeller stress sensor, the bed surface velocity is measured at the same region above the stress sensor, and for simplicity the bed height is measured at the wall. In addition, only the component of the bed surface velocity in the direction of the blade motion is regarded, i.e. the circumferential component. Also, parameters that could be changed and investigated experimentally using the custom-built stress sensor are the bed load or mass, sieve size of granules and the bed bulk density (by changing the type of granules).

4.3 Materials and methodology

4.3.1 Granule preparation and granule/particle properties

Dry granules of different powders and plastic balls (solid, polypropylene) were used for the dry bed experiments. Table 4.1 and Table 4.2 show the powder grades, their $d_{v,50}$ (median of the volume-based cumulative size distribution), true densities, ρ_t , and formulation of the various types of granules. Mannitol, lactose and microcrystalline cellulose (MCC) are typical excipients or filler materials, while hydroxypropyl cellulose (HPC) is a common binder ingredient in pharmaceutical drug formulations.

Table 4.1: Powder grades and properties.

<i>Powder</i>	<i>Grade</i>	$d_{v,50}$ (μm)	ρ_t (g/cm^3)
Mannitol	Pearlitol 50C	$\sim 50^a$	$\sim 1.52^a$
Lactose	Lactochem, fine grade	$\sim 39^a$	$\sim 1.53^a$
Microcrystalline cellulose (MCC)	Avicel PH101	78 ± 0.8^b	$\sim 1.56^a$
Calcium carbonate (CaCO_3)	Durcal 15	21 ± 0.3^b	$2.7\text{-}2.9^a$
Hydroxypropyl cellulose (HPC)	Klucel EXF Pharma Grade	99 ± 1.3^c	1.209 ± 0.001^c

^a manufacturer's specification.

^b mastersizer measurement, described in Chapter 3: Section 3.4.1.

^c obtained from (Picker-Freyer and Dürig, 2007).

Table 4.2: Formulation for the different granules.

<i>Name/Type</i>	<i>Composition (weight percentage)</i>	<i>Liquid (water) to solid weight ratio(L/S)</i>
Mannitol granules	75% mannitol, 21% MCC, 4% HPC	0.21
Lactose granules	96% α -lactose monohydrate, 4% HPC	0.12
MCC granules	96% MCC, 4% HPC	0.70
CaCO ₃ granules	96% calcium carbonate, 4% HPC	0.12

The granules were made using the ~10 L Zanchetta Roto Junior high shear granulator in 2 kg batches. Water, pre-mixed with red dye (Erythrosin B, Acid Red 51) for ease of identification and subsequent analysis, was spray added into the granulating system with the impeller rotated at 400 rpm to trigger the hydration of the HPC for binding effect. Following the spraying of water into the granulator, the granulating mixture was agitated for 5 minutes and the agglomerates were then collected and air dried for 2 days. For the spraying, a 0.71 mm orifice, atomising spray nozzle (1/4" LNN SS Atomizing from Spraying Systems Limited) with a spraying pressure of 0.8 bar was used. This gave a spraying rate of ~65 g/min for water (Appendix C shows the spray rate calibration for the spraying system in the Roto Junior). Several batches of each formulation were produced using the same conditions to obtain sufficient granules for subsequent measurements. For the granule size effect studies, the mannitol granules were sieved into 4 different size classes: 0.1-0.5 mm, 0.5-1.0 mm, 1.0-2.0 mm and 2.0-4.75 mm. For the study of different types of granules, granules in the size range of 0.1-2.0 mm were taken. Polypropylene balls with a size between 1.0-2.0 mm were used.

Table 4.3 displays the size and density properties of the produced granules and polypropylene balls. The granule sizes and apparent densities were measured using the Camsizer and liquid pycnometer method respectively, as described in Section 3.4.1 and 3.4.2 of Chapter 3. Bulk and apparent densities decreased slightly across the sieve sizes of the mannitol granules with similar bed porosities, except for the 2.0-4.75 mm granules. For granules of different materials, the densities of calcium carbonate granules are the highest, largely due to the denser calcium carbonate powder (Table 4.1), whilst lactose granules and polypropylene balls are the least dense. Also, spherical polypropylene balls have a lower bed porosity compared to the granules, indicating denser packing which is primarily related to the particles' shapes and surface roughness.

Table 4.3: Size and density properties of different formulation granules and polypropylene balls.

Material / Sieve size (mm)	Size data (mm)				Density (kg/m ³)		Bed porosity ^b
	$d_{v,10}$	$d_{v,50}$	$d_{v,90}$	Span ^a	Bulk, ρ_b	Apparent, ρ_a	
Mannitol granules (0.1-0.5 mm)	0.127 ±0.009	0.277 ±0.015	0.438 ±0.014	1.12 ±0.05	757±4	1418±5	0.47
Mannitol granules (0.5-1.0 mm)	0.496 ±0.014	0.669 ±0.020	0.936 ±0.020	0.66 ±0.01	740±7	1394±5	0.47
Mannitol granules (1.0-2.0 mm)	1.077 ±0.077	1.556 ±0.098	2.065 ±0.048	0.64 ±0.06	740±12	1362±4	0.46
Mannitol granules (2.0-4.75 mm)	2.368 ±0.043	3.340 ±0.057	4.502 ±0.075	0.64 ±0.01	673±18	1347±10	0.50
Lactose granules (0.1-2.0 mm)	0.256 ±0.018	0.558 ±0.045	1.418 ±0.063	2.09 ±0.11	600±12	1275±5	0.53
Mannitol granules (0.1-2.0 mm)	0.335 ±0.070	0.610 ±0.102	1.414 ±0.210	1.78 ±0.09	765±8	1359±4	0.44
MCC granules (0.1-2.0 mm)	0.239 ±0.052	0.515 ±0.072	1.038 ±0.106	1.57 ±0.12	762±7	1360±12	0.44
CaCO ₃ granules (0.1-2.0 mm)	0.346 ±0.045	0.562 ±0.035	0.894 ±0.055	0.98 ±0.08	982±4	2085±31	0.53
Polypropylene balls (1.0-2.0 mm)	0.992 ±0.004	1.446 ±0.004	1.849 ±0.012	0.59 ±0.01	644±9	996±9	0.35

^a Span = $(d_{v,90} - d_{v,10}) / d_{v,50}$

^b Bed porosity = $1 - (\rho_b / \rho_a)$

Figure 4.5 shows the microscopic images, taken with a Carl Zeiss Stereo Discovery V12 Stereo Microscope, of the different granule types and polypropylene balls. Very noticeable are the more irregular shapes of the granules (Figure 4.5a-d) compared to the spherical and smooth polypropylene balls (Figure 4.5e). For the different types of granules, calcium carbonate granules are the most spherical (Figure 4.5d) while microcrystalline granules are typically more elongated (Figure 4.5c). Also when observed visually, the surfaces of both the lactose and calcium carbonate granules are rougher compared to the others (Figure 4.5a&d), with smaller particles sticking out at the granule surfaces.

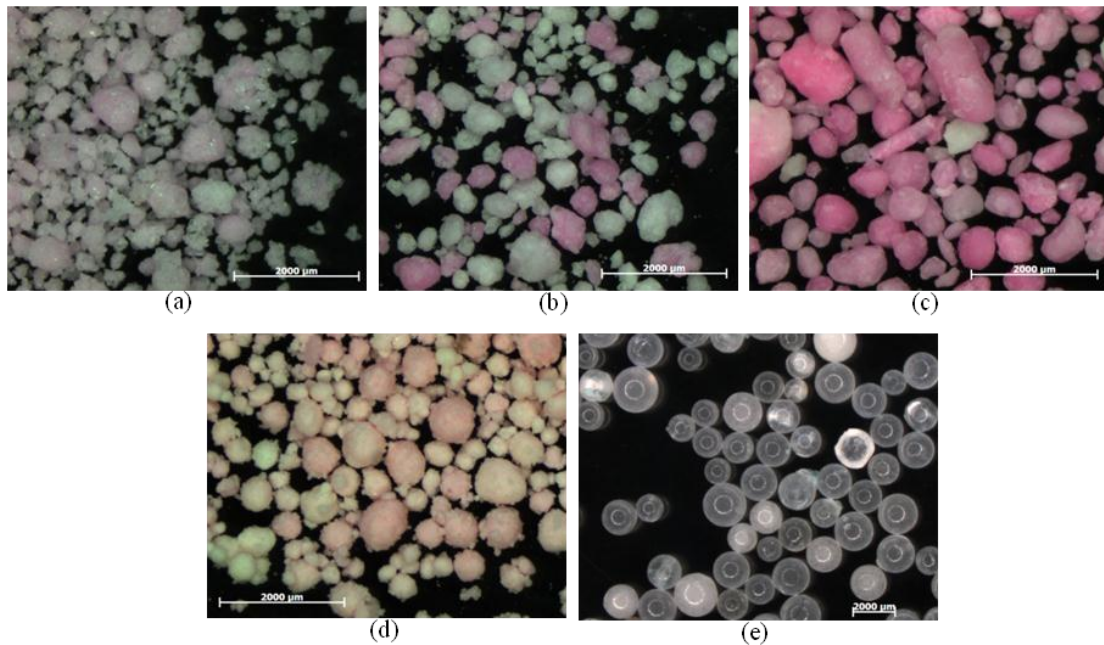


Figure 4.5: Microscopic images of (a) lactose granules, 0.1-2.0 mm (b) mannitol granules, 0.1-2.0 mm (c) microcrystalline cellulose granules, 0.1-2.0 mm (d) calcium carbonate granules, 0.1-2.0 mm and (e) polypropylene balls, 1.0-2.0 mm. Scale bars represent 2000 μm .

The strength of the granules and polypropylene balls were also ascertained using both the single granule diametric compression and uniaxial confined multiple granules compression methods described in Chapter 3: Section 3.4.3. The strength data presented in Table 4.4 represents the averages and standard deviations of at least 50 runs for the single granule compression and at least 10 runs for the multiple granules compression method. Single granule compressions were only applicable for granules or particles larger than 0.5 mm. On the other hand, mannitol granules of the largest sieve size (2.0-4.75 mm) could not be properly filled into the 10 mm diameter die for multiple granule compression. For granules of other materials of sieve size 0.1-2.0 mm, only the granule bulk strength is measured due to presence of the finer particles. From Table 4.4, the strength values for the multiple compression method are larger than those from single granule compressions. This has been discussed in several works comparing granule strength obtained from different methods (Gabbott, 2007; Samimi et al., 2005), who inferred that the multiple granule strength test often involves other factors, one being the die wall friction. Nonetheless, in this study, the multiple and single granule compression results show similar trends for materials which could be successfully measured using both methods and were both, therefore, assumed to be useful for drawing comparisons in

strength for other materials. To summarise, strength decreases with increasing granule sieve size, whilst for the different materials, polypropylene balls are evidently the strongest, followed by the microcrystalline cellulose and mannitol granules, with lactose granules being the weakest ones.

Table 4.4: Single and bulk granule/particle strength.

<i>Material</i>	<i>Strength (MPa)</i>	
	<i>Single granule tensile strength (τ_s in Equation 3.4)</i>	<i>Bulk strength parameter, τ_0 ' from Adam's equation (Equation 3.8)</i>
Mannitol granules (0.1-0.5 mm)	NA	22.6±2.7
Mannitol granules (0.5-1.0 mm)	7.7±2.7	16.3±2.3
Mannitol granules (1.0-2.0 mm)	6.4±1.9	10.3±2.4
Mannitol granules (2.0-4.75 mm)	3.9±0.9	NA
Lactose granules (0.1-2.0 mm)	NA	5.7±1.1
Mannitol granules (0.1-2.0 mm)	NA	18.2±2.3
MCC granules (0.1-2.0 mm)	NA	20.4±5.2
CaCO ₃ granules (0.1-2.0 mm)	NA	9.2±2.2
Polypropylene balls (1.0-2.0 mm)	25.7±3.3	112.5±24.9

4.3.2 Blade-bed stress, bed surface velocity and bed height measurements

After the dry granules or particles of certain bed loads were loaded into the granulator, the following were measured: blade-granule bed normal stress, granule bed surface velocity and granule bed height. Measurements were performed at impeller speeds from 50 to 350 rpm. For the stress measurements using the impeller stress sensor, reference readings were first taken for approximately 10 seconds in each run before the impeller was turned on so that the actual output change could be computed for that run. The impeller was then rotated for 20 to 40 seconds, and steady-state measurements from the impeller stress sensor were taken. In addition, build-up of material on the sensor plate should be negligible and the granule bed should not undergo considerable change in terms of size of bulk densities, primarily due to weakening, breakage from continuous impacts or attrition in the blade-floor gaps, which might affect the readings. To prevent this, a fresh batch of granules of the same sieve size or type was loaded into the granulator after each impeller speed run. The impeller running time was also chosen to ensure that sufficient readings were obtained and at the same time, to cause less weakening, breakage and attrition of granules. The used granules were then sieved to determine the broken fractions. For most materials, these were <5% except for the 2.0–4.75 mm mannitol granules at

300 and 350 rpm. Therefore, for this granule sieve size, only results from 50 to 250 rpm were taken. The measurement readings were analysed and converted to normal stress values using the methods described in Chapter 3: Section 3.2.2.2 and 3.2.2.3. The bed surface velocity and bed height were measured and analysed as described in Chapter 3: Section 3.3. As explained previously in Section 4.2.2, only the circumferential component of the bed surface velocities are used for the v_g term in the blade-bed stress equation (Equation 4.8). As such, from the high speed recorded images and PIV analysis, only $v_{surf,c}$ mentioned in Chapter 3:Section 3.3.2 was computed and discussed in this chapter.

For the blade-bed stress, bed surface velocity and bed height measurements, the time-averaged values and standard deviations were then calculated from the steady-state temporal data, and presented in the following sections. The standard deviations reflect the degree of fluctuation or fluctuation amplitude of the temporal data, i.e. large standard deviations indicate large fluctuations of the temporal data and vice versa. Chapter 7 of this thesis also studies the temporal values in more detail.

4.4 Bed-granule bed stress, bed surface velocity and bed height results

4.4.1 Bed load

For each of the materials listed in Table 4.3 and for the bed load investigations, as previously mentioned, measurements were carried out for impeller speeds of 50 to 350 rpm, corresponding to tip speeds of 0.7 to 5.1 m/s in the ~10 litre Roto Junior granulator. The bed transits through different flow regimes from 50 to 350 rpm (see Figure 4.6; images taken with Photron Fastcam 1024-PCI high speed camera); generally known as the “slow/frictional” and “toroidal/roping” flows (Litster et al., 2002; Mort, 2009) while increasingly becoming more “fluidised” as the bed gets lifted up more due to swift movements of the blades beneath. The bed profiles and characteristics of each flow regime are described and studied in Chapter 7 of this thesis. To summarise, three flow regimes (i.e. frictional, toroidal and fluidised) are identified with the transitions between the frictional to toroidal and toroidal to fluidised occurring mostly at 100-150 rpm and 250-300 rpm respectively.

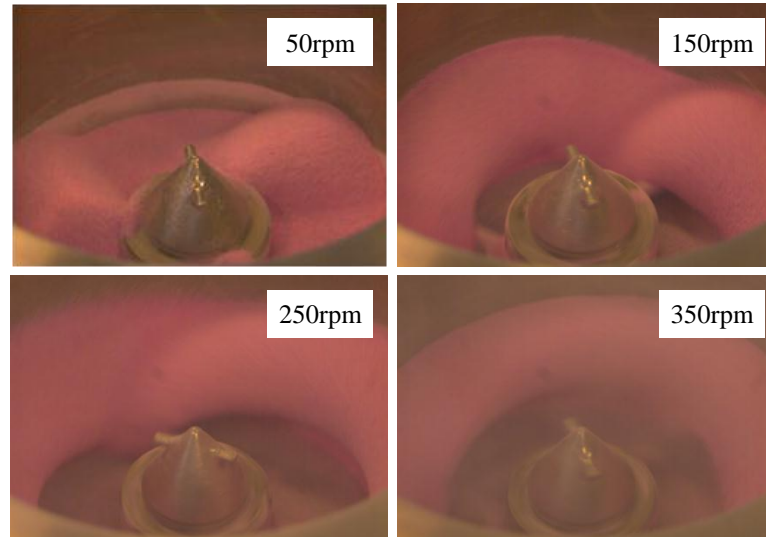


Figure 4.6: Granule bed images at different impeller speeds (mannitol granules, 1.0-2.0 mm sieve size, 1.5 kg load).

Figure 4.7 presents the time-averaged blade-granule bed stress, bed surface velocity (circumferential component) and bed height for different bed loads: 1, 1.5 and 2 kg. These experiments were carried out for mannitol granules of sieve size 0.5-1.0 mm. The error bars represent the standard deviations of the steady-state temporal data and for at least 3 measurement repetitions of each condition. Generally, an increment of the stress with the impeller speed is observed, which is expected due to the larger inertial force imparted by the blade to the granule bed (Figure 4.7a). The stress also increases quite consistently with the load size as a higher bed load requires larger force from the blade to push through the bed.

The average bed surface velocity, however, does not increase consistently across the impeller speeds (Figure 4.7b). For all cases, a noticeable increase is often observed from 50 to 150 or 200 rpm, after which the increase becomes less apparent, or a decrease in the surface velocity is noted, due to the surface becoming increasingly unaffected by the blade. The same behaviour was also reported by Litster and co-workers, where the increment of surface velocity in the "toroidal" flow regime is considerably lower than that in the "bumping" flow regime (Litster et al., 2002). Behaviour of surface velocities in different flow regimes is further discussed in Chapter 7: Section 7.5.1 of this thesis. In this study, the onset of the toroidal flow is approximately 150 rpm. As the impeller speed increases further, the surface of the bed becomes less sensitive to the motion of the blade beneath. In addition, the surface velocities are generally higher for a smaller bed load which is accelerated more by the blade. Fluctuations of

the surface velocities (from the standard deviation bars) are also larger for smaller bed loads. Also, for the 2 kg bed, the average surface velocities are almost the same for impeller speeds of 150 rpm and above.

For the time-averaged bed height, there is a prominent increase up to 200 rpm, after which the change is less prominent (Figure 4.7c). When the granule bed is entirely pushed towards the wall due to the dominant centrifugal effects, a further increase in speed will hardly change the bed height. This state is also shown in the granule bed image at 350 rpm, presented in Figure 4.6. For the different loads, an increase of bed height with the bed load is observed from 50 to 150 rpm, which is expected as more material is loaded into the mixer. However, between 200 and 250 rpm, the 1.0 and 1.5 kg beds are now lifted up more easily by the blade compared to the 2 kg bed. Like the surface velocity fluctuations, the bed height fluctuations also increase with smaller bed loads. The average height of the 2 kg bed does not change much after 150 rpm, again similar to the surface velocity results. As the surface velocity is closely related to the bed height, similar behaviours between these results could often be observed.

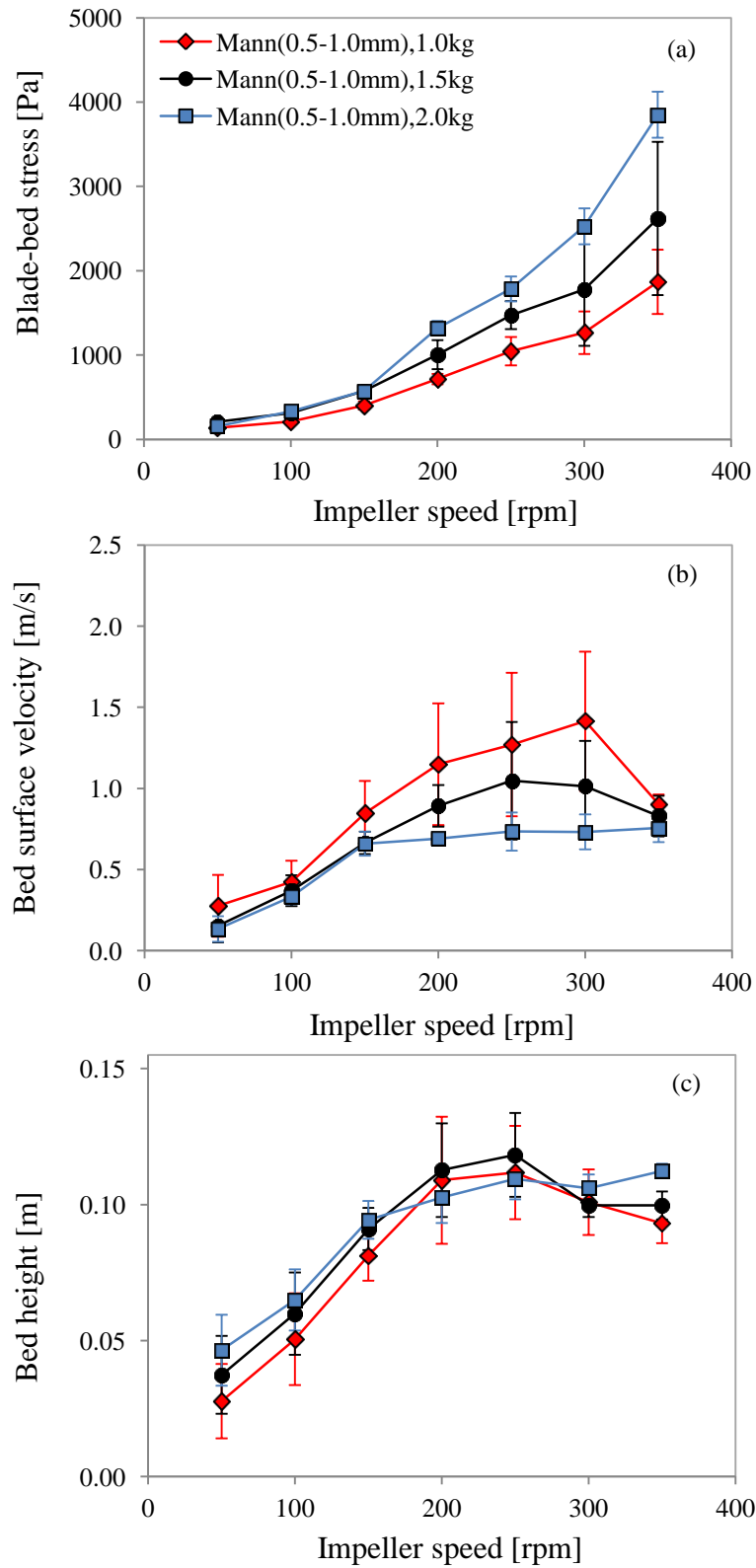


Figure 4.7: Time-averaged data for different bed loads (mannitol granules, 0.5-1.0 mm) (a) blade-granule bed stress (b) bed surface velocity (circumferential) and (c) bed height.

4.4.2 Granule size

There appears to be little difference in the time-averaged blade-granule bed stress across the difference sieve sizes of the mannitol granules (Figure 4.8a). The only observable differences are noted at impeller speeds of 300 and 350 rpm where the average blade-bed stress differs by a maximum of ~400 Pa. The same is observed for the time-averaged bed surface velocity and bed height results (Figure 4.8b-c). As previously mentioned in Section 4.3.2, measurements at above 250 rpm for the 2.0-4.75 mm granules could not be carried out due to a reasonable amount of the relatively large granules being attrited in the blade-floor gaps. Fluctuations of the surface velocities and the bed heights, however, reduce with larger granule sizes whereas the finer granules are more easily lifted up and down.

Another interesting area of study involved using an entire range of granule sizes (except for the 2.0-4.75 mm granules), rather than a specific sieve size cut. In Figure 4.8a-c, results of the 0.1-2.0 mm mannitol granules with the individual 0.1-0.5 mm, 0.5-1.0 mm and 1.0-2.0 mm sieve sizes are again similar. This indicates that the individual granule size does not affect the blade-bed stress in a dense flow system such as that in the high shear granulator, providing the bulk flow properties are similar. Also, the slight changes in the granule properties at different sieve sizes such as the densities, bed porosity and strength do not significantly affect the bed flow and measured stress. Consequently, for the study of different granule types in the next section, 0.1-2.0 mm granules are used for the measurements rather than a specific sieve cut, except for polypropylene balls which are available in 1.0-2.0 mm size range.

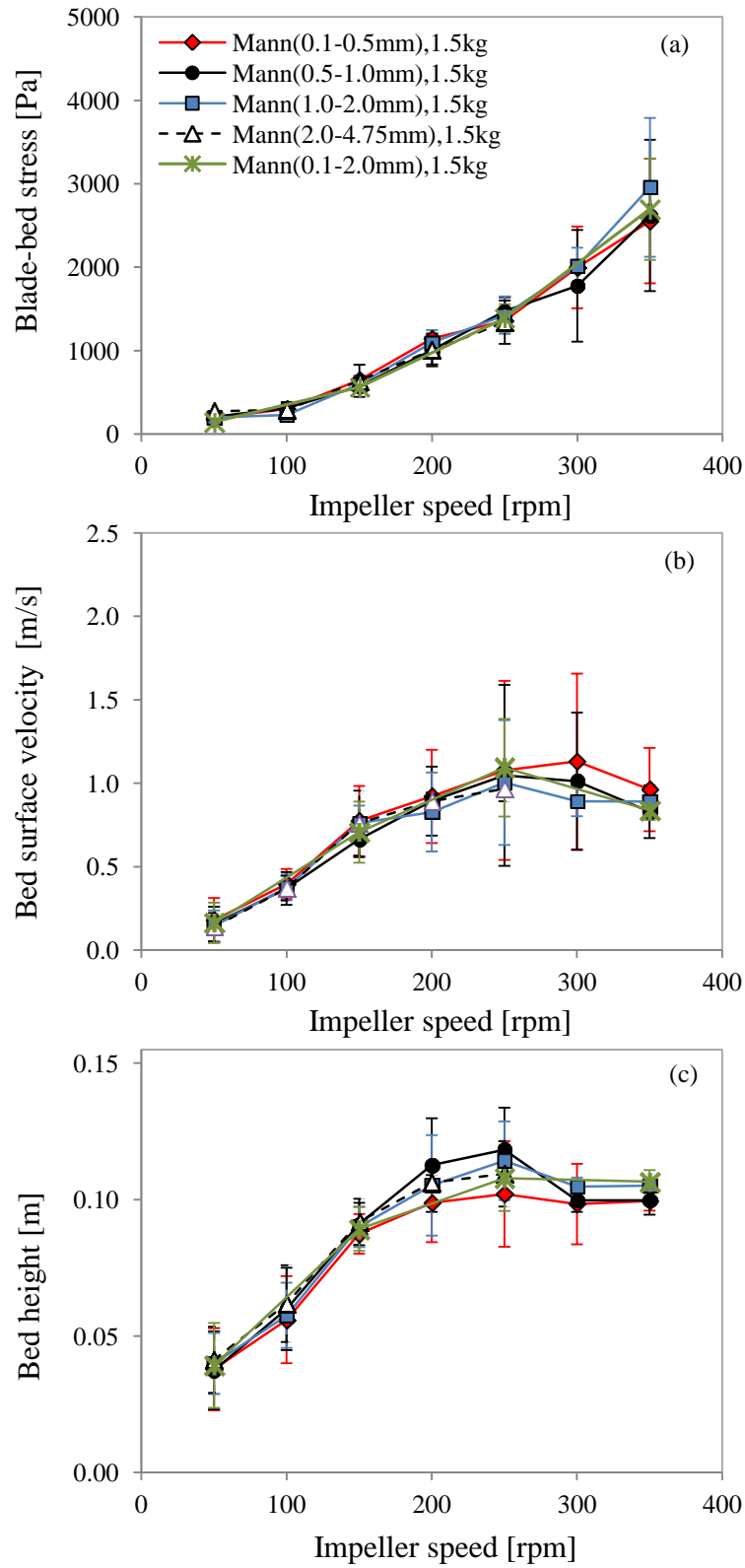


Figure 4.8: Time-averaged data for different sieve sizes (mannitol granules, 1.5 kg) (a) blade-granule bed stress (b) bed surface velocity (circumferential) and (c) bed height.

4.4.3 Granule/particle materials

Figure 4.9 presents the time-averaged blade-granule bed stress, bed surface velocity and bed height for 1, 1.5 and 2 kg beds of different types of granules. Runs for polypropylene balls were only carried out in 1.5 kg batches. As in Section 4.4.1, the average stress increases with bed load. The stresses for the polypropylene balls are generally lower than the granules, primarily due to the lower density ($\rho_b = 644 \text{ kg/m}^3$). In addition, there is not much difference between the different granules types. Nonetheless, stresses for densest calcium carbonate granules ($\rho_b = 982 \text{ kg/m}^3$) are generally the highest although these differences are not remarkable.

The average bed surface velocities for the various granule types at different bed loads also show similar trends as discussed in Section 4.4.1 and Figure 4.7b. Smaller bed loads are accelerated to higher velocities and show a more prominent increase with impeller speed followed by a dip (at 350 rpm), whereas the 2 kg bed has a flatter profile after the flow transits to the toroidal type. For the different granules types, lactose, mannitol and microcrystalline cellulose granules exhibit similar average surface velocities for all bed loads. The calcium carbonate granules however, have surface velocities higher than the rest, particularly at 250 rpm, and also the largest fluctuation. Due to the higher density, a smaller volume of calcium carbonate granules compared to the other less dense granules were added into the granulator for a certain bed load. A more fluctuating or turbulent motion of the bed ensued, also leading to higher surface velocities as observed.

Results for the bed height show that at 50, 150 and 350 rpm, the height is affected by the density of the granules; the least dense polypropylene balls having the highest bed due to more particles being loaded into the granulator and vice versa. At 250 rpm, however, the densest calcium carbonate and microcrystalline cellulose granules are lifted up the highest. This could be related to the unsteady surface movement observed near the end of the toroidal and onset of the fluidised flow regime (~250-300 rpm). In this flow regime region, the surface movement is the most turbulent or unsteady, characterised by the large velocity and bed height fluctuations seen in Figure 4.7b, Figure 4.8b and Figure 4.9.

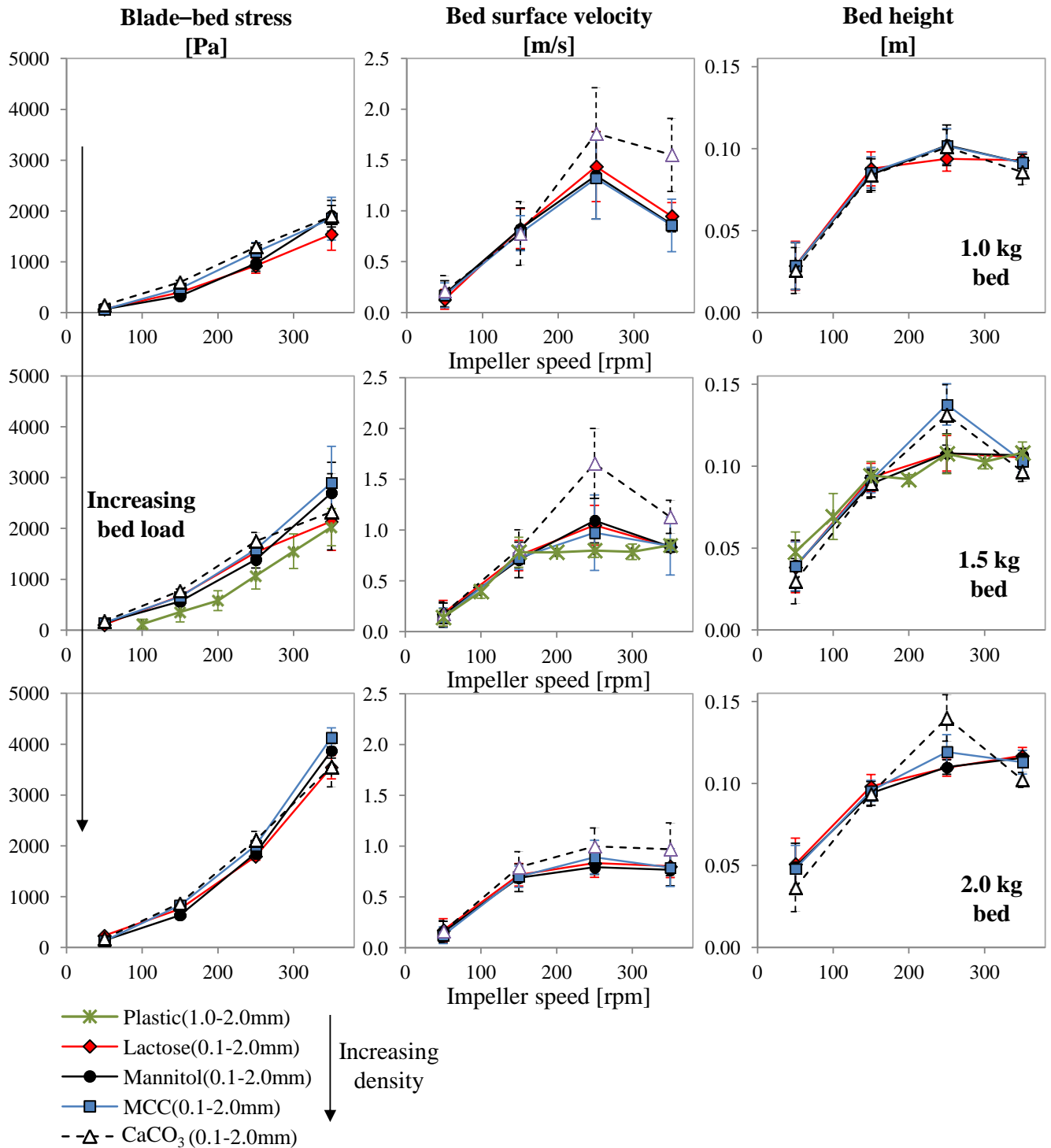


Figure 4.9: Time-averaged blade–granule bed stress, bed surface velocity (circumferential) and bed height of different granule types and polypropylene balls at different bed loads.

4.5 Blade-bed stress prediction from theory

All the measured parameters; the surface velocity (circumferential component), bed height (from Figure 4.7, Figure 4.8 and Figure 4.9) and bulk density (Table 4.3) are inserted into the v_g , $H_{g,r}$ and ρ_b parameters in the blade–granule bed stress equation (Equation 4.8) to determine its validity for an actual moving granule bed in the high shear granulator in which the flow regime or behaviour will change depending on the impeller speed, type and amount of material.

Figure 4.10a-c present the experimental results for the stress for the 0.5-1.0 mm mannitol granules at different bed loads and the values predicted by Equation 4.8. An overestimation of stress begins after toroidal flow is reached (approximately 150 rpm) and this difference increases with the impeller speed. Several reasons could be proposed for this occurrence. Firstly, the surface velocity values are chosen as the bed characteristic velocity, v_g . Based on Equation 4.8 derived for the continuous bed block, this would mean a bed block of a certain height is moving entirely at this surface velocity. In this study, the bed heights are 1.5-7 times the height of the blade, and across this height there should be a variation of velocities. This could lead to the overestimation of the $(v_I - v_g)$ or the relative velocity term and hence, the predicted stress. Secondly, the bed goes through different flow regimes from 50 to 350 rpm, and as the speed increases, the bed gets increasingly fluidised with the bed surface becoming increasingly less affected by the blade motion. The effective weight of the bed which is being carried or pushed by the blade thereby reduces with increasing speeds.

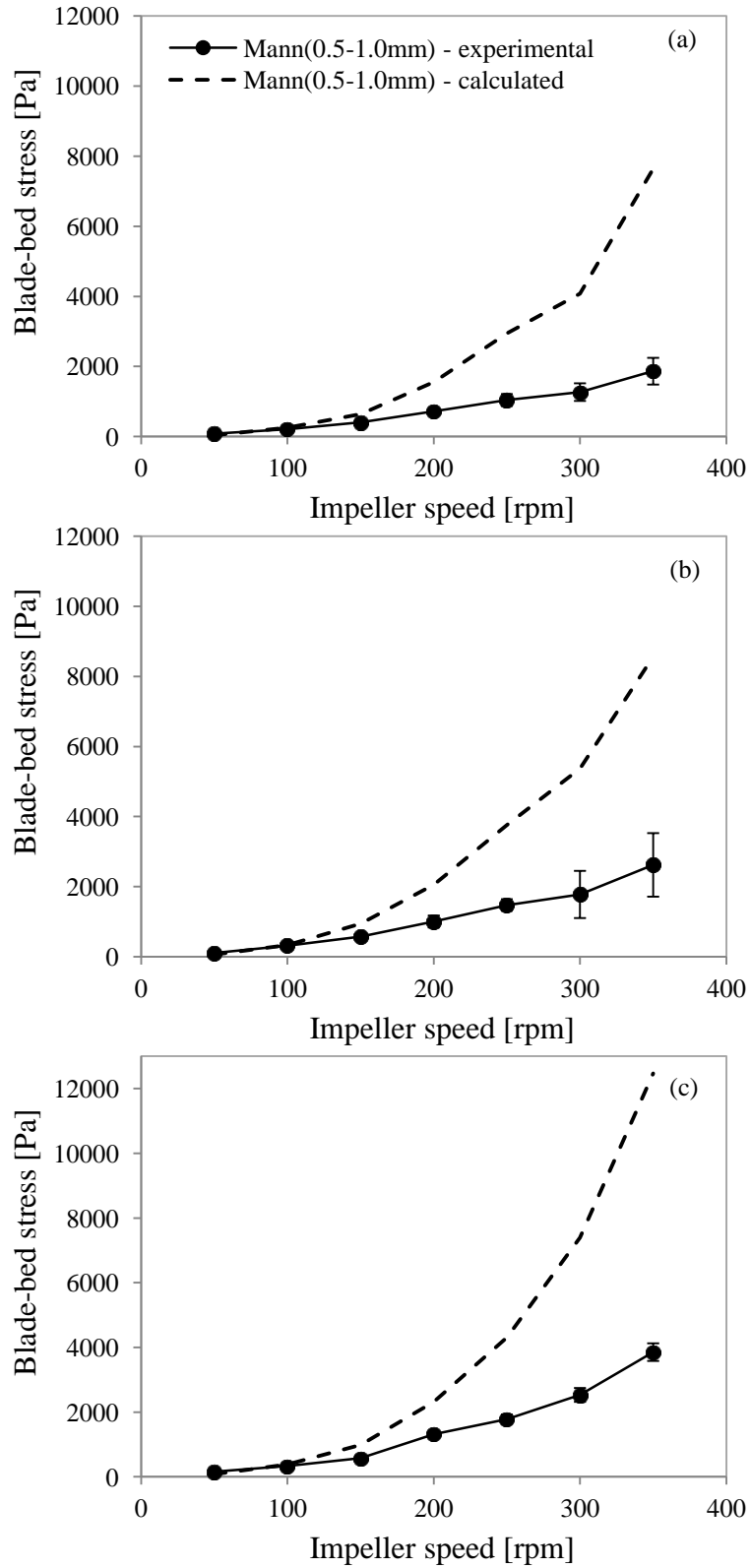


Figure 4.10: Experimental and calculated (Equation 4.8) blade–bed stress (mannitol granules, 0.5-1.0 mm) at bed loads of (a) 1.0 kg (b) 1.5 kg (c) 2.0 kg.

Further insight on the internal bed velocity could be achieved via simulations using the Discrete Element Method (DEM), as this is not possible with the current bed velocity measurement setup, i.e. using the high speed camera. Chapter 6 details the DEM model and methodology employed. From the simulations, the circumferential components of the particle velocities are calculated and plotted against the bed height (Figure 4.11). These are time-averaged results for a 1.5 kg bed of 3.5 mm, spherical, mono-sized particles, with the circumferential velocities extracted specifically at the sensor region (Chapter 6: Section 6.4). For easier comparison, the bed velocities and heights are normalised with the impeller tip speed and blade inclined height, i.e. 0.0185 m, respectively. The top most value for each data series indicates the time-averaged surface velocity and the arrow indicates the height range of the free bed surface. The results show that for 200 rpm onwards, the bed velocity reduces consistently with the bed height, excluding the values at the bottom of the bed due to constraints of the mixer floor. Interestingly, this is also when the overestimation of the calculated stress from Equation 4.8, as shown in Figure 4.10, begins. At lower impeller speeds (50-150 rpm), the velocity reduction with height is not as pronounced. Further inspection of the results also shows a faster motion of the free surface compared to the immersed particles just beneath the surface, particularly for 50-200 rpm.

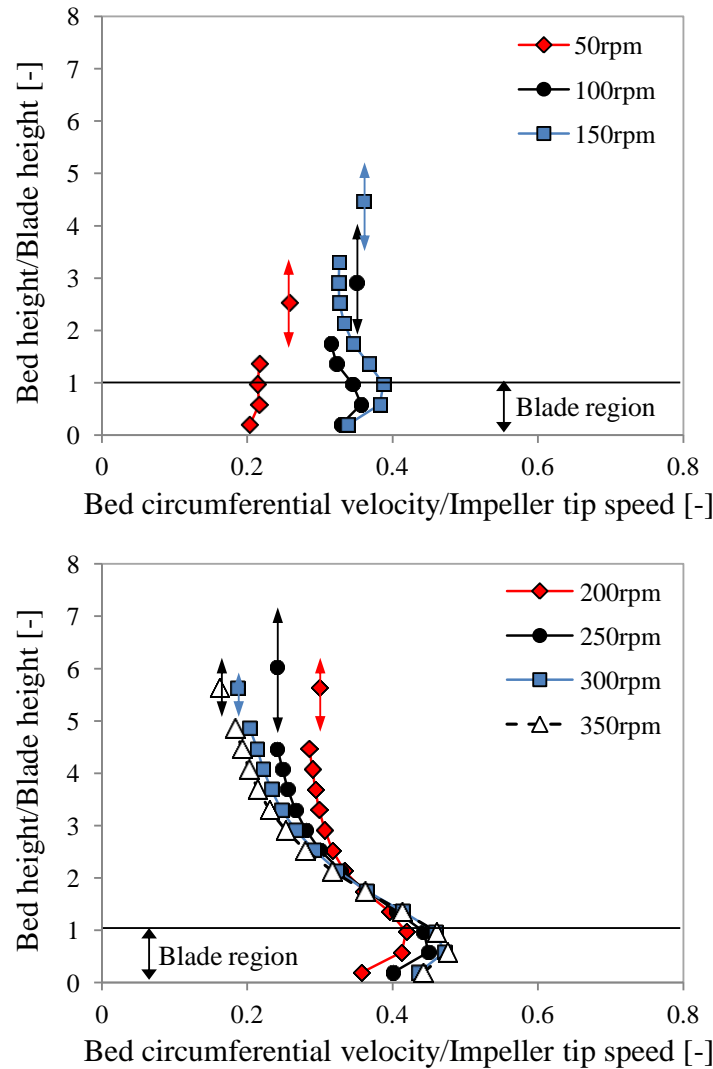


Figure 4.11: Variation of the normalised bed velocity (circumferential) with the normalised bed height from DEM simulations (3.5mm monosized particles, 1.5 kg bed load). The top most value for each series indicates the average surface velocities and the respective arrows indicate the surface height fluctuation range.

Therefore, a correction parameter, B_I , to take into account the aforementioned factors is proposed to give a modified stress equation, $\sigma_{i(r)cor}$ (Equation 4.9). This correction parameter is related to the relative velocity, v_{rel} (Equation 4.10). A high v_{rel} , i.e. a large difference between the blade and surface velocity, occurs at higher impeller speeds and also when the surface velocity is less sensitive to the blade. In other words, v_{rel} is used to indirectly represent the flow behaviour; an increasing v_{rel} indicates a bed being increasingly lifted up from the floor and its surface becoming less affected by the blade movement.

$$\sigma_{i(r)cor} = B_1 \sigma_{i(r)} = \frac{B_1 \rho_b H_{g,r} (v_l - v_g)^2 (1 - \cos \theta_l)}{h_l}$$

Equation 4.9

$$B_1 = f\left(\frac{1}{v_{rel}}\right)$$

Equation 4.10

B_1 is determined from the measured stress and the calculated $\sigma_{i(r)}$ (Equation 4.8) and plotted with $1/v_{rel}$ in Figure 4.12. From the figure, B_1 is almost proportional to $1/v_{rel}$ for the mannitol granule beds and also for other materials, with a proportionality constant, K_1 , of about 1. The blade–granule bed stress equation with the correction factor B_1 can also be rewritten as Equation 4.12.

$$B_1 = K_1 \frac{1}{v_{rel}}$$

Equation 4.11

$$\sigma_{i(r)cor} = \frac{K_1 \rho_b H_{g,r} (v_l - v_g)^2 (1 - \cos \theta_l)}{h_l}$$

Equation 4.12

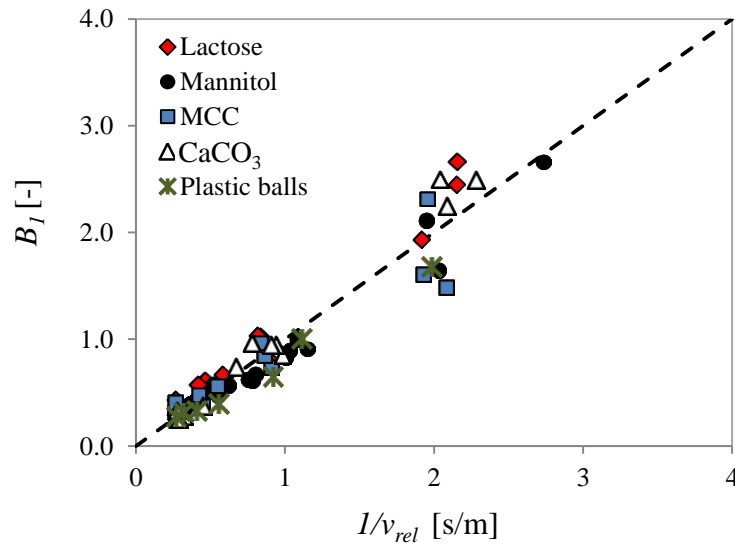


Figure 4.12: Plot of B_1 and $1/v_{rel}$ for all materials. Dashed lines represent $x = y$.

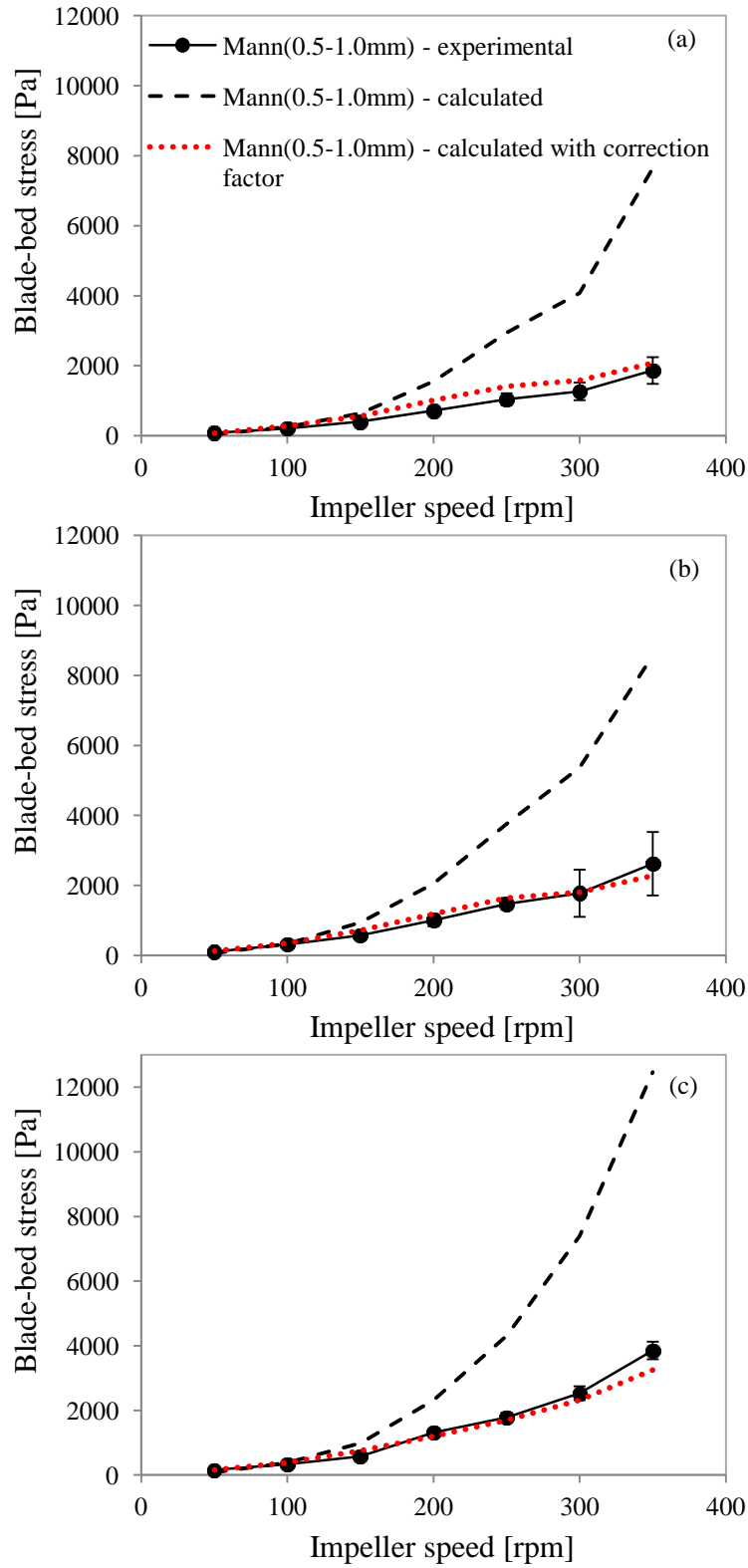


Figure 4.13: Comparison of the calculated blade–bed stress without (Equation 4.8) and with the correction parameter B_I (Equation 4.12) with the experimental results (mannitol granules, 0.5-1.0 mm) at bed loads of (a) 1.0 kg (b) 1.5 kg (c) 2.0 kg.

Equation 4.12 now gives a much better prediction of the stress for the various bed loads as presented in Figure 4.13a-c, indicated by the dotted lines. Figure 4.14 also presents the plot of the measured stress against the predicted stress from Equation 4.12 for mannitol granules of all bed loads and sieve sizes (Figure 4.14a), and for different granule types and polypropylene balls (Figure 4.14b), where the dotted lines represent the $x = y$ line. It could be seen that the blade-bed stress equation with the correction parameter could now reasonably predict the stresses for dry granule beds of different densities, strengths and sizes from the bed height and surface velocity data.

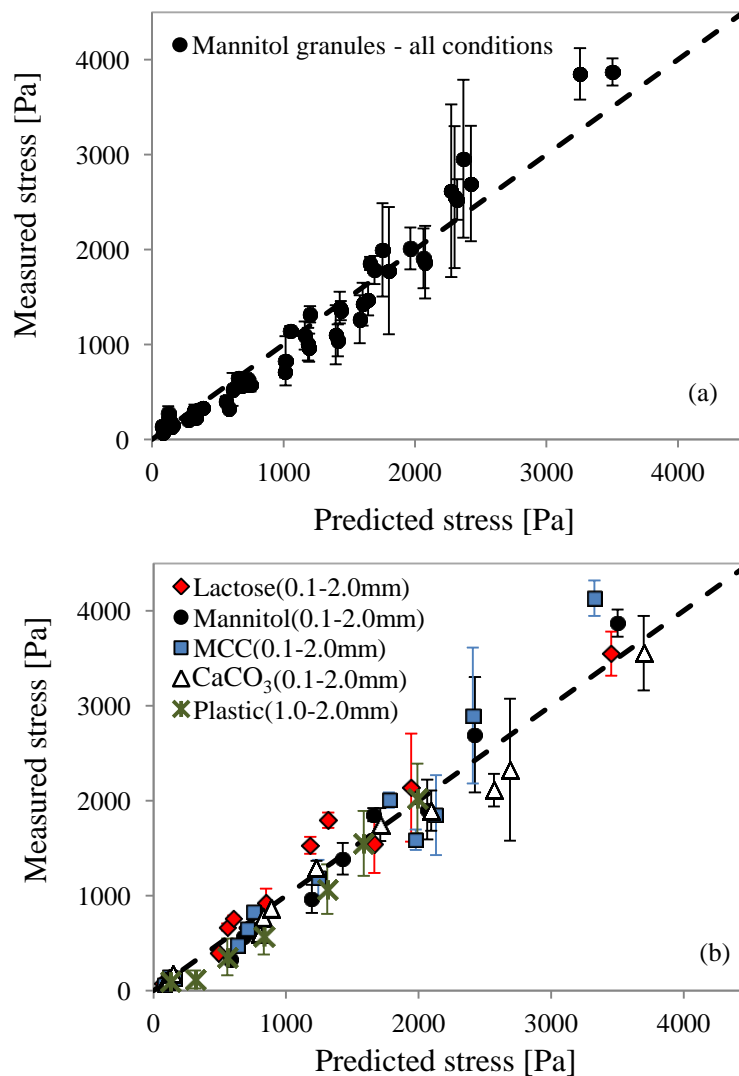


Figure 4.14: Plotted measured stress with the predicted values with the correction parameter B_1 (Equation 4.12) for (a) mannitol granules of all sieve sizes and bed loads and (b) different granule types and polypropylene balls. Dashed lines represent $x = y$.

4.6 Chapter summary and conclusions

The current chapter studied the blade-bed stress, bed surface velocity and bed height for dry granule beds of different materials and polypropylene balls. The blade-bed stress is characterised, for the first time for high shear granulator systems, which was also directly measured by the novel telemetric impeller stress sensor introduced in the previous chapter.

From theory, a blade-granule bed stress equation for the high shear granulator was derived based on the imparted inertial force for a cohesionless, continuous bed. The bed surface velocities were used for the characteristic bed velocity term in the equation, and the bed height at the wall was also measured as the representative bed height.

For the characterisation, the blade-bed stresses, bed surface velocity and bed height at steady-state were measured with several conditions changing: impeller speed, bed load, granule sieve size and types of materials. The impeller speed was varied so that it transits through several flow regimes although limitations of the setup deter any further investigations beyond 350 rpm. Important findings following the analyses of the time-averaged values of the blade-bed stress, surface velocity and bed height at the different conditions could be summarised as follows:

- The average blade-bed stress increases consistently with the impeller speed due to the larger inertial force exerted by the impeller, as observed in all cases. Additionally, visual observation of the bed flow behaviour clearly shows that the bed transits through several flow regimes throughout the range of the impeller speeds in study. A more pronounced average bed surface velocity and bed height increase is observed from 50-150 or 200 rpm, as compared to the higher impeller speeds;
- While a higher bed load leads to an increase in the average blade-bed stress, a slower and less turbulent surface motion is observed. Similar tendencies between the average surface velocity and bed height are obtained;
- The average blade-bed stress is found to be similar across the studied granule size ranges, which have different tensile strengths. These results demonstrate that the average bulk stress is least likely to be affected by the individual granule sizes provided the bulk behaviour of the granule bed is similar, affirmed by the similar averaged bed surface velocities and bed heights; and

- Different types of granules show some varied blade-bed stress, surface velocity and height behaviours across the impeller speed range, primarily depending on the granule/granule bed density. Higher density granules which give a lesser bed volume for a certain bed load experience a faster and more turbulent surface motion. Differences in the average blade-bed stress between the calcium carbonate granules (bulk density: 980 kg/m^3) and polypropylene balls (640 kg/m^3) are observed with the denser calcium carbonate granules resulting in a larger blade-bed stress.

The measured time-averaged blade-bed stresses are compared with the predicted values from theory. It is shown that the equation over-predicts the stress for impeller speeds above 150 rpm. Additionally, results from DEM simulation demonstrate the reduction of bed velocity with bed height, also for impeller speeds above 150 rpm. A correction factor, B_I , is applied to account for the increasing "fluidisation" of the bed and the use of surface velocity, which is taken to be related to the inverse of the relative velocities between the blade and bed surface, i.e. $1/v_{rel}$. Fitting of the experimental data to the corrected equation yields a constant, K_I , of ~ 1 for all conditions studied, i.e. impeller speed, bed load, particle size and particle densities.

Chapter 5

Wet granule/particle bed characterisation: experimental

5.1 Introduction

This chapter focuses on both the steady-state and unsteady-state blade-bed stress for wet granule or particle beds in the Roto Junior, which are again measured using the custom-built impeller stress sensor. The chapter is presented according to below:

- Description of the materials and methodology for steady-state measurements of wet beds;
- Blade-bed stress, bed surface velocity and bed height results for the steady-state wet particle beds with different liquid amounts and prediction of the blade-bed stress from theory introduced in the previous chapter;
- Description of the materials and methodology for unsteady-state measurements of wet beds, i.e. blade-bed stress measurements during the wet granulation process; and
- Results and discussion for the unsteady-state measurements.

5.2 Steady-state stress for wet beds

5.2.1 Materials and methodology

Dry and wet beds of polypropylene balls of 1.0-2.0 mm sieve size, also used in the previous chapter, were studied in this section. Properties of the polypropylene balls were given in Table 4.3 in the previous chapter. For a wetted bed, water (distilled) was added incrementally, in terms of liquid to solid weight percentage, from 2 to 25%w/w. To keep the total bed load constant, as the imparted force and stress depends on the load, the weight of polypropylene balls plus the weight of water was maintained at 1.5 kg for each liquid to solid ratio. Furthermore, since water can penetrate into the pores of the dry granules, only polypropylene balls (with no internal pores) were used in this study to produce surface-wet particles only. In addition to water, a 8%w/w HPC (hydroxypropylcellulose, Klucel EXF Pharma Grade, properties given in Table 4.1 in the previous chapter) solution in distilled water was also used. HPC is a water soluble polymer although it has a tendency to agglomerate and hence, cause lumping when wetted. This occurs due to hydration of the outer surface of the HPC powders,

consequently forming a viscous gel layer that impedes wetting of the inner materials and also causes lumps of material to be formed when more powder is added to the water. For that reason, to minimise lump formation the solutions were prepared by adding the HPC powder slowly into well-agitated water (using a top-driven impeller) at room temperature. The solution was agitated continuously until a gel-free solution was obtained. The viscosity and surface tension of the 8% HPC solution were measured using the methods described in Chapter 3: Section 3.4.4 and 3.4.5. The viscosity of the solution is 0.116 Pa.s, approximately 100 times than that of water (~ 0.001 Pa.s); while the surface tension is 42.6 mN/m, less than two times smaller than that of water (~ 72 mN/m). From these values, it is regarded that the viscosity change is the primary influence of the differences of both liquids' rheological properties. Measurements for wet beds using the 8% HPC solution were carried out for two liquid contents, i.e. 5 and 15% w/w solution.

Figure 5.1 displays the microscopic images of the polypropylene balls with different amounts of water added. 0.005% w/w red dye (Erythrosin B, Acid Red 51) was added to the water for easier identification of the water and formed liquid bridges. Viscosity and surface tension measurements confirmed that the viscosity and surface tension of the water do not change significantly with addition of the dye (i.e. viscosity: 0.001 Pa.s, surface tension: 69 mN/m). A transition of the liquid saturation states for the wetted polypropylene balls was observed microscopically with increasing water content. Figure 5.2 also presents the general liquid saturation states for liquid-bound particles (Newitt and Conway-Jones, 1958). In Figure 5.1, at low water contents, i.e. 2 and 5% w/w water, the polypropylene balls are held together predominantly by pendular liquid bridges at their contact points, also known as the pendular state. At higher liquid content, funicular (10 and 15% w/w water) and capillary states (25% w/w water) are subsequently obtained. The capillary state occurs when all the interparticle voids are filled with liquid and the surface liquid is pulled back into the voids from capillary action; and the transitional state between the pendular and capillary states is the funicular state, where the voids are not fully occupied by liquid.

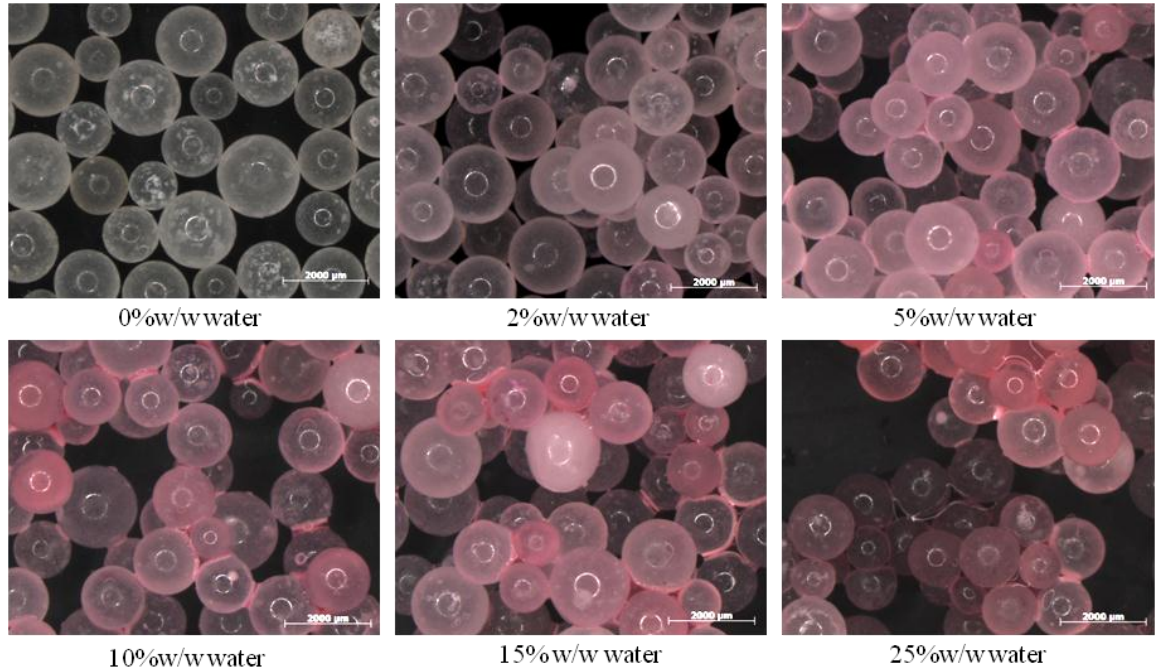


Figure 5.1: Microscopic images of polypropylene balls wetted with different water content. Scale bar represent 2000 μm .

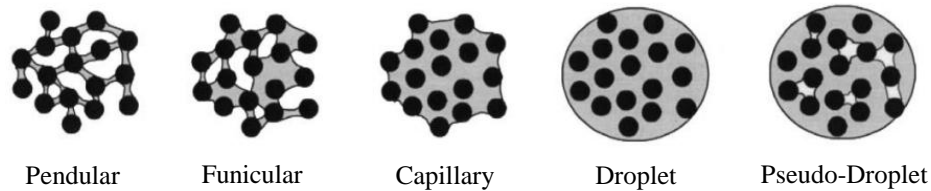


Figure 5.2: Saturation states of liquid-bound particles (modified from Newitt and Conway-Jones, 1958).

In each measurement run the polypropylene balls and liquid were loaded into the granulator and mixed under low impeller speed (50 rpm) for a maximum of 1 min to fully disperse the liquid. The blade-bed stress measurement method was similar to that described in the previous chapter (Section 4.3.2): Following the mixing of the polypropylene balls and liquid, the impeller was stopped after the mixing and reference readings were taken for approximately 10 seconds. The impeller was then run at the required speed for another 20 seconds and the measurement values were read. The output change (i.e. reference minus measurement value) was converted to the corresponding pressure/normal stress from the calibration model. The bed surface velocity and bed height were measured and analysed with the methods described in

Chapter 3: Section 3.3 and like the previous chapter, only the circumferential component of the bed surface velocity was presented. In addition, due to material build-up at the wall with liquid addition, the height of the freely moving part of the bed was taken instead of the height of materials sticking onto the wall.

5.2.2 Blade-bed stress, bed surface velocity and bed height results

The time-averaged blade-bed stress from impeller speeds of 50 to 350 rpm at different water to polypropylene ball ratios up to 25%w/w are shown in Figure 5.3a. Like the time-averaged results in the previous chapter, the error bars indicate the standard deviation of the steady-state temporal data and for at least 3 measurement repetitions for each case. From the figure, large blade-bed stress fluctuations (reflected by the standard deviation bars) are obtained in the 25%w/w water case. As shown in the microscopic images in the previous section (Figure 5.1), at relatively low water content (2 and 5%w/w), pendular liquid bridges are predominantly formed between the polypropylene balls. With increasing water content, funicular and subsequently capillary (25%w/w water) states are obtained. With more water, there is an increase in the cohesiveness of the bed as a consequence of liquid bridging, which is experimentally observed from the formation of clumps of polypropylene balls held loosely together by water and increasing roughness or irregularity of the moving bed surface in the high shear granulator (Figure 5.4). Especially at 25%w/w water, the considerable fluctuation of the bed-blade stress suggests that clumps of material were hitting and lifting up from the blade surface at the higher impeller speeds. Equivalently, the surface behaviour is also quite turbulent, indicated by the large fluctuations of the surface velocity results in Figure 5.3b at this water content. Due to unsteady behaviour and large fluctuations at 25%w/w water, subsequent results are discussed for only up to 15%w/w water.

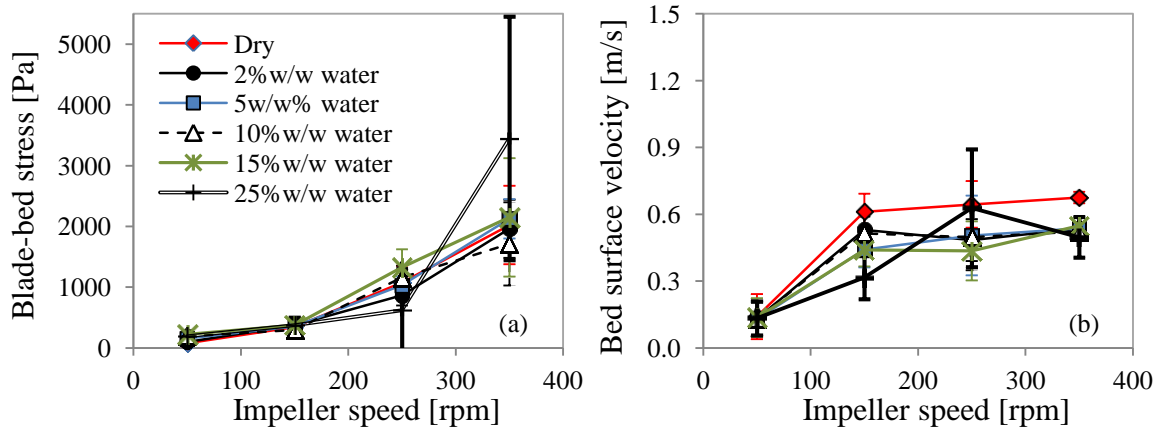


Figure 5.3: Time-averaged blade-bed stress and bed surface velocity for different water content: large fluctuations at 25%w/w water.

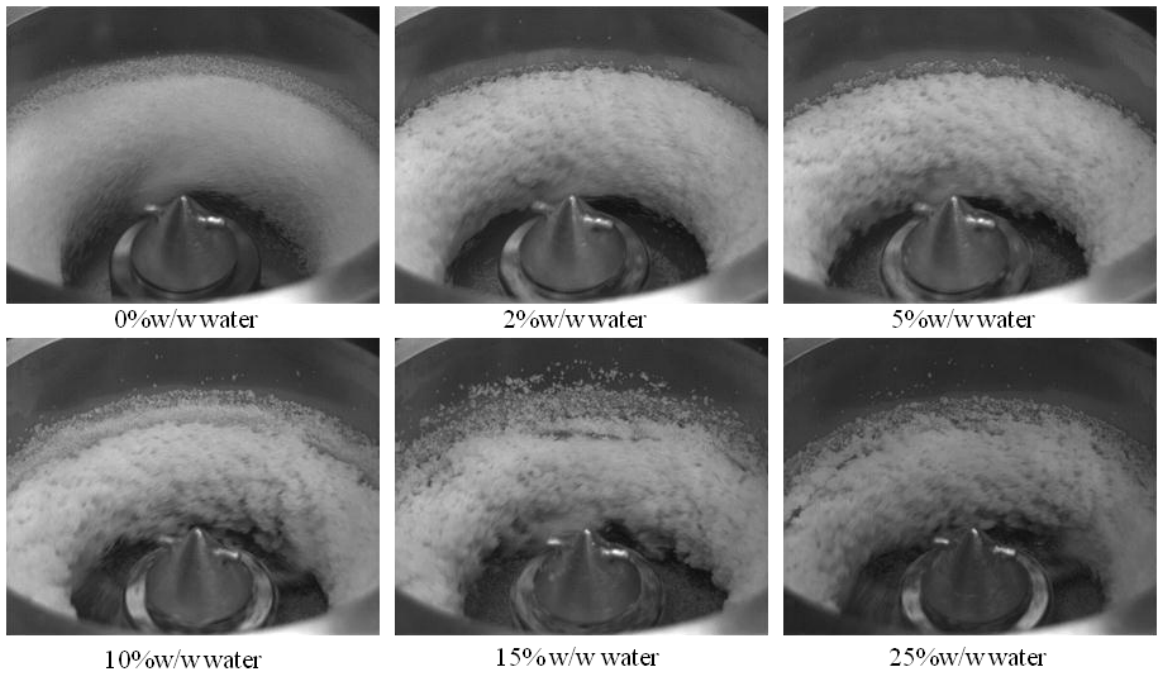


Figure 5.4: Bed flow images for different water content at 350 rpm.

Figure 5.5 displays time-averaged results including the bed surface velocity and bed height for different water contents. In Figure 5.5a, the average stresses increase with impeller speed as expected. The wet beds' average blade-bed stresses are found to be similar to the dry bed when the total bed load (weight of the solid plus liquid) was kept constant. It can also be seen from the results that addition of water retards the motion of the granule/particle bed in the granulator due to larger kinetic energy dissipation by the liquid, shown by the reduction in the average bed surface velocity (Figure 5.5b). This was also discovered by previous experimental and computer simulation results of the bed surface velocity for the vertical axis, cylindrical granulators (Lekhal et al., 2006; Radl et al., 2010; Washino, 2011). In this study, after the initial reduction of the surface velocity when water is added (compared to the dry bed), the subsequent increasing water content does not change the surface velocity significantly. Addition of water to the particle bed was previously found to increase heap formation and hence, the bed porosity (Iveson et al., 1996). This was also observed in this study from the bed bulk density measurements which are reported in Table 5.1, together with the calculated bed porosity. It can be seen that the bed bulk density reduces (bed porosity increases) as more water is added and then increases again in the capillary state (25%w/w water). The reported values are the averages and standard deviations of 5 measurements. The wet beds using 8% HPC solutions also have similar bed bulk density and bed porosity values to the wet beds with water. Due to the increased heap formation and bed porosity with water addition, the measured bed height (free moving part) for the dynamic beds in the granulator increases initially (Figure 5.5c) and subsequently decreases with increasing water content, which can be attributed to increasing material build-up at the wall.

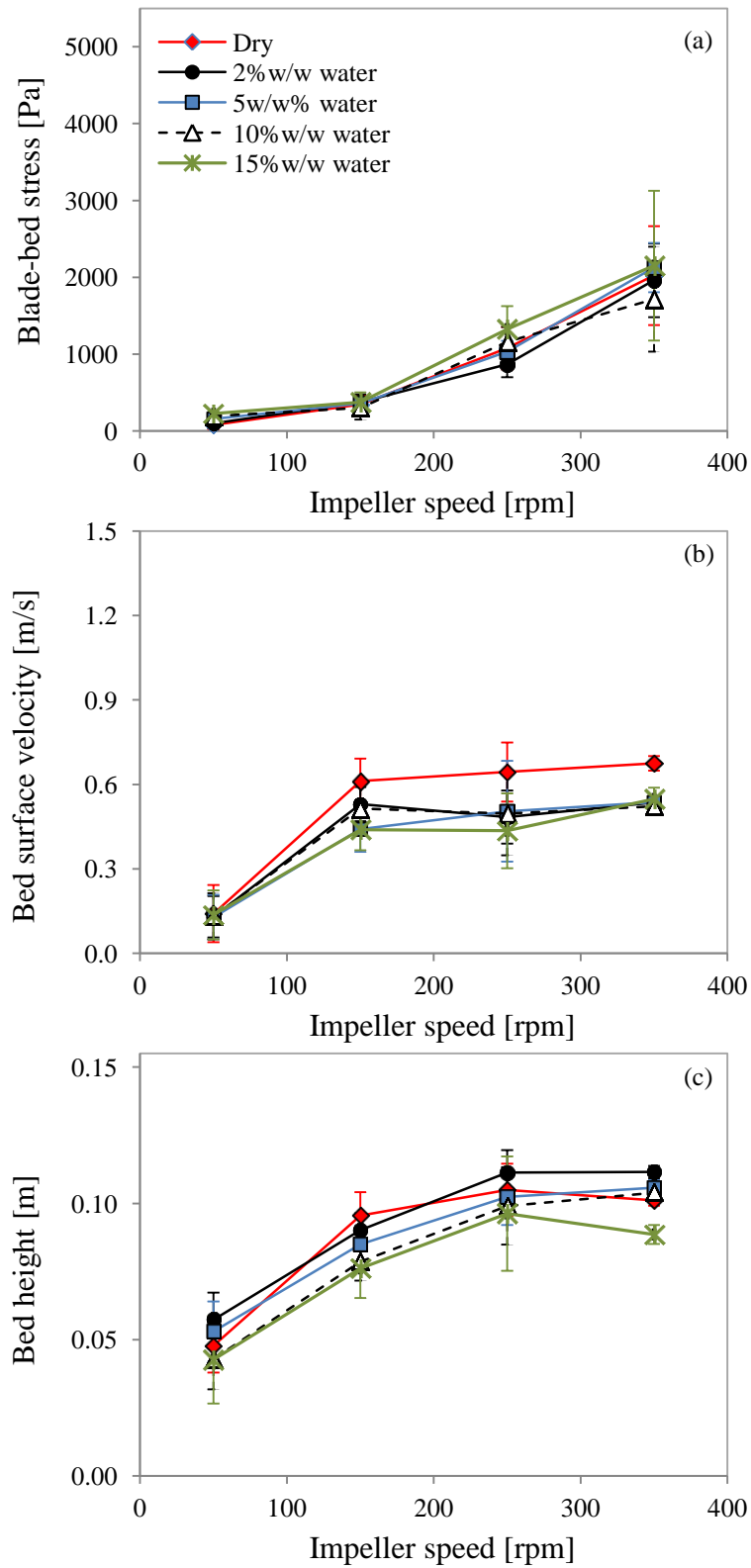


Figure 5.5: Time-averaged data for different water content (a) blade-bed stress (b) bed surface velocity (circumferential) and (c) bed height.

Table 5.1: Bed bulk density and bed porosity of the dry and wet beds.

Liquid/polypropylene balls weight ratio (%w/w)	Bed bulk density (kg/m^3)[Bed porosity (-) ^a]	
	Water (Viscosity = 0.001 Pa.s Surface tension = 72 N/m Density = 998 kg/m^3)	8% HPC solution (Viscosity = 0.116 Pa.s Surface tension = 42.6 N/m Density = 1058 kg/m^3)
0 (Dry)	644±9 [0.35]	
2	501±13 [0.50]	-
5	465±20 [0.53]	470±8 [0.53]
10	448±1 [0.55]	-
15	453±7 [0.55]	458±10 [0.54]
25	498±4 [0.50]	-

^a Bed porosity = $1 - (\rho_b/\rho_a)$, ρ_b = bed bulk density, $\rho_a = \frac{\rho_l \rho_s}{\rho_l \phi_s + \rho_s \phi_l}$ for wet beds, where ρ_l and ρ_s are the liquid/solution density and solid density respectively, and ϕ_l and ϕ_s are the liquid and solid fractions respectively.

Figure 5.6 presents the results for the addition of 8% HPC solution into the bed of polypropylene balls. Similar to the addition of water cases in Figure 5.5a, at a constant bed load, the differences in the blade-bed stress are again not pronounced with the addition of the more viscous liquid, with only a slight increase in the wet bed stress observed at 150 and 250 rpm (Figure 5.6a). The bed surface velocity also reduces with increasing HPC solution content (Figure 5.6b), implying a larger kinetic energy dissipation from the added solution. An increase in the measured bed height at the wall for the dynamic HPC solution-wetted beds is observed (Figure 5.6c), which can also be attributed to the increase in heap formation or bed porosity when liquid is added as shown in Table 5.1.

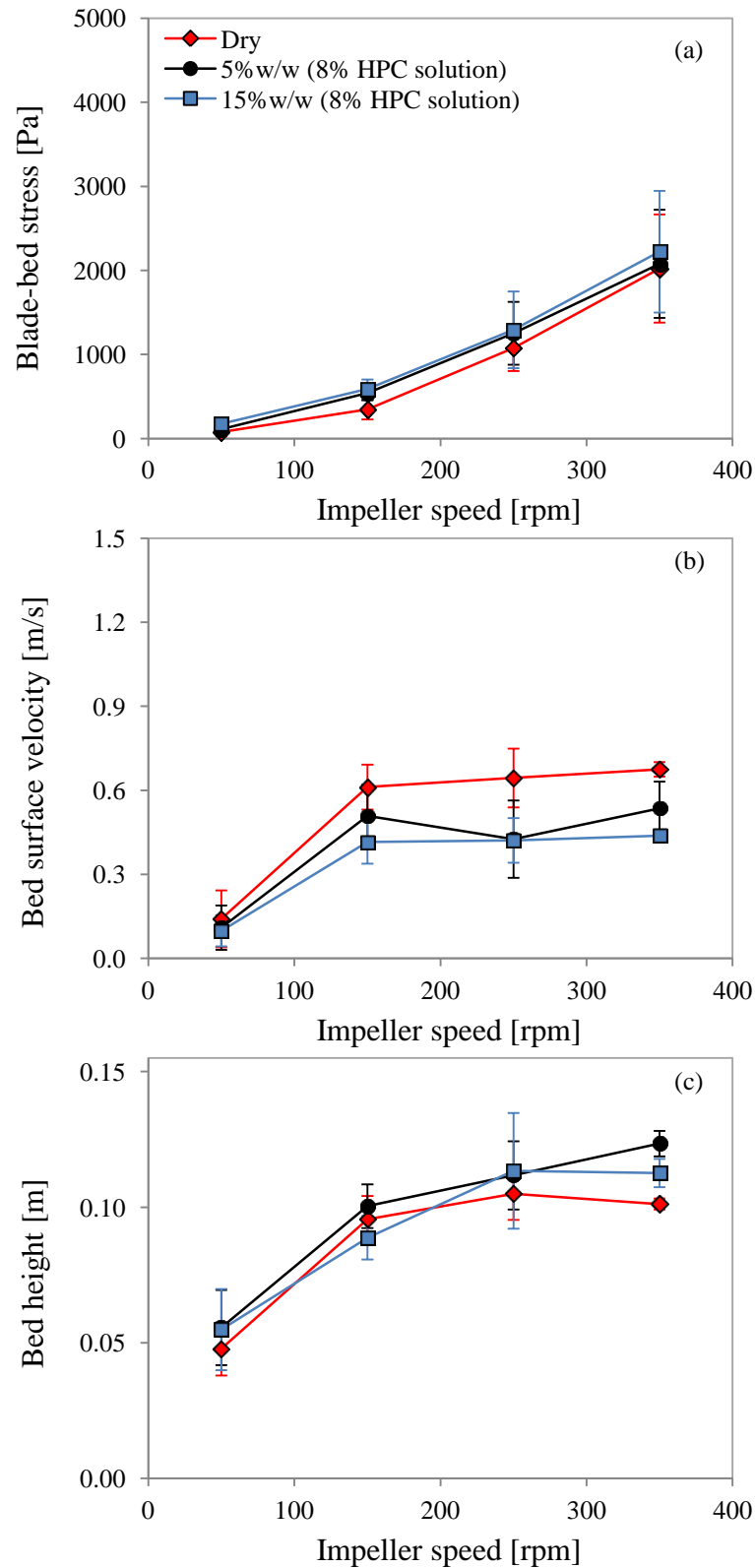


Figure 5.6: Time-averaged data for different 8% HPC solution content (a) blade-bed stress (b) bed surface velocity (circumferential) and (c) bed height.

5.2.3 Blade-bed stress prediction from theory

Results of the wet, cohesive beds from the previous section are fitted into the blade-bed stress equation introduced in the previous chapter, which was originally derived for the imparted inertial force and hence stress from the moving blade to a cohesionless bed. As explained in the previous chapter, to consider the effect of the increasing "fluidisation" of the bed and the use of the surface velocity, the blade-bed stress equation with the correction factor (Equation 4.9) is used, with the correction factor proportional to the inverse of the relative velocity between the blade and the bed (Equation 4.11).

The plots of B_I versus $1/v_{rel}$ for both the wet beds using water and the 8% HPC solution are given in Figure 5.7. The dashed lines represent $x = y$. It is interesting to note that from the plots, $K_I \approx 1$ for the wet beds, the same as that obtained in the previous chapter for dry beds. Using $K_I = 1$ in Equation 4.11, the plot of the measured and predicted blade-bed stress values with the correction factor B_I (Equation 4.9) for all conditions (Figure 5.8) shows reasonable correlation. The same correction factor obtained for the range of water contents and with a more viscous liquid (100×) studied here suggests that the effect of bed cohesion from these liquids on the blade-bed stress for the dynamic beds can be adequately taken into account by the bed surface velocity and bed height behaviours. Whether the same correction factor applies to very viscous liquids or for liquids of very low/high surface tensions remains to be studied. Additionally, Equation 4.9 reasonably predicts the average blade-bed stress provided the liquid saturation level is below the capillary state which might lead to the bed behaving unsteadily as exhibited by the 25%w/w water case.

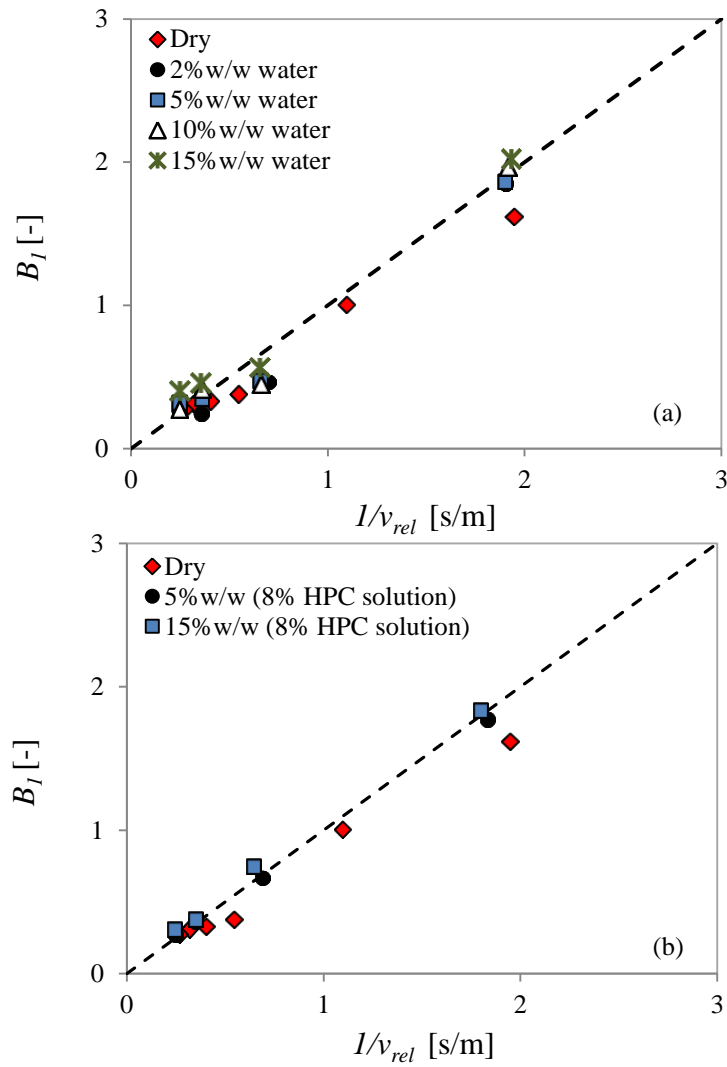


Figure 5.7: Plots of B_I and $1/v_{rel}$ for (a) different water content and (b) different 8% HPC solution content. Dashed lines represent $x = y$.

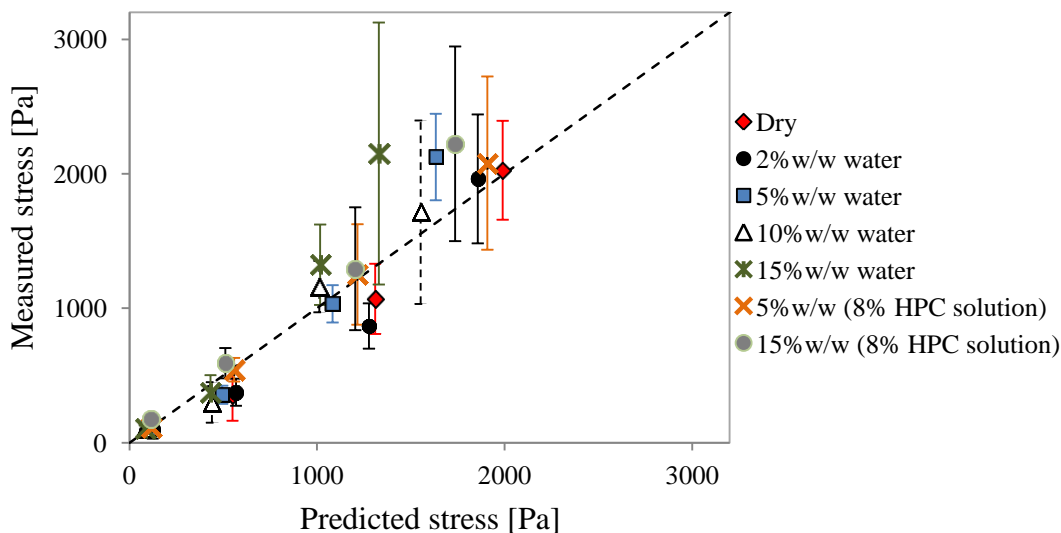


Figure 5.8: Plotted measured stress with the predicted values with the correction parameter B_1 (Equation 4.9) for dry and wet polypropylene beds. Dashed lines represent $x = y$.

5.3 Unsteady-state stress for wet beds

5.3.1 Materials and methodology

The unsteady-state blade-bed stresses for wet beds, i.e. stresses during the actual granulation process, were measured for the formulation and conditions listed in Table 5.2. The powder mixture is composed of mannitol, microcrystalline cellulose (MCC) and HPC; their grades and properties are given in Chapter 4: Table 4.1. HPC was included in the powder mixture instead of being added in solution form and water was spray added into the powders to hydrate the HPC and activates its binding capabilities. This process is also known as "dry adding" and is also the method employed to produce the different granules in Chapter 4. For the spraying, the same atomising spray nozzle described in Chapter 4: Section 4.3.1 was used (0.71 mm orifice, 1/4" LNN SS Atomizing from Spraying Systems Limited), and with a spraying pressure of 0.9 bar that gives a water spraying of ~ 70 g/min (Appendix C shows the spray rate calibration for the spraying system in the Roto Junior). 0.005% red dye (Erythrosin B, Acid Red 51) was also added into the water. Three different water to powder weight (or liquid to solid) ratios, L/S , were studied; i.e. 0.21, 0.28 and continuous water adding, with the impeller speeds kept at 300 rpm for all cases from the start of water adding until the end of the granulation process. The chopper was not operated in these processes. The temperature of the granulating mixture was

also monitored throughout the granulation process via a temperature probe inserted into the bed to make sure that the mixture was not overheated (i.e. temperature ensured to be $<25^{\circ}\text{C}$ in all cases).

Table 5.2: Granulation formulation and operating conditions for unsteady-state measurements.

<i>Powders and composition (weight percentage)</i>	75% mannitol, 21% microcrystalline cellulose (MCC), 4% hydroxypropyl cellulose (HPC)
<i>Spraying liquid</i>	Water
<i>Liquid to solid weight ratio(L/S)</i>	0.21, 0.28 and continuous (w/w)
<i>Bed load</i>	1 kg
<i>Impeller speed</i>	300 rpm

For each liquid to solid ratio, the powder (1 kg) was loaded into the granulator and mixed for ~1 min at 100 rpm. The mixing was then stopped and reference readings from the impeller stress sensor were taken for 10 seconds. Both the impeller rotation (300 rpm) and water spraying were then started. For the L/S : 0.21 and 0.28 cases, "wet massing" of the granules after the water spraying finished was carried out for a certain time depending on the granules formed. For continuous water adding, the process was stopped when the system was overwet, i.e. large paste-like lumps formed. To monitor the change in granule properties, samples were taken intermittently during the granulation process and air-dried for about 2 days, to be analysed for their size and strength. The dry granule size and bulk strength (across the entire granule size range) were determined with the Camsizer and multiple granule compression using the Zwick/Roell Z0.5 compression machine respectively; these methods were previously described in Chapter 3: Section 3.4.1 and Section 3.4.3.2. Additionally, in this study, granules/lumps >10 mm in size are reported as "oversize" in the results, and their size and strength could not be measured using the aforementioned techniques.

5.3.2 Results and discussion

Figure 5.9a presents the measured blade-granule bed stress during granulation of the mannitol, MCC and HPC powders with water spray added continuously. The blade-granule bed stress increases from initially small values, where the granulating mixture only consists of the fine powders. This implies that the stress transmission of the powder bed is low (Mort, 2009; Tardos et al., 2004) and, consequently, the effective weight of the powders carried by the blade is small while the powder bed above the blade is quite unaffected by the blade motion. With liquid addition into the powder bed, the bed cohesion results in the entire bed being rotated by the blade, and visual observations of the moving bed (at 300 rpm) also showed a "fluidised regime" bed flow pattern similar to that observed in the dry granule beds in the previous chapter (Figure 4.6) and for the dry and wet beds of polypropylene balls earlier in this chapter (Figure 5.4). With increasing liquid addition and hence the total mass of the system, the blade-bed stress increased consistently, as observed in Figure 5.9a. The bed also undergoes continuous granule coalescence with water addition, reflected by the increasing $d_{v,10}$, $d_{v,50}$ and $d_{v,90}$ sizes (Figure 5.9b) and a water addition time of around 4 minutes (L/S : 0.28) marks the onset of significant granule growth. This can be seen visually from Figure 5.10 and from the pronounced increase particularly for the $d_{v,10}$ and $d_{v,50}$ sizes from 4 to 4.5 minutes in Figure 5.9b. Accordingly, the dry granules bulk strength also increases significantly at these water addition times (Figure 5.9c). It can also be seen that for the studied formulation and impeller speed, the range of critical water content for granule growth is small, since at around 4.75 minutes (L/S : 0.33), the granulating mixture is now made up mostly of large, pasty lumps > 10 mm, shown in Figure 5.10 and reported as "oversize" in Figure 5.9. In terms of the blade-bed stress measurements, large fluctuations of the readings are obtained when overgranulation occurs (≥ 4.75 min), which can probably be explained by the impacts of the oversized granules on the blade, i.e. a large reading is registered when a lump hits the sensor.

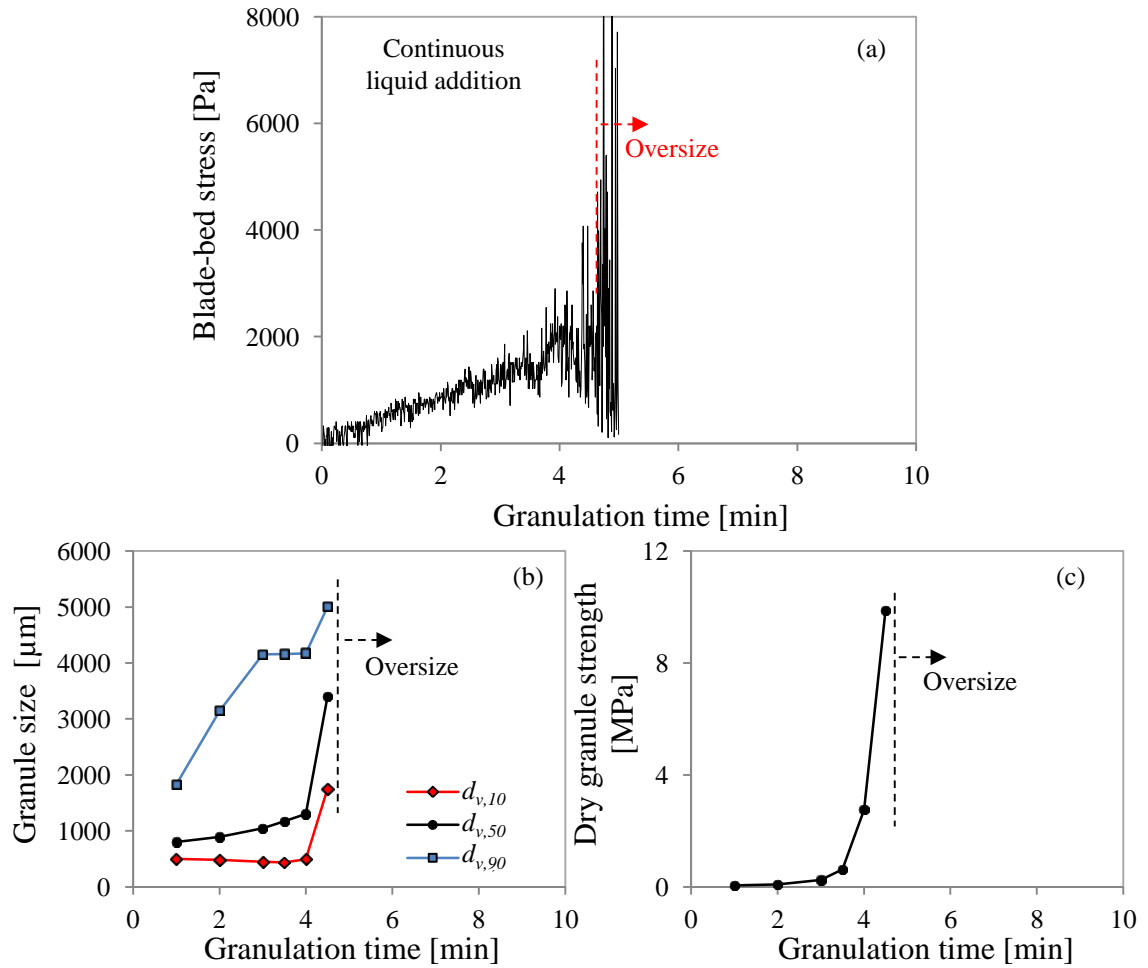


Figure 5.9: Results for continuous water adding (a) blade-bed stress during granulation (b) size of dried granules and (c) bulk strength of dried granules.

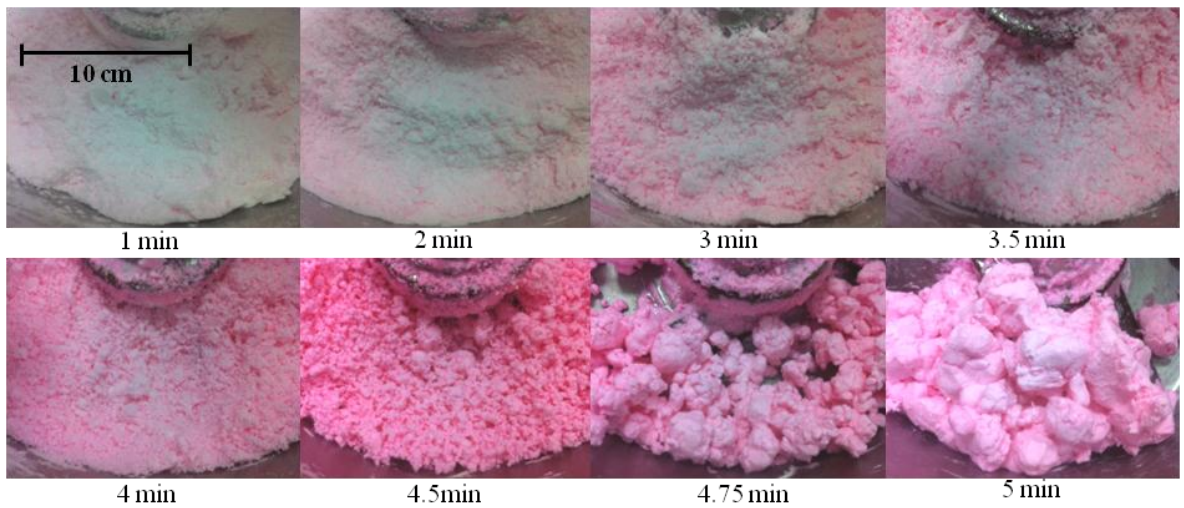


Figure 5.10: Granule images with granulation time for continuous water adding.

The blade-bed stress profile for $L/S = 0.21$ is shown in Figure 5.11a. Water addition took ~3 minutes followed by 5 minutes of wet massing. Following the initial growth/coalescence during water addition, no significant granule growth is noted during the wet massing stage from the dry granule size measurements (Figure 5.11b) and the granule images in Figure 5.12. The dry granule bulk strength on the other hand increases during wet massing (Figure 5.11c), indicating continuous densification or consolidation of the granules which reduces the intragranular porosity, hence producing stronger granules. Granule consolidation during wet granulation was also previously observed by Fu and co-workers (Fu et al., 2005), evidenced by the reduction of intragranular porosity and increasing granule strength. The blade-bed stress measurements show the initial increase during the water addition stage, followed by a plateau region during the wet massing stage (Figure 5.11a). The slight, gradual increase of the blade-bed stress in the wet massing stage can, therefore, be attributed to the densification of the granules (which increases the bed bulk density), as reflected by the granule strength results. Fluctuations in the readings are also noted, which amplitude is smaller than that observed in the previous case when predominantly oversized granules are formed (Figure 5.9a). These fluctuations may result from the small percentages of lumps formed in the granulating mixture throughout the wet massing stage (8-15% w/w) since the chopper was not employed in these measurements.

For granulation with $L/S = 0.28$, water addition took ~4 minutes followed by the wet massing stage. The granulation was stopped however after 2 minutes of wet massing because of the formation of oversized granules (Figure 5.14) from uncontrolled granule growth, possibly due to saturation of binder at the granule surfaces which promotes rapid coalescence. The dry granule size results show an increment of the $d_{v,10}$ and $d_{v,50}$ in the first minute of wet massing time (Figure 5.13b), and in the second minute of the wet massing stage the granules grow uncontrollably. Densification of the granules is again observed during the wet massing, indicated by the apparent increase of dry granule bulk strength in Figure 5.13c. The blade-bed stress readings, again increase in the liquid addition stage, followed by a plateau during the first minute of wet massing (Figure 5.9a). Subsequently, large fluctuations are noted in the second minute of wet massing when oversize granules are formed, the same behaviour shown at the end of the continuous water adding case.

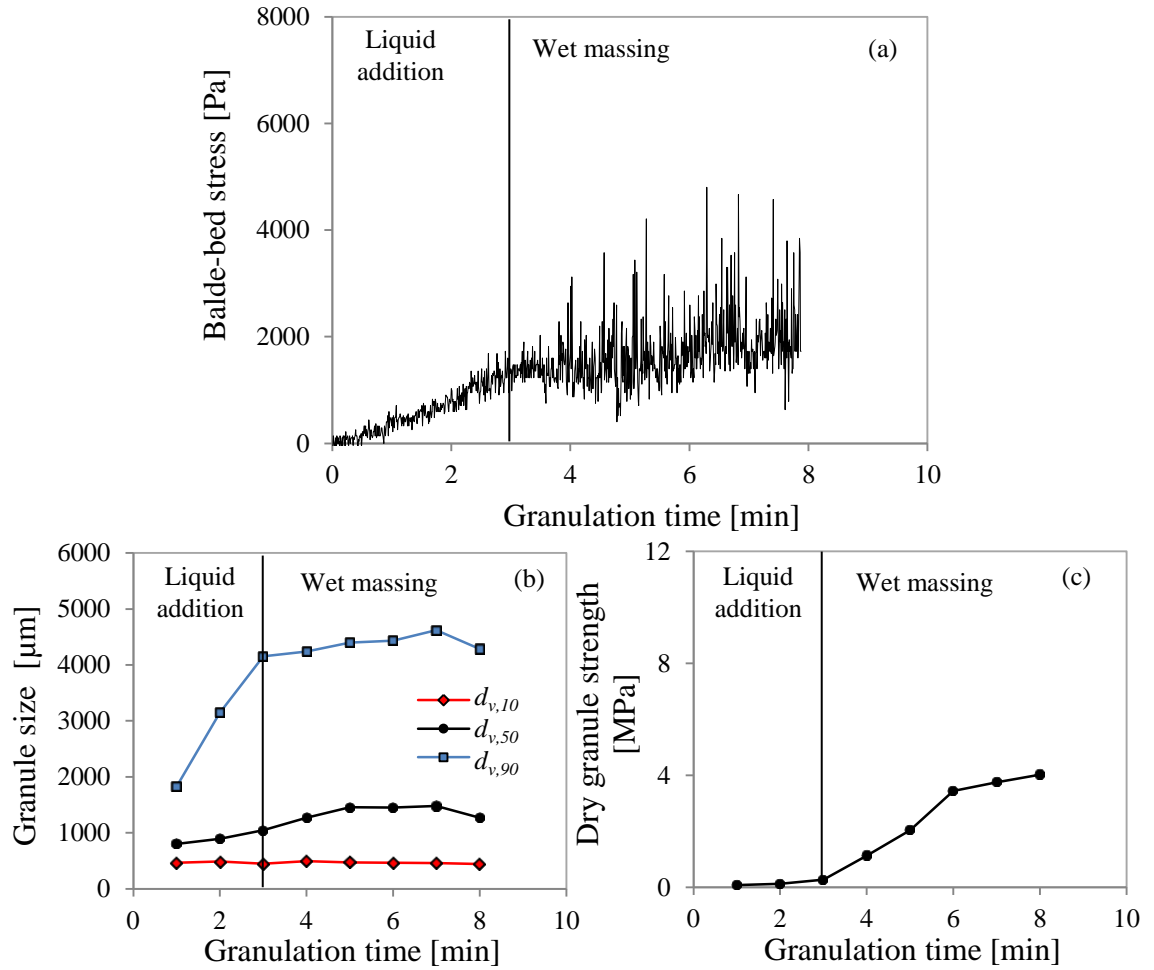


Figure 5.11: Results for $L/S: 0.21$ (a) blade-bed stress during granulation (b) size of dried granules and (c) bulk strength of dried granules.

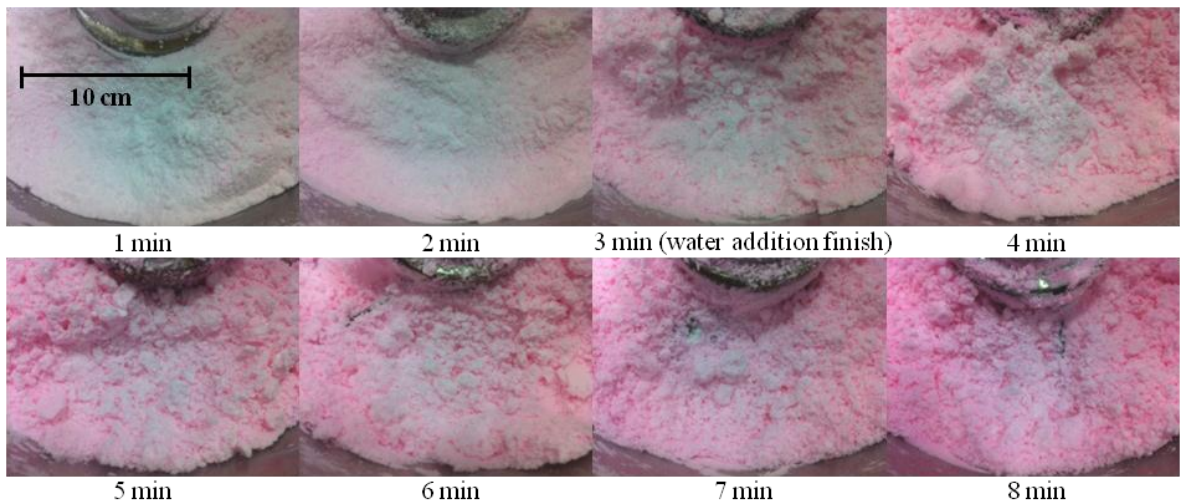


Figure 5.12: Granule images with granulation time for $L/S: 0.21$

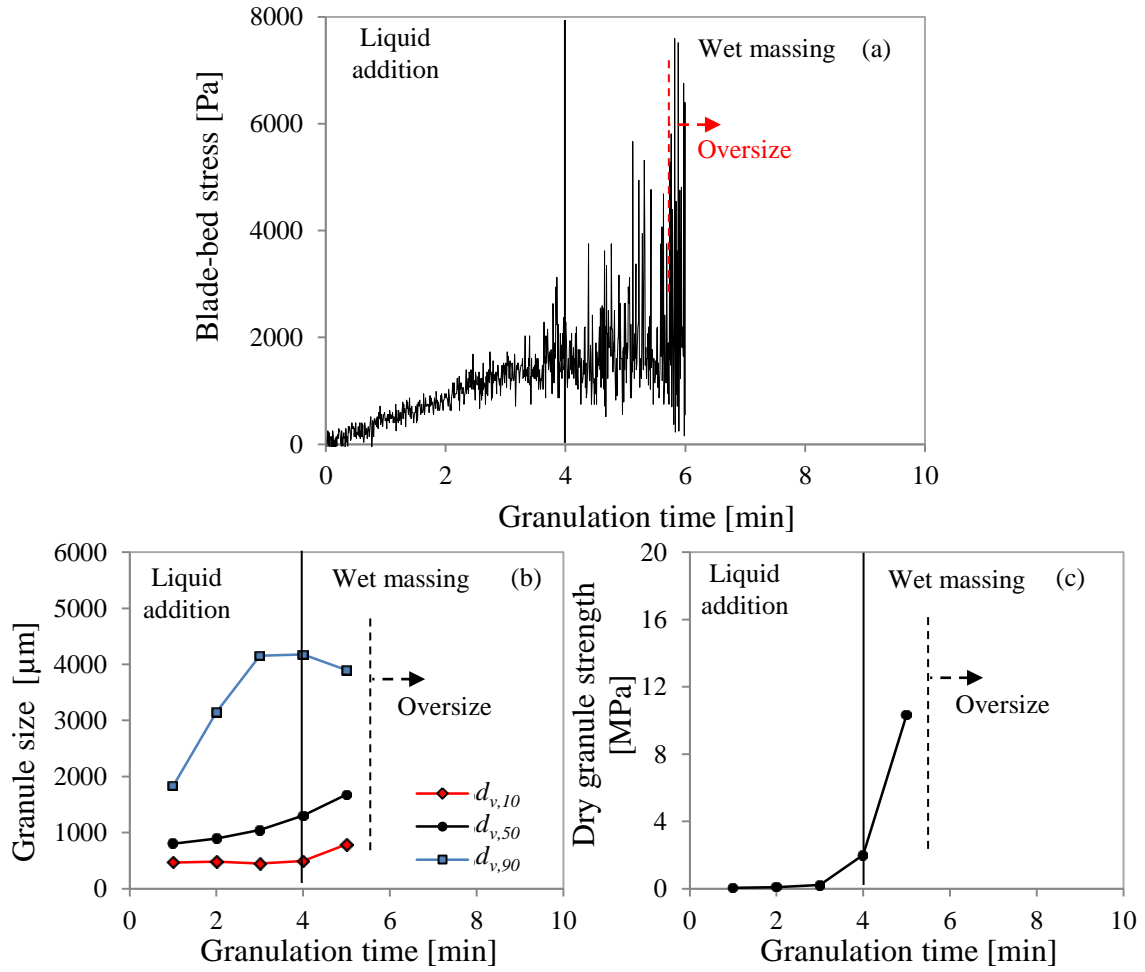


Figure 5.13: Results for $L/S: 0.28$ (a) blade-bed stress during granulation (b) size of dried granules and (b) bulk strength of dried granules.

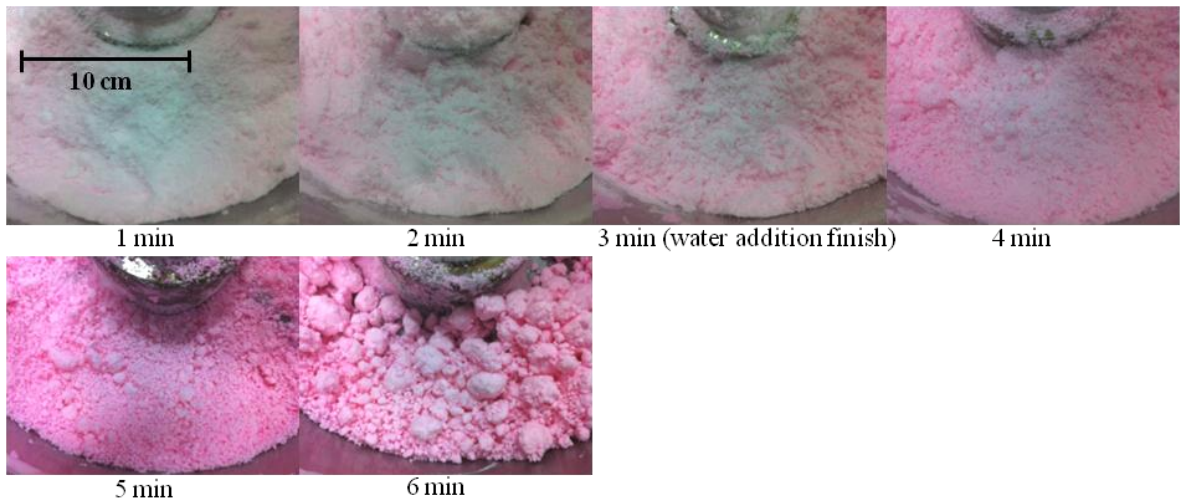


Figure 5.14: Granule images with granulation time for $L/S: 0.28$

These results also suggest the potential use of the blade-bed stress measurements as a means of granulation monitoring. As reviewed in Chapter 2: Section 2.4.2, direct impeller torque and the granulator motor power consumption measurements are commonly used for this purpose. The additional advantage of the blade-bed stress over the torque and power is the direct knowledge of the stresses exerted on the granule bed which can be further applied for granule growth kinetic or growth behaviour studies reviewed in Chapter 2: Section 2.3.

From literature, the general power or torque curves show an initial steep rise during addition of the binder solution, followed by a less steep region (or plateau) during steady granule growth and finally large fluctuations when overgranulation occurs (Chitu et al., 2011; Leuenberger, 1982; Leuenberger et al., 1990; Levin, 2007). Figure 5.15 shows both power and torque curves for a 10 liter Fielder PMA high shear granulator. Ohike and co-workers also showed that the vibration intensities, measured using a probe inserted into the granule bed from above, exhibited the following pattern: a steep increase during binder addition followed by a small increment or plateau region during steady growth of granules (Ohike et al., 1999). Based on these profiles, granules with optimal properties were typically obtained in the plateau or steady growth region (Leuenberger, 1982). The blade-bed stress measurements discussed earlier seem to show the same trends to the above results: where a steeper rise during binder addition is observed, followed by plateau region during wet massing for both the L/S : 0.21 and 0.28 cases. In the L/S : 0.21 case, blade-bed stress increases slightly primarily due to the increasing densification of the granules. When oversized or overwet materials are formed, large blade-bed stress fluctuations are obtained. Talu and co-workers, who measured both normal and shear wall-granule bed stresses in a Fluidised Couette Device, discovered that the fluctuation amplitudes of the normal stress increase with the presence of large granules in the mixture (Talu et al., 2001). Besides the average and fluctuation intensities of the monitoring measurements, some authors also studied the frequency distribution of the power consumption measurements (Terashita et al., 1990b; Watano et al., 1995). The authors found that the frequency distribution of the signals reaches steady-state when the granule growth rate becomes constant. Due to the limited sampling interval of the current impeller stress sensor system, i.e. 2 Hz compared to the blade frequency of 15 Hz at 300 rpm, frequency analysis of the readings could not be carried out in this study.

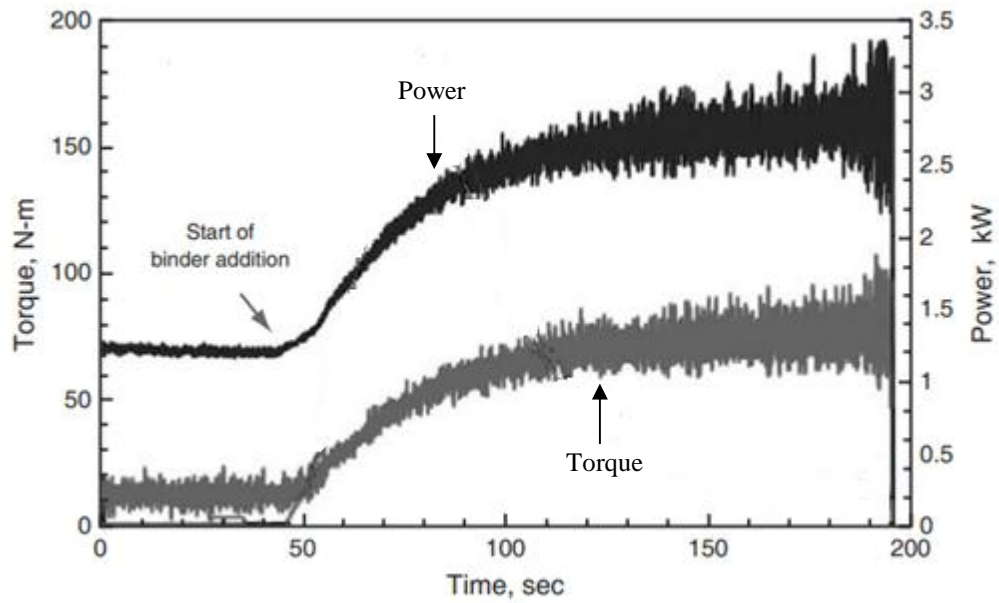


Figure 5.15: Impeller torque and power consumption in a Fielder PMA 10 (10 liter) high shear granulator (modified from Levin, 2007).

5.4 Chapter summary and conclusions

This chapter focused on both steady-state and unsteady-state blade-bed stress measurements for wet beds. The main findings of each part are summarised below.

- Steady-state measurements and prediction:
 - For steady-state wet beds using polypropylene balls wetted with water or HPC solution, liquid amounts corresponding to different liquid saturation states are studied. When the bed is the capillary liquid saturation state, i.e. 25% w/w water, it is found that the bed behaves unsteadily due to large clumps of wetted polypropylene balls moving in the granulator, as evidenced by the large fluctuations of the blade-bed stress and bed surface velocity. With a constant bed load, addition of the liquid does not change the blade-bed stress significantly. A decrease in the surface velocity of the wetted beds was also observed, as expected, due to the larger energy dissipation. The increased bed cohesiveness also increases heap formation or bed porosity.

- Applying the blade-bed stress equation with the correction factor B_l to account for the increasing bed “fluidisation” and use of surface velocity gives a fitted K_l value of ~ 1 for the wet beds, the same as that obtained for the dry granule/particle beds in the previous chapter. The corrected blade-bed stress equation reasonably predicts the average stress for liquid contents below the liquid capillary saturation state.
- Unsteady-state measurements during granulation process:
 - For the studied granulation using different water to powder weight ratios, the blade-bed stress measurements indicate an initial steep increase during the binder addition stage, followed by a plateau region with a small increase when the granules are growing steadily or undergoing densification/consolidation. Spikes in the readings in the plateau region can be attributed to the presence of small percentages of lumps in the granulating mixture since a chopper wasn't used. Large fluctuation are obtained when overgranulation occurs, i.e. predominantly oversized granules or pasty lumps being formed. The behaviour of the blade-bed stress shown in these results conform to the general impeller torque or power consumption curves exhibited for wet granulation, suggesting that future granulation monitoring studies can be carried out using impeller stress sensors.

Chapter 6

Dry particle bed characterisation: simulation

6.1 Introduction

This chapter presents further insight on the impeller blade-particle bed interactions using Discrete Element Method (DEM) simulations, particularly for other impeller speeds, parameters and geometries that could be not carried out experimentally in Chapter 4. DEM is a widely used approach in simulating particulate systems by modelling packed assemblies of discrete elements, thus enabling evaluation of the micromechanics of the assemblies. First introduced by Cundall and Strack for granular materials (Cundall and Strack, 1979), and used in their work to study rock masses, more sophisticated solver schemes have since been put forward, with most recent advances involving the incorporation of fluid interactions into solid models. For this chapter, only the solid models are employed and the chapter contents are presented in the following order:

- Description of the DEM principle and the contact models used in this work;
- Description and explanation of the simulation input parameters for different parameter studies listed below:
 - (a) particle/particle bed properties: bed load, particle size, particle density, interparticle friction coefficient, restitution coefficient and Young's modulus;
 - (b) blade geometries: blade width/height, blade angle and number of blades;
 - (c) granulator scales;
- Description of the analysis methods of the blade-bed stress, bed surface velocity and bed height, and validation of the DEM results by experimental comparison;
- Initial insight of the blade-bed stress, bed surface velocity and bed height along the radial position;
- Discussion of the simulation results for the studied parameters; and
- Theoretical predictions of the blade-bed stress.

6.2 Principle of Discrete Element Method (DEM)

6.2.1 Description and equations of motion

For an assembly of discrete particles, motion of individual particles could be classified into two types; translational and rotational, which arise from particle-wall, particle-particle and particle-fluid interactions under the influence of the gravitational force. These motions are described by the elementary Newton's law of motion. For only interparticle and particle-wall interactions, the equations of motion of a particle i are given by Equation 6.1 and Equation 6.2.

$$m_i \frac{d\mathbf{v}_i}{dt} = m_i \mathbf{g} + \mathbf{F}_{Ci}$$

Equation 6.1

$$I_i \frac{d\boldsymbol{\omega}_i}{dt} = \mathbf{M}_{Ci}$$

Equation 6.2

m_i , \mathbf{v}_i , I_i and $\boldsymbol{\omega}_i$ are the mass, translational velocity, moment of inertia and rotational velocity of particle i respectively, and \mathbf{g} is the gravitational acceleration. \mathbf{F}_{Ci} is the total interparticle and particle-wall contact force on particle i . \mathbf{M}_{Ci} is total torque on particle i which is generated due to the tangential forces acting at the contact surfaces causing the particles to rotate. The velocity (and subsequently position) and angular velocity of particle i are calculated by discretising Equation 6.1 and Equation 6.2 with small time steps, Δt , to give Equation 6.3, Equation 6.4 and Equation 6.5.

$$\mathbf{v}_i = \mathbf{v}_i^0 + \left(\frac{\mathbf{F}_{Ci}}{m_i} + \mathbf{g} \right) \Delta t$$

Equation 6.3

$$\mathbf{x}_i = \mathbf{x}_i^0 + \mathbf{v}_i \Delta t$$

Equation 6.4

$$\boldsymbol{\omega}_i = \boldsymbol{\omega}_i^0 + \frac{\mathbf{M}_{Ci}}{I_i} \Delta t$$

Equation 6.5

\mathbf{x}_i is the particle position and superscript ^{“0”} signifies the value of the previous time step.

To solve Equation 6.3, Equation 6.4 and Equation 6.5, the interparticle and particle-wall interactions, namely the contact forces, \mathbf{F}_{Ci} , and torque, \mathbf{M}_{Ci} , need to be computed. In general, contact interactions between the colliding bodies involve a range of complex phenomena, from stress and strain distributions within the colliding bodies, plastic deformation to thermal,

acoustical and frictional energy dissipation. The hard and soft sphere models are two most common instances of contact force models applied in DEM simulations. The hard-sphere model (Hoomans et al., 1996) regards collisions as instantaneous by assuming the particles are rigid in nature. In the soft-sphere model (Cundall and Strack, 1979), deformable particles are considered and contact forces are generated due to the deformation when the particles contact (Figure 6.1). The soft-sphere model also enables multiple contacts to take place at the same time. On the contrary, the hard sphere model only allows for binary collisions. The soft-sphere model is, therefore, more often used for densely packed particle/granular flow systems and will also be used in this thesis (for a dense, granule bed in the high shear granulator).

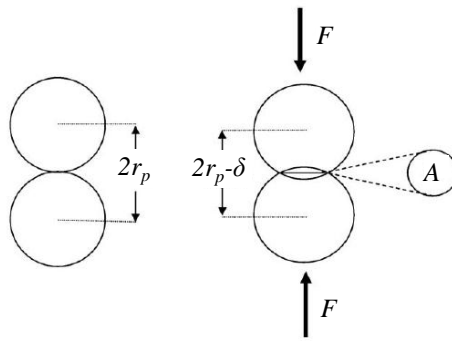


Figure 6.1: Contact between two spherical particles of radius r_p . A is the area of deformation and δ is depth of the contact deformation (taken from Campbell, 2006).

6.2.2 Soft-sphere DEM model

Cundall and Strack proposed the soft-sphere model by modelling interparticle and particle-wall contacts using a combination of spring, dashpot and frictional slider (Figure 6.2). Forces are divided into normal and tangential forces (Cundall and Strack, 1979). Normal forces are modelled using a spring and a dashpot in parallel (Figure 6.2a), analogous to the Kelvin-Voigt model for visco-elastic materials, to represent the elastic repulsion force and viscous damping (energy dissipation) respectively. Tangential forces are modelled using the spring-dashpot combination or the frictional slider (Figure 6.2b), which represent the static and dynamic frictions respectively.

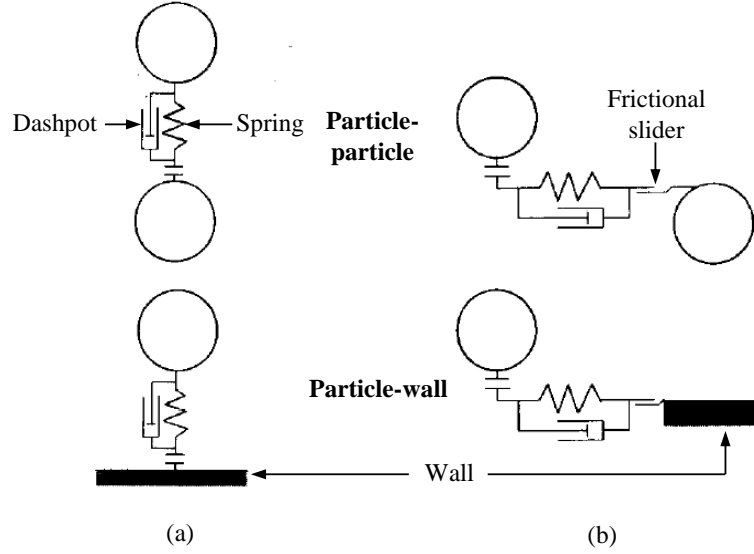


Figure 6.2: Soft-sphere DEM model for (a) normal force (b) tangential force (modified from Tsuji et al., 1992).

Figure 6.3 shows a 2-D illustration of the normal and tangential contact forces ($\mathbf{F}_{Cn,ij}$ and $\mathbf{F}_{Ct,ij}$) and torque ($\mathbf{M}_{C,ij}$) of two particles (particle i and particle j) in contact. In the soft-sphere model by Cundall and Strack, the normal component of the contact force, $\mathbf{F}_{Cn,ij}$, when particle i comes into contact with particle j or the wall, is given by the sum of the elastic repulsion and viscous damping forces (Equation 6.6).

$$\mathbf{F}_{Cn,ij} = (-k_n \delta_{n,ij}^{3/2} - \eta_n \mathbf{v}_{r,ij} \mathbf{n}_{ij}) \mathbf{n}_{ij}$$

Equation 6.6

$\delta_{n,ij}$ is the depth of the particle deformation or displacement due to the normal force (also δ shown in Figure 6.1), $\mathbf{v}_{r,ij}$ is the relative velocity between particle i and j while \mathbf{n}_{ij} is the unit vector of the centre of particle i to the centre of particle j . k_n and η_n are the normal stiffness and damping coefficient respectively. A non-linear spring model is used for the elastic repulsion force (first term of the right hand side), i.e. the force is proportional to the displacement to the power of n . Employing the well-known Hertzian contact theory, n is 3/2. The tangential component of the contact force, $\mathbf{F}_{Ct,ij}$, is given in Equation 6.7.

$$\mathbf{F}_{Ct,ij} = \begin{cases} -k_t \delta_{t,ij} \mathbf{t}_{ij} - \eta_t \mathbf{v}_{rt,ij} & \text{if } |-k_t \delta_{t,ij} \mathbf{t}_{ij} - \eta_t \mathbf{v}_{rt,ij}| \leq -\mu_f |\mathbf{F}_{Cn,ij}| \\ -\mu_f |\mathbf{F}_{Cn,ij}| \mathbf{t}_{ij} & \text{if } |-k_t \delta_{t,ij} \mathbf{t}_{ij} - \eta_t \mathbf{v}_{rt,ij}| > -\mu_f |\mathbf{F}_{Cn,ij}| \end{cases}$$

Equation 6.7

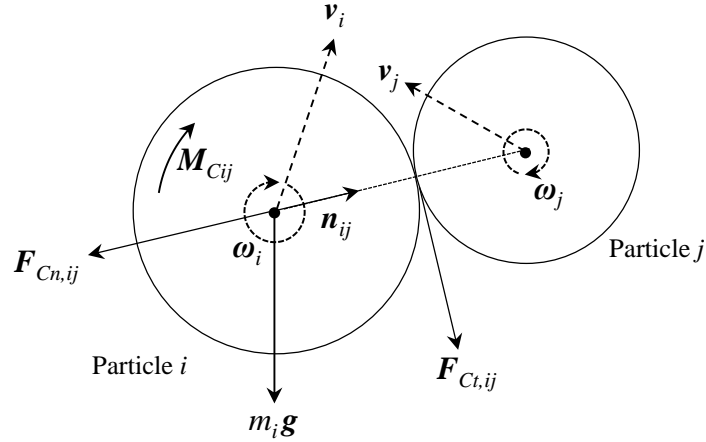


Figure 6.3: Forces and torque of two spherical particles (i and j) in contact.

Here, $\delta_{t,ij}$ is the tangential displacement, \mathbf{t}_{ij} is the unit vector in the tangential direction given in Equation 6.8, $\mathbf{v}_{rt,ij}$ is the relative tangential velocity (slip velocity) at the contact surface calculated from the sum of translational and rotational velocities (Equation 6.9) and μ_f is the sliding friction coefficient. k_t and η_t are the tangential stiffness and damping coefficient respectively. The first and second cases in Equation 6.7 calculate the tangential forces from the spring and dashpot combination and the frictional slider respectively. When the spring-dashpot tangential forces overcome the friction of the slider, particle i will start to slide along the contact plane and the force is modelled by the frictional slider as dictated by Coulomb's Law of Friction.

$$\mathbf{t}_{ij} = \frac{\mathbf{v}_{rt,ij}}{|\mathbf{v}_{rt,ij}|}$$

Equation 6.8

$$\mathbf{v}_{rt,ij} = [\mathbf{v}_{r,ij} - (\mathbf{v}_{r,ij} \mathbf{n}_{ij}) \mathbf{n}_{ij}] + [r_p (\boldsymbol{\omega}_i + \boldsymbol{\omega}_j) \times \mathbf{n}_{ij}]$$

Equation 6.9

r_p is the particle radius for same size particles.

Finally, the total collision force and torque exerted on particle i due to multiple interparticle and/or particle-wall collisions are given in Equation 6.10 and Equation 6.11 respectively. The second term of the right hand side of Equation 6.11 computes the torque generated due to the rolling friction (Beer and Johnson, 1976; Zhou et al., 1999) and μ_r is the rolling friction coefficient.

$$\mathbf{F}_{Ci} = \sum_{j=1}^k (\mathbf{F}_{Cn,ij} + \mathbf{F}_{Ct,ij})$$

Equation 6.10

$$\mathbf{M}_{Ci} = \sum_{j=1}^k \left(r_p \mathbf{n}_{ij} \times \mathbf{F}_{Ct,ij} - \mu_r |\mathbf{F}_{Cn,ij}| r_p \frac{\boldsymbol{\omega}_i}{|\boldsymbol{\omega}_i|} \right)$$

Equation 6.11

6.2.2.1 Stiffness and damping coefficients

As previously mentioned, the non-linear spring model is used in this work. According to the Hertzian contact theory, when two particles collide, the elastic repulsion force is proportional to the particle displacement to the power of 3/2 for perfectly smooth, isotropic particles. Table 6.1 summarises the contact forces and torque models and presents the stiffness and damping coefficients models used in this thesis. The normal stiffness, k_n , in Equation 6.6 is expressed by Equation 6.12 or Equation 6.13 in Table 6.1 for particle-particle or particle-wall contacts respectively, based on the Hertzian contact theory. The tangential stiffness, k_t , in Equation 6.7 was modelled by Mindlin (Mindlin, 1949) for non-slip contact surfaces cases (Equation 6.14 and Equation 6.16). G_p , the shear modulus, is calculated from the Young's modulus, E_p , and Poisson's ratio, ν_p (Equation 6.15).

The normal damping coefficient, η_n in Equation 6.6, for the non-linear spring model was proposed by Tsuji and co-workers (Tsuji et al., 1992) using a spring-dashpot system for normal contact, as previously shown in Figure 6.2. They obtained a solution for η_n in the form of Equation 6.17 by solving the equation of motion of the particle in the spring-dashpot system in one dimension heuristically and assuming that the particle restitution coefficient, e , is independent of the impact velocity. In the solution (Equation 6.17), β is a parameter which can be related to the restitution coefficient and Figure 6.4 plots this correlation. The tangential damping coefficient, η_t , is difficult to model, and thus for simplicity η_t is assumed to be the same as η_n by Tsuji and co-workers (Equation 6.7).

Table 6.1: Stiffness and damping coefficients models used for the DEM soft sphere model in this thesis.

Normal contact force Equation 6.6		$\mathbf{F}_{cn,ij} = (-k_n \delta_{n,ij}^{3/2} - \eta_n \mathbf{v}_{r,ij} \mathbf{n}_{ij}) \mathbf{n}_{ij}$		
Tangential contact force Equation 6.7		$\mathbf{F}_{ct,ij} = \begin{cases} -k_t \delta_{t,ij} \mathbf{t}_{ij} - \eta_t \mathbf{v}_{rt,ij} & \text{if } -k_t \delta_{t,ij} \mathbf{t}_{ij} - \eta_t \mathbf{v}_{rt,ij} \leq -\mu_s \mathbf{F}_{cn,ij} \\ -\mu_f \mathbf{F}_{cn,ij} \mathbf{t}_{ij} & \text{if } -k_t \delta_{t,ij} \mathbf{t}_{ij} - \eta_t \mathbf{v}_{rt,ij} > -\mu_s \mathbf{F}_{cn,ij} \end{cases}$		
Torque Equation 6.11		$\mathbf{M}_{c,ij} = r_p \mathbf{n}_{ij} \times \mathbf{F}_{ct,ij} - \mu_r \mathbf{F}_{cn,ij} r_p \frac{\boldsymbol{\omega}_i}{ \boldsymbol{\omega}_i }$		
Stiffness/damping coefficients		Equation	Notation	Reference
Normal stiffness, k_n	Particle-particle (same size particles)	$k_n = \frac{\sqrt{2r_p} E_p}{3(1 - v_p^2)}$ Equation 6.12	r_p : particle radius; E_p : Young's modulus of the particles; v_p : Poisson's ratio of the particles.	Hertzian contact theory for elastic particles
	Particle-wall	$k_n = \frac{4\sqrt{r_p}}{3} \frac{E_p E_w}{1 - v_p^2 + \frac{1 - v_w^2}{E_w}}$ Equation 6.13	E_w : Young's modulus of the wall; v_w : Poisson's ratio of the wall.	Hertzian contact theory for elastic particles
Tangential stiffness, k_t	Particle-particle (same size particles)	$k_t = \frac{2\sqrt{2r_p} G_p}{2 - v_p} \delta_{n,ij}^{1/2}$ Equation 6.14	G_p : shear modulus of the particles; $\delta_{n,ij}$: particle normal displacement.	Midlin's theory for non-slip cases (Mindlin, 1949)
	Particle-wall	$G_p = \frac{E_p}{2(1 + v_p)}$ Equation 6.15		
	Particle-wall	$k_t = \frac{8\sqrt{r_p} G_p}{2 - v_p} \delta_{n,ij}^{1/2}$ Equation 6.16		Midlin's theory for non-slip cases (Mindlin, 1949)
Normal damping coefficient, η_n		$\eta_n = \beta (m_p k_n)^{1/2} \delta_{n,ij}^{1/4}$ Equation 6.17	β : parameter function of the restitution coefficient; m_p : mass of particle.	(Tsuji et al., 1992)
Tangential damping coefficient, η_t		Same value as the normal damping coefficient		(Tsuji et al., 1992)

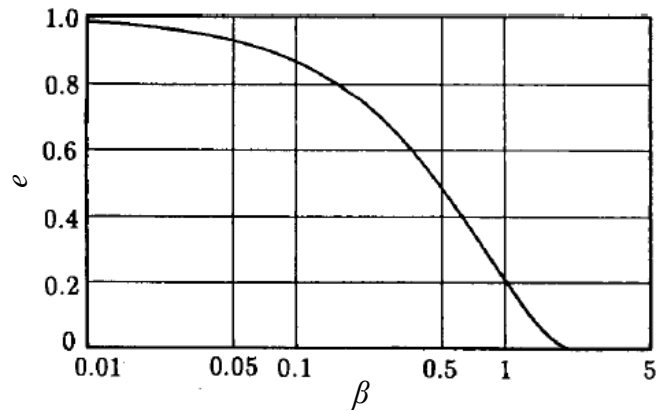


Figure 6.4: Relationship between parameter β and restitution coefficient, e (taken from Tsuji et al., 1992).

Implementation of these contact forces have been widely used in simulation studies of particles in mixers, mainly focusing on the bed flow, mixing characteristics and the force network (Chandratilleke et al., 2009; Remy et al., 2009; Stewart et al., 2001; Washino, 2011; Zhou et al., 2004).

6.3 Simulation geometries and parameters

6.3.1 Main description

In this thesis, the simulations were run using an in-house Fortran code written by Washino (Washino, 2011) which incorporated the equations of motion and soft sphere DEM model described in the previous section. A granulator with dimensions and impeller identical to the Roto Junior used in Chapter 4 was simulated (diameter: 0.28 m, height: 0.18 m). Figure 6.5 presents the experimental and simulated geometry with the 32°, three-bladed impeller. To apply an external geometry into the DEM Fortran code for the simulations, mesh data of the geometry has to be first supplied directly. A simulation pre-processing geometry builder package, Gambit 2.0 by Fluent Inc., was first used to construct the geometries. From the drawings, equilateral triangular surface meshes were generated (mesh edges can be seen in Figure 6.5) and exported.

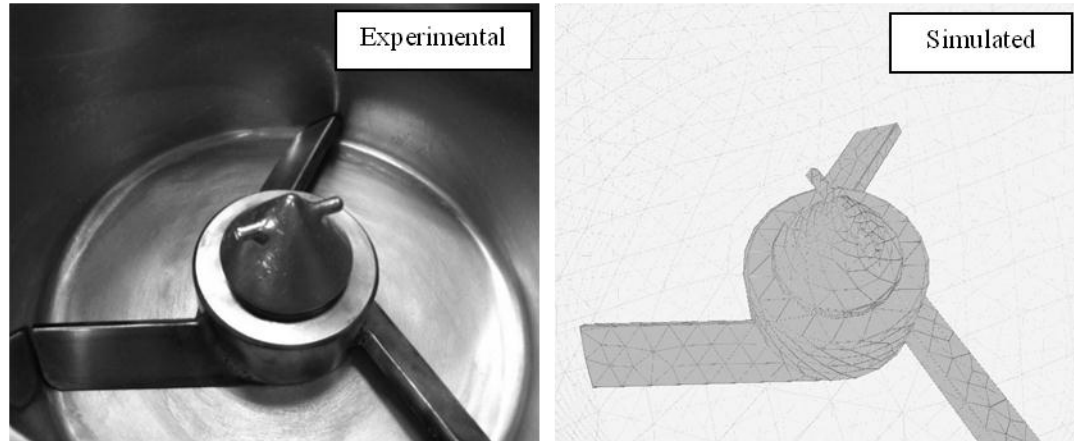


Figure 6.5: Experimental and simulated geometry (~10 L mixer, three-bladed impeller with 32° inclined blades).

6.3.2 Particle bed/particle properties

It is important to mimic the experiments conditions used in the Chapter 4 for comparison and validation of the simulated results before further studies of other parameters. For validation, the simulation results were compared with the mannitol granules used in Chapter 4. However, due to physical limitations of the current DEM code and limitations in computer expenses, certain conditions have to be defined or assumed based on reasonability. Monosized particles were simulated instead of multisized particle beds used in the experiments in Chapter 4. In addition, as the current code is incapable of incorporating particles of irregular geometries, spherical particles were simulated. The irregular granule shapes generally affect the bed packing and, therefore, bed bulk density. This is taken into consideration in the simulations, as explained later for the particle density parameter selection.

For the effect of varying particle sizes, particle diameters of 2, 3.5, 5 and 10 mm were selected for the simulations. The current DEM code is capable of handling up to ~400000 particles and for a standard bed load of 1.5 kg and particle density (explained below), this gave a smallest simulated particle diameter of ~2 mm. The sieve sizes of the mannitol granules used for the measurements in Chapter 4 were 0.1-0.5, 0.5-1.0, 1.0-2.0 and 2.0-4.75 mm (Table 4.3). For validation of the simulations, the simulated 2 mm and 3.5 mm particles were compared with the 1.0-2.0 mm ($d_{v,50} = 1.6$ mm) and 2-4.75 mm ($d_{v,50} = 3.4$ mm) mannitol granules respectively. Also, for study of other parameters, the 3.5 mm simulated particles rather than the 2 mm ones were used to reduce computer expenses.

The simulated bed of spherical and monosized particles should maintain a similar bulk flow to a bed of irregular and multisized granules in the granulator. To achieve this, the simulated bed bulk density was kept the same as the experimental. Consequently, the simulated particle true density, ρ_t , can be determined from Equation 6.18. ρ_b is the bed bulk density taken from the experiment, ε_b is the bed porosity and $1-\varepsilon_b$ is the packing density. The experimental bed bulk density is 740 kg/m^3 , i.e. the measured bed bulk densities for the 0.5-1.0 mm and 1.0-2.0 mm mannitol granules sieve sizes in Chapter 4 (Table 4.3). For spherical, monosized particles packed by gravity, the packing density ($1-\varepsilon_b$) is ~ 0.6 from literature (McGeary, 1961; Tory et al., 1973). Hence from Equation 6.18, the simulated particle true density is 1230 kg/m^3 .

$$\rho_t = \frac{\rho_b}{(1 - \varepsilon_b)}$$

Equation 6.18

The Young's modulus was determined experimentally from the single granule diametric compression described in Chapter 3: Section 3.4.3.1 and Table 6.2 presents the values for different sieve sizes of the mannitol granules. The Young's modulus for the 2.0-4.75 mm sieve size, i.e. 160 MPa was chosen for the simulations. Other simulation parameters for the varying particle sizes are shown in Table 6.3. Values of the sliding friction coefficients and restitution coefficient were chosen to be 0.3. The rolling friction coefficient was taken to be 100 times smaller than the sliding friction coefficients. For dense particle flow systems, Kuo et al reported that quantitative differences between their DEM simulations and experiments were generally observed only when extreme values of frictional coefficient (0) or restitution coefficient (1.0) were used (Kuo et al., 2002). Table 6.3 also displays the simulation parameters for other varied conditions, i.e. bed load, particle density, restitution coefficient, sliding friction coefficients and Young's modulus.

Table 6.2: Measured Young's modulus of dry mannitol granules.

<i>Mannitol granules sieve sizes (mm)</i>	<i>Young's Modulus (MPa)</i>
0.5-1.0	569±124
1.0-2.0	345±89
2.0-4.75	160±50

Table 6.3: Simulation parameters for different particle bed/particle properties.

Parameters	Varying particle size	Varying bed load	Varying particle density	Varying sliding friction coefficient	Varying restitution coefficient	Varying Young's modulus
Particle diameter [mm]	2.0, 3.5, 5.0, 10.0	3.5	3.5	3.5	3.5	3.5
Total bed load [kg]	1.5	1.0, 1.5, 2.0, 3.0	1.5	1.5	1.5	1.5
Number of particles [-]	291137, 54323, 18633, 2329	36215, 54323, 72431, 108646	111362, 54323, 26727	54323	54323	54323
Particle density [kg/m ³]	1230	1230	600, 1230, 2500	1230	1230	1230
Restitution coefficient [-] ^a	0.3	0.3	0.3	0.3	0.1, 0.3, 0.5, 0.7, 0.9	0.3
Young's modulus [MPa] ^a	160	160	160	160	160	0.1, 1, 100, 160, 1000
Poisson's ratio [-] ^a	0.25	0.25	0.25	0.25	0.25	0.25
Sliding friction coefficient [-] ^a	0.3	0.3	0.3	0.02, 0.1, 0.3, 0.5, 0.9 ^b	0.3	0.3
Rolling friction coefficient [-] ^a	0.003	0.003	0.003	0.003	0.003	0.003
Impeller rotational speed [rpm]	50-700	50-700	50-700	50-700	150, 350	150, 350
Mixer diameter [mm]	280					
Mixer height [mm]	180					
Blade angle [°]	32					
Blade width/blade inclined height [mm]	35/18.5					
Number of blades [-]	3					

^a same value for particle-particle and particle-blade/particle-wall interactions.

^b only varied for particle-particle interaction, value for particle-wall is fixed at 0.3.

6.3.3 Impeller geometries

In addition to the particle bed/particle properties, impellers of different geometries, i.e. blade width, blade angle and number of blades, were also simulated (Table 6.4, Figure 6.6). The definition of the blade angle, width and inclined height are also indicated in Figure 6.6.

Table 6.4: Simulation parameters for different impeller geometries.

<i>Parameters</i>	<i>Varying blade width</i>	<i>Varying blade angle</i>	<i>Varying number of blades</i>
Particle diameter [mm]		3.5	
Total bed load [kg]		1.5	
Number of particles [-]		54323	
Particle density [kg/m ³]		1230	
Restitution coefficient [-] ^a		0.3	
Young's modulus [MPa] ^a		160	
Poisson's ratio [-] ^a		0.25	
Sliding friction coefficient [-] ^a		0.3	
Rolling friction coefficient [-] ^a		0.003	
Impeller rotational speed [rpm]		50-700	
Mixer diameter [mm]		280	
Mixer height [mm]		180	
Blade angle [°]	32	20, 32, 45, 65, 90	32
Blade width/blade inclined height [mm]	20/10.6 35/18.5, 50/26.5, 65/34.4	35/12.0, 35/18.5, 35/24.7, 35/31.7, 35/35.0	35/18.5
Number of blades [-]	3	3	2, 3, 4

^a same value for particle-particle and particle-blade/particle-wall interactions.

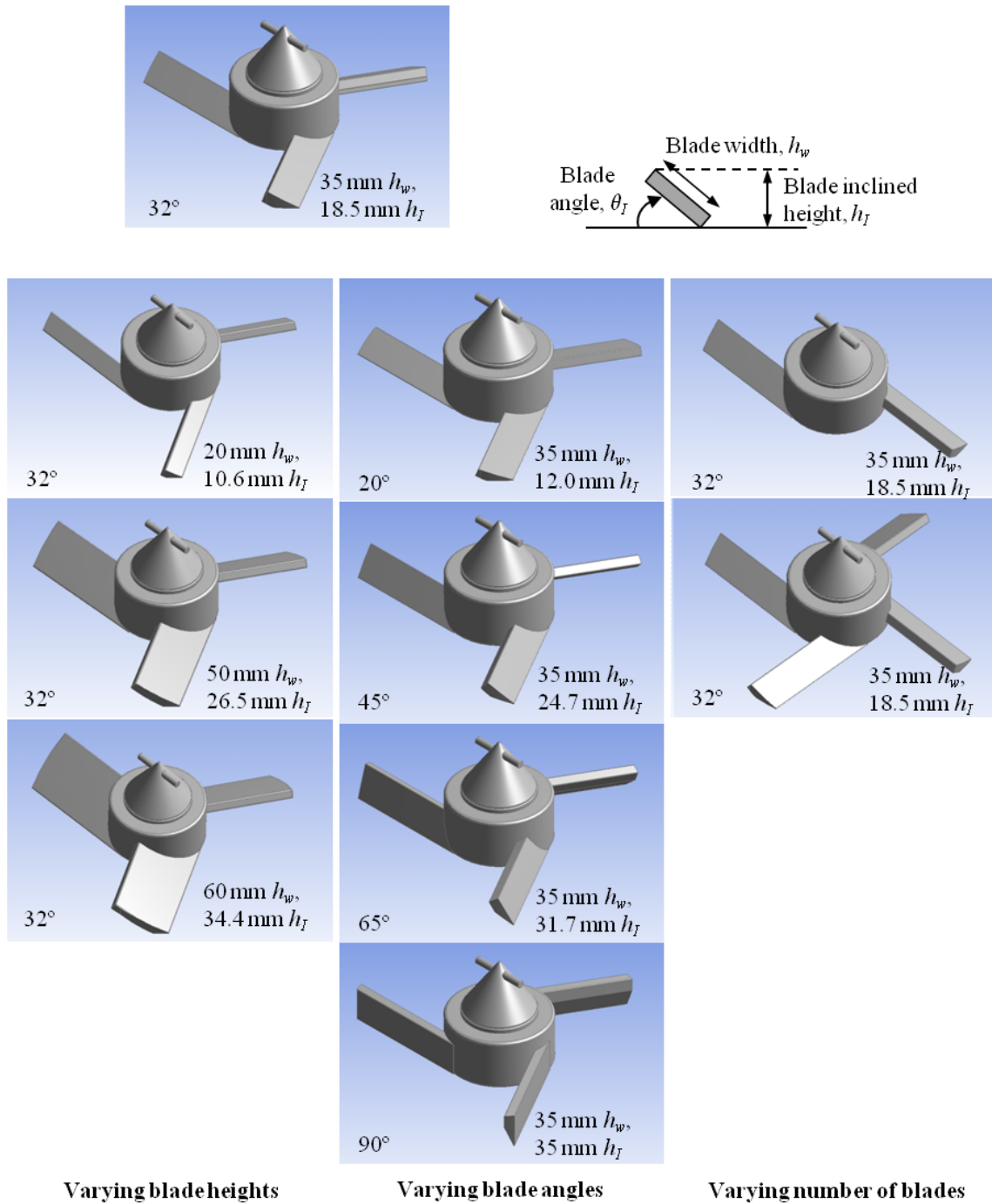


Figure 6.6: Simulated blade geometries.

6.3.4 Granulator scale

Simulations were also carried out for 4 geometrically-similar granulator scales, covering a range of 0.173 L to 88.7 L granulators. The particle size was maintained across all scales, i.e. 3.5 mm particles which gave different mixer diameter to particle diameter ratios (D/d_p). For additional comparison, the same D/d_p cases for different scales were also simulated, i.e. $D/d_p = 80$, by varying the particle size. Impeller speeds corresponding to the same Froude numbers (Equation 6.19), i.e. ratio of the centrifugal to gravitational forces, were selected to maintain similar flow behaviours across the scales. The simulation parameters for different granulator scales are given in Table 6.5.

$$Fr = \frac{\omega_I^2 D}{g}$$

Equation 6.19

Table 6.5: Simulation parameters for different granulator scales.

<i>Parameters</i>	<i>Constant particle diameter, d_p</i>	<i>Constant mixer diameter to particle diameter ratio, D/d_p</i>
Particle diameter [mm]	3.5	0.875, 1.75, 3.5, 7
Mixer diameter to particle diameter ratio [-]	20, 40, 80, 160	80
Total bed load [kg]	0.0234, 0.1875, 1.5, 12	
Number of particles [-]	849, 6790, 54323, 434584	54323
Particle density [kg/m^3]	1230	
Restitution coefficient [-] ^a	0.3	
Young's modulus [MPa] ^a	160	
Poisson's ratio [-] ^a	0.25	
Sliding friction coefficient [-] ^a	0.3	
Rolling friction coefficient [-] ^a	0.003	
Impeller rotational speed [rpm]	100-1400 (0.173 L granulator), 71-990 (1.39 L granulator), 50-350 (11.1 L granulator), 35-247 (88.7 L granulator).	
Mixer diameter [mm]	70, 140, 280, 560	
Mixer height [mm]	45, 90, 180, 360	
Mixer volume [L]	0.173, 1.39, 11.1, 88.7	
Blade angle [°]	32	
Blade width/blade inclined height [mm]	8.75/4.625, 17.5/9.25, 35/18.5, 70/37.	
Number of blades [-]	3	

^a same value for particle-particle and particle-blade/particle-wall interactions.

6.4 Simulation and analysis method of the blade-bed stress, bed velocities and bed height

For each simulation case, particles were generated in an ordered lattice above the impeller and left to settle under gravity. The impeller was then rotated until steady-state bed flow was achieved, depending on the impeller speed. The time step for most cases was 1×10^{-5} s for stable calculations. An approximation of the time step can be based from the Hertzian particle contact time (Equation 6.20) for the non-linear spring contact model, which depends on the particle mass, m_p , particle radius, r_p , Young's modulus, E_p , Poisson's ratio, ν_p , and the relative particle velocity, $v_{p,rel}$. The impeller tip speed was assumed for the relative particle velocity. To ensure that the particle contacts are resolved appropriately, a fraction of the calculated contact time, i.e. ~15% was then taken as the time step.

$$t_{contact,H} = 2.87 \left(\frac{m_p^{*2}}{r_p^{*2} E_p^* v_{p,rel}} \right)^{1/5}$$

Equation 6.20

$$m_p^* = \left(\frac{1}{m_{p1}} + \frac{1}{m_{p2}} \right)^{-1}, r_p^* = \left(\frac{1}{r_{p1}} + \frac{1}{r_{p2}} \right)^{-1}, E_p^* = \left(\frac{1 - \nu_{p1}^2}{E_{p1}} + \frac{1 - \nu_{p2}^2}{E_{p2}} \right)^{-1}$$

The simulation outputs, i.e. position, velocities and contact forces of individual particles were saved at intervals of 0.005 s. For comparison with blade-bed normal stress measured using the impeller stress sensor in Chapter 4 and subsequent analyses, the normal component of the blade-particle contact force ($F_{Cl,n}$) for particles in contact with the blade at the location of the sensor plate (Figure 6.7) for all three blades were summed, averaged with the number of blades, n_I , and divided by the contact area of the sensor, A_p (Figure 6.7) (Equation 6.21).

$$\sigma_n = \frac{\left(\sum F_{Cl,n} \Big|_{A_p} \right) / n_I}{A_p}$$

Equation 6.21

Velocity results were compared with the experiment by extracting the bed surface velocity at the same region recorded and analysed in the experiments (Figure 6.8), i.e. a fixed bed region. Circumferential (or tangential), $v_{surf,c}$, and radial velocity, $v_{surf,r}$, components were calculated from the particles' x and y velocities, i.e. v_x and v_y , from Equation 6.22 and Equation

6.23 respectively. ϑ is the angular displacement of the particle from the +x-axis, also indicated in Figure 6.8, and calculated from the inverse tangent of the ratio of the particle's y and x positions from the centre of the granulator. From the equations, $+v_{cir}$ denotes a counter-clockwise motion, which is the direction of the impeller's rotation; whilst $+v_{rad}$ points to the radial direction away from the centre of the mixer.

$$v_{surf,c} = -(v_x \times \sin\vartheta) + (v_y \times \cos\vartheta) \quad \text{Equation 6.22}$$

$$v_{surf,r} = (v_x \times \cos\vartheta) + (v_y \times \sin\vartheta) \quad \text{Equation 6.23}$$

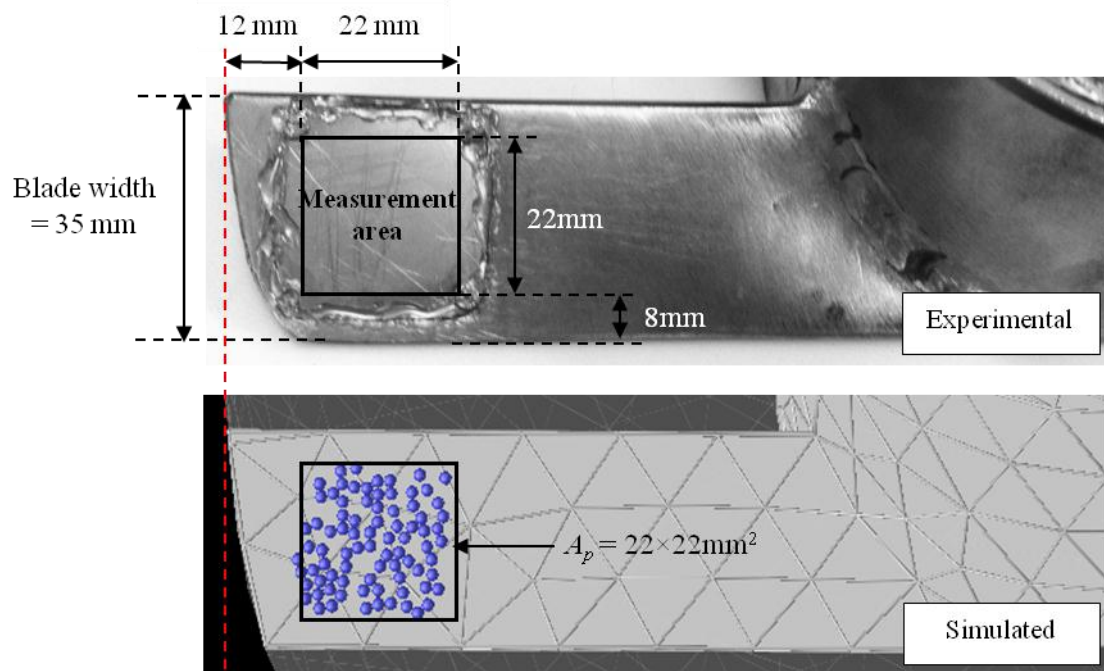


Figure 6.7: Experimental impeller stress sensor plate and analysed contact region for the simulations.

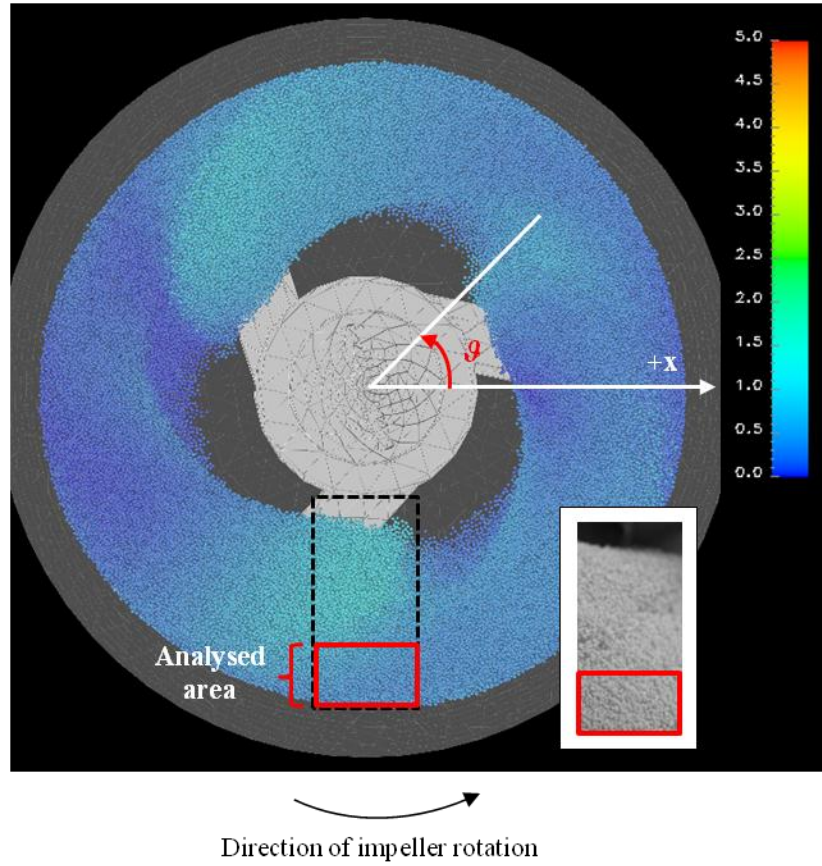


Figure 6.8: Top view of the granulator and the bed surface velocities analysis region. Inset: High speed camera recorded image. The colour bar indicates the particle total velocity in m/s.

6.5 DEM validation: experimental comparison

To validate the DEM method employed, the simulation results were compared with the experimentally measured blade-bed stress, bed surface velocity and bed height. Prior to that, images of the moving bed at 50, 150 and 350 rpm in Figure 6.9 demonstrate the similar characteristic bed flow profiles between the experiment and simulation at each impeller speed. The comparisons are made between the 1.0-2.0 mm sieve size ($d_{v,50} = 1.6$ mm) mannitol granules and the simulated, 2.0 mm monosized particles. The latter size is the minimum size achievable in the simulations, explained earlier in Section 6.3.2. Additionally, similar flow patterns are also exhibited by the 2.0 and 3.5 mm simulated particle beds.

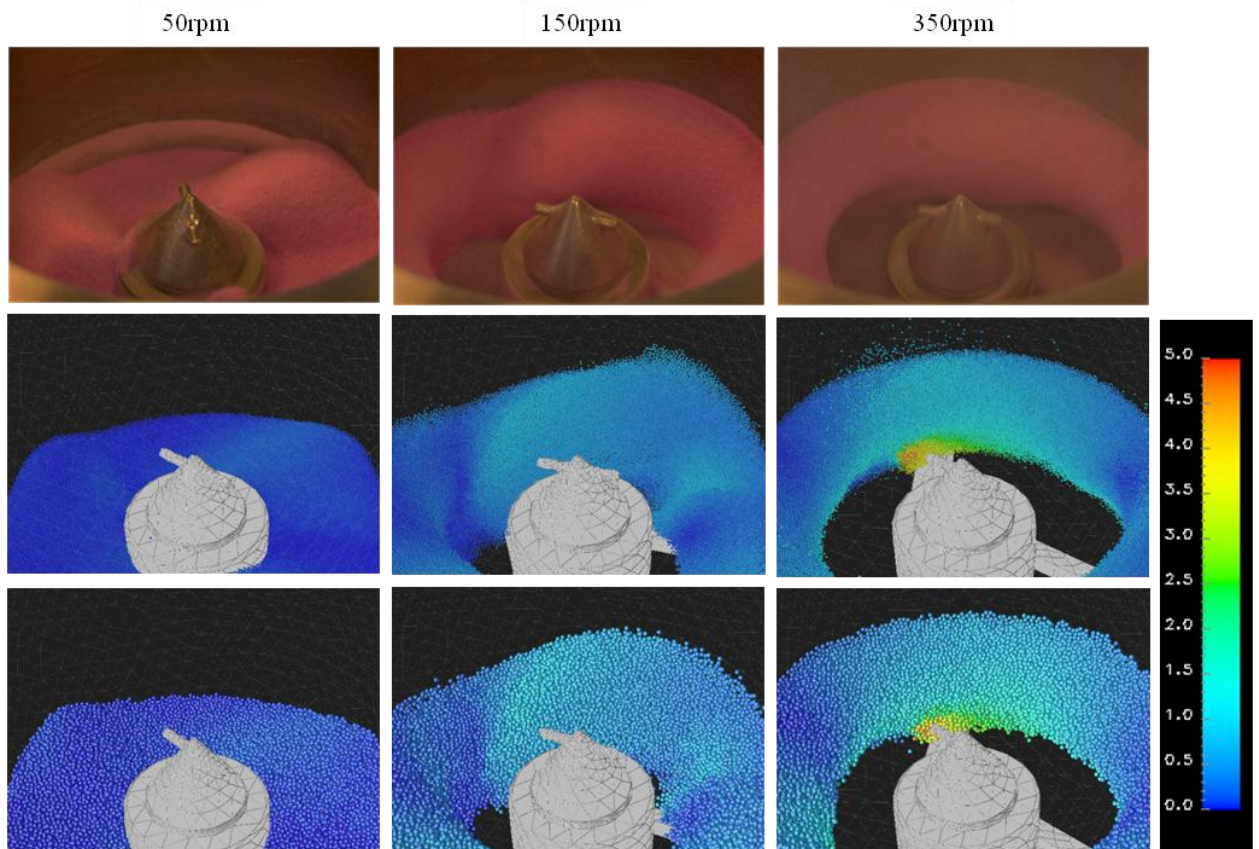


Figure 6.9: Images of the granule/particle bed at three different impeller speeds for 1.5 kg bed load. Top row: 1.0-2.0 mm mannitol granules; Middle row: simulated 2.0 mm particles; Bottom row: simulated 3.5 mm particles. The colour bar indicates the particle total velocity in m/s.

The temporal blade-bed stresses at steady-state, measured experimentally and simulated are displayed in Figure 6.10 and Figure 6.11, which compares the 1.0-2.0 mm sieve size ($d_{v,50} = 1.6$ mm) mannitol granules and 2.0 mm simulated particles, and the 2.0-4.75 mm ($d_{v,50} = 3.34$ mm) mannitol granules and 3.5 mm simulated particles, respectively. There are no experimental results for the 2.0-4.75 mm mannitol granule bed at 350 rpm (Figure 6.11a) due to excessive granule breakage, as discussed in Chapter 4: Section 4.3.2. Reiterating, the output intervals from the telemetric impeller stress sensor and from the simulations are 0.5 and 0.005 seconds respectively.

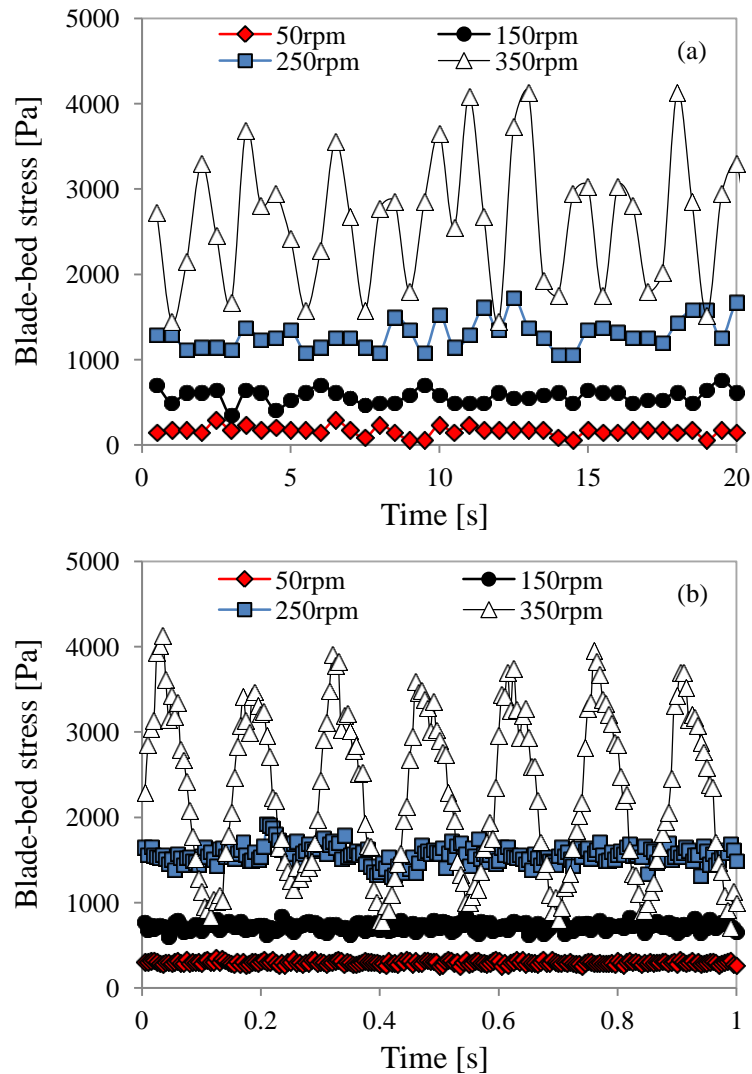


Figure 6.10: Temporal blade-bed stress for the 1.5 kg bed load of (a) 1.0-2.0 mm mannitol granules and (b) simulated 2.0 mm particles.

Figure 6.10 shows the qualitative similarity of the stress fluctuation behaviours exhibited by both the simulations and experimental measurements, i.e. small fluctuations from 50-250 rpm and the large fluctuations at 350 rpm. The simulated 350 rpm output (Figure 6.10b) also suggests a periodic fluctuation of the blade-bed stress at this impeller speed. Further insight on this behaviour is presented in Chapter 7 of this thesis. Similarly, Figure 6.11a shows the blade-bed stress fluctuation at 350 rpm for the 3.5 mm simulated particles, albeit being smaller in amplitude compared with the smaller 2.0 mm simulated particles.

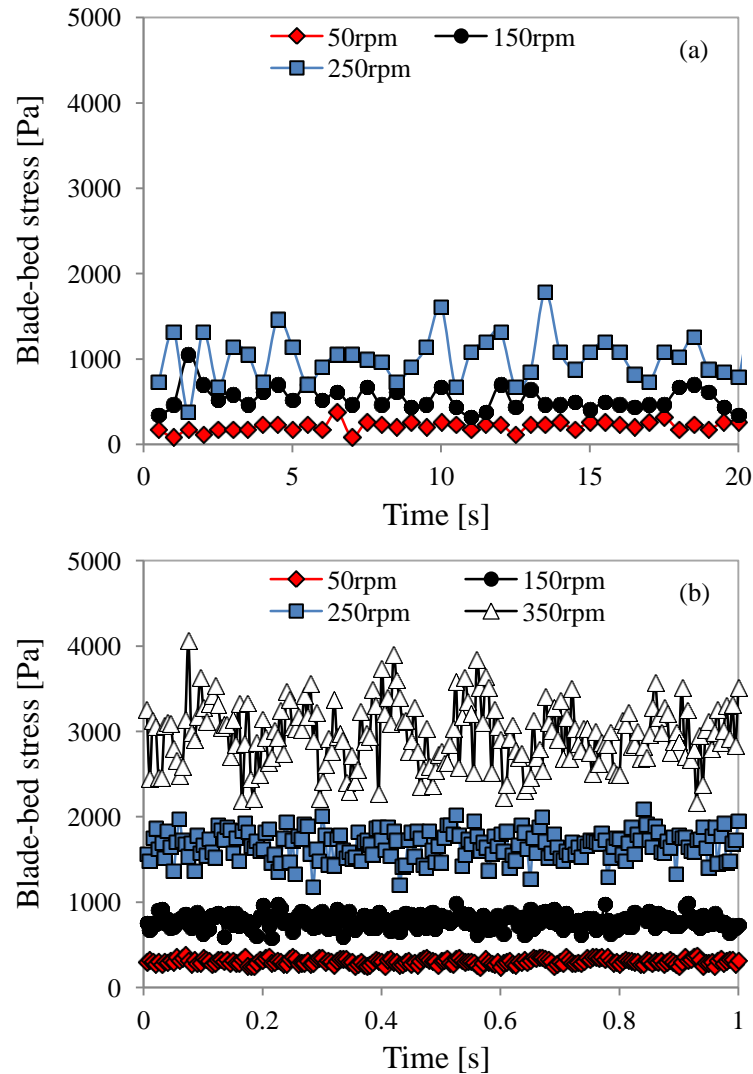


Figure 6.11: Temporal blade-bed stress for the 1.5 kg bed load of (a) 2.0-4.75 mm mannitol granules and (b) simulated 3.5 mm particles. * No measurement data for the 2.0-4.75 mm mannitol granules at 350 rpm.

The experimental and simulated time-averaged values of the blade-bed stresses are plotted in Figure 6.12, again for both granule/particle sizes compared in Figure 6.10 and Figure 6.11. The simulations reasonably predict the average stresses and also the fluctuation amplitude, indicated by the standard deviation bars, using the selected simulation parameters and assumptions discussed previously. These results also demonstrate that the time-averaged blade-bed stresses are similar between the two different simulated size particles, corroborating the experimental findings in Chapter 4 where the granule sieve size does not affect the bulk, time-

averaged blade-bed stresses. Section 6.7.1 of this chapter presents additional results for other simulated particle sizes.

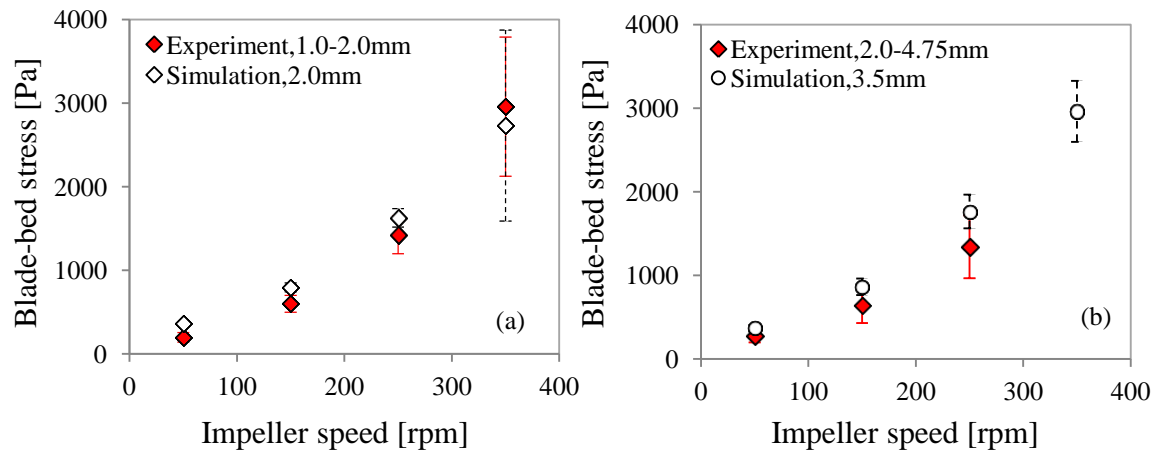


Figure 6.12: Time-averaged blade-bed stress for the 1.5 kg bed load of (a) 1.0-2.0 mm mannitol granules and simulated 2.0 mm particles and (b) 2.0-4.75 mm mannitol granules and simulated 3.5 mm particles.

Figure 6.13 and Figure 6.14 compares the temporal bed surface velocities at the analysed region for the two different granule sieve sizes and simulated particle sizes. The plots include both circumferential and radial velocity components, where the circumferential velocity is higher in magnitude due to it being the dominant motion in the granulator. On the whole, similar fluctuation periodicities are observed, with slight differences in the amplitudes for the radial surface velocities, particularly for the 1.0-2.0 mm granules and 2.0 mm simulated particles comparison (Figure 6.13). This could be attributed to the slightly smaller granule sizes compared to the achievable simulated size, which seemingly results in greater radial fluctuations. Figure 6.14 indicates that smaller surface radial velocity fluctuations are obtained for the larger 3.5-4.75 granule sieve size and 3.5 mm simulated particle size. In addition, experimental results of the smaller mannitol granules sieve sizes (0.1-0.5 mm and 0.5-1.0 mm) also demonstrate larger radial surface velocity fluctuations (Refer to Figure 7.5a(i) and a(ii) in Chapter 7, where the fluctuation amplitude is reflected by the standard deviation bars).

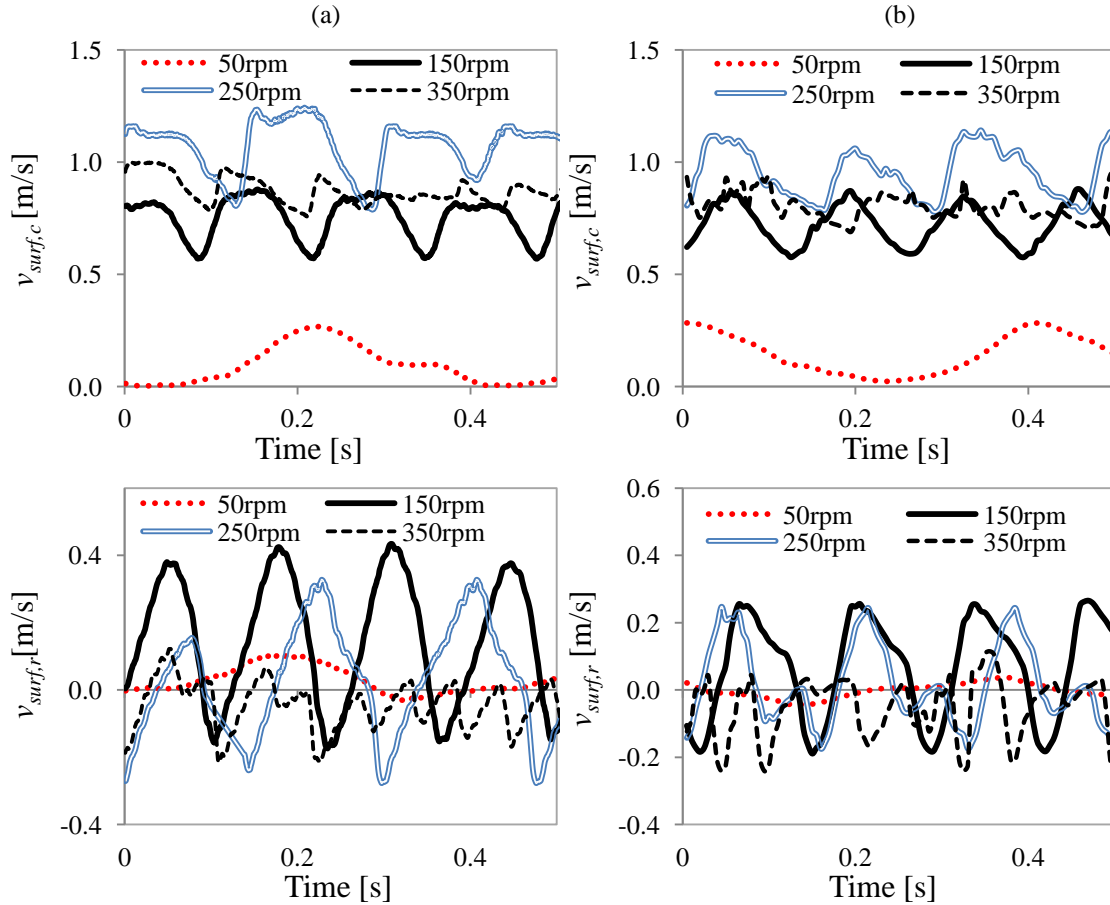


Figure 6.13: Temporal bed surface velocity for the 1.5 kg bed load of (a) 1.0-2.0 mm mannitol granules and (b) simulated 2.0 mm particles. Top and bottom rows show the circumferential and radial components respectively.

Distinguishing features of the surface velocity fluctuations include periodic fluctuations from 50-250 rpm due to the bed deflection from the blade motion, although the periodicity ceases in 350 rpm. For the periodic circumferential velocities, the bed is accelerated in the circumferential direction when a blade approaches and decelerates after the blade passes. The maxima are obtained when a blade passes through the recorded area. On the other hand, the radial velocity fluctuates about the x -axis, indicating a change of direction. It can also be observed that at 50 rpm the radial velocities peak slightly before the circumferential velocities. For 150 and 250 rpm, the peaks of the radial velocities appear after the circumferential velocities, immediately after the blade passes through the observed area. At 350 rpm, the loss of periodicity and reduction in the fluctuation amplitude, especially for the circumferential velocity could be explained by the increasingly fluidised bed, where the surface motion

becomes increasingly less affected by the blade. The surface velocity fluctuations are further discussed in Chapter 7. Reasonable quantitative agreement between the experimental and simulated bed surface velocity results is affirmed in Figure 6.15, which shows the time-averaged values and standard deviations.

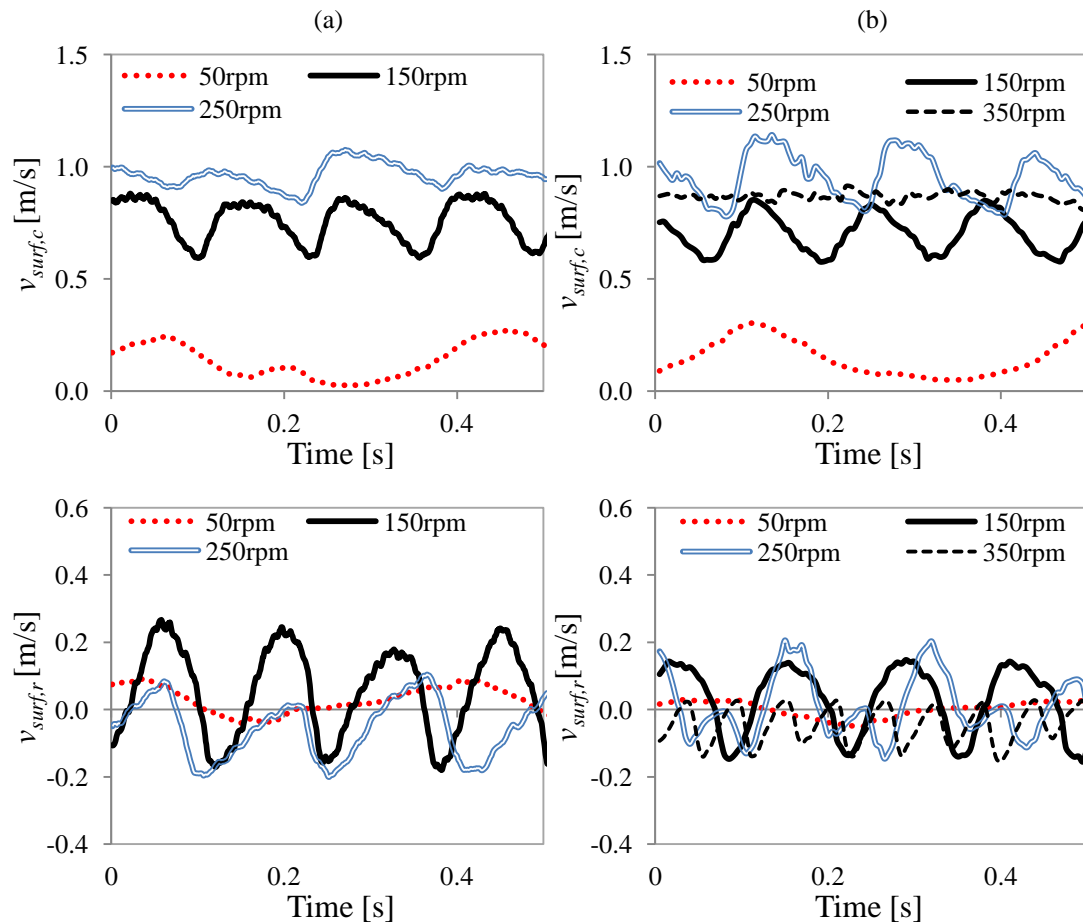


Figure 6.14: Temporal bed surface velocity for the 1.5 kg bed load of (a) 2.0-4.75 mm mannitol granules and (b) simulated 3.5 mm particles. Top and bottom rows show the circumferential and radial components respectively.

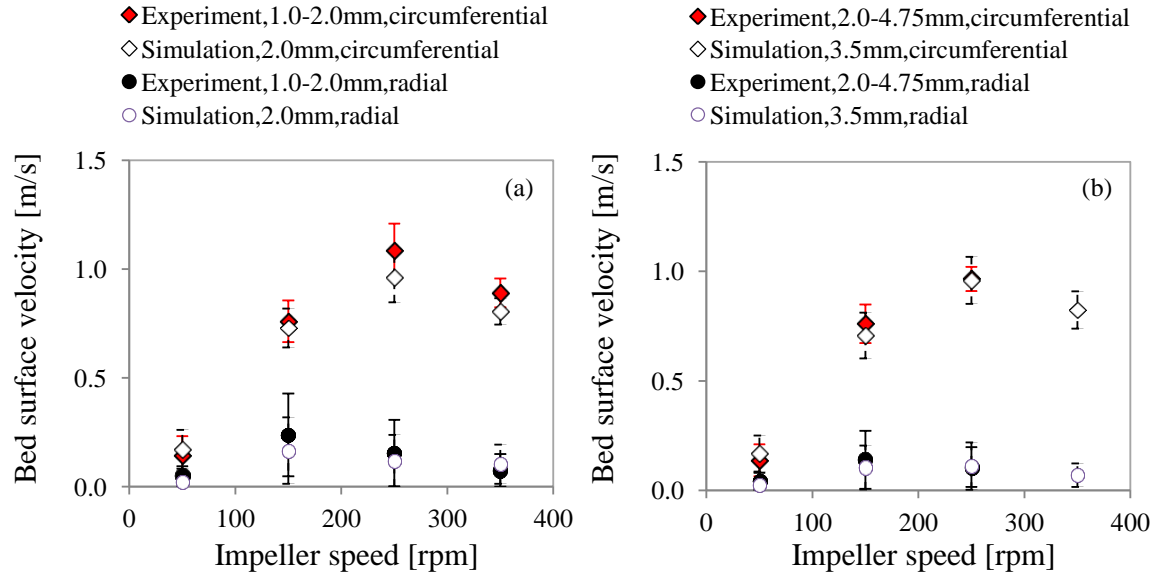


Figure 6.15: Time-averaged bed surface velocities for the 1.5 kg bed load of (a) 1.0-2.0 mm mannitol granules and simulated 2.0 mm particles and (b) 2.0-4.75 mm mannitol granules and simulated 3.5 mm particles.

The simulated bed height at the wall also exhibits similar fluctuation behaviour to the experiments, as shown in Figure 6.16 and Figure 6.17. Similar to the surface velocity results in Figure 6.13 and Figure 6.14, periodic fluctuations of the bed height are obtained from 50-250 rpm, followed by a loss of fluctuation periodicity and a decrease in fluctuation amplitude at 350 rpm. The time-averaged bed height values are given Figure 6.18, which also shows reasonable quantitative agreement.

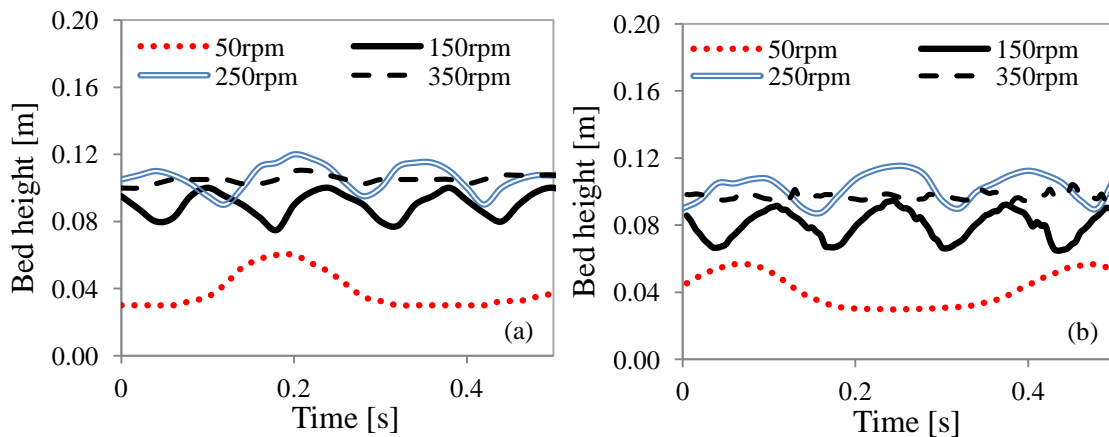


Figure 6.16: Temporal bed height at the wall for 1.5 kg bed load of (a) 1.0-2.0 mm mannitol granules and (b) simulated 2.0 mm particles.

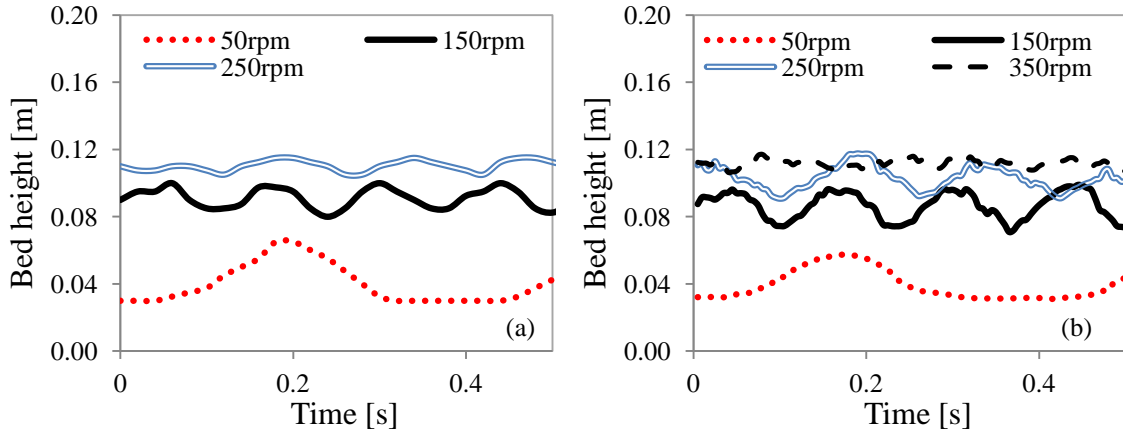


Figure 6.17: Temporal bed height at the wall for 1.5 kg bed load of (a) 2.0-4.75 mm mannitol granules and (b) simulated 3.5 mm particles.

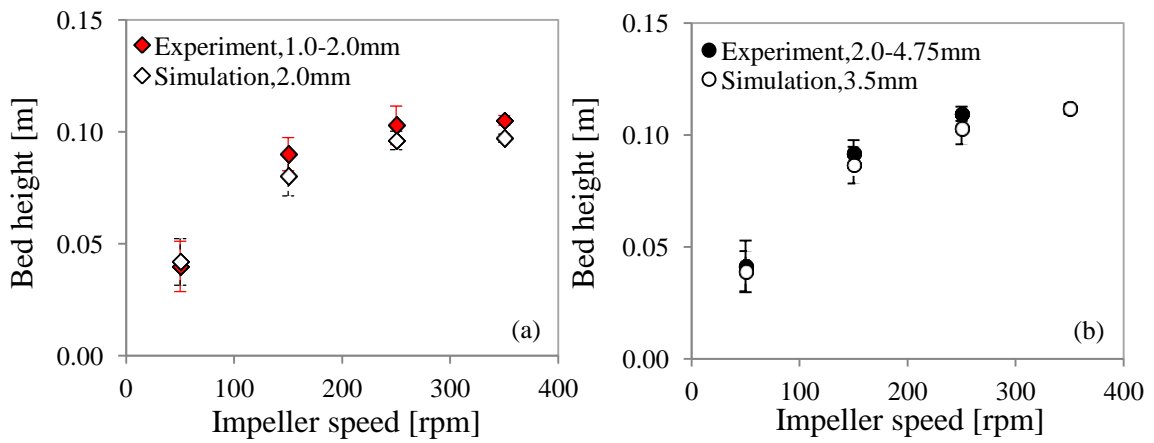


Figure 6.18: Time-averaged bed height at the wall for the 1.5 kg bed load of (a) 1.0-2.0 mm mannitol granules and simulated 2.0 mm particles and (b) 2.0-4.75 mm mannitol granules and simulated 3.5 mm particles.

6.6 Simulation results: impeller speed and radial position

An advantage of the DEM simulations is the capability to analyse any region in the simulated system, which could often be difficult to achieve in experiments. In this case, the variation of the blade-bed stress (Figure 6.19), bed height (Figure 6.20) and bed surface velocity (Figure 6.21) along the radial position can be obtained from the simulations. The data points at each radial position represent the time-averaged values with the error bars indicating the standard deviation of the temporal values. This is particularly useful to gain more insight to the system since the impeller stress sensor only measures the stress in a particular radial position. The figures show the time-averaged results for the 1.5 kg bed of 3.5 mm particles from 50 to 1400 rpm (0.7-20.5 m/s tip speed). Experimental measurements are previously carried out from 50 to 350 rpm. The radial positions where the sensor is located are also indicated in the figures.

For all impeller speeds, the blade-bed stress increases with the radial position (Figure 6.19) due to larger blade tip speeds and amount of particles. With increasing impeller speed, the particles become increasingly pushed towards the wall due to centrifugal effects, shown from the bed height variation along the radial position in Figure 6.20. More particles accumulate towards the wall and an increasing empty region near the centre of the granulator is observed. At very high impeller speeds, i.e. 700 and 1400 rpm, this results in a region of high blade-bed stress being developed at the near wall area which then reduces significantly in the sensor region (the 700 and 1400 rpm results are plotted additionally on an adjusted y-axis with the 350 rpm data in Figure 6.19). From Figure 6.20, a steep decrease of the bed height in the sensor region is also observed at 700 and 1400 rpm.

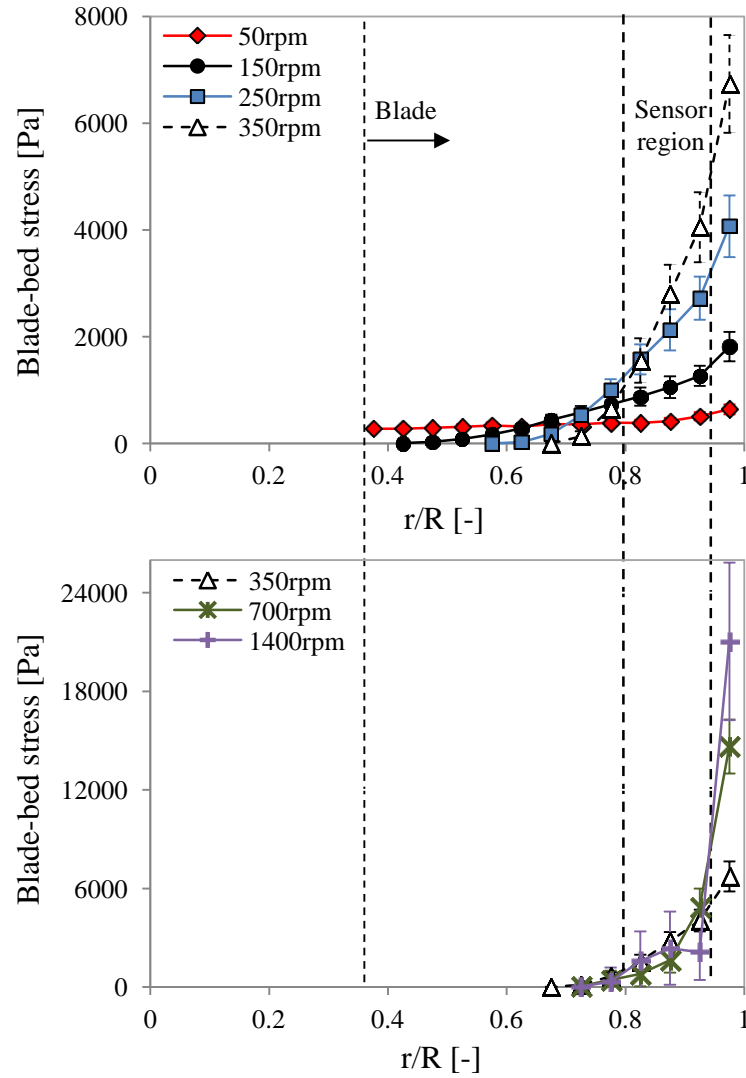


Figure 6.19: Simulated time-averaged blade-bed stress along the radial position (normalised with the blade radius) for the 1.5 kg, 3.5 mm particle beds.

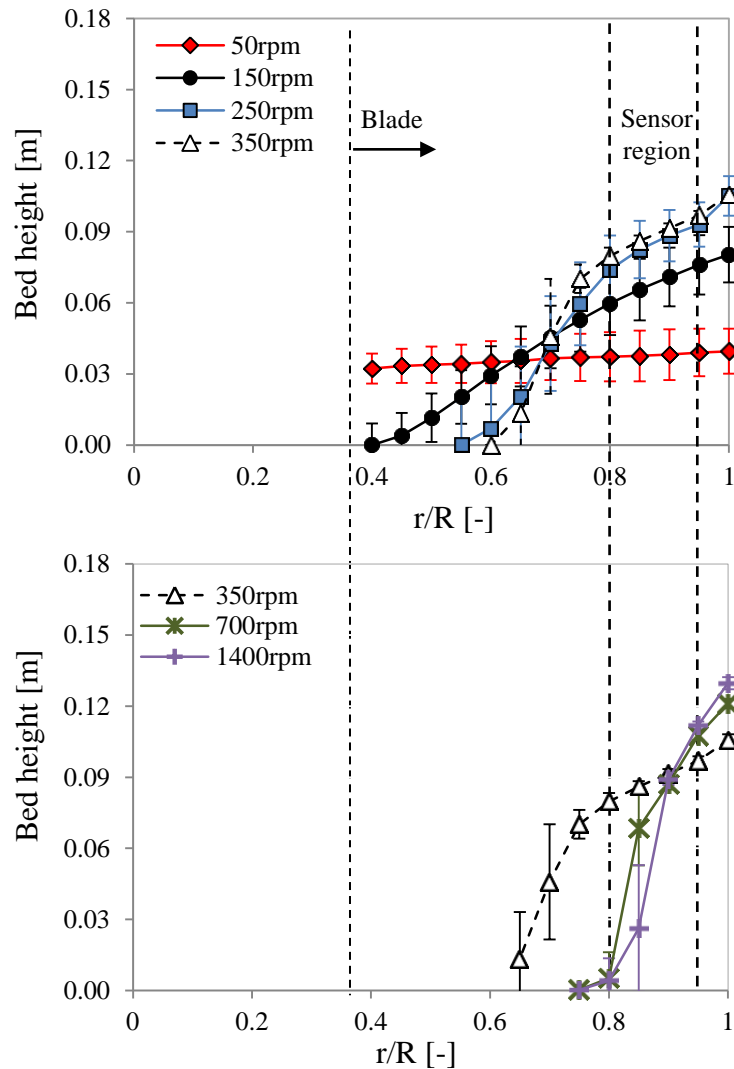


Figure 6.20: Simulated time-averaged bed height along the radial position (normalised with the blade radius) for the 1.5 kg, 3.5 mm particle beds.

The bed surface velocities (circumferential component) along the radial position at different impeller speeds are shown in Figure 6.21. At 50 rpm, a gradual increase of the surface velocity with the radial position followed by a dip towards the wall is observed (see the top graph in Figure 6.21 for the data plotted on an adjusted y -axis). On the contrary, for impeller speeds of 150 rpm onwards, the circumferential surface velocities decrease with the radial position. These behaviours could be linked to the flow regime of the bed. At 50 rpm, the bed is in the slow or frictional flow regime, as pointed out in Chapter 4: Section 4.4.1. In terms of the bed profile/shape, in this regime, the particles occupy the entire area between the shaft

and the wall (Figure 6.9) with little increase of the bed height along the radial position, as shown in Figure 6.20. The surface velocities are consequently dependent on the blade linear velocity and increase with the radial position, although wall constrictions lead to the retardation of the surface motion towards the wall. For additional comparison, Figure 6.22 plots the bed surface velocities with the (a) bed height-averaged velocity (average velocity across the entire bed height at a particular radial position), (b) the bed velocity for only particles in contact with the blade and (c) the blade linear velocity. From the 50 rpm figure, the bed height-averaged bed velocity also exhibits a similar trend as the surface velocity while the average velocity of particles in direct contact with the blade increases consistently with the radial position.

The flow then transits to toroidal at ~150 rpm and subsequently fluidised which sees the bed height increasing with radial position. Since particle velocities reduce with the bed height (also shown in Figure 4.11 in Chapter 4), the surface velocities decrease with the radial position. Additionally, larger surface velocity and bed height fluctuation are observed at the inner bed surfaces for impeller speeds above 150 rpm (Figure 6.20 and Figure 6.21). In Figure 6.22, the bed height-averaged velocities exhibit the same tendencies as the surface velocity while the average velocity of particles in contact with the blade increases with the radial position. To summarise, the surface velocity variation along the radial position in a granulator could be related to the flow regime.

Previously reported works also conformed to the differing observations explained above. In Washino's work, the bed surface velocity was found to increase with the radial position and subsequently reduces towards the wall for a 0.084 m diameter mixer and impeller speed of 86.7 rpm (Fr : 0.02) both in experiment and simulation, and visual observations also confirmed that the particle bed is in the “frictional” flow state (Washino, 2011). This is similar to the 50 rpm case in this work. On the other hand, in Murugama's simulations of a 0.36 m tumbling granulator rotated at 300 rpm (Fr : 0.92), the surface velocity decreases with the radial position as particles are pushed towards the wall, thus exhibiting a curved bed profile shown in the impeller speeds ≥ 150 rpm cases in this work (Murugama et al., 2000).

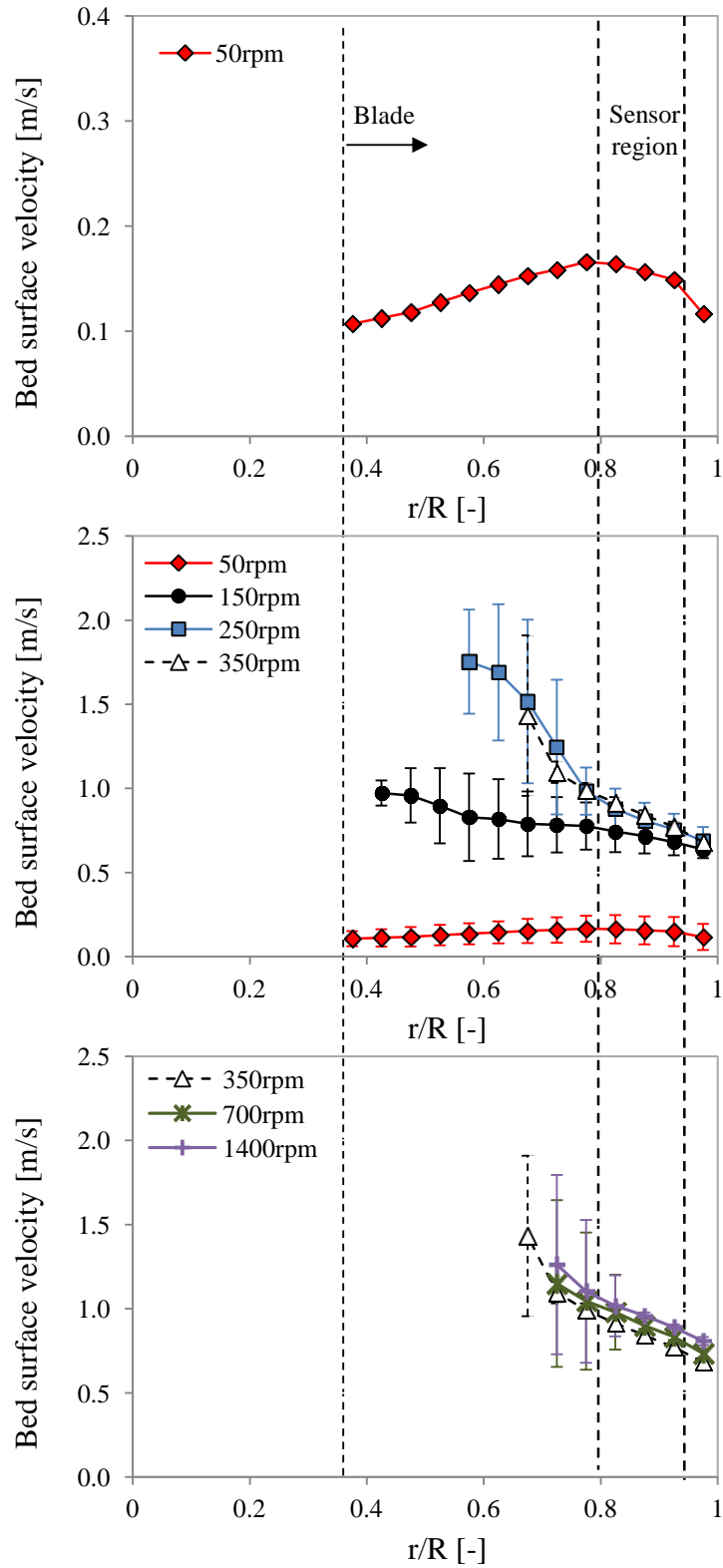


Figure 6.21: Simulated time-averaged bed surface velocity (circumferential) along the radial position (normalised with the blade radius) for the 1.5 kg, 3.5 mm particle beds. *The top graph for the 50 rpm case is plotted additionally on an adjusted y-axis.

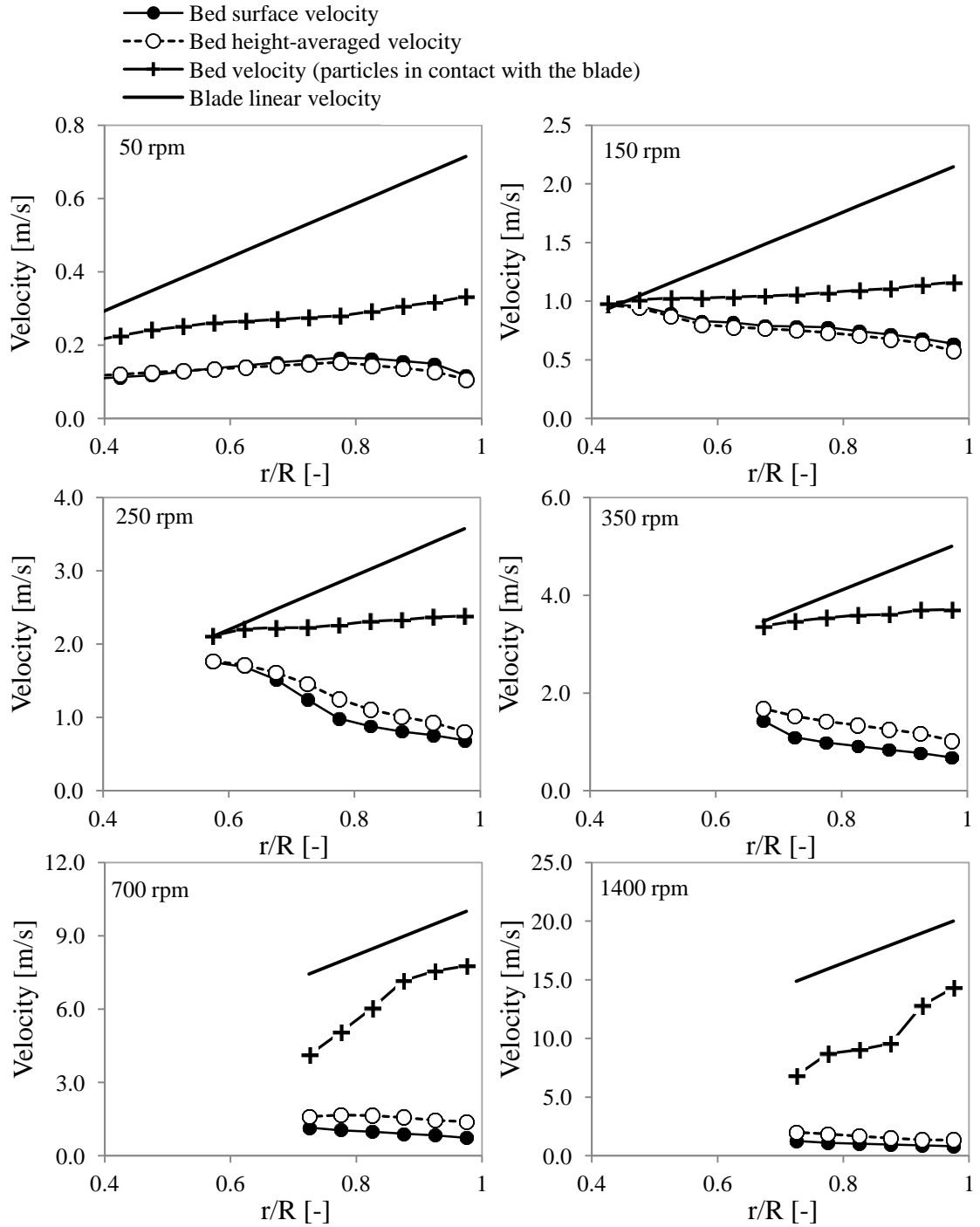


Figure 6.22: Simulated time-averaged particle bed velocities (circumferential) and blade linear velocity along the radial position at different impeller speeds for the 1.5 kg, 3.5 mm particle beds.

Following the above results at varying radial position, the sensor region-averaged results (values averaged over the radial positions where the experimental stress sensor is located as previously shown in Figure 6.7 and also indicated in Figure 6.19, Figure 6.20 and Figure 6.21), particularly at higher impeller speeds, i.e. > 350 rpm, which are not obtained experimentally, are studied. Figure 6.23 plots the sensor region-averaged blade-bed stresses for impeller speeds up to 1400 rpm. Additionally, the tip region averaged blade-bed stresses for an annulus of 7 mm from the granulator wall are also compared on the same plot. Clearly, while the averaged blade-bed stress increases with impeller speed up to 1400 rpm at the tip region, it becomes constant after ~ 350 rpm if the sensor region averaged values are taken. This is explicable since at the higher impeller speeds, there is a steeper decrease of the blade-bed stress from the tip to the sensor region, as can be observed for the 700 and 1400 rpm cases in Figure 6.19 and Figure 6.20.

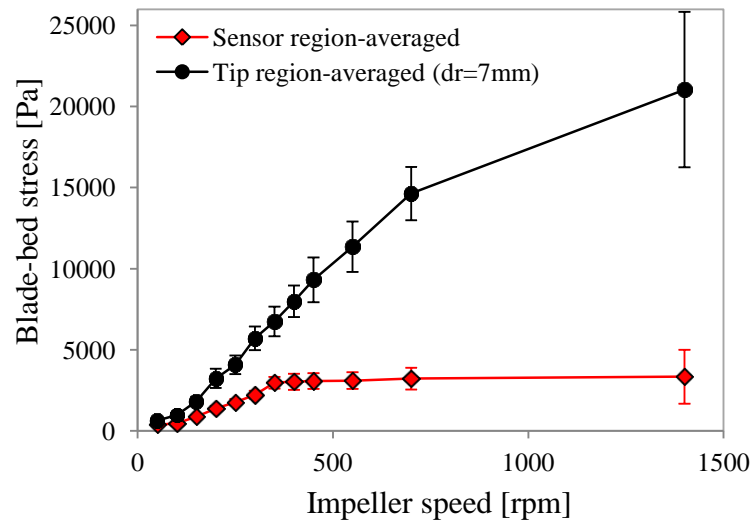


Figure 6.23: Simulated time-averaged blade-bed normal stress at the sensor and blade tip regions for the 1.5 kg, 3.5 mm particle beds.

For additional comparison, Figure 6.24 shows both the normal and shear components of the blade-bed stress at the sensor region, as previous discussions have focused on only the normal component. The shear stress at the sensor region is calculated in a similar way to the normal blade-bed stress in Equation 6.21, except that the tangential component of the blade-particle contact force (i.e. direction along the blade surface) is now taken instead of the normal component. From Figure 6.24, it can be clearly seen that both components exhibit the same

trends across the impeller speed range and that the normal stress is the dominant component (~200-300% larger than the shear).

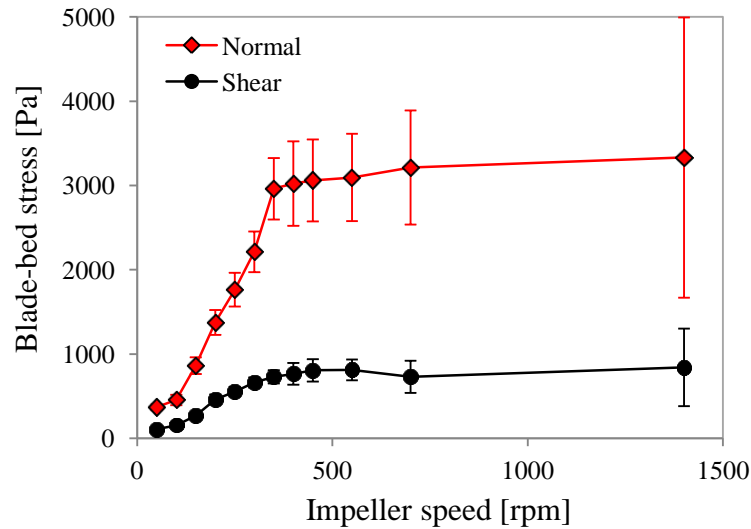


Figure 6.24: Simulated time-averaged blade-bed normal and shear stress at the sensor regions for the 1.5 kg, 3.5 mm particle beds.

Figure 6.25 plots the sensor region-averaged bed surface velocity (circumferential component), again for an extended impeller speed up to 1400 rpm. Once the bed achieves “fluidised flow”, i.e. > 300 rpm, the bed surface velocity does not change significantly. Also included in Figure 6.25 are the bed height-averaged velocities at the sensor region. From 50-150 rpm, the bed surface and bed height-averaged velocities are similar, after which the bed height-averaged values exceed the surface velocities due to the increasing reduction of particle velocity with bed height, also previously shown in Figure 4.11. This is of interest since the bed surface velocity was assumed as the bed characteristic velocity for the blade-bed stress equation, since it’s easier to measure, rather than the bed height-averaged velocities. Section 6.8 presents further discussions on the blade-bed stress predictions using the bed height-averaged velocities.

Finally, the bed height at the wall, which is also the bed height measured experimentally and used in the blade-bed stress equation (Equation 4.9) in Chapter 4 and Chapter 5, is presented in Figure 6.26. In the same plot, the actual sensor region-averaged bed heights are also included. For the 1.5 kg bed, the bed height at the wall increases steadily until 250 rpm, followed by a

slight dip and then a slow increment with higher impeller speeds. The sensor region-averaged bed height however reduces steadily above ~ 350 rpm due to more particles being accumulated in the tip region and resulting in a relatively smaller bed height in the sensor region, also as previously shown in Figure 6.20. This behaviour of course, depends largely on the material fill level in the granulator, and the sensor region-averaged bed heights of other bed loads are shown in the following section (Section 6.7.1).

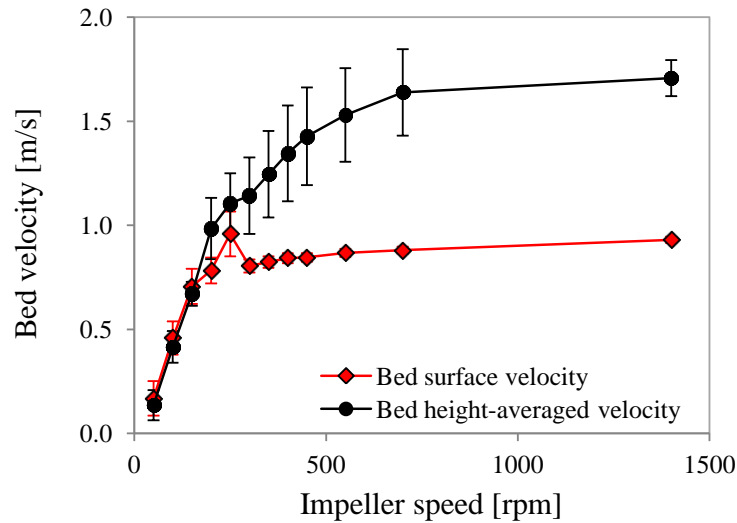


Figure 6.25: Simulated time-averaged bed surface and bed height-averaged velocities (circumferential component) for the 1.5 kg, 3.5 mm particle beds.

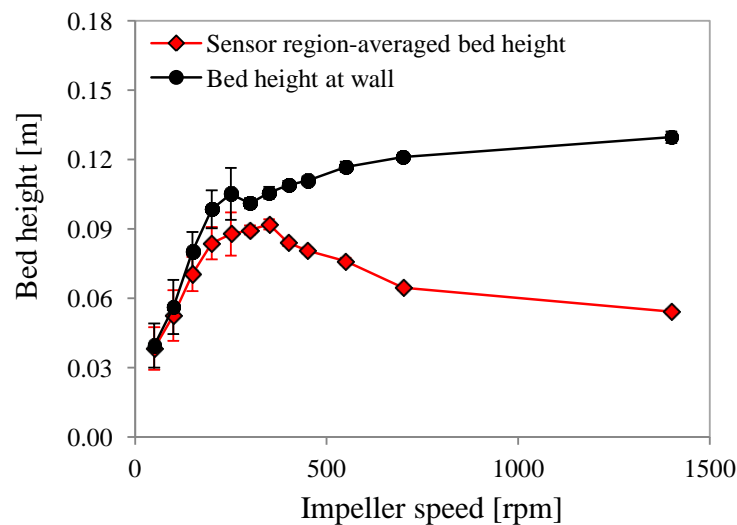


Figure 6.26: Simulated time-averaged bed height at the sensor region and at the wall for the 1.5 kg, 3.5 mm particle beds.

In this section, results for impeller speeds from 50-1400 rpm were presented which gave Froude numbers from 0.02-15.5. Table 6.6 shows the maximum Froude numbers attainable in various commercial high shear granulators with different volume capacities (5-3000 L). The maximum Froude number also generally reduces with increasing granulator volumes, due to the reduced maximum impeller speeds achievable for larger granulators. Therefore, for subsequent studies of the different particle/particle bed properties, impeller geometries and granulator scale results for up to only 700 rpm, which gives a Froude number of 3.88, are reported. This is also the maximum impeller speed achievable in the Roto Junior granulator used for the experiments in this thesis. Additionally, this impeller speed range should give reasonable representations of the flow behaviour and hence, results that could occur in most granulators.

Table 6.6: Froude numbers in commercial high shear granulators.

<i>Equipment</i>	<i>Maximum Froude Number</i>
Roto mixers by IMA Pharma ^a	~5 ^b
Gral mixers by Collette	~2.8 ^c
PMA mixers by Fielder	~3.5 ^c
Diosna mixers	~1.8 ^c
Powrex mixers by Glatt	~8 ^c

^a previously by Zanchetta & C. s.r.l.

^b (IMAPharma, 2012a, b)

^c (Levin, 2007)

6.7 Simulated blade-bed stress, bed surface velocity and bed height results

The results presented in this section are the sensor-region averaged results from the simulations, for comparison and discussion of some of the results with the measured values in Chapter 4. The only difference is that the sensor region-averaged bed heights are reported here, rather than the bed height at the wall measured in the experiments. Appendix D displays all images of the simulated beds reported in this section.

6.7.1 Particle/particle bed properties

Figure 6.27a-c presents the simulated time-averaged blade-bed stress, bed surface velocity (circumferential component) and bed height results for different bed loads. The bed loads of 1.0-3.0 kg in the 11.1 L granulator correspond to the undisturbed bed height to blade inclined height ratios H_{g0}/h_I , of 1.5-3.7, where the undisturbed bed height is the height without impeller rotation. The blade-bed stress increases steadily with bed load (Figure 6.27a), similar to that measured for 1.0-2.0 kg beds of 0.5-1.0 mm mannitol granules in Chapter 4 (Figure 4.7a). Also as previously mentioned, the simulation results for the 700 rpm impeller speed case, which could not be studied experimentally, are reported. As discussed in the previous section for a bed load of 1.5 kg, the blade-bed stress at the sensor region does not change much > 350 rpm. In Figure 6.27a, results for larger bed loads, i.e. 2.0 and 3.0 kg show that the blade-bed stress increases up to 700 rpm. To corroborate the results, the blade-bed stress and bed height along the radial position for the 1.0, 2.0 and 3.0 kg beds are also provided in Figure 6.28, with the sensor region indicated. Clearly, with increasing bed load in the granulator, a less steep bed height and, therefore, blade-bed stress reduction from the granulator wall towards the centre is obtained at 700 rpm. Similar to the experimental results for different bed loads (Figure 4.7b), a lighter and also smaller volume bed experiences a faster bed surface motion as shown in Figure 6.27b. For the 1.0 kg and 1.5 kg beds, a peak in the bed surface velocity is observed at ~250 rpm and with large velocity fluctuations (from the standard deviation bars), before the bed transits to the fluidised flow regime with subsequently less change to the surface velocity (from 350 to 700 rpm). In comparison, the 2.0 and 3.0 kg bed surfaces are observably steadier at 250 rpm with a gradual, slight surface velocity increase from 150 rpm onwards.

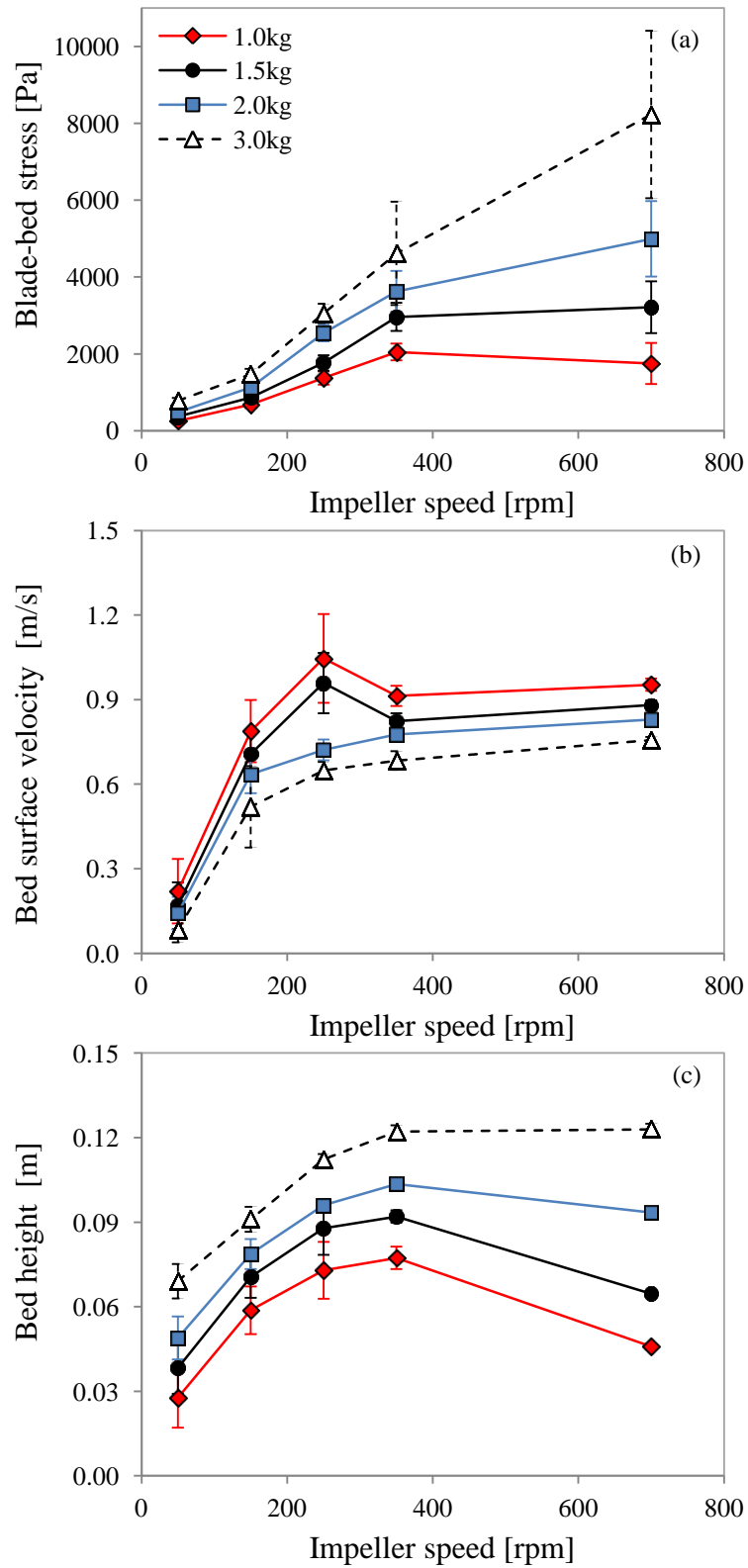


Figure 6.27: Simulated time-averaged data for different bed loads (a) blade–bed stress (b) bed surface velocity (circumferential) and (c) bed height.

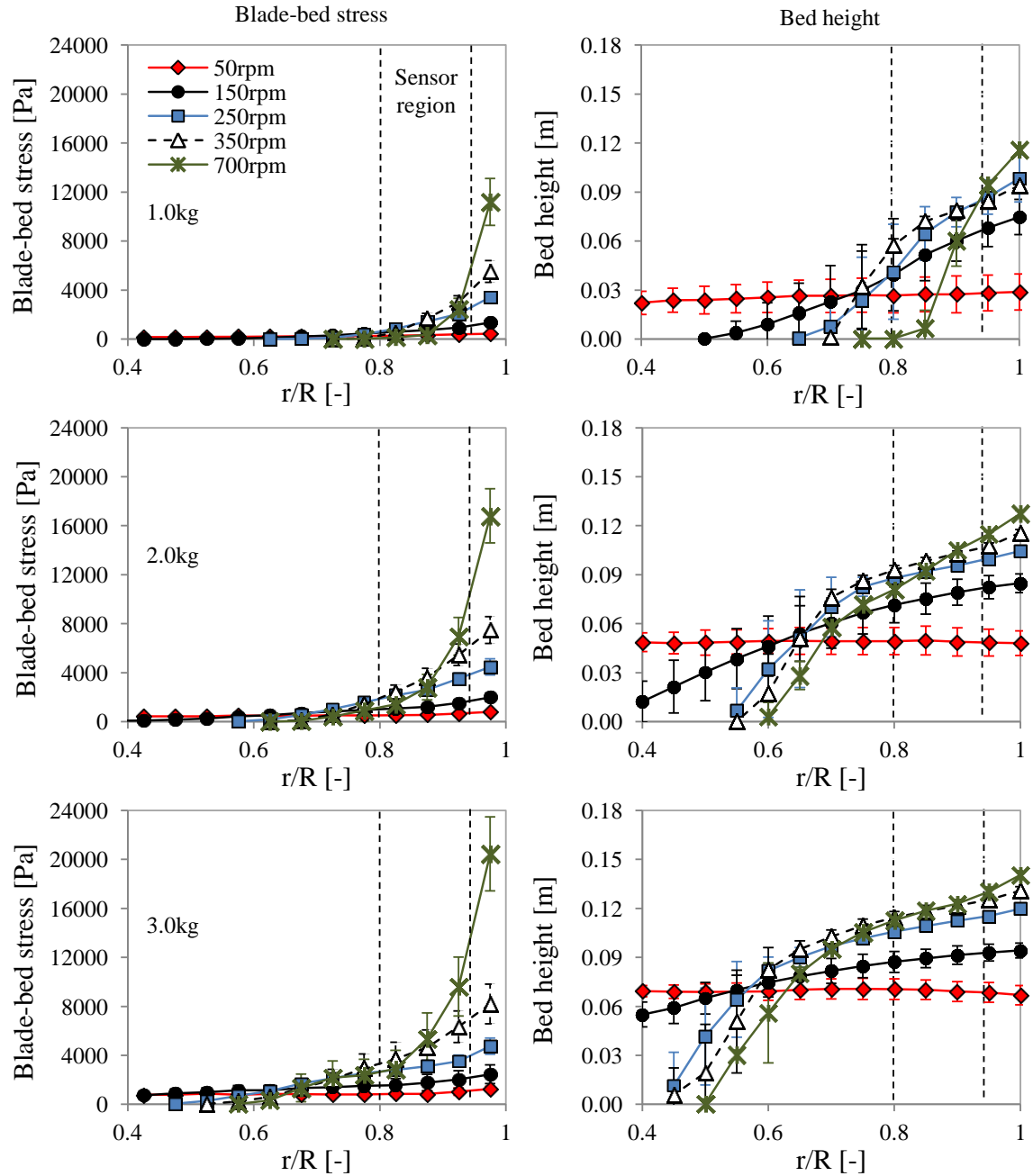


Figure 6.28: Simulated time-averaged blade-bed stress (left column) and bed height (right column) along the radial position at different bed loads.

Results for different simulated particle sizes show that the average blade-bed stresses, bed surface velocity and bed height at the sensor region are similar for impeller speeds up to 700 rpm (Figure 6.29a-c). This similarity is likewise obtained experimentally for granules of different sieve sizes from 0.1 mm to 4.75 mm as described in Chapter 4, Figure 4.8. In these simulations, particles from 2.0 mm to 10.0 mm are studied which gives approximately 80 to 3 particles in contact with the sensor region on the blade respectively. In terms of blade-bed stress fluctuation amplitudes, larger fluctuations are observed for the 2.0 mm particles compared to the 3.5 mm particles at 350 rpm and 700 rpm in the fluidised flow regime. However, a further increase in particle size, i.e. 5.0 mm and 10.0 mm particles, also sees an increase in stress fluctuation amplitude across the impeller speeds. Additionally, the peak of the bed surface velocity at 250 rpm also reduces with increasing particle size.

Figure 6.30a-c displays the time-averaged results for simulated particles of different densities. With a constant bed load of 1.5 kg, the different densities give the undisturbed bed height to blade inclined height, H_{g0}/h_I , ratios of 1.3-4.3. The blade-bed stress reduces at lower particle or bed bulk densities (Figure 6.30a), except at 700 rpm where the 360 kg/m³ bed has the highest blade-bed stress. Again, this is simply due to the larger bed height at the sensor region compared to the 740 kg/m³ and 1500 kg/m³ density beds. The bed surface velocities increase with particle/particle bed density due to the smaller bed volume or H_{g0}/h_I (Figure 6.30b). The bed height and surface velocity fluctuation amplitudes also increase with particle/particle bed density.

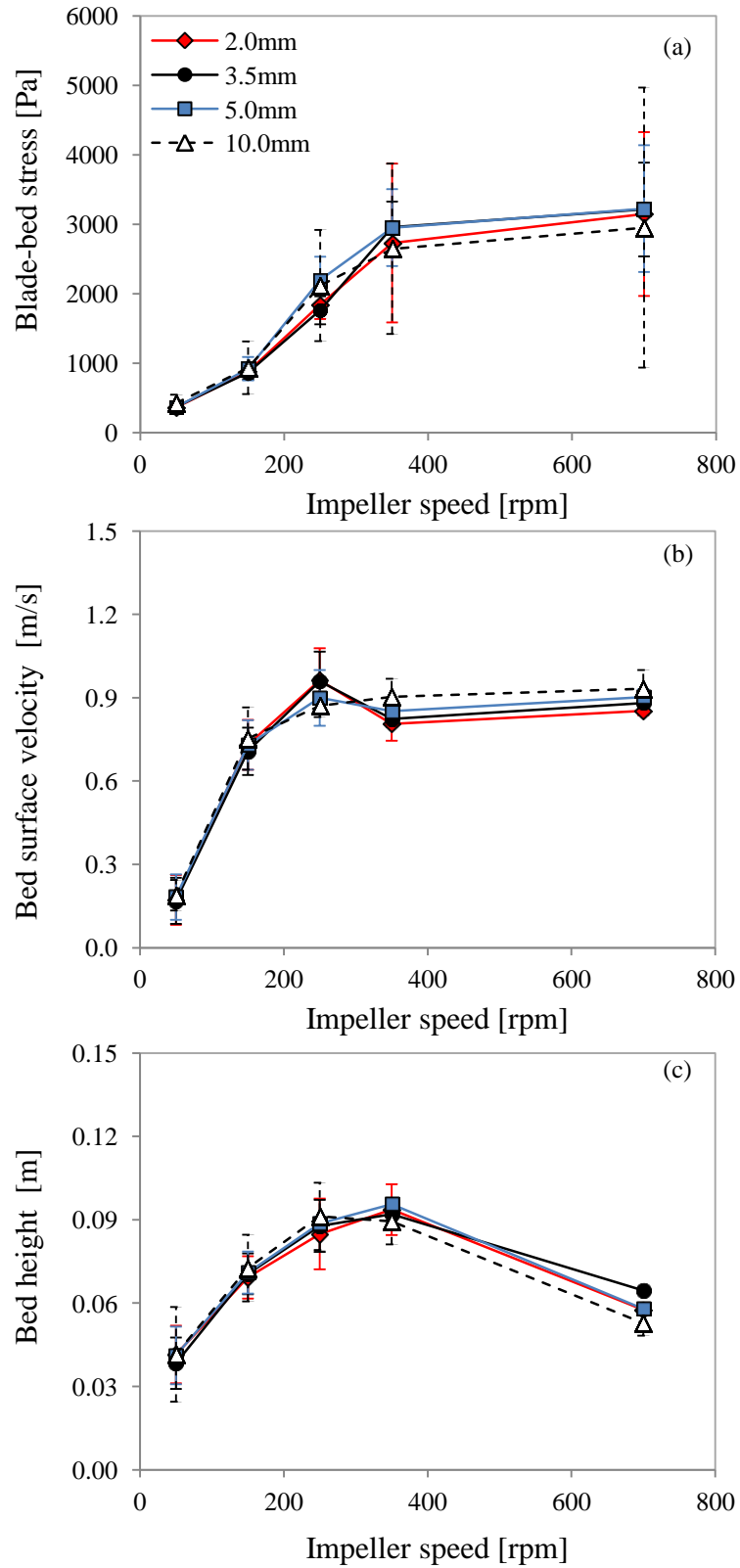


Figure 6.29: Simulated time-averaged data for different particle sizes (a) blade–bed stress (b) bed surface velocity (circumferential) and (c) bed height.

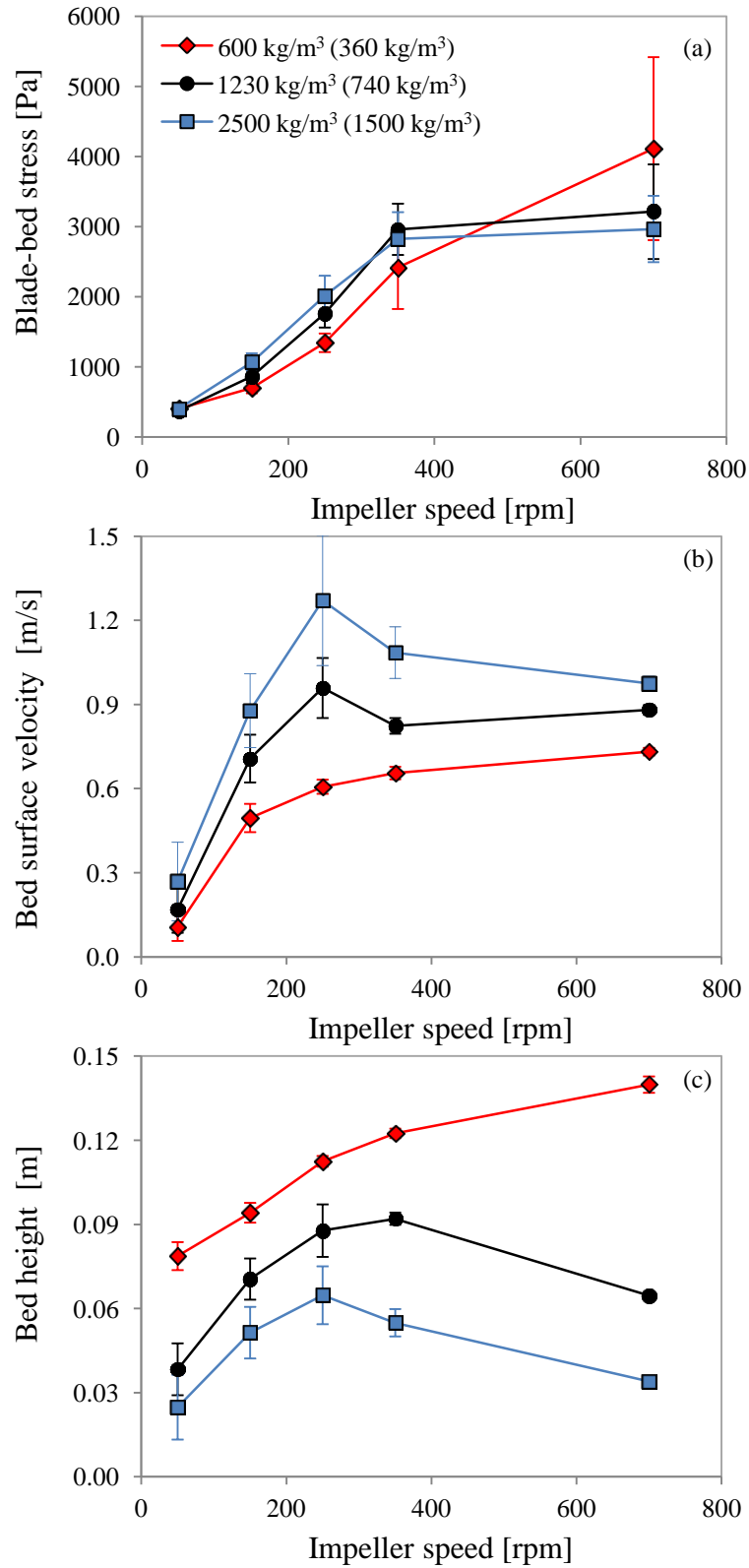


Figure 6.30: Simulated time-averaged data for different particle densities (a) blade–bed stress (b) bed surface velocity (circumferential) and (c) bed height. *Numbers in brackets are the bed bulk density.

When varying the interparticle sliding friction coefficient, μ_f , observable differences of the blade-bed stress and bed surface velocity are obtained from 0.02 to 0.3, and ≥ 0.3 the results are similar across the impeller speeds (Figure 6.31). The same is also observed for the shear component of the blade-bed stress (Figure 6.32). The particle-wall friction was kept constant at a value of 0.3. Logically, a low friction coefficient reduces the frictional dissipation of the system's kinetic energy and, therefore, the bulk bed is accelerated to a larger velocity (Kuo et al., 2002; Remy et al., 2010; Remy et al., 2009; Stewart et al., 2001). This is reflected in this study by the higher bed surface velocities observed at μ_f of 0.02 and 0.1 (Figure 6.31b). The surface velocities however are similar for $\mu_f \geq 0.3$. To compare with some previous simulation works, Stewart and co-workers reported that the flow structure and velocity results in a vertical axis, cylindrical granulator (i.e. mean velocities, velocity fields, particle dispersion and velocity frequency distributions) does not change much from μ_f of 0.3-0.5 compared to that from 0.2-0.3 at a very low Froude number (0.001). The sensor region-averaged bed heights are similar for the different μ_f (Figure 6.31c). Additional analysis of the bed profile however shows that at very low μ_f , i.e. 0.02, the bed height at the wall is larger followed by a steeper decrease of the bed height towards the centre for impeller speeds ≥ 150 rpm. This also corresponds to a steeper reduction of the blade-bed stress from the wall towards the centre. The bed height and blade-bed stress profiles at other μ_f are similar (Images of the simulated beds for different μ_f are presented in Appendix D, Section D.1.4: Figure D.7, Figure D.8 and Figure D.9, and the time-averaged results along the radial position for $\mu_f = 0.02$ and $\mu_f = 0.3$ are plotted in Figure D.10).

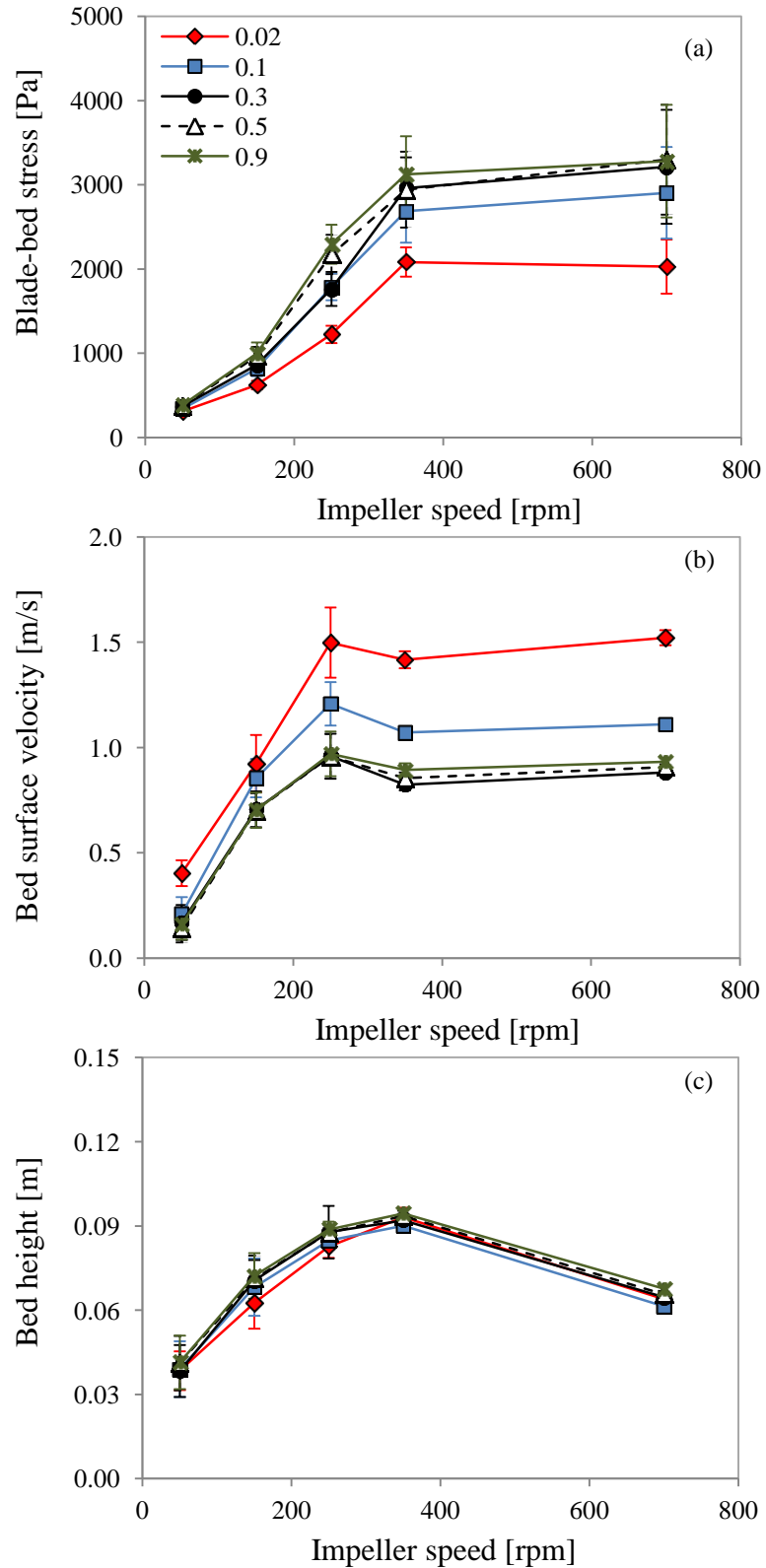


Figure 6.31: Simulated time-averaged data for different interparticle sliding friction coefficients (a) blade-bed stress (b) bed surface velocity (circumferential) and (c) bed height.

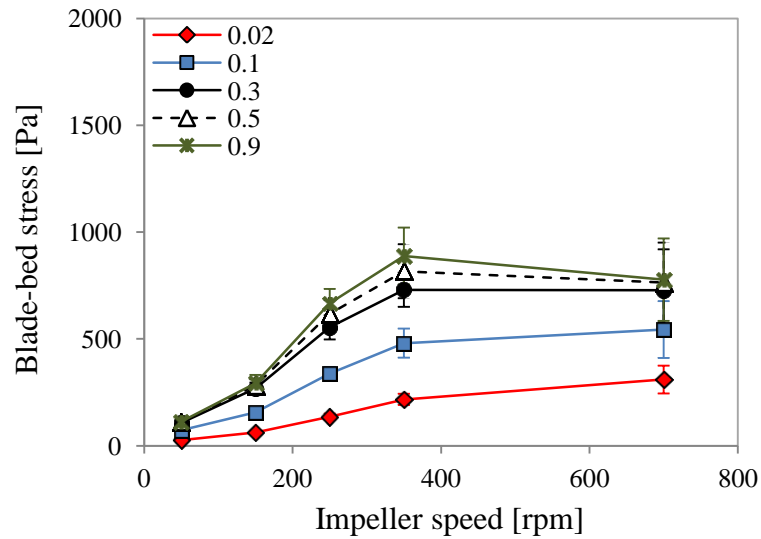


Figure 6.32: Simulated time-averaged blade-bed stress (shear component) for different interparticle sliding friction coefficients.

Different restitution coefficient results (from 0.1-0.9, same value for particle-particle, particle-impeller and particle-wall contacts for each case) show that the time-averaged values of blade-bed stress, bed surface circumferential velocity and bed height are similar. The only differences are that the standard deviations which show the fluctuations amplitudes increase slightly with higher restitution coefficients. The average surface velocities and bed heights are unaffected by the restitution coefficients, although flow images of the simulated beds show an increasing amount of 'flying' particles at the bed free surfaces at high restitution coefficients, i.e. 0.7 and 0.9 (Appendix D, Section D.1.5: Figure D.11). These findings also conform to Kuo and co-workers work, previously mentioned in Section 6.3.2, that for dense flow systems, the restitution coefficient does not affect the average bulk flow for reasonable restitution coefficient values.

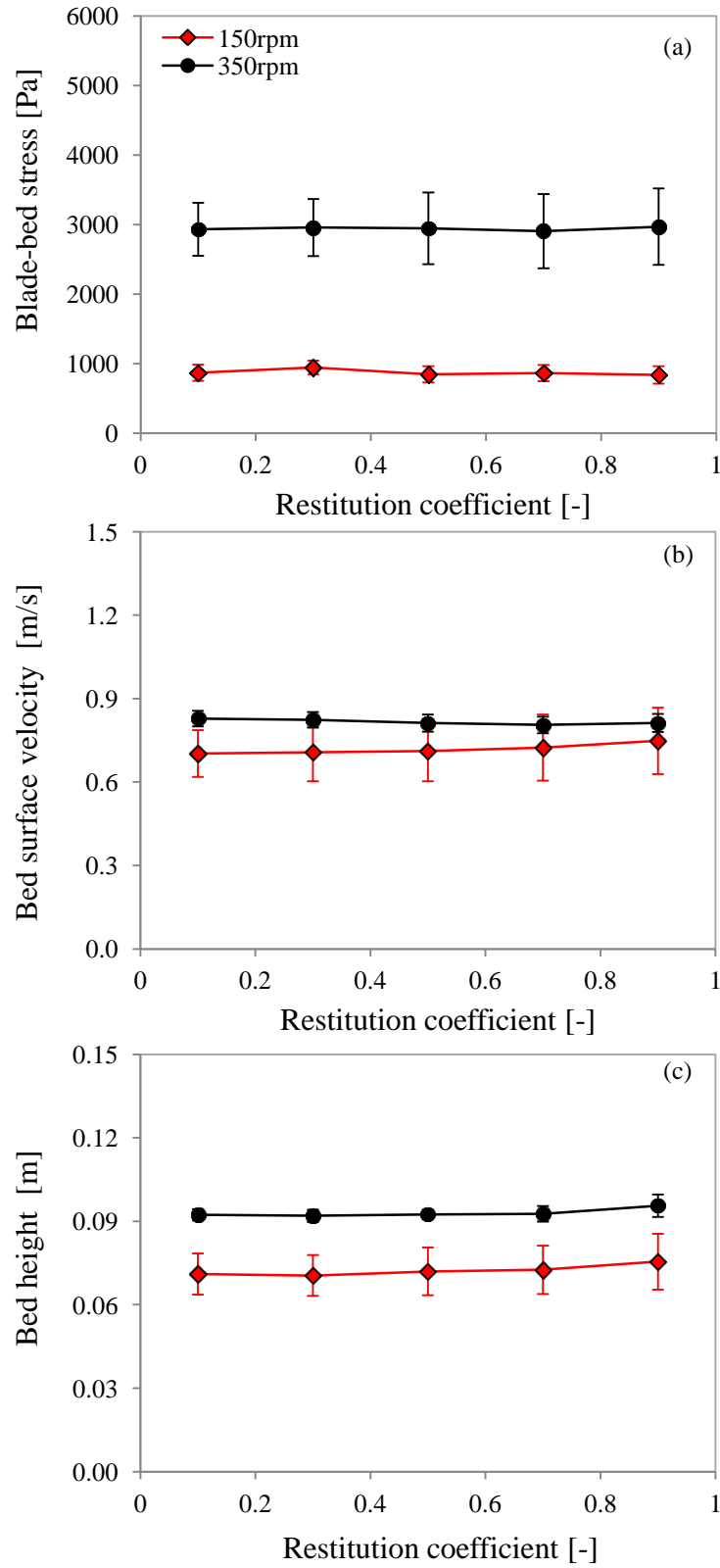


Figure 6.33: Simulated time-averaged data for different restitution coefficients (a) blade–bed stress (b) bed surface velocity (circumferential) and (c) bed height.

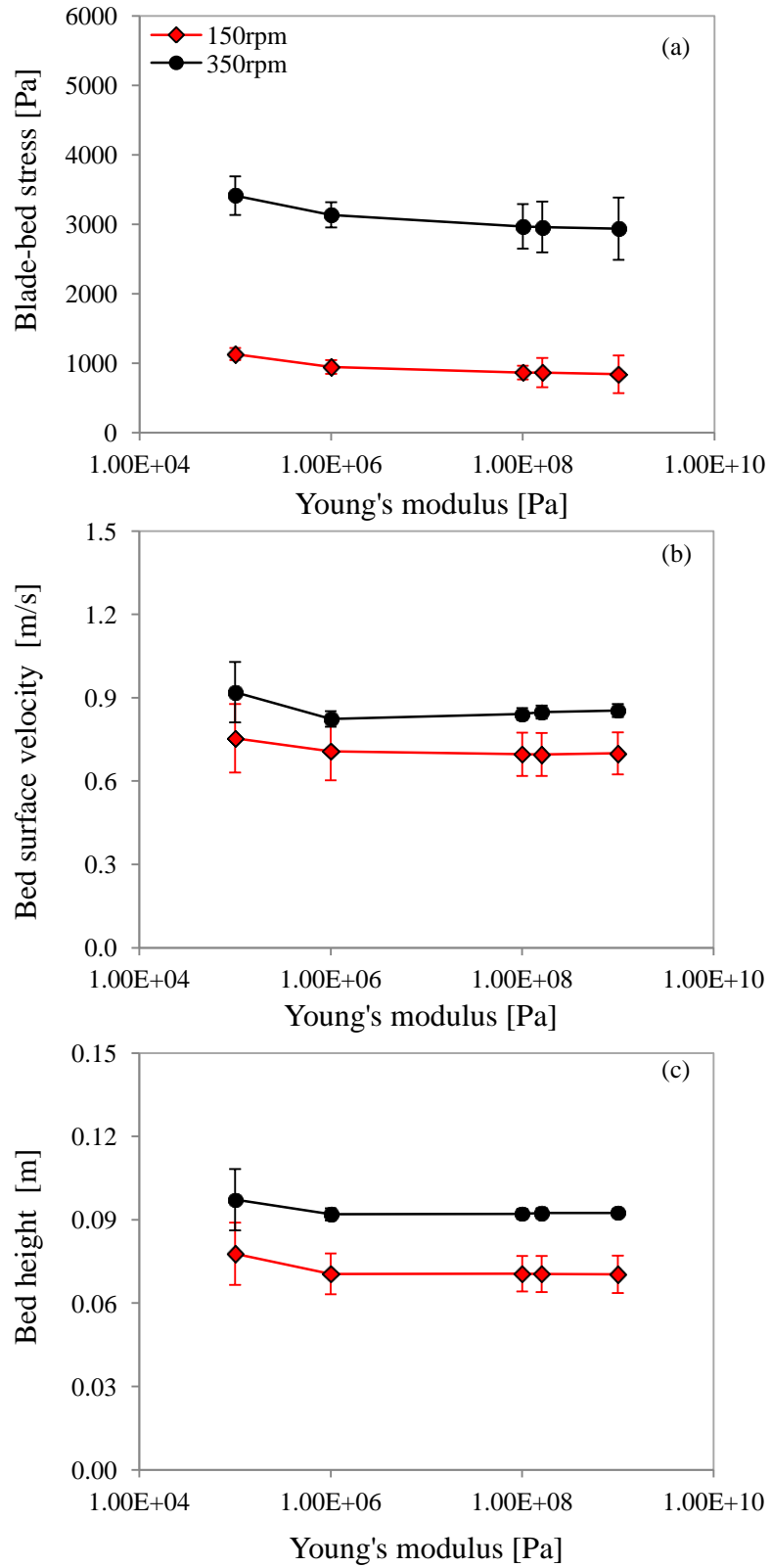


Figure 6.34: Simulated time-averaged data for different Young's modulus (a) blade–bed stress (b) bed surface velocity (circumferential) and (c) bed height.

Results for varying Young's modulus (from 0.1 MPa to 1 GPa and the same value for particle-particle, particle-impeller and particle-wall contacts for each case) showed a decrease of the blade-bed stress, surface velocity and bed height from 0.1 to 1 MPa and these subsequently converge (Figure 6.34). For the 'softest' particles with Young's modulus of 0.1 MPa, a more fluctuating surface motion is also observed (larger surface velocity and height fluctuations). The results obtained at 0.1 MPa is due to the potentially unrealistic large overlap between these 'softest' particles (δ in Figure 6.1) which also allows a larger number of contacts in the dense system, ultimately resulting in larger contact forces (Refer to Figure D.13 in Appendix D: Section D.1.6 which shows the number of particles in contact with the blade at the sensor region for different Young's modulus). It is also worthwhile to note that from literature, reported Young's modulus and restitution coefficient values of some wet and dry granules of different materials are ~ 20 -900 MPa and less than 0.3 respectively (Cheong et al., 2005; Fu, 2006; Iveson and Litster, 1998c; Mangwandi et al., 2011; Mangwandi et al., 2007).

6.7.2 Impeller geometries

Different blade widths (h_w in Figure 6.6) for the 32° inclined blade were simulated (20-65 mm) which gave inclined heights (h_l in Figure 6.6) of 10.6-34.4 mm and undisturbed bed height to blade inclined heights ratios, H_{g0}/h_l , of 1.4-3.6. For the different blade widths, the analysis region for the blade-bed contacts are adjusted accordingly relative to the region indicated in Figure 6.7 (i.e. a larger blade width will have a bigger analysed region and vice versa). Increasing the blade width results in larger total blade-bed normal force (sum of the normal contact forces of the blade and particles) (Figure 6.35) due to increased contacts or interactions between the blade and particle bed at the analysis region. Due to the larger impact area however, the blade-bed stress values exhibits the opposite trend and reduces with blade width (Figure 6.36a). Fluctuation amplitudes of the total blade-bed force and hence blade-bed stress is also larger for smaller blade widths. This fluctuation behaviour is studied further and explained in Chapter 7. A larger blade width (smaller H_{g0}/h_l) also accelerates and deflects the particle bed more, as shown by the bed surface velocities and bed heights results in Figure 6.36b-c.

Varying the blade inclination angle from 20-90° also changes the H_{g0}/h_I ratio from 1.4-3.2. The blade-bed stress increases with the inclination angle (Figure 6.37a). Normal force network diagrams presented by Chandratilleke and co-workers also showed higher forces generated in front of the blade for the 90° inclined blade compared to the 45° inclined blade. Additionally, an acute angled blade (i.e. 135° from the horizontal) showed even higher forces at the blade-front region (Chandratilleke et al., 2009). A larger blade angle (smaller H_{g0}/h_I) also accelerates and deflects the bed more, thereby yielding higher surface velocities and bed height (Figure 6.37b-c). Also worth noting is that with a smaller fill level or as indicated by the H_{g0}/h_I ratio, the bed surface velocity is larger (i.e. bed accelerates faster) as seen in the bed load (Figure 6.27b), particle/bed density (Figure 6.30b), blade width (Figure 6.36b) and blade angle (Figure 6.37b) cases.

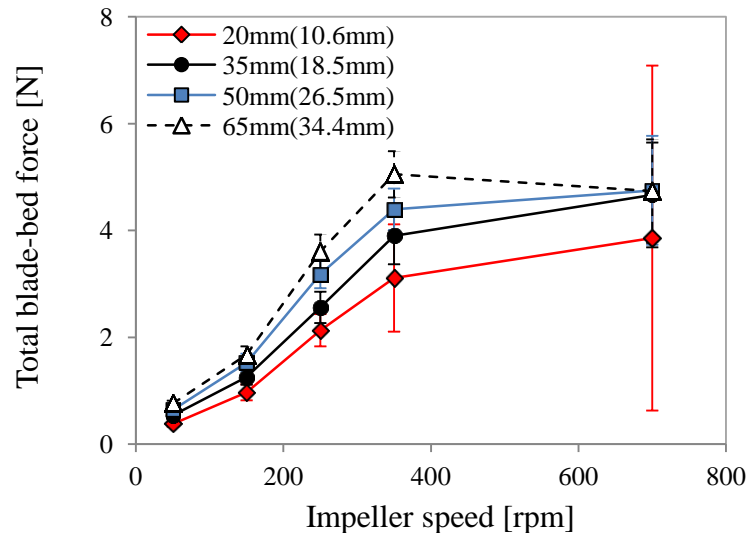


Figure 6.35: Simulated time-averaged total blade-bed force for different blade widths *Legends indicate the blade width, h_w , and blade inclined height, h_I in brackets.

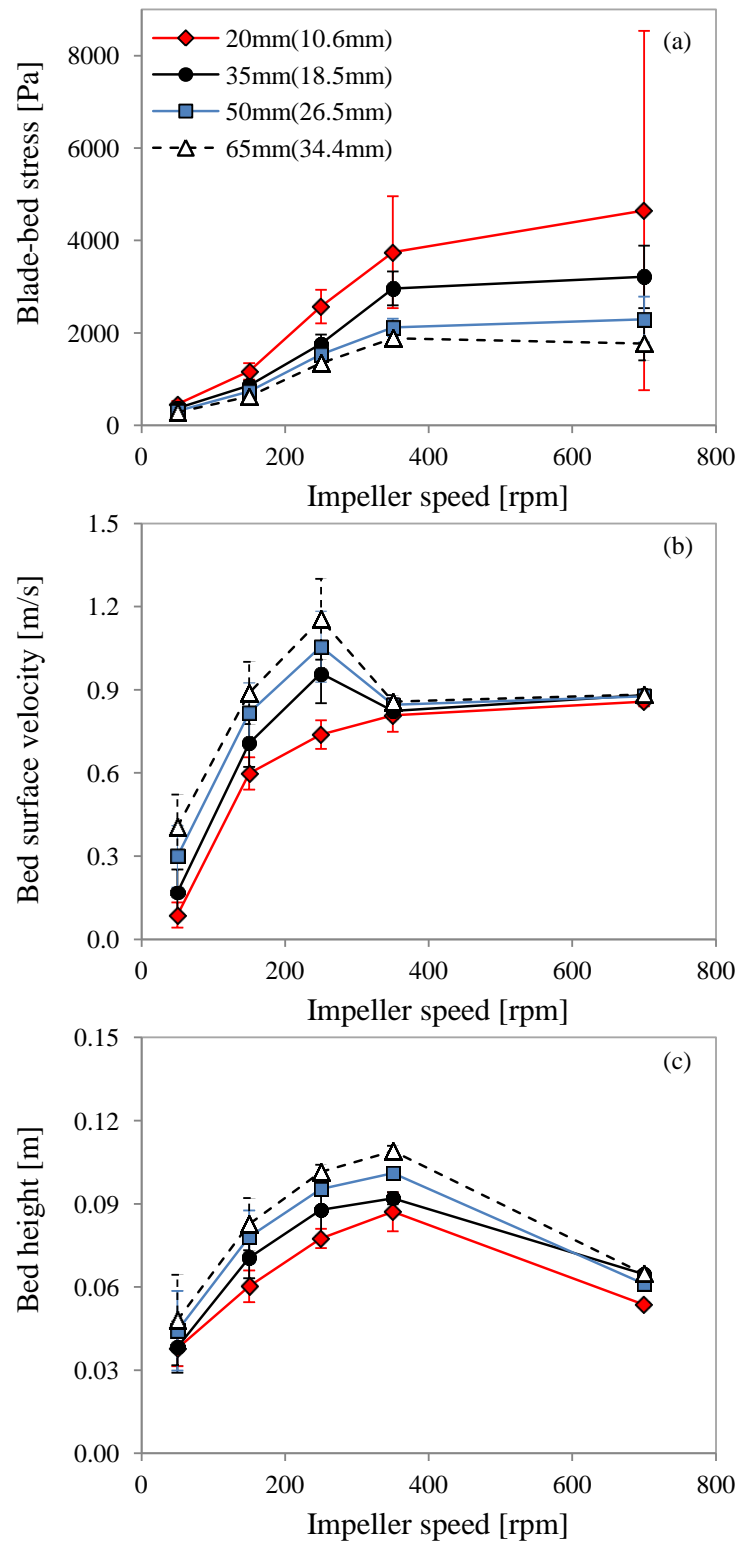


Figure 6.36: Simulated time-averaged data for different blade widths (a) blade–bed stress (b) bed surface velocity (circumferential) and (c) bed height. *Legends indicate the blade width, h_w , and blade inclined height, h_i in brackets.

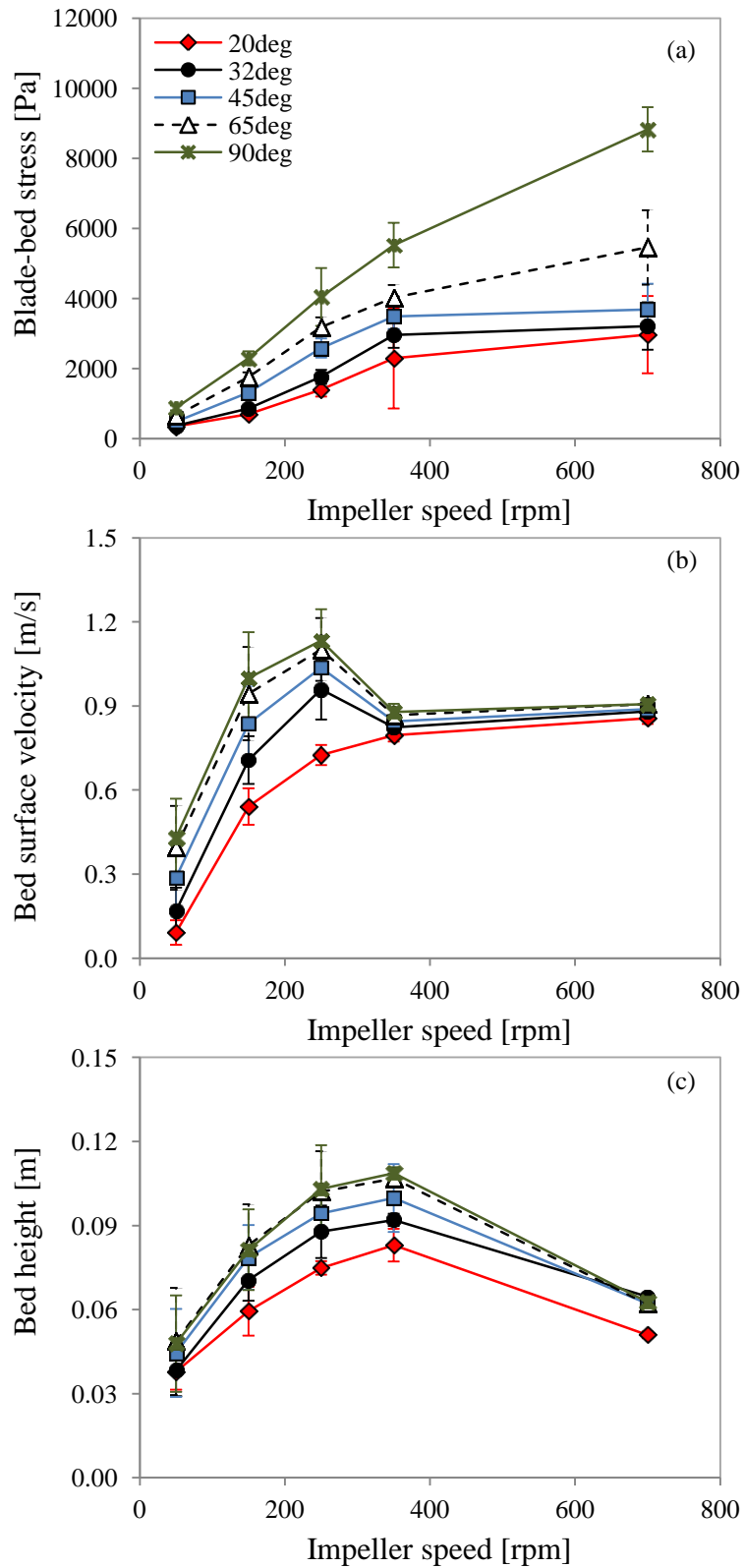


Figure 6.37: Simulated time-averaged data for different blade angles (a) blade–bed stress (b) bed surface velocity (circumferential) and (c) bed height.

With an increasing number of blades, the total blade-particle bed interactions and hence, total blade-particle bed force, also generally increases as shown in Figure 6.38. The resulting blade-bed stress, on the contrary, is similar for different number of blades with a more pronounced difference observed at 700 rpm (Figure 6.39a). This can again be explained by the larger bed height at the sensor region for the 2-bladed impeller case at this speed compared with the 3 and 4-bladed impeller cases in which steeper bed height reductions from the wall are obtained (the particle bed becomes increasingly pushed towards the wall) (Refer to Figure D.22 in Appendix D: Section D.2.3 which displays the the blade-bed stress and bed height along the radial position for different number of blades). The time-averaged bed height results in Figure 6.39c also show the reduction of the sensor region-averaged height with increasing number of blades at 700 rpm.

Other than the bed height at 700 rpm, the bed surface velocity and bed height generally are similar for the different number of blades (Figure 6.39b-c). The 2-bladed impeller, however resulted in larger surface velocity and bed height fluctuations, especially at 150 to 350 rpm, and also increased average surface velocity and height at 350 rpm, due to significant deflections of the bed and less steady bed motion compared to the 3 and 4-blade impellers at these impeller speeds (also confirmed by the bed flow images shown in Appendix D, Section D.2.3: Figure D.20 and Figure D.21).

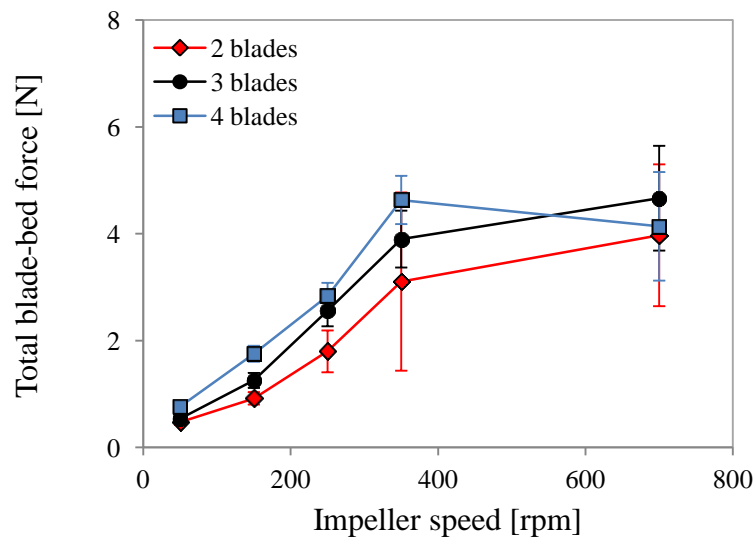


Figure 6.38: Simulated time-averaged total blade-bed force (at the sensor region for all blades) for different number of blades.

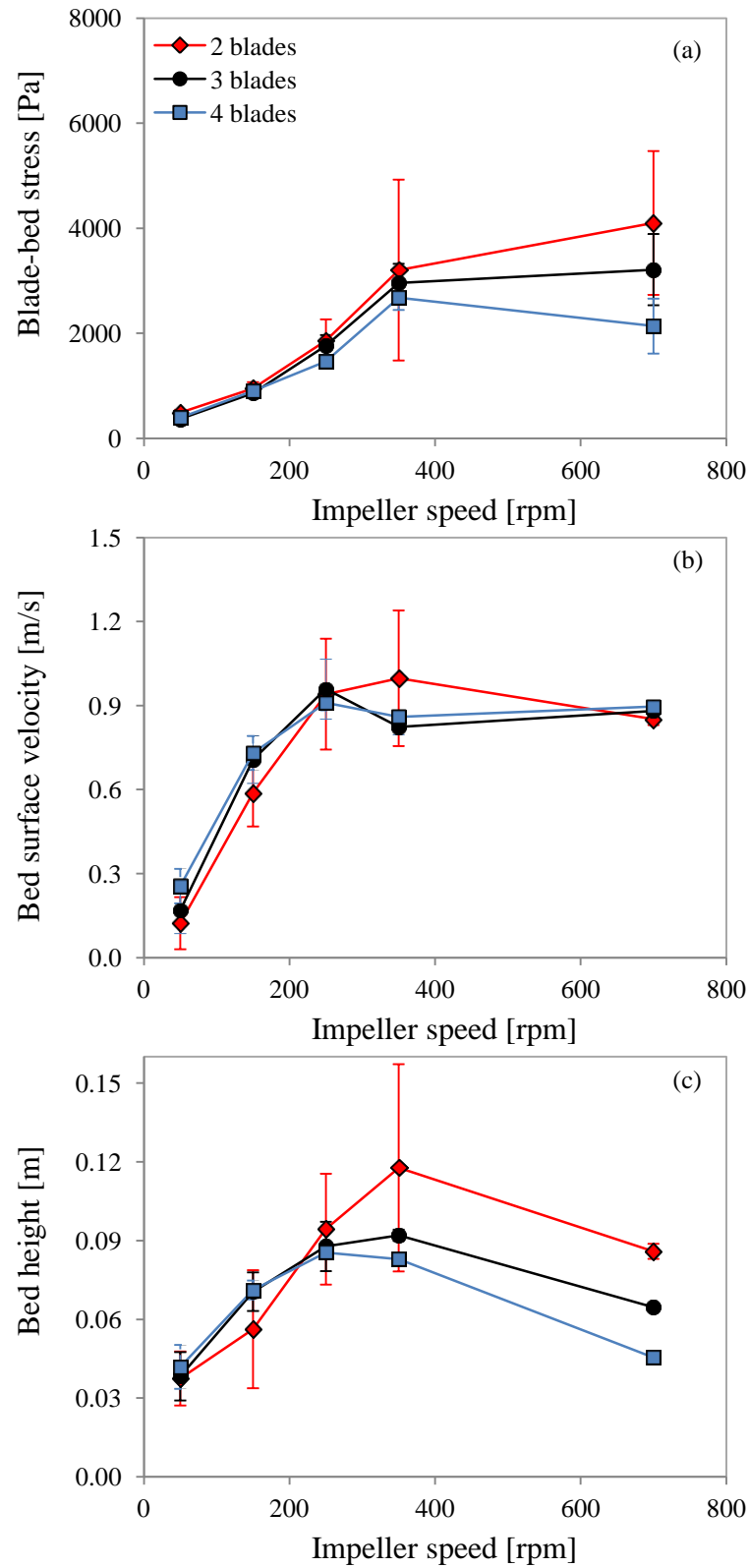


Figure 6.39: Simulated time-averaged data for different number of blades (a) blade-bed stress (b) bed surface velocity (circumferential) and (c) bed height.

6.7.3 Granulator scale

Simulations for different granulator scales were carried out for granulator volumes from 0.173-88.7 L, with diameters from 0.07-0.56 m. A constant particle size is used, therefore giving different mixer diameter to particle diameter ratios, i.e. $D/d_p = 20$ -160. The Froude number also is kept constant across the scales to maintain similar flow behaviour (0.02-3.88). The fill ratios are also maintained, therefore the bed load increases 8 times for each increase in scale. Figure 6.40 shows the particle bed images at a Froude number of 0.18 (onset of toroidal flow) for the different scales. The bed profiles are similar, except at the smallest granulator scale, i.e. $D/d_p = 20$, where the bed flow becomes increasingly irregular with comparatively lesser particles in the system. At other Froude numbers, the bed profiles are also similar for the studied granulator scales for $D/d_p \geq 40$ (Appendix D, Section D.3: Figure D.23 and Figure D.24).

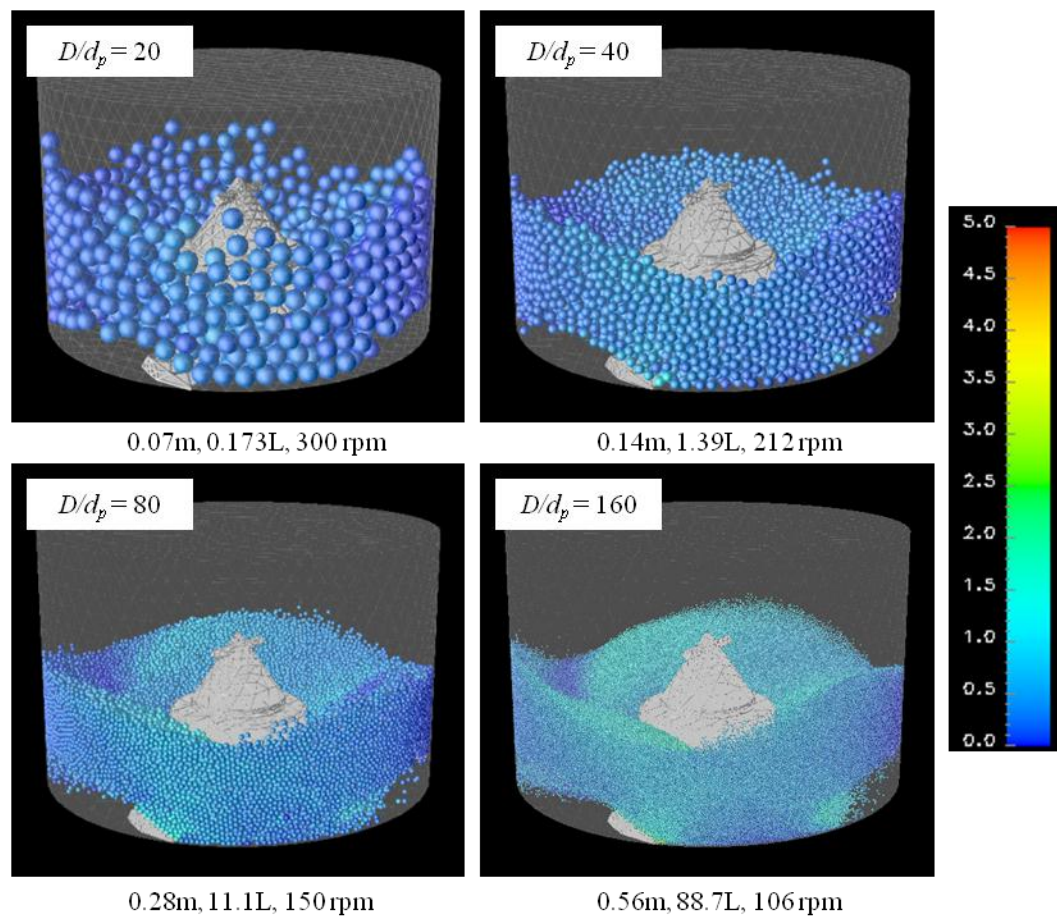


Figure 6.40: Bed flow images from simulation for different granulator scales at a Froude number of 0.18 for the same particle size (3.5 mm) and different D/d_p . The colour bar indicates the particle total velocity in m/s.

The time-averaged results are plotted against the Froude number in Figure 6.41 for the different granulator scales. For additional comparison, the same D/d_p cases are also plotted in the same figure (left column). Flow images for the same D/d_p cases are also given in Appendix D, Section D.3: Figure D.25 and Figure D.26, where since D/d_p is 80 (i.e. > 40), similar bed flow profiles are obtained for different scales at a same Froude number. The blade-bed stress increases with scale due to the larger bed load (Figure 6.41a), and similarly for the bed height (Figure 6.41c). Surface velocities also increase with scale since for certain particular Froude numbers, the impeller linear velocities are higher for larger diameter blades (Figure 6.41b). Also, the average values of the results are generally the same for the same scale granulator, even when the particle sizes are different, except for when $D/d_p = 20$ in the 0.173 L granulator. In this condition, the particles are relatively larger compared to the blade dimensions and only 1-2 particles impact the sensor region, and give higher average blade-stress values compared to when $D/d_p = 80$ (smaller particle size) in the same granulator. Previous studies of different particle sizes from both the experiments (Chapter 4, Section 4.4.2: Figure 4.8, for $D/d_p \approx 83$ -1000) and simulations (Figure 6.29, for $D/d_p = 28$ -140) also showed that average similar blade-bed stress are obtained from $D/d_p = 28$ -1000.

It is also shown that the blade-bed stresses can be scaled with the bed load and hence, the bulk bed pressure, $\rho_b g H_{g,r}$, at the same Froude numbers, except for $D/d_p = 20$ as explained above (Figure 6.42a). The bed surface velocity and bed height also scale with the impeller linear velocity and blade inclined height respectively (Figure 6.42b-c). Remy and Glasser who simulated 10-300 L mixers which gave $D/d_p = 31.5$ -94.5, found that the average particle normal and shear stresses, and the bed velocities can be scaled with the bulk bed pressure and impeller tip speeds respectively for $D/d_p = 63$ and 94.5 and not when $D/d_p = 31.5$ (Remy and Glasser, 2010).

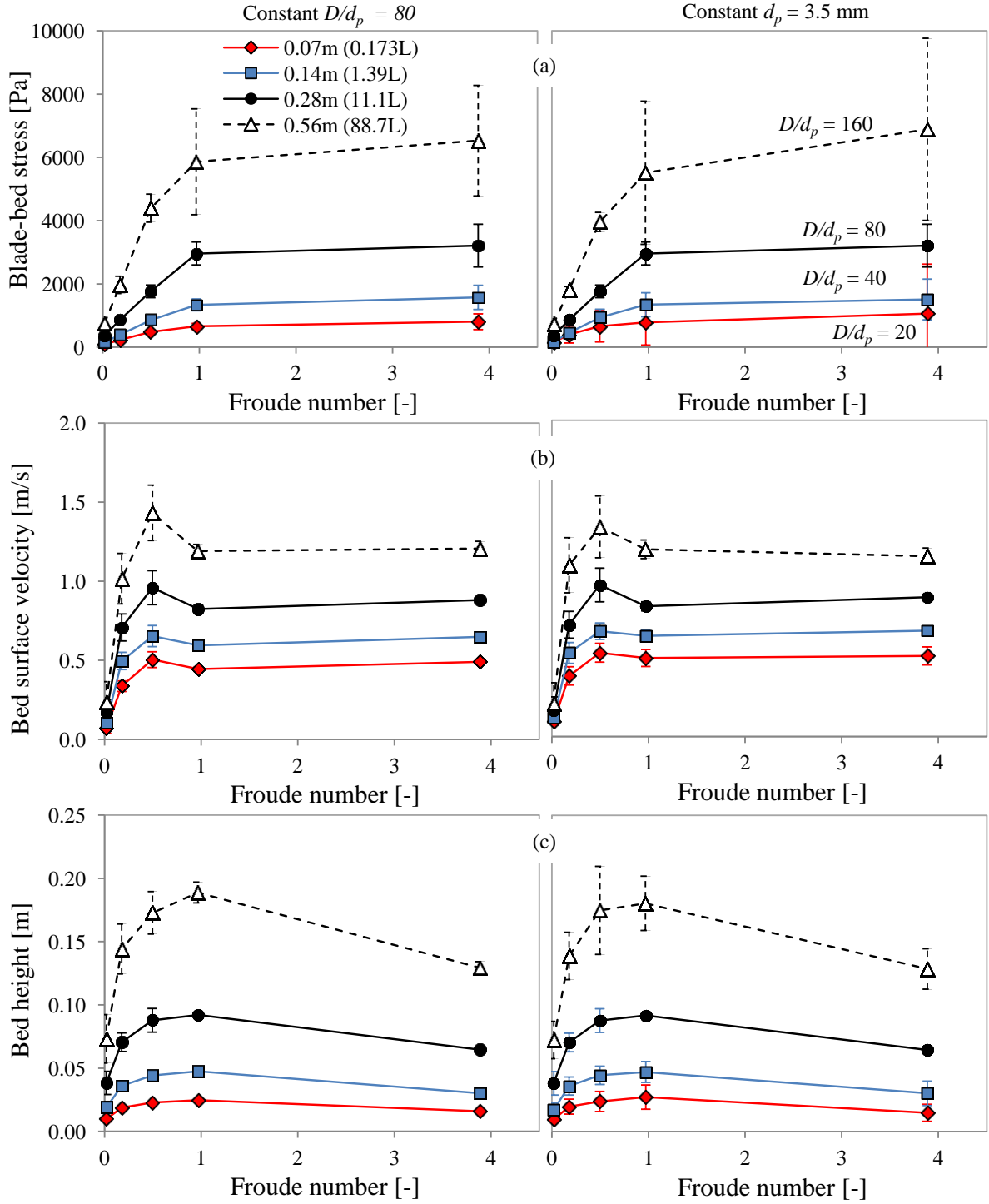


Figure 6.41: Simulated time-averaged data for different granulator scales (a) blade–bed stress (b) bed surface velocity (circumferential) and (c) bed height. Left column: constant D/d_p , right column: constant d_p .

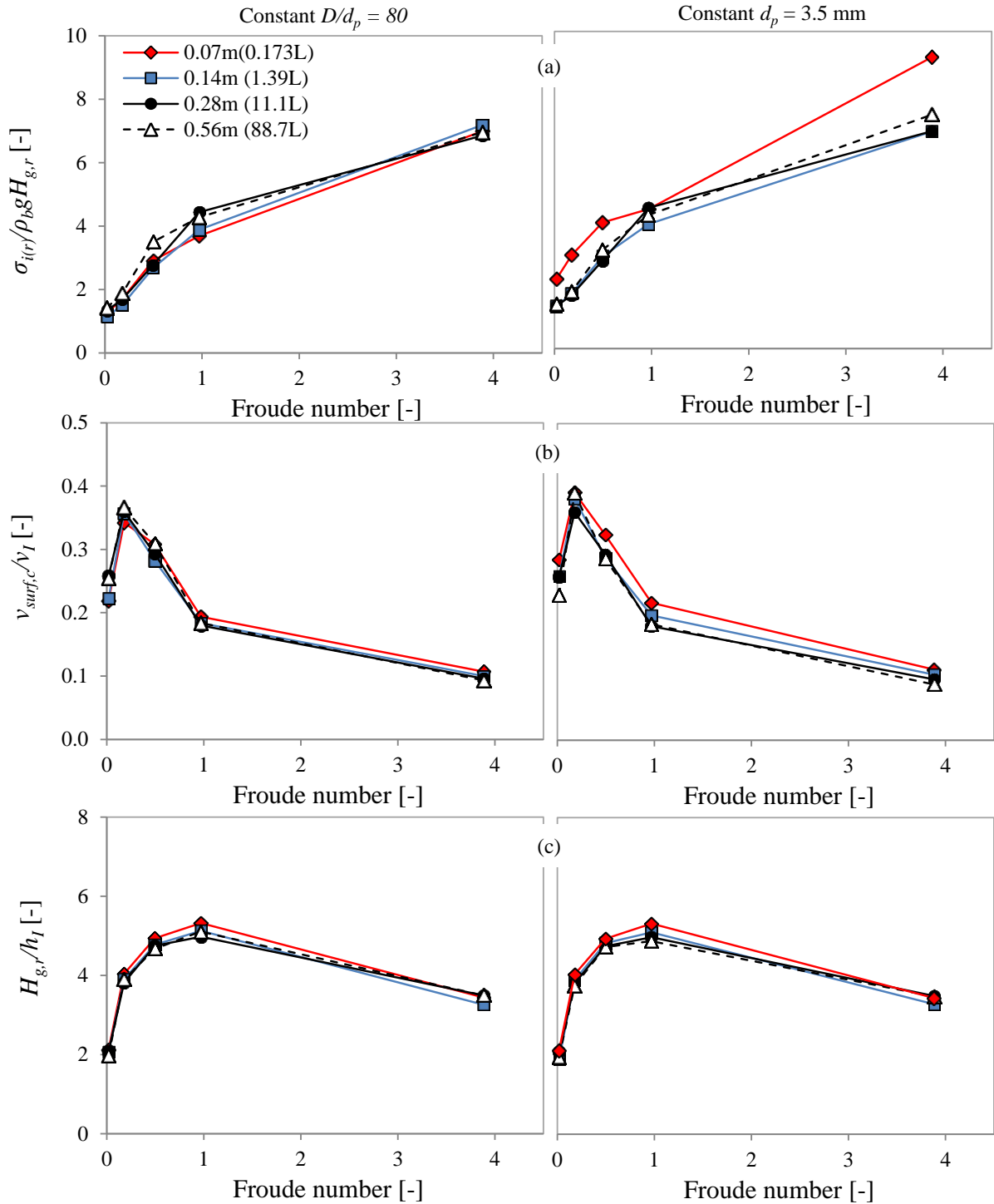


Figure 6.42: Scaled parameters for different simulated granulator scales (a) normalised blade-bed stress (b) bed surface velocity (circumferential) to impeller linear velocity ratio (c) bed height to blade inclined height ratio. Left column: constant D/d_p , right column: constant d_p .

6.8 Blade-bed stress prediction from theory

In Chapter 4 (Section 4.5) and Chapter 5 (Section 5.2.3), it was shown that the blade-bed stress equation with a correction factor to account for the increasing “fluidisation” of the bed and use of the surface velocity could reasonably predict the blade-bed stress for different bed loads, granule/particle sieve size, particle density and liquid content for impeller speeds up to 350 rpm ($Fr: 0.97$). In this section, the simulation results are applied to study and validate the blade-bed stress equation predictions particularly at higher impeller speeds (i.e. up to 700 rpm or $Fr: 3.88$) which is not attainable in the experiments and for the other particle/particle bed properties, impeller geometries and granulator scales simulated and discussed in the previous sections.

6.8.1 Predictions using different bed heights

The blade-bed stress predictions from theory are first studied for the different types of bed heights used, i.e. bed height at the wall or the sensor region-averaged bed height, particularly since in the experiments, the bed height at the wall is used because the sensor region-averaged bed height is difficult to determine experimentally. Figure 6.43 presents the simulated time-averaged blade-bed stress values for the 1.5 kg bed of 3.5 mm particles and the predicted values from Equation 4.8, i.e. without any correction factor using either the simulated bed height at the wall (black dashed lines) or the simulated sensor region averaged-bed height values (red dotted lines) as the $H_{g,r}$ values. Also included in the same plot for comparison are the experimental results for the 1-2 mm mannitol granules from Chapter 4, which are similar to the simulated values as validated earlier in Section 6.5. In Figure 6.43, the blade-bed stress equation over-predicts the simulated average blade-bed stress values after about 150 rpm, equivalent to that obtained from the experimental results in Figure 4.10 of Chapter 4. In addition, due to the higher bed height at the wall compared to the sensor region-averaged bed height, larger predicted values are shown when using the bed height at the wall (black dashed lines).

The correction factor B_l is then applied to the blade-bed stress equation (Equation 4.9) for the flow regime and surface velocity correction as explained in Chapter 4 and Chapter 5, which is taken to be proportional to the inverse of the relative velocities (Equation 4.11). Figure 6.44

plots the fitted B_I versus $1/v_{rel}$ for different bed loads using either the bed height at the wall (Figure 6.44a) or the sensor region-averaged bed height (Figure 6.44b). The proportionality constant, K_I , using the bed height at the wall (Figure 6.44a) is 1.1, reasonably similar to $K_I \approx 1$ obtained in the previous chapters from the experiments; while K_I increases to ~ 1.4 when the sensor averaged-bed height is used (Figure 6.44b).

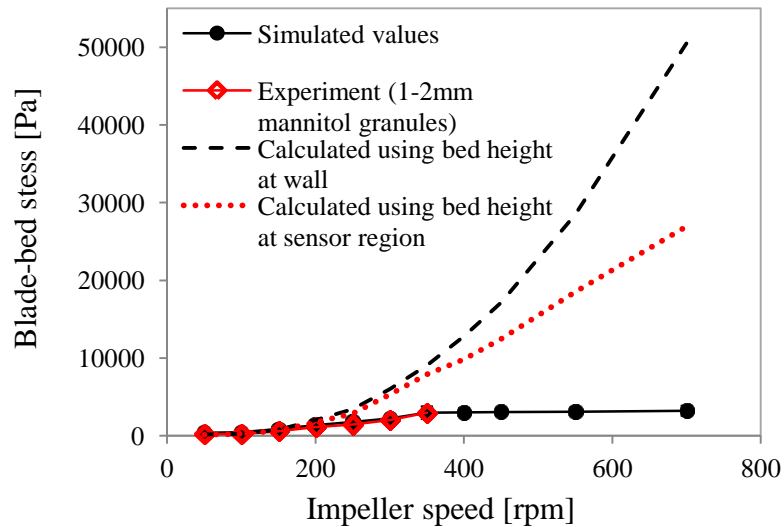


Figure 6.43: Comparison of the calculated blade–bed stress with no correction factor (Equation 4.8) using either the simulated bed height at the wall or sensor region-averaged bed height, with the simulated blade-bed stress for the 3.5 mm particles, 1.5 kg bed. The measured blade-bed stresses for the 1-2 mm sieve size mannitol granule are also included in the plot.

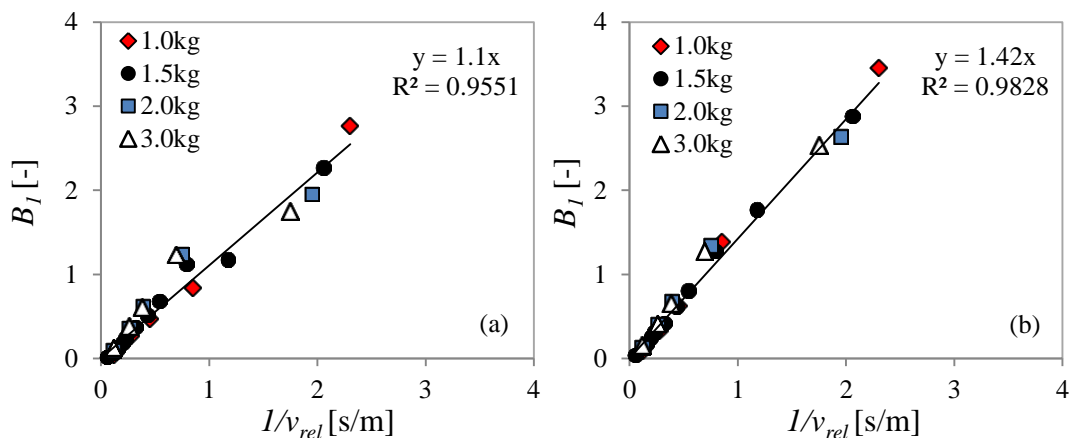


Figure 6.44: Plot of B_I versus $1/v_{rel}$ for different simulated bed loads using the (a) bed height at the wall and the (b) sensor region-averaged bed height.

Figure 6.45 now compares the simulated values with predicted values using the blade-bed stress equation with the correction factor (Equation 4.9), again using either the bed height at the wall ($K_I = 1.1$) or the sensor region averaged bed height ($K_I = 1.4$), for the different bed loads. Both the bed heights can be used to predict the blade-bed stresses at all bed loads up to 350 rpm, but beyond this impeller speed, using the bed height at the wall still over-predicts the stress for the 1.0, 1.5 and 2.0 kg bed loads. This is simply because of the steep bed height reductions from the wall towards the centre for impeller speeds above 350 rpm at these bed loads (Figure 6.28) and, therefore, the sensor region averaged-bed height does not correlate with the bed height at the wall. From this, it should be noted that using the bed height at the wall in the experiments beyond 350 rpm could have overestimated the blade-bed stress at the sensor region unless the bed load is large enough, i.e. for the 3.0 kg bed load case from the simulations. Also, for subsequent blade-bed stress predictions of the simulation results in the following sections, the sensor region-averaged bed height will be used.

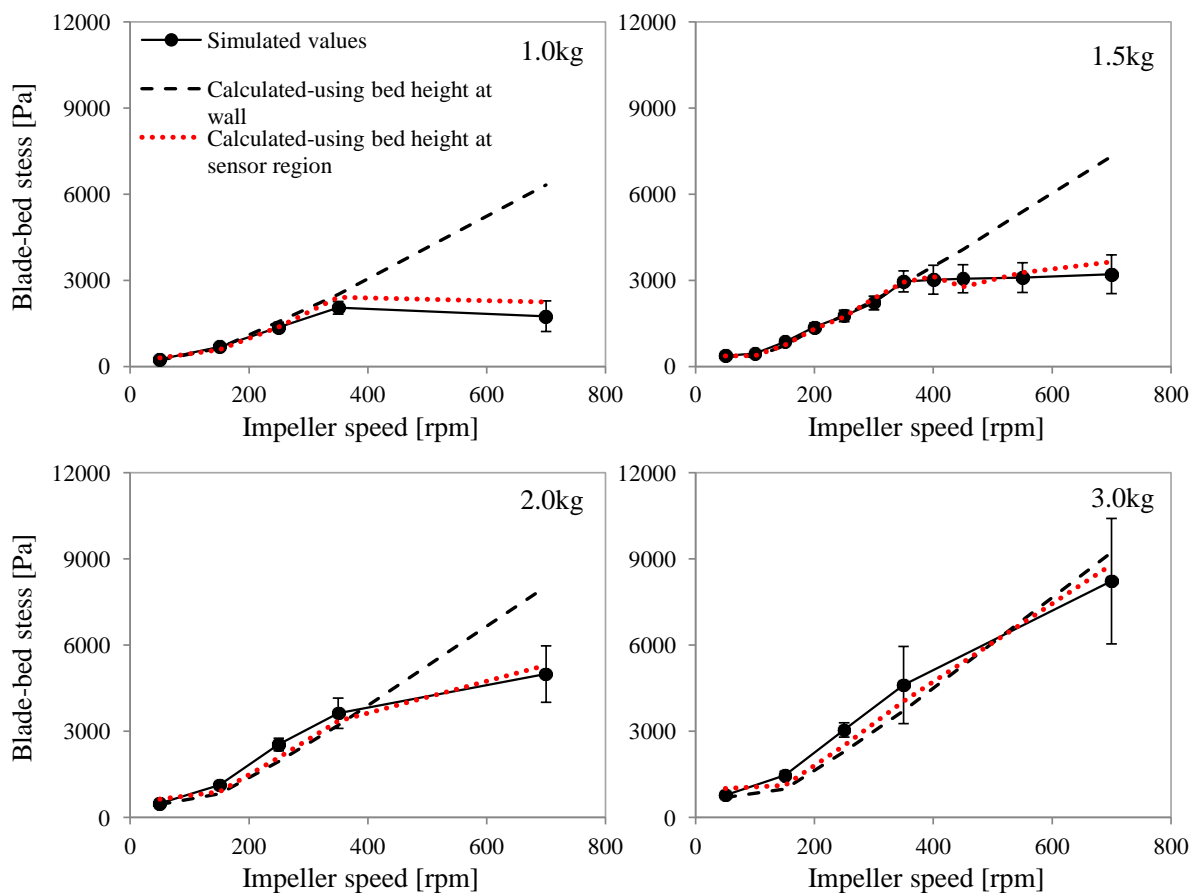


Figure 6.45: Comparison of the calculated blade-bed stress with correction factor B_I (Equation 4.9) with the simulated blade-bed stress at different bed loads.

6.8.2 Fittings for different parameters

Figure 6.46 and Figure 6.47 present fitted B_I versus I/v_{rel} plots for other particle/particle bed properties, impeller geometries and granulator scales, using the sensor region-averaged bed heights. Similar K_I values (~ 1.4) are obtained for different bed loads (Figure 6.46a), particle size (Figure 6.46b), particle density (Figure 6.46c), interparticle sliding friction coefficient (Figure 6.46d) and number of blades (Figure 6.47a). Different K_I values however, are obtained for the blade angle, blade width and granulator scale cases (Figure 6.47b-d).

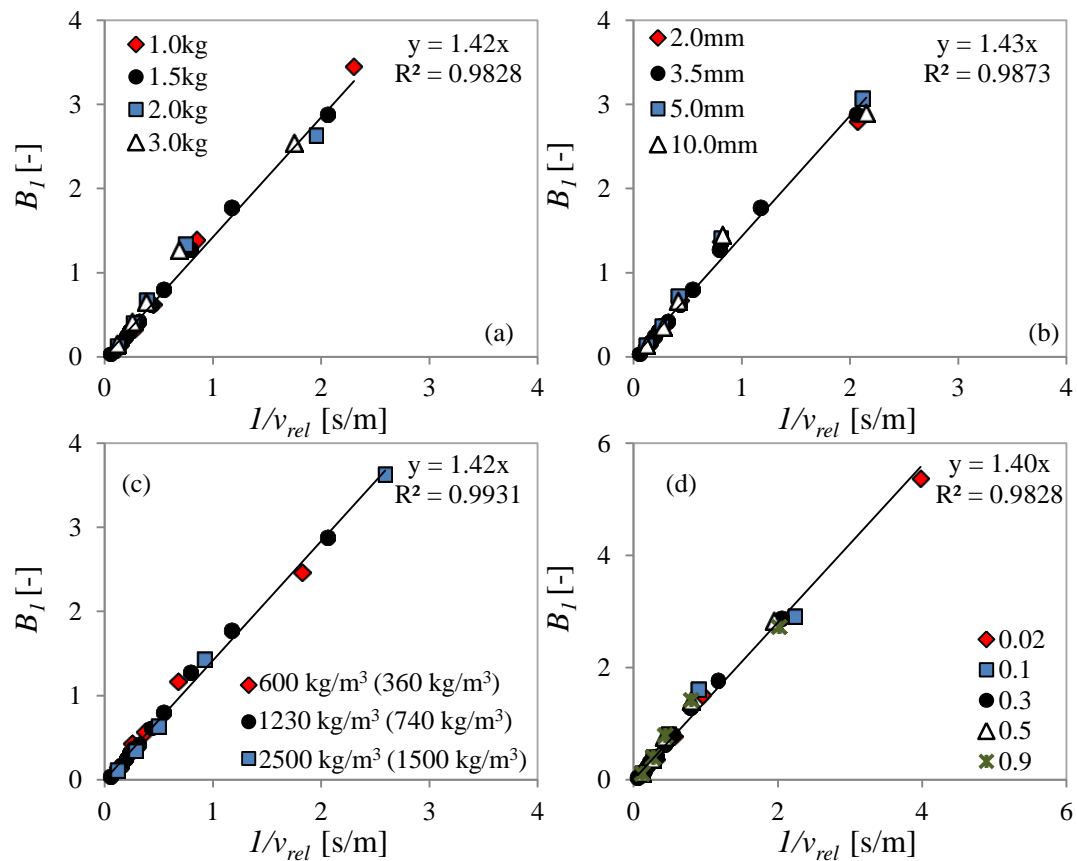


Figure 6.46: Plot of B_I versus I/v_{rel} for different simulated particle bed/particle properties (a) bed load (b) particle size (c) particle density (bed bulk density in brackets) and (d) interparticle sliding friction coefficient.

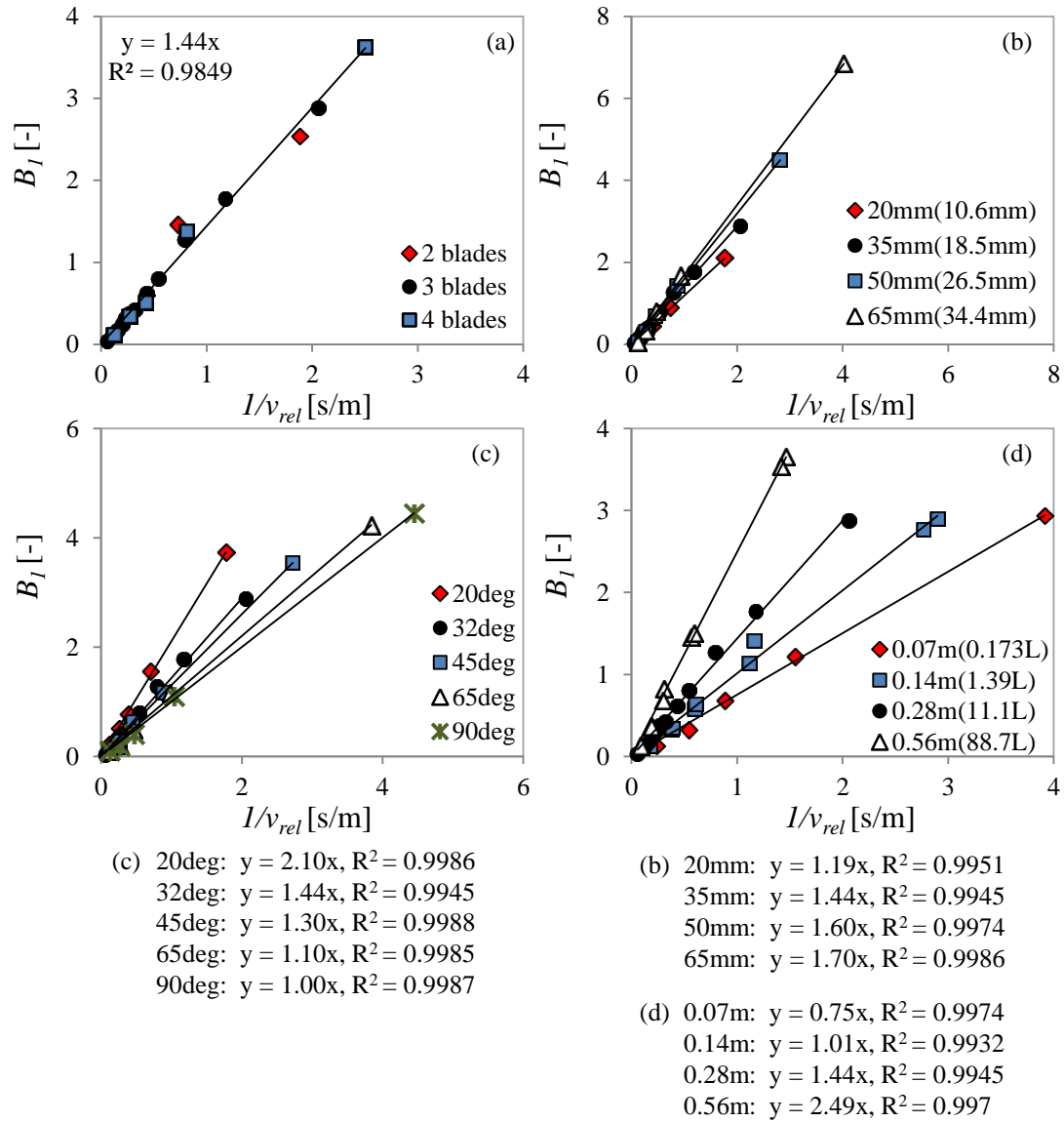


Figure 6.47: Plot of B_I versus $1/v_{rel}$ for different simulated impeller geometries and granulator scales (a) number of blades (b) blade width (blade inclined height in brackets) (c) blade angle and (d) granulator scales.

For the different granulator scales, the fitted B_I values are similar when the Froude number is the same for different scales. However, the relative velocities vary across scales with the same Froude numbers (Figure 6.48a). Knight and co-workers previously introduced a relative Froude number term ($Fr_{rel}^{0.5}$) (Equation 6.24) to account for the relative motion between the impeller and the granule bed for impeller torque predictions in a high shear granulator (Knight et al., 2001). Figure 6.48b plots the $Fr_{rel}^{0.5}$ across the Froude numbers (impeller) from the simulation results which are now similar across the scales, thus showing that instead of the relative velocities, the correction parameter should be related to this relative Froude number. Meanwhile, for different blade widths, the K_I value differences can be accounted by the larger blade-bed force with increasing blade width (Figure 6.35) due to increased particle-bed contacts. The blade-bed force and hence stress derived previously in Chapter 4: Section 4.2.2 (Equation 4.6) does not consider the change in force due to the blade width.

$$Fr_{rel}^{0.5} = \frac{(\omega_I - \omega_g)\sqrt{D}}{\sqrt{g}} = \frac{(v_I - v_g)}{\pi\sqrt{D}\sqrt{g}}$$

Equation 6.24

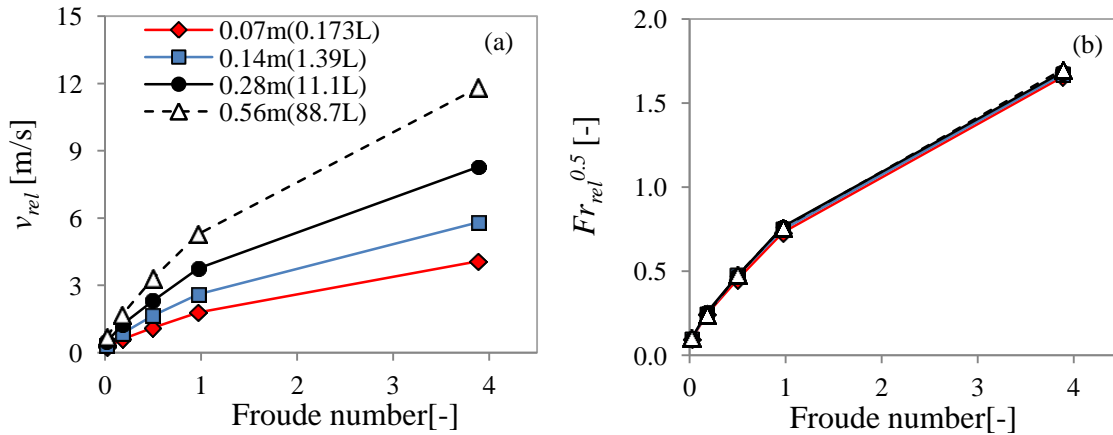


Figure 6.48: Results of (a) relative velocity, v_{rel} , and (b) relative Froude number, $Fr_{rel}^{0.5}$, for different granulator scales.

Considering the aforementioned factors, a modified correction parameter is applied to the blade-bed stress equation (Equation 6.25 and Equation 6.26). This correction parameter is proportional to (a) the inverse of square root of the relative Froude number, $Fr_{rel}^{0.5}$, between the impeller blade and the granule bed surface (to account for different granulator scales) and (b)

the ratio of the blade width, h_w , to the impeller radius, R (or $D/2$), to the power of n (to account for different blade widths). Note that the blade width, h_w , rather the blade inclined height, h_l , is used since different angled blades would also give different h_l values (Figure 6.6). For the blade width correction term, fitting of the simulated blade width results give a value of the exponent, $n \sim 0.3$ (refer to Figure D.16 in Appendix D: Section D.2.1 for the fitting plot).

$$\sigma_{i(r)cor} = \frac{B_2 \rho_b H_{g,r} v_{rel}^2 (1 - \cos\theta_l)}{h_l}$$

Equation 6.25

$$B_2 = K_2 \frac{1}{Fr_{rel}^{0.5}} \left(\frac{h_w}{D/2} \right)^n$$

Equation 6.26

Figure 6.49 and Figure 6.50 now present plots for the modified correction parameter, B_2 with $(2h_w/D)^{0.3}/Fr_{rel}^{0.5}$ for the different particle/particle bed properties, impeller geometries and granulator scales. Results for both the granulator scales and blade widths (Figure 6.50b&d) now collapse into single lines and the proportionality constant values, K_2 are 0.42-0.46 for most cases. Different K_2 values are still obtained for different angled blades (Figure 6.50c). This suggests further characterisation for different blade angles but in the scope of this work, a power law relationship between K_2 and the blade angle is given in Figure 6.51.

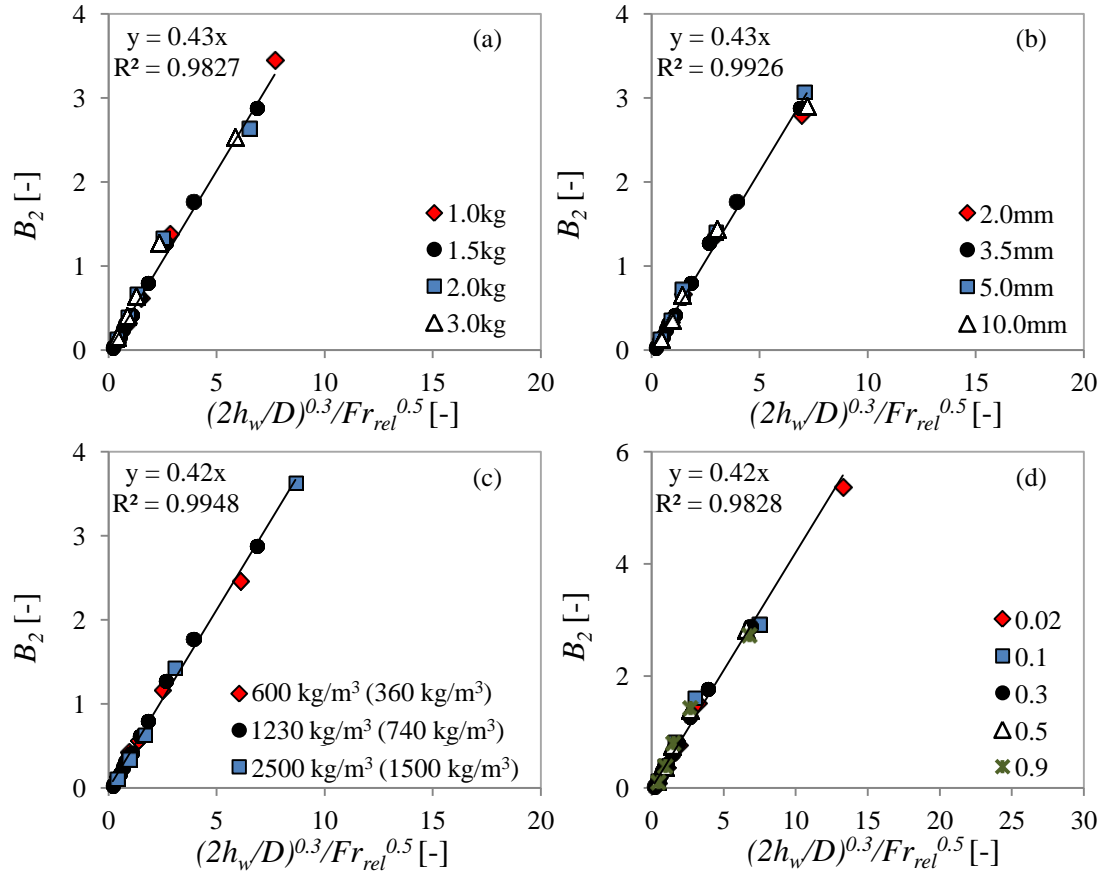


Figure 6.49: Plot of B_2 versus $(2h_w/D)^{0.3}/Fr_{rel}^{0.5}$ for different simulated particle bed/particle properties (a) bed load (b) particle size (c) particle density (bed bulk density in brackets) and (d) interparticle sliding friction coefficient.

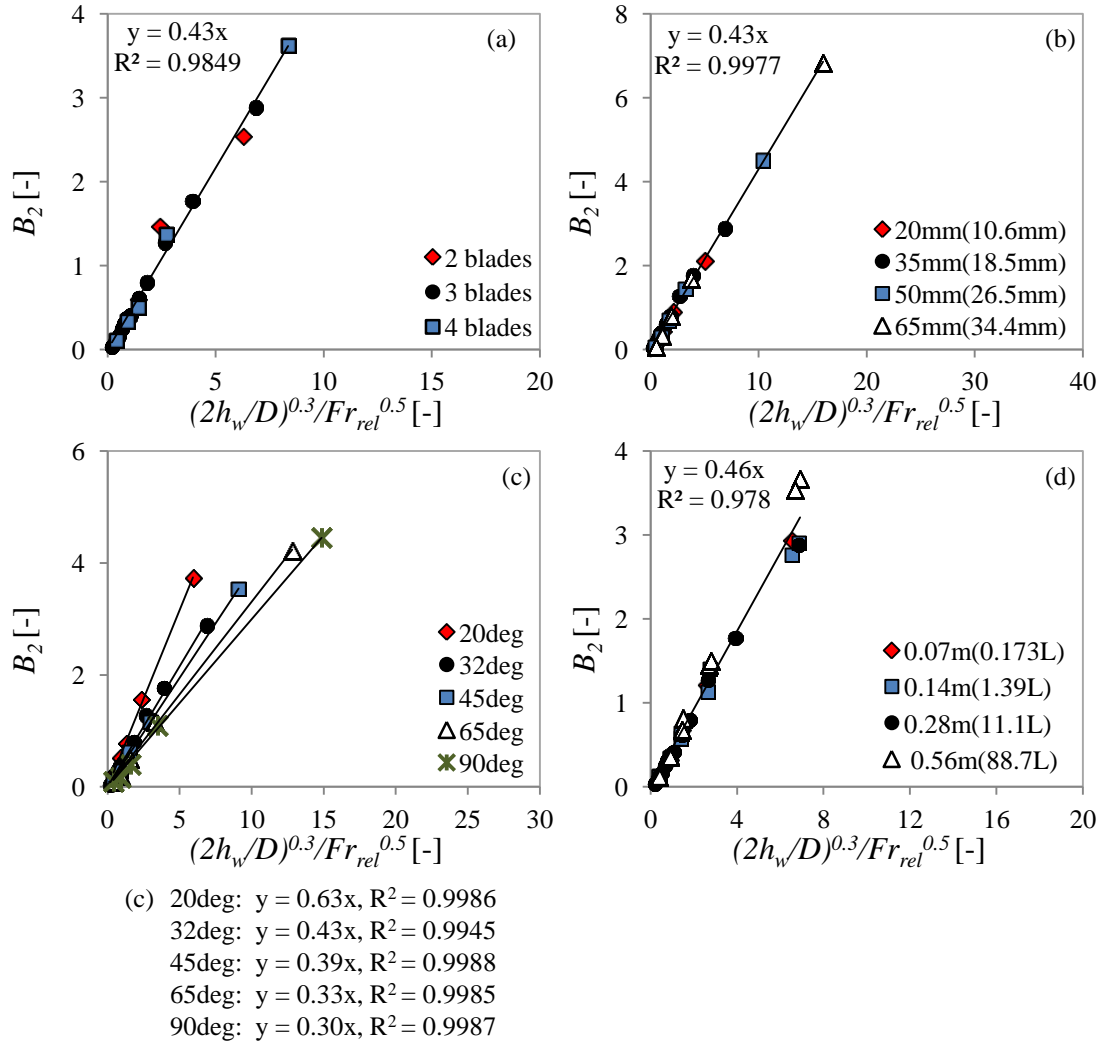


Figure 6.50: Plot of B_2 versus $(2h_w/D)^{0.3}/Fr_{rel}^{0.5}$ for different simulated impeller geometries and granulator scales (a) number of blades (b) blade width (blade inclined height in brackets) (c) blade angle and (d) granulator scales.

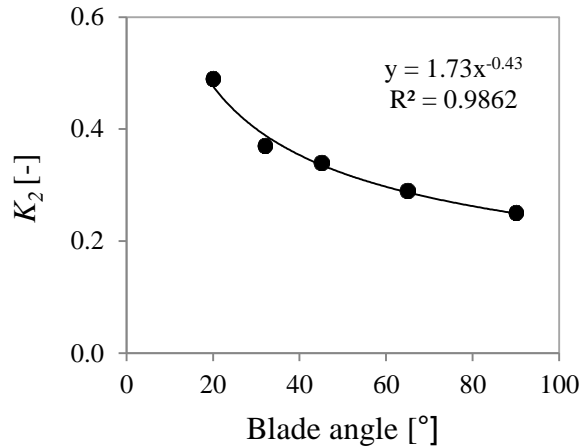


Figure 6.51: Variation of K_2 values with blade angle.

6.8.3 Predictions using different bed velocities

In Chapter 4: Section 4.5, it was deduced that one of the factors that contributes to the over-prediction of the blade-bed stress after toroidal flow is achieved, is the use of the bed surface velocity instead of the average velocity of a granule block, i.e. bed height-averaged velocity, and the other being the increasing “fluidisation” of the bed. Here, Figure 6.52 shows comparisons of the blade-bed stress predictions without any correction factors (Equation 4.8) when using either the simulated bed surface velocity (red dotted lines) or bed height-averaged velocities (black dashed lines), with the simulated blade-bed stress for the 1.5 kg bed of 3.5 mm particles. Also, the sensor region-averaged bed height is used in the equation. The predicted stress values using the bed height-averaged velocities are still over-predicted after 200 rpm.

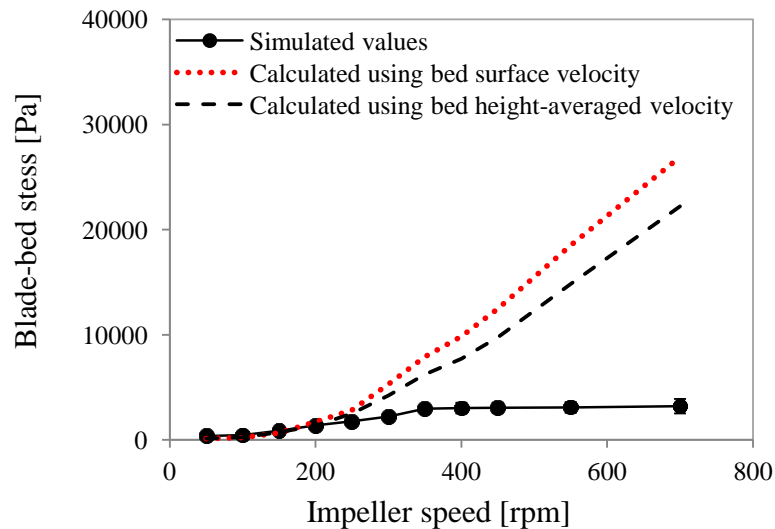


Figure 6.52: Comparison of the calculated blade–bed stress with no correction factor (Equation 4.8) using either the simulated bed surface velocity or bed height-averaged velocity, with the simulated blade-bed stress for the 3.5 mm particles, 1.5 kg bed.

In all of the simulation cases discussed in the previous sections, the largest difference between the bed height-averaged velocity and the surface velocity are mostly observed at the highest studied impeller speed (700 rpm) or Froude number (3.88), i.e. ~ 2 times higher (can also be seen in Figure 6.25). This gives the largest v_{rel} and v_{rel}^2 differences of $\sim 10\%$ and $\sim 20\%$ respectively. Consequently, the largest difference of the predicted blade-bed stresses without the correction factor is $\sim 20\%$ at Fr : 3.88. Additionally, when the correction factor B_2 (Equation

6.25 and Equation 6.26) is applied, the averaged fitted K_2 values across the impeller speed or Froude number ranges are similar regardless of which velocity values are used. Figure 6.53 and Figure 6.54 show the fittings using the bed height-averaged velocity in Equation 6.25 and Equation 6.26. It is reasonable to conclude from these results that the dominant factor in the over-prediction of blade-bed stress with increasing impeller speeds or Froude numbers is due to the increasing “fluidisation” of the bed, rather than the use of the surface velocity.

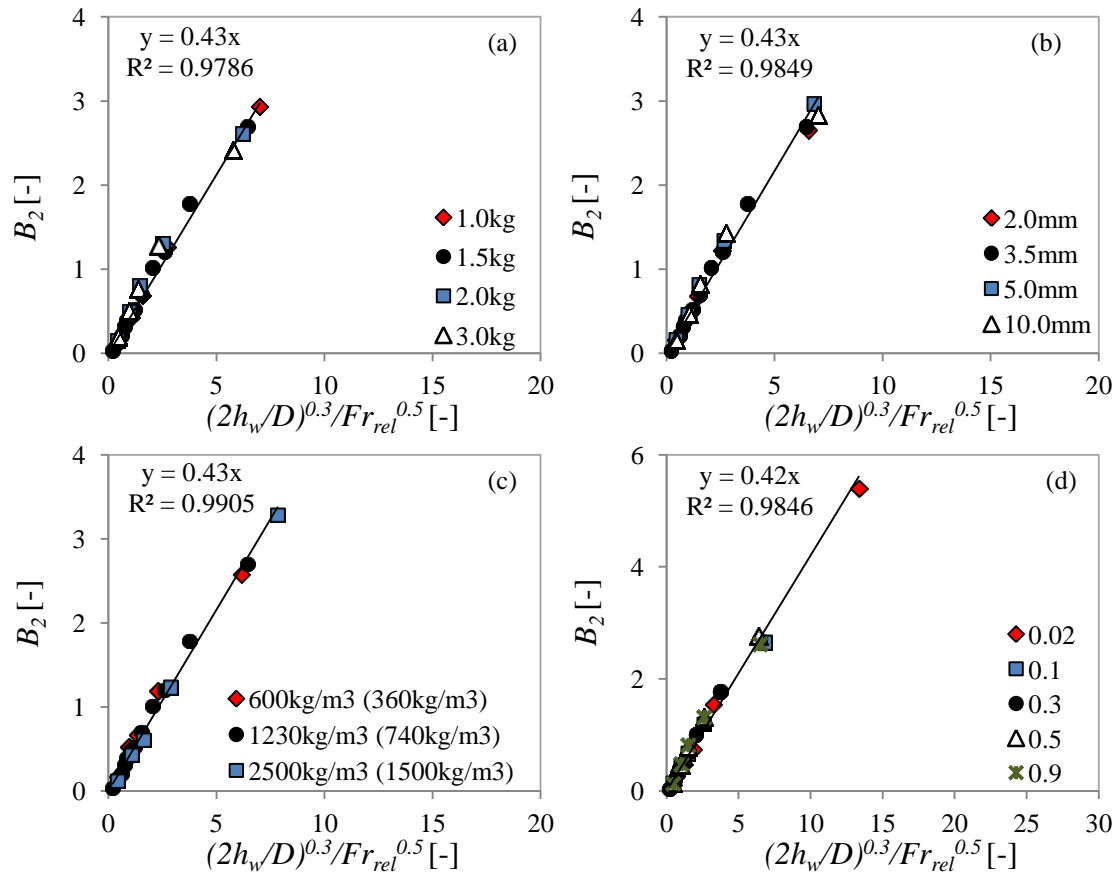


Figure 6.53: Plot of B_2 versus $(2h_w/D)^{0.3}/Fr_{rel}^{0.5}$ using the simulated bed height-averaged velocities for different simulated particle bed/particle properties (a) bed load (b) particle size (c) particle density (bed bulk density in brackets) and (d) interparticle sliding friction coefficient.

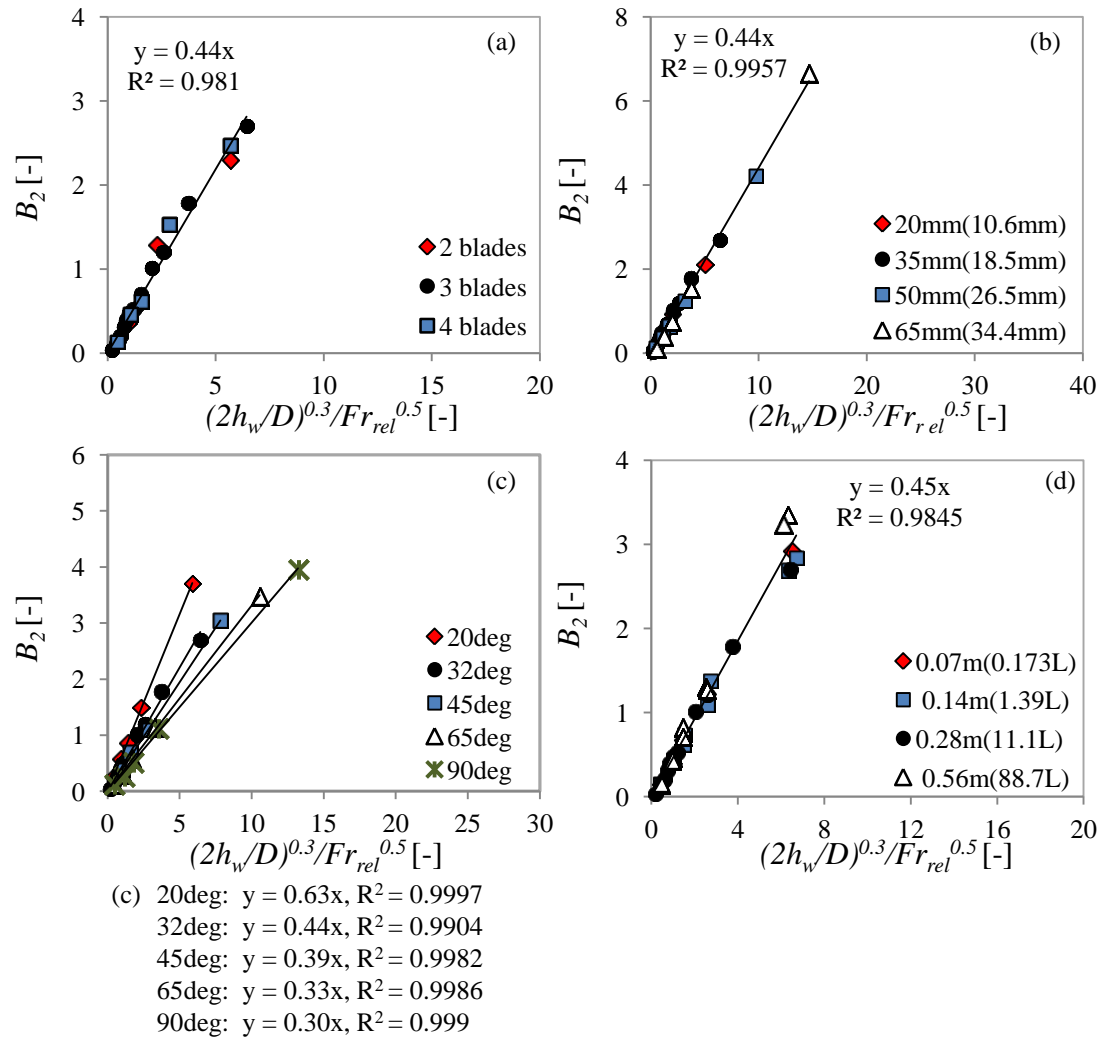


Figure 6.54: Plot of B_2 versus $(2h_w/D)^{0.3}/Fr_{rel}^{0.5}$ using the simulated bed height-averaged velocities for different simulated impeller geometries and granulator scales (a) number of blades (b) blade width (blade inclined height in brackets) (c) blade angle and (d) granulator scales.

6.9 Chapter summary and conclusions

This chapter has focused on DEM simulations of the high shear granulator, thus enabling further parameter study for the blade-bed stress characterisation, especially those that could not be studied experimentally and for a larger impeller speed range. The main achievements of this chapter are given as follows:

- Comparison between the simulations and experiments show that the DEM contact models employed can reasonably predict the temporal characteristics and time-averaged values of the blade-bed stress, bed surface velocity and bed height, even with assumed reasonable values of the interparticle friction coefficients (0.3), restitution coefficient (0.3) and Poisson's ratio (0.25). Additionally, the simulations are validated with the experiments for impeller speeds up to 350 rpm (maximum in the experiments) and are subsequently applied further to study higher impeller speeds (i.e. up to 700 rpm or Fr : 3.88) to give a better range of the bed flow and hence, results obtainable in most real life, commercial granulators;
- With the simulations, the blade-bed stress, bed surface velocity and bed height along the radial position can be extracted. It is shown that the blade-bed stress variation along the radial position is very much affected by the bed height profile of the particle bed. Besides that, the variation of the surface velocity along the radial position is also found to differ according to the flow regime of the particle bed;
- While it was previously found from the experiments in Chapter 4 and Chapter 5 that the average blade-bed stress at the sensor region increases steadily with impeller speed up to 350 rpm, the simulation results show that the blade-bed stress could be constant/reduce with a further increase in impeller speed up to 700 rpm, such as for low bed fill level cases (i.e. small bed load or larger particle density). This depends on the sensor region-averaged bed height which is also found to decrease at 700 rpm for the aforementioned cases. The average bed surface velocity, on the other hand, does not change much after 350 rpm for most cases;
- Results from the simulations for all the studied cases/parameters are applied for the blade-bed stress predictions using the blade-bed stress equation with the correction factor B_I (Equation 4.9 and Equation 4.11) introduced in Chapter 4. A K_I value of 1.1 from fitting of the simulation results, close to the K_I value of about 1 from the experimental fittings in

Chapter 4 and Chapter 5, is obtained. However, the use of the corrected bed height, i.e. sensor-averaged bed height, instead of the bed height at the wall which was also used previously in experiments, is crucial for reasonable blade-bed stress predictions > 350 rpm impeller speeds (Fr : 0.97), especially at low bed fill levels;

- A modified correction parameter, B_2 (Equation 6.25 and Equation 6.26) which is related to the inverse of the relative Froude number and the blade width to impeller radius ratio, is applied to consider the effect of different granulator scales and blade width. Improved fitting constants, K_2 , for the modified correction parameter were obtained except for different blade angle cases, and a power law relationship between K_2 and the blade inclined angle is obtained. Table 6.7 presents a summary of the fitted K values for both correction parameters, B_1 and B_2 , for the different studied parameters using the corrected (sensor region-averaged) bed heights; and
- It was hypothesised previously in Chapter 4 that the blade-bed stress over-prediction with increasing impeller speeds is due to the use of bed surface velocity as the characteristic velocity and the increasing bed “fluidisation”, which reduces the effective bed weight carried by the blade. Comparisons of the bed surface velocity and bed height-averaged velocities results conclude that the usage of the bed surface velocity plays a small role in the blade-bed stress over-prediction and that the dominant factor is the increasing bed “fluidisation”.

Table 6.7: Summary of the fitted constants for the correction factors.

<i>Conditions/parameters</i>		$B_1 = K_1 \frac{1}{v_{rel}}$ (Equation 4.11)	$B_2 = K_2 \frac{1}{Fr_{rel}^{0.5}} \left(\frac{h_w}{D/2} \right)^{0.3}$ (Equation 6.26)
		K_1	K_2
Particle/ particle bed properties	Bed load	1.42	0.43
	Particle size	1.43	0.43
	Particle density	1.42	0.42
	Interparticle sliding friction coefficient	1.40	0.42
Impeller geometries	Blade width	1.19-1.70	0.43
	Blade angle	1.00-2.10	0.30-0.63
	Number of blades	1.44	0.43
Granulator scale		0.75-2.49	0.46

Other findings from the parameter study of the effect of particle/particle bed properties, impeller geometries and granulator scale can be summarised as follows:

- Particle/particle bed properties:
 - The effect of bed load, particle size and particle density on the average blade-bed stress, bed surface velocity and bed height are equivalent to that obtained from the experiments in Chapter 4.
 - The average blade-bed stress, surface velocity and bed height are similar for the studied restitution coefficients, for Young's modulus ≥ 1 MPa and interparticle sliding friction coefficient ≥ 0.3 . At low friction coefficients, smaller average blade-bed stresses and faster bed surface motion are obtained due to less frictional dissipation of the kinetic energy.
- Impeller geometries:
 - A larger blade width or inclined height gives increased blade-bed interactions, and thus total blade-bed forces. The average blade-bed stress however, reduces due to a larger blade-bed impact area. The average bed surface velocity and height increases with the blade width (smaller H_{g0}/h_I) from the larger bed acceleration and deflection.
 - A larger blade inclined angle increases the average blade-bed stress. Like the blade width cases, larger average bed surface velocities and heights are obtained for the more inclined blades (smaller H_{g0}/h_I) because of the larger bed acceleration and deflection.
 - The average blade-bed stress is similar for 2 to 4 bladed impellers, except at 700 rpm. The average bed surface velocity and bed height are also generally similar for the different number of blades, although the 2-bladed impeller showed significantly higher surface velocity and bed height fluctuations from 150-350 rpm (i.e. a more turbulent surface motion at these impeller speeds).
- Granulator scales:
 - Similar flow behaviours are obtained at the studied granulator scales when keeping the Froude number constant, for cases where the mixer diameter to particle diameter ratio (D/d_p) is ≥ 40 . Also for $D/d_p \geq 40$, the average blade-bed stress, bed surface velocity and bed height can be scaled with the bed bulk pressure, impeller linear velocity and blade inclined height respectively.

Chapter 7

Further insight: variability studies across flow regimes

7.1 Introduction

This chapter constitutes studies of the behaviour of dry and wet steady-state beds in each identified flow regime (i.e. frictional, toroidal and fluidised) in the Roto Junior. In Chapter 4, Chapter 5 and Chapter 6, the blade-granule bed stress, bed surface velocity and bed height were mostly discussed in terms of the time-averaged values for the different conditions or parameter change. Also in Chapter 4 (Figure 4.6), it was highlighted that the granule bed transits through several flow regimes with increasing impeller speeds. Therefore, in this chapter, the changes in the blade-bed stress and bed surface behaviour in each flow regime are studied, concentrating on the variability/fluctuation of the temporal values. Contents of this chapter are presented in the following order:

- Brief review of previous granule bed flow studies in vertical axis, cylindrical high shear granulators;
- Materials and methodology used;
- Description of the granule/particle bed flow regimes;
- Results and discussions on the bed surface behaviour (from the bed surface velocities and bed height) across flow regimes; and
- Results and discussions on the blade-bed stress across flow regimes.

7.2 Flow studies

Despite the simple geometry of cylindrical mixers, the flow of the granule bed in these mixers is in fact, quite complicated. The dominant movement of the granule bed is along the circumferential direction due to the blade motion. The flow pattern of the bed depends largely on the centrifugal force from the impeller rotational motion, the gravitational force from the bed load and also granule properties (frictional and cohesion properties) (Mort, 2009). Flow studies in bladed cylindrical mixers have been carried out by a considerable number of researchers, generally using high speed imaging to study the motion of the top or side surfaces

of the bed (Conway et al., 2005; Darelius et al., 2007; Dorvlo, 2009; Lekhal et al., 2006; Litster et al., 2002; Murugama et al., 2000; Nilpawar et al., 2006; Remy et al., 2010) or the PEPT (Particle Emission Positron Tracking) method to study the internal bed flow (Saito et al., 2011; Stewart et al., 2001; Wellm, 1997). Advances in computer simulations have also enabled the particle bed flow in cylindrical mixers to be studied via Discrete Element Method (DEM) (Conway et al., 2005; Remy et al., 2010; Remy and Glasser, 2010; Remy et al., 2009; Stewart et al., 2001; Zhou et al., 2004) or Computational Fluid Dynamics (CFD) (Darelius et al., 2008).

Litster and co-workers first separated the bed flow pattern in a cylindrical mixer into distinct regimes, i.e. bumping and toroidal (Litster et al., 2002). Transition between regimes takes place at a particular impeller speed or Froude number. In addition, equipment (mixer and blade) geometries and granule properties will also affect the transition (Litster et al., 2002; Remy et al., 2010). So far, the behaviour of the granule bed in each flow regime has only been discussed in terms of the powder or granule bed surface motion (Litster et al., 2002; Remy et al., 2010). In this chapter, both the bed surface behaviour (bed surface velocity and bed height) and the blade-granule bed interactions (blade-granule bed stress) in each flow regime are studied for dry and wet beds. DEM results for the blade-granule bed stresses were also used to gain further insight on the stress variability/fluctuation, especially since the impeller stress sensor system has a limited sampling frequency.

7.3 Materials and methodology

The granule bed behaviour across different flow regimes in the ~10 L Roto Junior high shear granulator was studied by analysing the temporal results of the blade-bed stress, bed surface velocity and bed height of the following:

- Dry, mannitol granule beds prepared and used in Chapter 4 with different sieve sizes and bed loads;
- Dry and wet beds of polypropylene balls used in Chapter 4 and Chapter 5; and
- Simulated dry particle beds presented in Chapter 6 for different particle/particle bed properties, blade geometries and granulator scales.

The "variability or fluctuation" of the temporal data are discussed in terms of the following:

- "Fluctuation amplitude" to look at the degree of fluctuation, quantitatively represented by the relative standard deviations (RSD), i.e. ratio of the standard deviation to the mean; and/or
- "Fluctuation periodicity" to look at the periodic (or lack of) behaviour of the temporal values, quantitatively represented by the frequency. The frequency is obtained from the peak frequencies in the power spectrum graph generated by Fast Fourier Transform (FFT) of the data sets.

7.4 Granule/particle bed flow regimes

7.4.1 Dry beds

For each granule sieve size and bed load, measurements were performed at impeller speeds of 50 to 350 rpm at 50 rpm intervals, with the exception of the 2.0-4.75 mm granules at high impeller speeds, due to attrition of granules at the blade-floor gaps as previously explained in Chapter 4. Across these impeller speeds, the bed profile changes (Figure 7.1). At 50 and 100 rpm, the granules occupy the entire area between the wall and the centre of the impeller as the blade moves slowly underneath the bed (Figure 7.1a). The surface of the bed is almost horizontal along the radial length of the mixer. From 150 to 250 rpm, granules are increasingly pushed to the mixer wall due to centrifugal effect resulting in a clear, empty space at the centre and an angled bed surface along the radial length (Figure 7.1b). Deflection of the bed surface due to the blade movement could still be clearly observed, also as indicated in Figure 7.1b. Finally, at 300 and 350 rpm a less distinct upwards deflection of the granule bed surface from the blade movement results in the granule bed shape resembling a torus (Figure 7.1c). At these impeller speeds, the bed becomes increasingly fluidised and lifts up from the swift movements of the blades underneath. Granules are continuously lifted up and then fall back onto the blades.

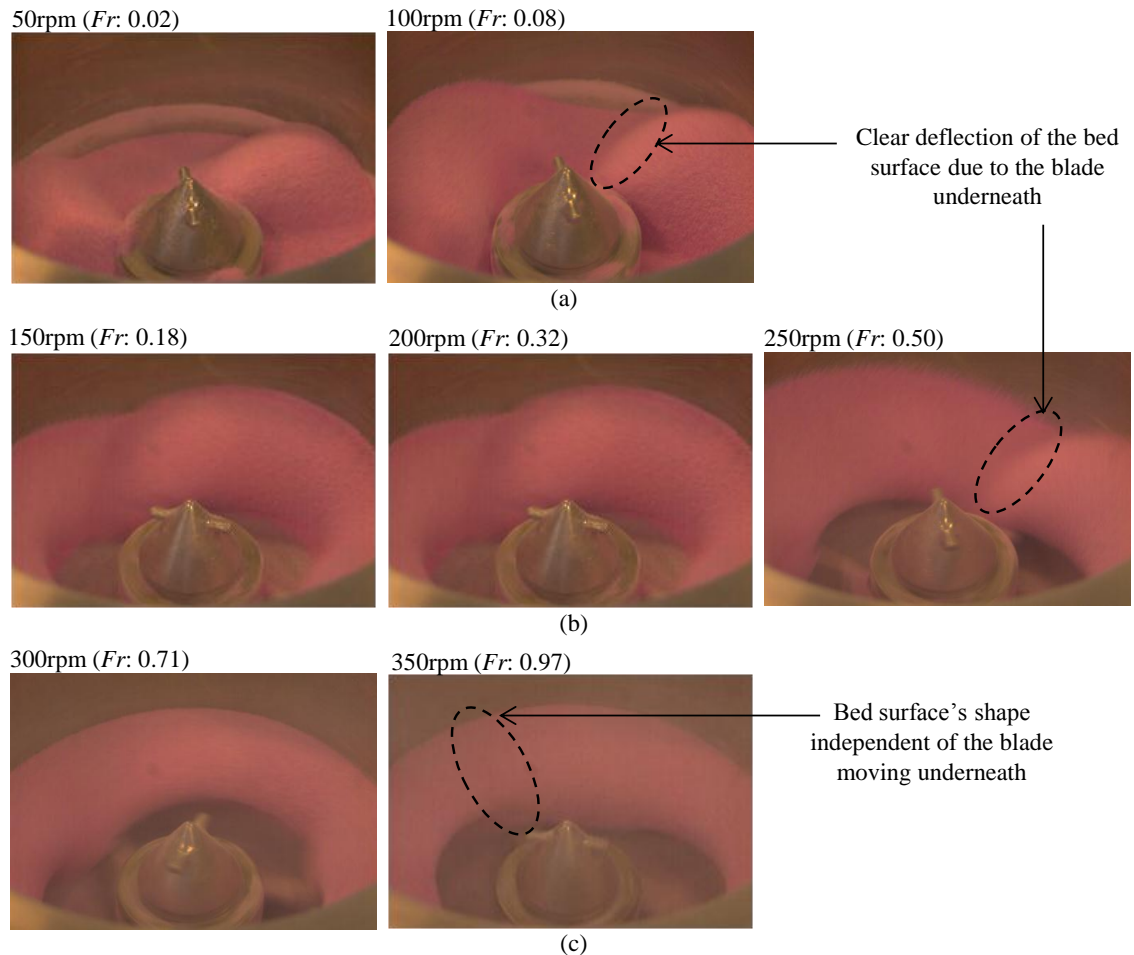


Figure 7.1: Granule bed flow regimes for 1.0-2.0 mm, 1.5 kg dry mannitol bed at different speeds/Froude number: (a) slow/frictional (b) toroidal and (c) fluidised.

Observation of different flow regimes in vertical axis high shear granulators have also been reported by several researchers. In Litster's work, the authors summarised and separated the granule bed flow into two distinct regimes (Litster et al., 2002). At low impeller speeds or Froude number, they described a similar flow pattern to that observed at 50 and 100 rpm in this work, where the bed surface remained horizontal as it moved up and down when the blade passed underneath. At higher speeds, the roping or toroidal behaviour was observed, where the bed moved upwards along the mixer wall and tumbled downwards at the free surface of the bed towards the centre, producing a rotating movement in a plane perpendicular to the blade's circumferential motion. This toroidal motion has been previously noted by several authors (Holm et al., 1996; Ramaker et al., 1998; Schaefer et al., 1993) and verified by PEPT measurements in Wellm's work (Wellm, 1997). Following Litster's work, other authors have

also studied and discussed the two regimes (Mort, 2009; Remy et al., 2010). In this work, the roping or toroidal pattern could be applied for the granule bed flow at impeller speeds of 150 rpm and above. As there was no specific mention or distinction of the fluidised behaviour in previous works, the flow at 300-350 rpm will be identified as the fluidised regime (Figure 7.1). Note that "fluidised" here indicates that the bed is increasingly lifted up while the bed surface becomes less sensitive to the blade motion, and is not analogous to the behaviour in fluidisation processes whereby fluid or gas is passed through a solid bed to change it to a dynamic fluid-like state. The flow behaviours at 50-100 rpm and 150-250 rpm are known as the slow/frictional and toroidal regimes respectively. In terms of Froude number (Equation 6.19), the flow regime transitions occur at Fr : 0.08-0.18 and Fr : 0.50-0.71.

7.4.2 Wet beds

For the wet beds, Figure 7.2 and Figure 7.3 display images of the dry and wet beds of polypropylene balls with increasing water content (total bed load: 1.5 kg). For the dry polypropylene balls, similar bed profiles to the dry mannitol beds (Figure 7.1) across the impeller speeds are observed, although at 250 rpm there is a less clear deflected or deformed bed surface from the blade motion. As described previously, with increasing amount of water added, the bed surfaces become more irregular and rough due to formation of clumps of material held loosely by the liquid. At low water contents, i.e. 2%w/w and 5%w/w water (Figure 7.2), the bed profiles and flow behaviours are overall similar to the dry bed, despite the increasing roughness of the bed surface. For higher water contents, i.e. 10-25%w/w water, unsteady bed motions (large bed deflection and surface motions) are observed at 250 rpm before they transit to the fluidised state at 350 rpm. In addition, there is also noticeable sticking of material at the granulator walls or wall make-up $\geq 10\%$ w/w water at 250 and 350 rpm. Also previously mentioned in Chapter 5, for these conditions, the bed height of the freely moving part of the particle bed is taken instead of the height of material sticking on the wall.

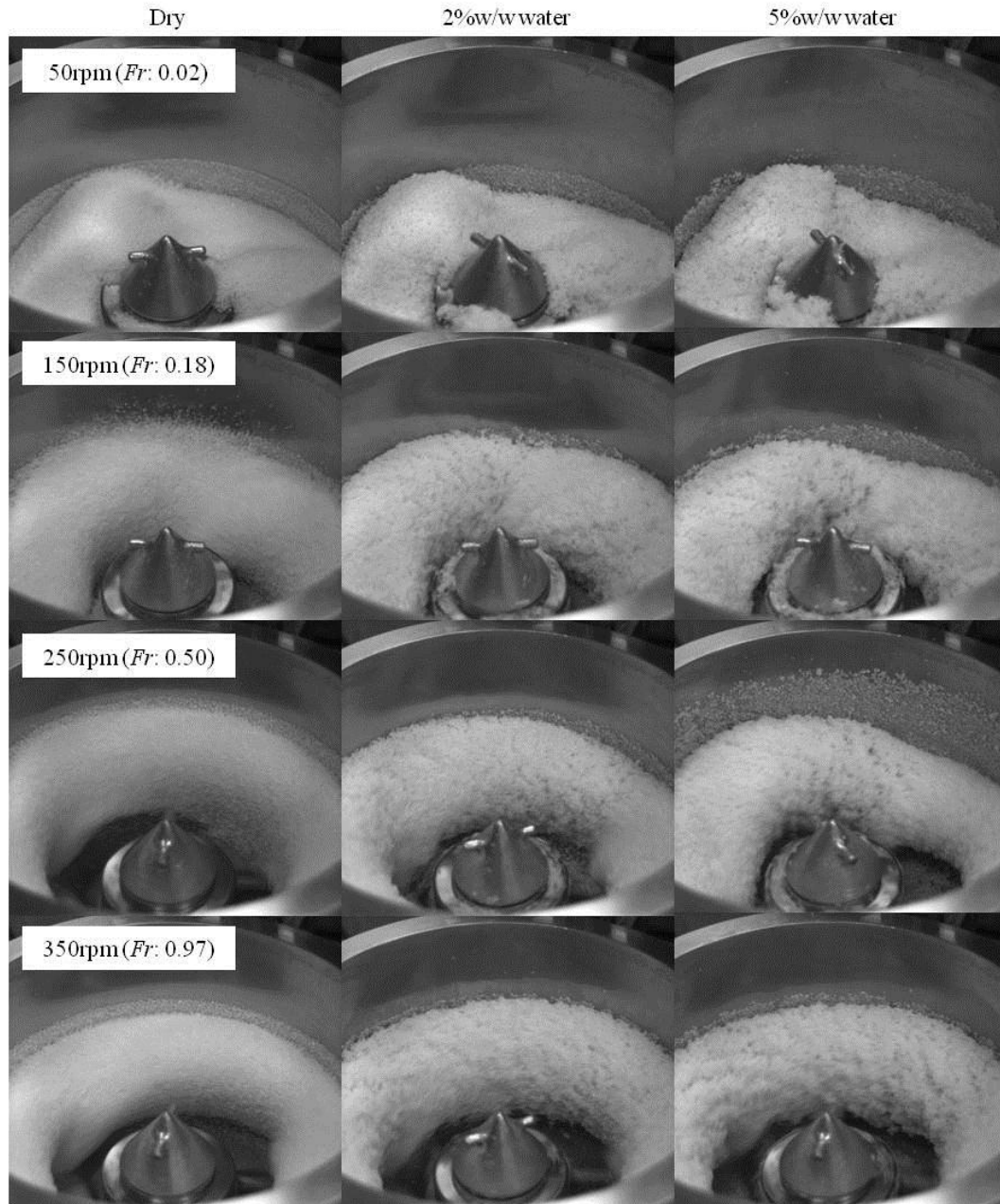


Figure 7.2: Bed flow images for 1.5 kg bed of dry and wet (2%w/w and 5%w/w water) polypropylene balls.

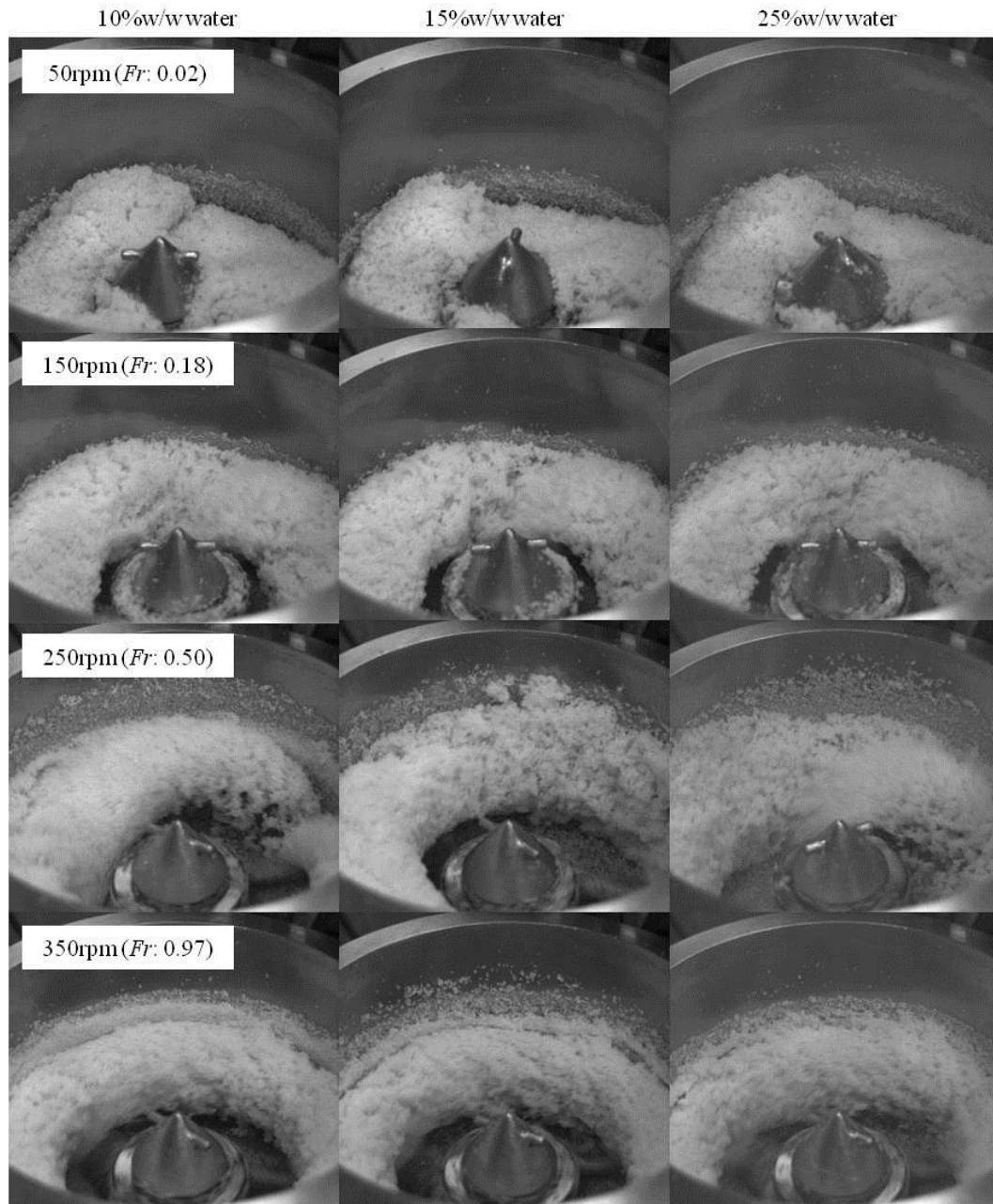


Figure 7.3: Bed flow images for 1.5 kg bed of wet (5%w/w, 15%w/w, and 25%w/w water) polypropylene balls.

7.5 Behaviour of the bed surface

7.5.1 Experimental bed surface velocity and bed height

7.5.1.1 Dry beds

The variability studies for bed surface velocity were carried out on the total bed surface velocity, $v_{surf,t}$, from the recorded high speed images (Chapter 3, Section 3.3.2: Figure 3.14) which includes both the circumferential, $v_{surf,c}$, and radial components, $v_{surf,r}$. Note that the time-averaged surface velocities presented previously in Chapter 4, Chapter 5 and Chapter 6 were only the circumferential components. Figure 7.4a-i,ii are typical plots of the temporal values of the total bed surface velocity, $v_{surf,t}$, which was spatially averaged over the observed region. The presented plots are for one of the dry mannitol granule beds with an intermediate bed load and granule sieve size, i.e. the 1.5 kg of 0.5-1.0 mm granule bed with an undisturbed bed height to blade inclined height ratio, H_{g0}/h_I , of 2. Figure 7.4b-i and Figure 7.4c-i show plots of the time-averaged values with the Froude number for the different granule sieve sizes and bed loads, with the error bars representing the standard deviation of the temporal values. The circumferential, $v_{surf,c}$, and radial components, $v_{surf,r}$, of the bed surface velocity are also presented in Figure 7.5. In all cases, the circumferential velocities are higher than the radial, reaffirming that the circumferential motion is dominant. The circumferential surface velocities of different sieve sizes are similar while an increase in the surface radial motion is observed for finer granules. With decreasing bed load, both the circumferential and radial surface velocities increase.

The increment of the time-averaged values and variability of the total bed surface velocity differs according to the flow regimes. First noted in Chapter 4: Section 4.4, the total bed surface velocity does not increase consistently with the Froude number or impeller speed, with the more apparent increase being observed in the frictional regime compared to the toroidal regime. This was also reported in Litster's work (Litster et al., 2002). The transition between the toroidal and fluidised flow is generally accompanied with a decrease in the surface velocities as the bed becomes increasingly lifted up and its surface becomes less sensitive to the motion of blade beneath. This is also corroborated by normalising the surface velocity with the impeller tip speed, v_{tip} , where it could be seen that $v_{surf,t}/v_{tip}$ generally increases in the frictional regime and then decreases in the toroidal and fluidised regime (Figure 7.4b-ii and Figure 7.4c-ii). Analysis of the fluctuation amplitude across the flow regimes, indicated by the relative

standard deviation (Figure 7.4a-iii), shows that the amplitude at 50 rpm ($Fr: 0.02$) is the largest as the bed only lifts up and moves when the blade passes through underneath. The fluctuation amplitude decreases until toroidal flow is reached at 150 rpm ($Fr: 0.18$), followed by an increase again up to 250 rpm ($Fr: 0.5$). At this point, the surface movement becomes most turbulent or unsteady. The amplitude then decreases in the fluidised regime. The transitions between flow regimes are largely similar across the sieve sizes and bed loads except for the smallest sieve size and bed load cases (0.1-0.5 mm and 1.0 kg beds) in this study. For finer granules or a lighter bed, transition from toroidal to fluidised flow occurs at a higher impeller speed (350 rpm, $Fr: 0.97$), reflecting an increased sensitivity to the blade motion.

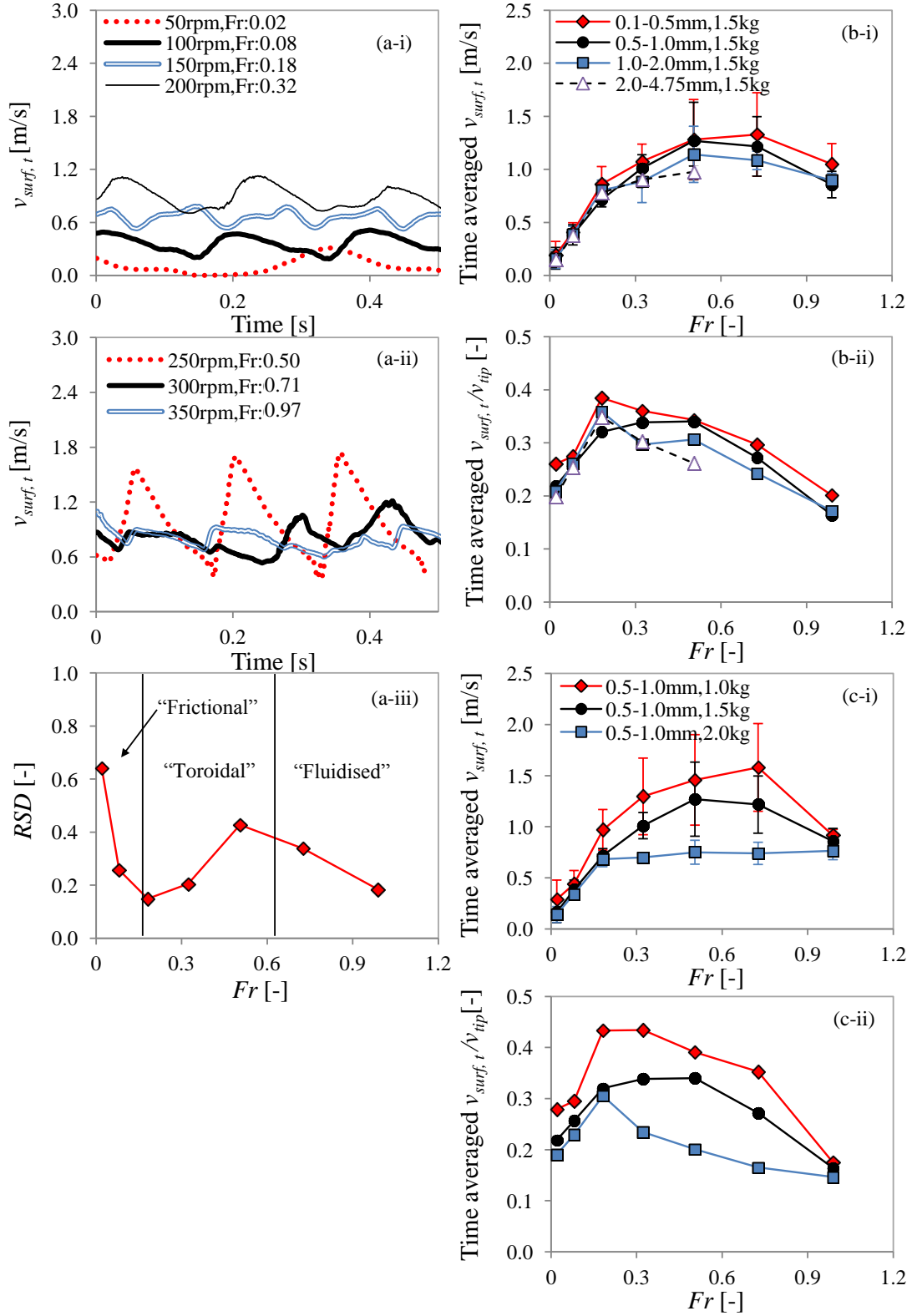


Figure 7.4: Total bed surface velocity ($v_{surf,t}$) results: (a) temporal values and RSD (relative standard deviation) for 0.5-1.0 mm, 1.5 kg granule bed (b) time-averaged values for different sieve sizes (i) actual values (ii) normalised values (c) time-averaged values for different bed loads (i) actual values (ii) normalised values.

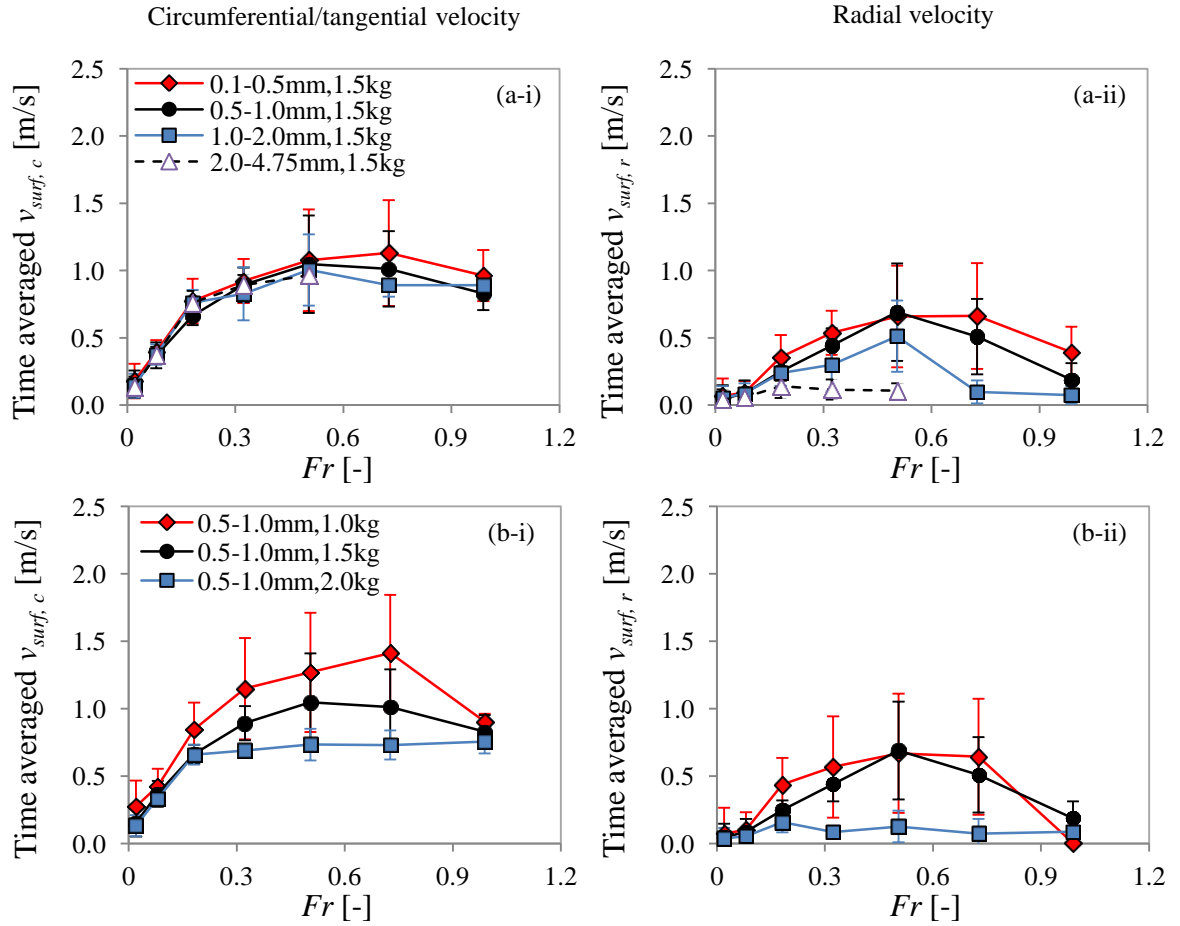


Figure 7.5: Circumferential ($v_{surf,c}$) and radial ($v_{surf,r}$) velocity results: (a) time-averaged values for different sieve sizes (b) time-averaged values for different bed loads

Plotting the total bed surface velocity with the impeller rotation (Figure 7.6) demonstrates the relationship between the motion of the bed surface and the blade. At impeller speeds up to 250 rpm (Fr : 0.50), a clear periodicity of the velocity fluctuations is observed. From 50 to 150 rpm (Fr : 0.02-0.18), three periodic fluctuations are obtained for each impeller rotation, conforming to the motion of the three blades passing through, thus accelerating the observed bed area. The frequency of the fluctuations corresponds to the single blade frequency, i.e. frequency of each blade pass, corroborated by FFT analyses carried out for the signals. An example of the power spectrum from the analysis is shown in Figure 7.6. For the 100 rpm case, the power spectrum yields a clear peak at the blade's frequency (5 Hz). The frequency of the bed surface velocity corresponding to the blade frequency has been observed in several reported works (Dorvlo, 2009; Nilpawar et al., 2006; Washino, 2011).

Interestingly, at 200 and 250 rpm (Fr : 0.32 and 0.50) the number of periodic fluctuations is halved for each impeller rotation, and Fourier analyses show that the frequency of the fluctuations corresponds to every two blade passes (see the FFT analysis of 200 rpm in Figure 7.6). After the sweep of the first blade, the bed is lifted and hence, not affected by the next blade sweep, only to be disturbed again by the following blade and so on. A further increase in the impeller speed and when the bed is in the fluidised regime (Fr : 0.71 and 0.97) leads to no periodicity of the velocity fluctuation. The loss of periodicity at high impeller speeds was also previously observed by Remy and co-workers (Remy et al., 2010) for dry beds of glass beads.

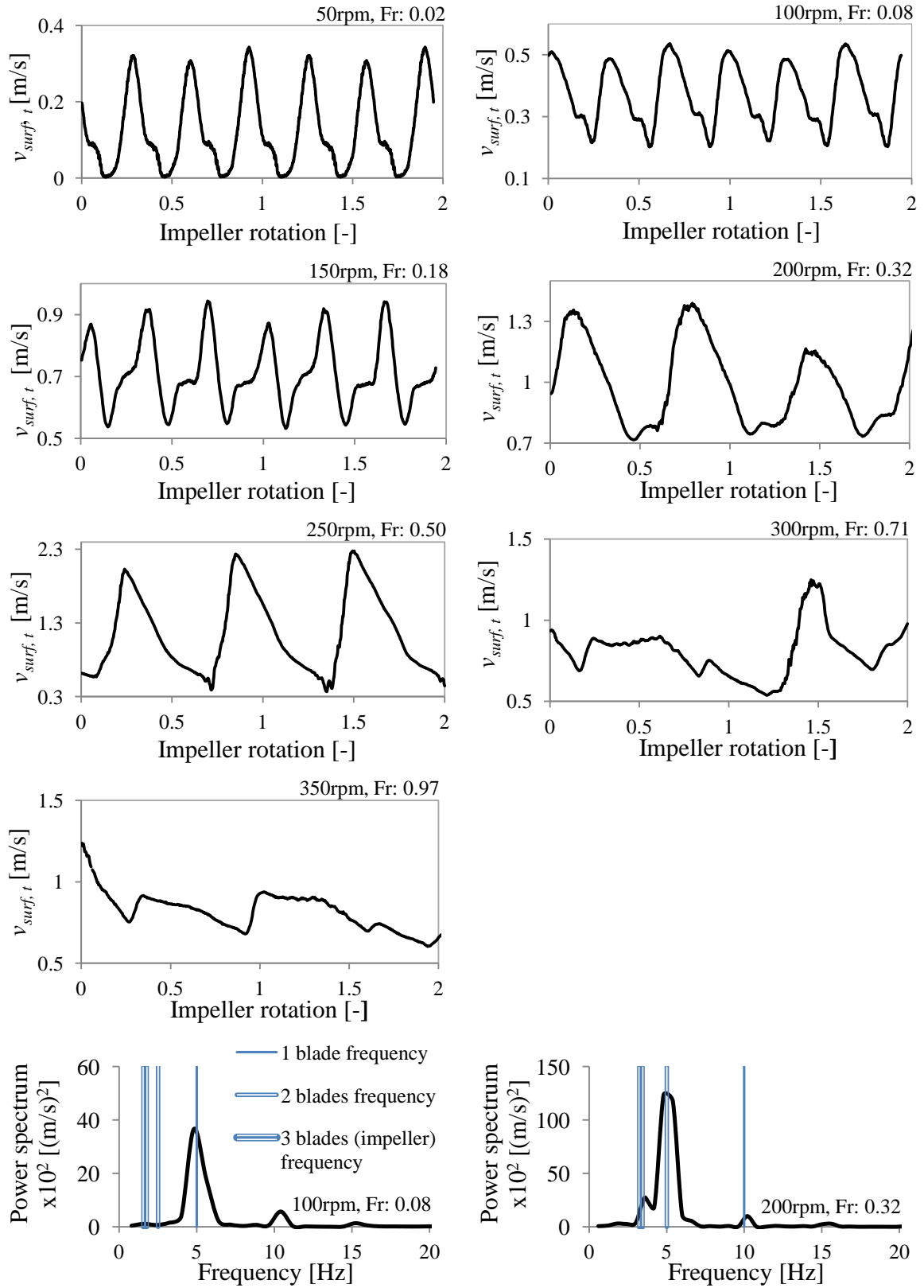


Figure 7.6: Total bed surface velocity ($v_{surf,t}$) with impeller rotation and FFT analysis for 0.5-1.0 mm, 1.5 kg granule bed.

Figure 7.7 and Figure 7.8 present the results for the bed height at the wall which also reflects the vertical motion of the bed surface. Similar trends of the fluctuation periodicities, fluctuation amplitudes and average values across the different flow regimes are observed as in the case of the bed surface velocity analysis.

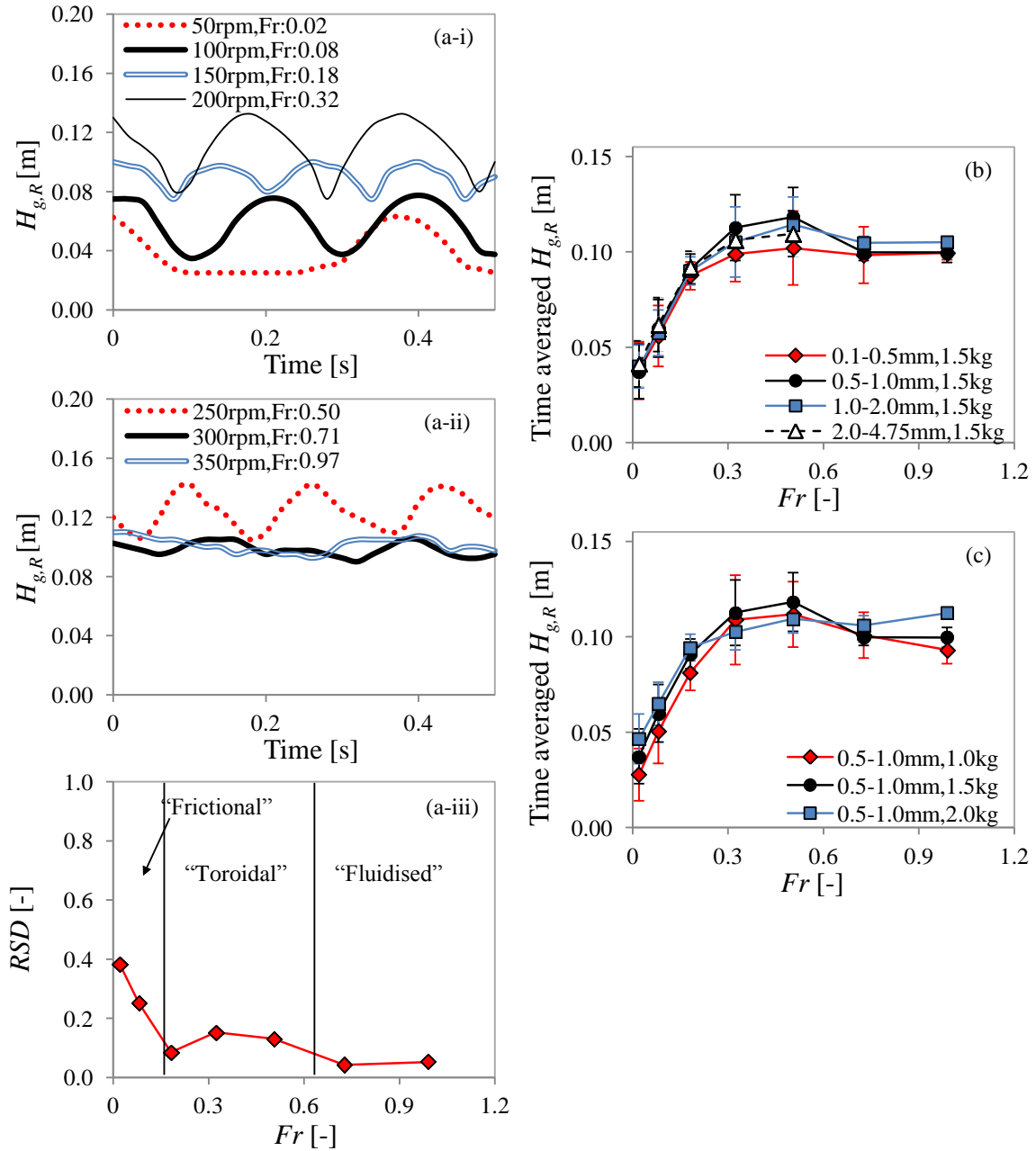


Figure 7.7: Bed height at the wall ($H_{g,R}$) results: (a) temporal values and RSD (relative standard deviation) for 0.5-1.0 mm, 1.5 kg granule bed (b) time-averaged values for different sieve sizes (c) time-averaged values for different bed loads.

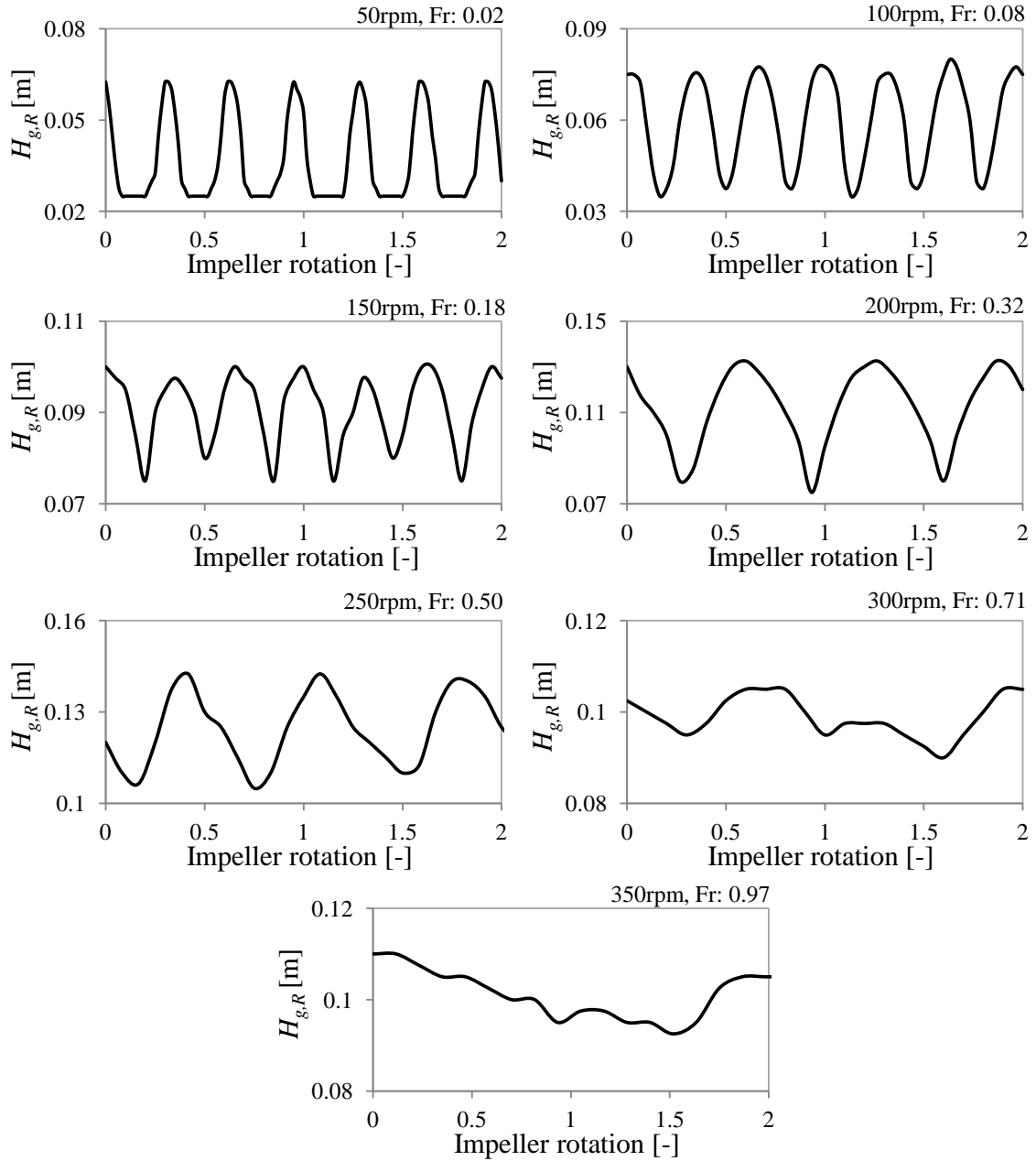


Figure 7.8: Bed height at the wall ($H_{g,R}$) with impeller rotation for 0.5-1.0 mm, 1.5 kg granule bed.

7.5.1.2 Wet beds

The time-averaged total surface velocity and RSD results for the dry and wet beds of polypropylene balls are presented in Figure 7.9. Equivalent to the dry mannitol granule beds, the more apparent increase of the average surface velocity is generally noticed in the frictional flow regime (from 50-150 rpm, Fr : 0.02-0.18) compared to the toroidal and fluidised flow regimes (from 150-350 rpm, Fr : 0.18-0.97), except for the 25% w/w water case (Figure 7.9a). When normalised with the impeller tip speed (Figure 7.9b), the normalised surface velocities increase in the frictional flow regime and reduce in the toroidal and fluidised states, the same behaviour exhibited by the dry mannitol beds (Figure 7.4b-ii and c-ii). The increment of the normalised velocity in the frictional flow regime however, decreases with increasing water content. The fluctuation amplitude, again similar to the dry mannitol beds, decreases in frictional flow regime, followed by an increase in the toroidal state, and finally reduces again in the fluidised state (Figure 7.9c).

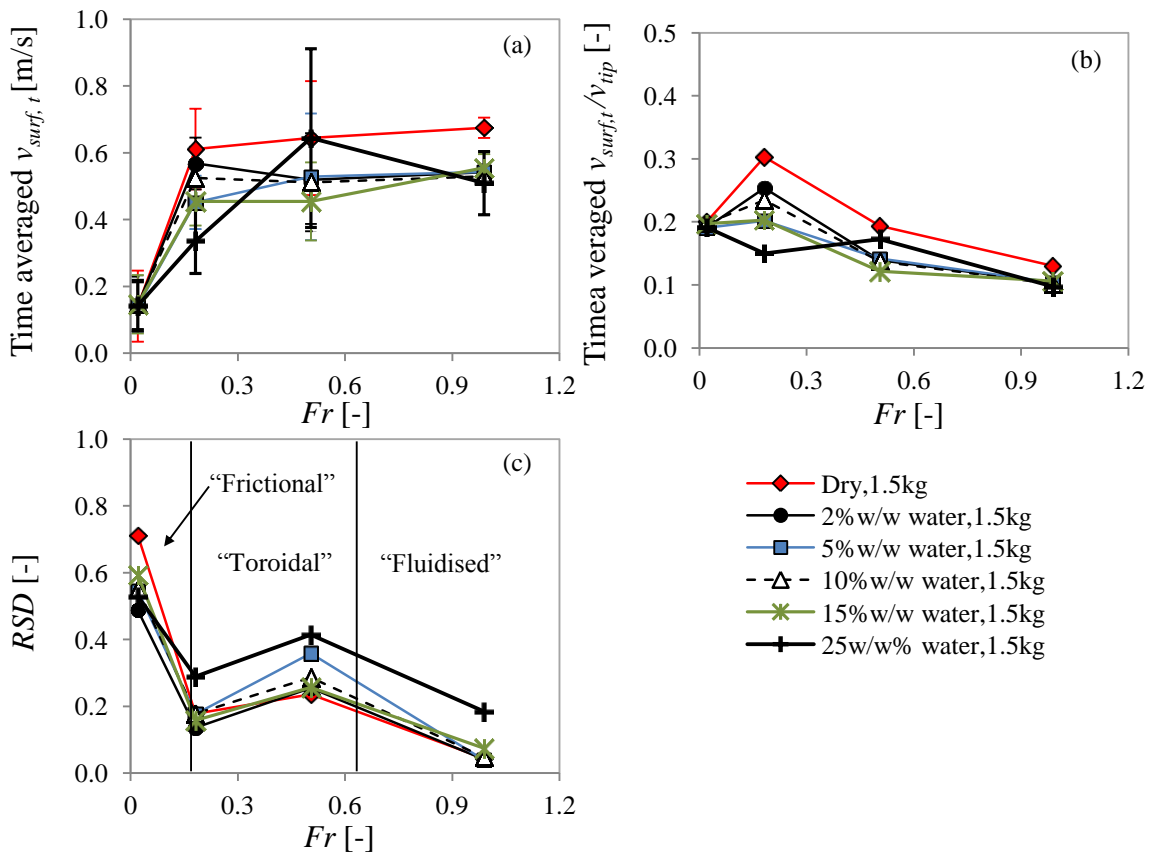


Figure 7.9: Time-averaged total bed surface velocity ($v_{surf,t}$) results for dry and wet beds of polypropylene balls (a) actual values (b) normalised values and (c) RSD (relative standard deviation).

Figure 7.10, Figure 7.11 and Figure 7.12 present plots of the surface velocities plotted against the impeller rotation for the dry and wet beds of polypropylene balls. At high water content (15 and 25%w/w water), smaller, secondary fluctuations or "noise" are obtained in main fluctuations (Figure 7.12), compared to the smoother profiles at lower water contents and dry beds (Figure 7.10 and Figure 7.11). This is due to an increasingly rough or irregular bed surface structure (i.e. clumps of materials moving rather than a smooth bed surface). Another thing to note is that at 50 rpm (Fr : 0.02) for most dry and wet cases, secondary fluctuations are obtained at the trough (minima) region. These findings correspond to the slight rearrangement of the bed after the blade passes through the analysed area (i.e particles move forward to fill up the space previously occupied by the blade) when the blade is moving slowly.

For all cases, the periodicity of the fluctuations at 50 and 150 rpm (Fr : 0.02 and 0.18) are the same as that observed for the dry mannitol granule beds, i.e. three periodic fluctuations for each impeller rotation, corresponding to each blade passing through the observed bed area. At 250 rpm (Fr : 0.50) however, while the dry polypropylene balls bed show the similar periodicity observed for the dry mannitol beds, i.e. one periodic fluctuation every two blade pass, the fluctuations start to show both irregular, and at certain times, periodic fluctuations when water is added. Finally in the fluidised state at 350 rpm (Fr : 0.97), the surface velocity becomes noticeably flatter without any periodic fluctuations for the dry polypropylene balls bed, again similar to the dry mannitol beds. On the contrary, this behaviour changes when water is added; although the fluctuation amplitudes decrease, periodic fluctuations are now observed. These fluctuations correspond to every blade pass. This suggests that due to the bed cohesiveness from water addition, the wet bed surfaces are affected by the blade motion, and could therefore be deflected every time the blade passed through the bed even when the bed is in the fluidised flow regime. Whether or not these periodic fluctuations occur at higher impeller speeds or Froude numbers for the wet beds remains to be investigated.

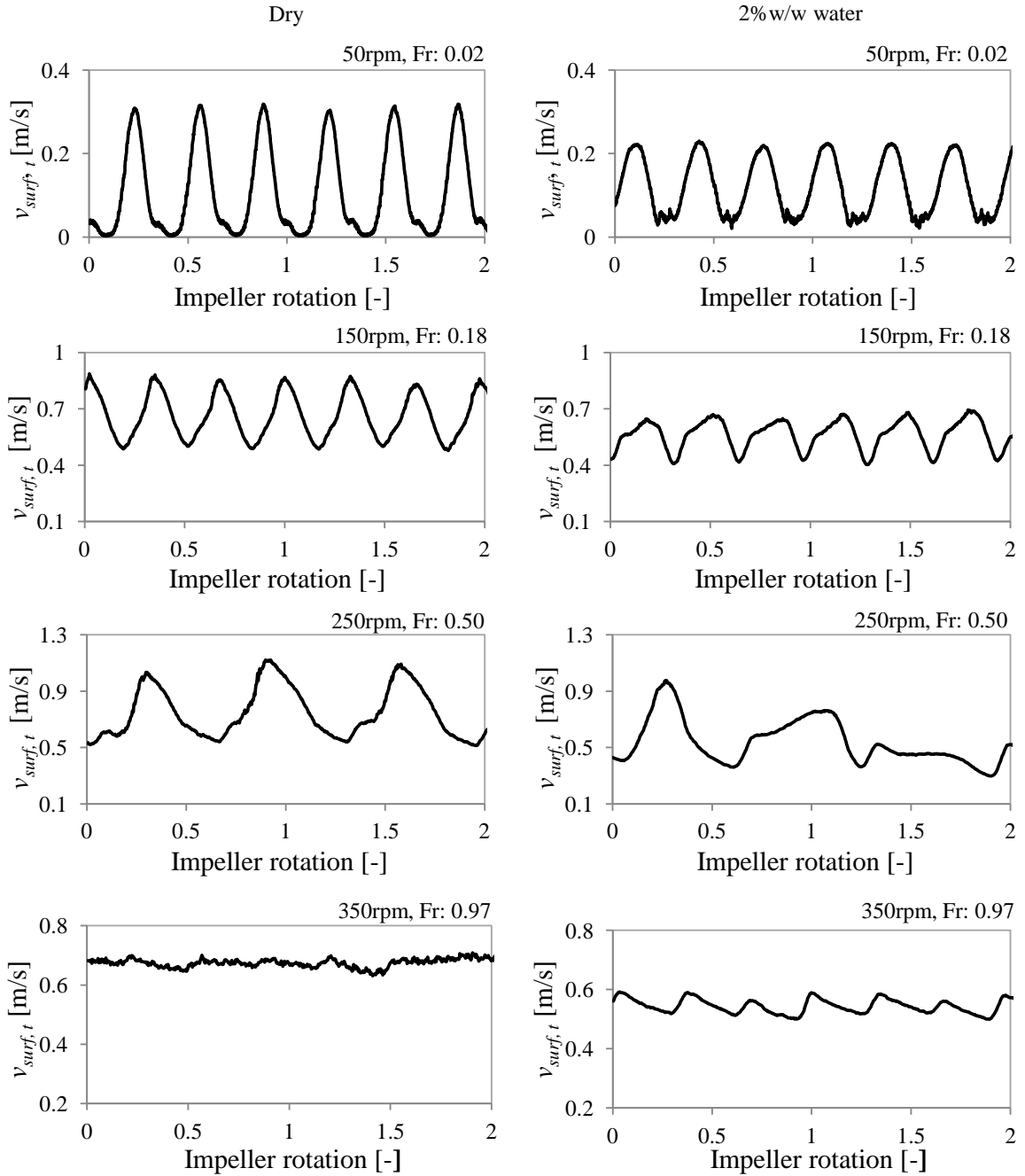


Figure 7.10: Total bed surface velocity ($v_{surf,t}$) with impeller rotation for dry and wet (2%w/w water) bed of polypropylene balls.

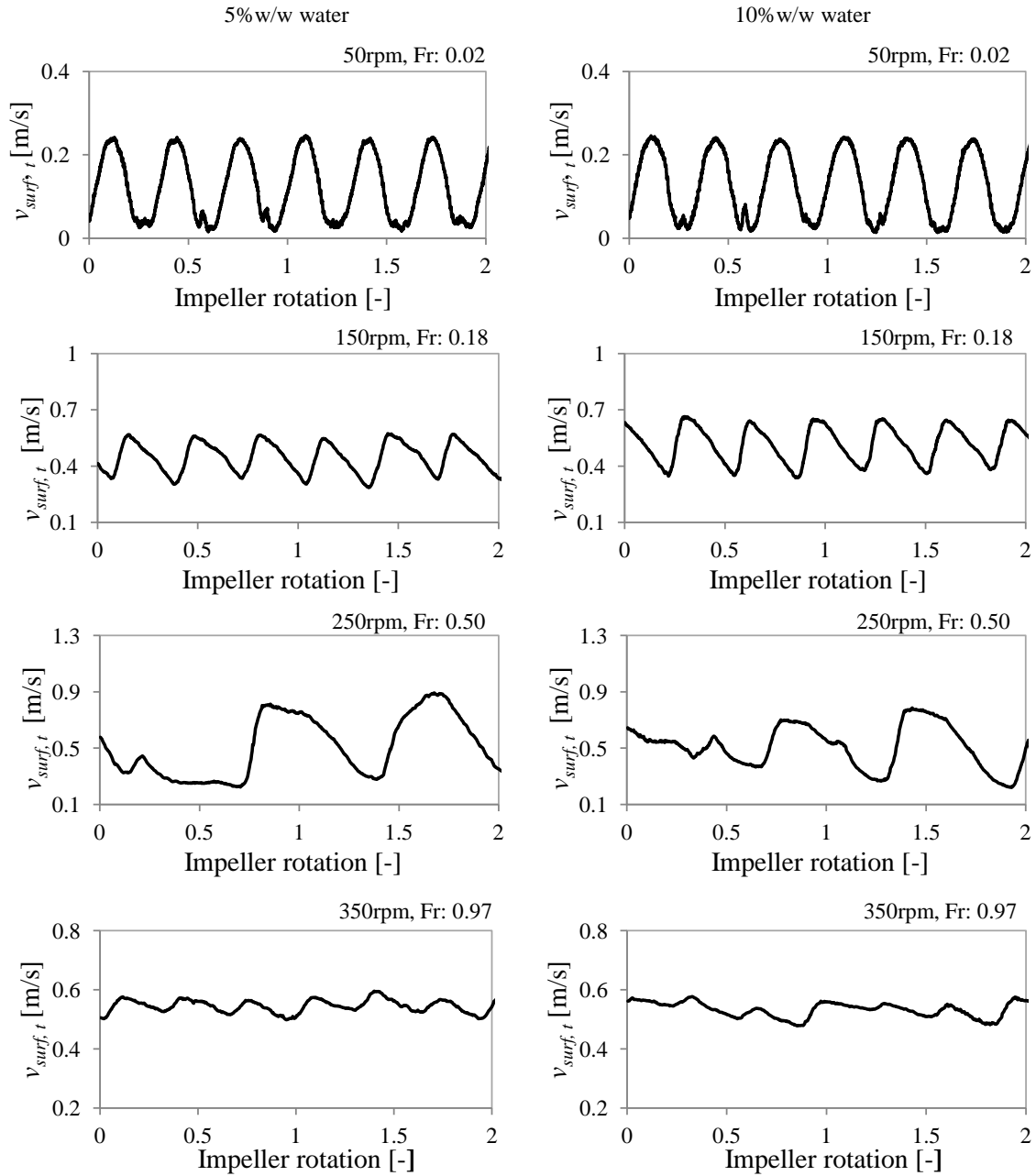


Figure 7.11: Total bed surface velocity ($v_{surf,t}$) with impeller rotation for wet (5%w/w and 10%w/w water) bed of polypropylene balls.

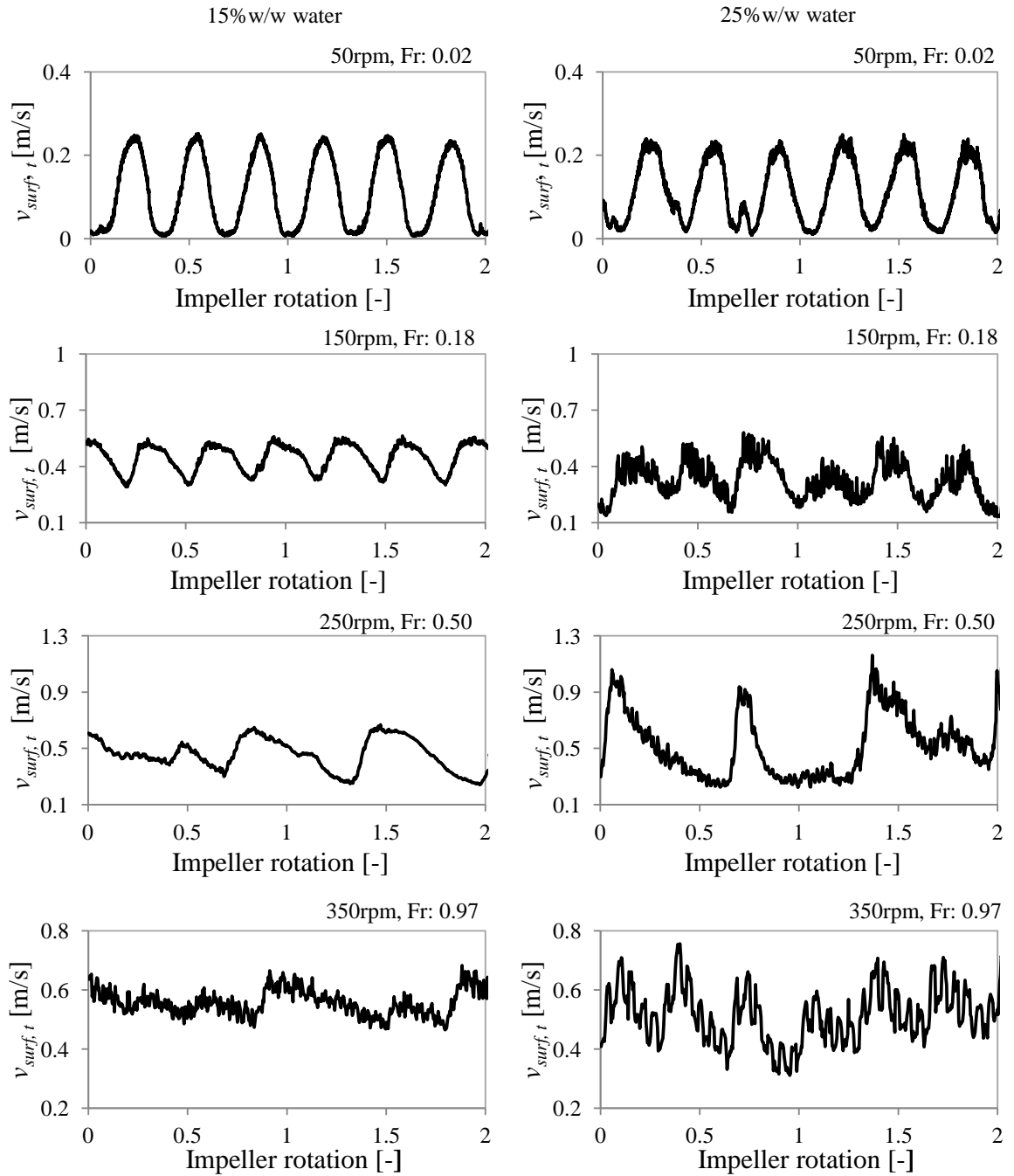


Figure 7.12: Total bed surface velocity ($v_{surf,t}$) with impeller rotation for wet (15%w/w and 25%w/w water) bed of polypropylene balls.

Table 7.1 summarises the bed surface velocity and bed height variability results for the rest of the dry mannitol beds studied. "1 blade frequency" and "2 blades frequency" represent the velocity fluctuation frequency corresponding to every one or two blade passes respectively, while "irregular" indicates no periodicity of the fluctuation. The flow regimes are represented by the shading of the cells. For the dry beds, the fluctuation periodicity correlates quite well with the flow regimes except at 150 rpm (Fr : 0.18), as the bed surface motion is still very much affected by the blade even though a toroidal flow pattern is achieved. The bed surface still deflects each time the blade sweeps through underneath, as in the case for the lower impeller speeds in the frictional flow regime. As the impeller speed increases in the toroidal flow regime, the bed surface velocity and height becomes less sensitive to the blade motion and deflects every two blade passes. The fluidised flow regime is marked by the irregular and flatter surface profiles, now independent from the blade motion.

Table 7.1: Summary of the fluctuation periodicity of the bed surface velocity and bed height for dry mannitol granule beds.

Granule size (1.5 kg)	H_{g0}/h_1	Impeller speed [rpm]/ Froude number [-]						
		50/0.02	100/0.08	150/0.18	200/0.32	250/0.50	300/0.71	350/0.97
0.1-0.5 mm	2	1 blade fre.	1 blade fre.	1 blade fre.	2 blades fre.	2 blades fre.	2 blades fre.	Irregular
0.5-1.0 mm	2	1 blade fre.	1 blade fre.	1 blade fre.	2 blades fre.	2 blades fre.	Irregular	Irregular
1.0-2.0 mm	2.2	1 blade fre.	1 blade fre.	1 blade fre.	2 blades fre.	2 blades fre.	Irregular	Irregular
2.0-4.75 mm	2.2	1 blade fre.	1 blade fre.	1 blade fre.	2 blades fre.	2 blades fre.	NA	NA
<i>Bed load</i> (0.5-0.75 mm)								
1.0 kg	1.5	1 blade fre.	1 blade fre.	1 blade fre.	2 blades fre.	2 blades fre.	2 blades fre.	Irregular
1.5 kg	2	1 blade fre.	1 blade fre.	1 blade fre.	2 blades fre.	2 blades fre.	Irregular	Irregular
2.0 kg	2.5	1 blade fre.	1 blade fre.	1 blade fre.	2 blades fre.	2 blades fre.	Irregular	Irregular

Unshaded cells: frictional flow, shaded cells: toroidal flow, diagonal striped cells: fluidised flow.

A summary of the surface velocity periodicity for the dry and wet beds of polypropylene balls, and further results of the wet beds using the 8% HPC solution are given in Table 7.2. For the dry bed, the periodicity at different flow regimes is the same as that for the dry mannitol granule beds in Table 7.1. When liquid is added, the periodicity changes to the "2 blades

frequency" and "irregular" behaviour at 250 rpm (Fr : 0.50). This is also when the bed surface motion is the most turbulent before it transits to the fluidised state. In the fluidised state, the periodicity reverts to the "1 blade frequency" behaviour for the cohesive beds.

Table 7.2: Summary of the fluctuation periodicity of the bed surface velocity and bed height for dry and wet beds of polypropylene balls.

Water content (%w/w)	H_{g0}/h_1	Impeller speed [rpm]/ Froude number [-]			
		50/0.02	150/0.18	250/0.50	350/0.97
0 (Dry)	2.6	1 blade fre.	1 blade fre.	2 blades fre.	Irregular
2	3.1	1 blade fre.	1 blade fre.	2 blades fre./irregular	1 blade
5	2.9	1 blade fre.	1 blade fre.	2 blades fre./irregular	1 blade
10	2.5	1 blade fre.	1 blade fre.	2 blades fre./irregular	1 blade
15	2.3	1 blade fre.	1 blade fre.	2 blades fre./irregular	1 blade
25	1.8	1 blade fre.	1 blade fre.	2 blades fre./irregular	1 blade
<i>8% HPC solution content (%w/w)</i>					
5	3	1 blade fre.	1 blade fre.	2 blades fre./irregular	1 blade
15	2.5	1 blade fre.	1 blade fre.	2 blades fre./irregular	1 blade

Unshaded cells: frictional flow, shaded cells: toroidal flow, diagonal striped cells: fluidised flow.

7.6 Behaviour of blade-bed region

7.6.1 Experimental blade-bed stress

The blade-granule bed stress results for different dry mannitol beds measured using the impeller stress sensor system is given in Figure 7.13. As described in Chapter 4.4: Section 4.4.1, the time-averaged blade-bed stress increases with the impeller speed or Froude number due to the larger imparted inertial force by the blade (also shown here in Figure 7.13b-c). Fluctuation amplitudes (Figure 7.13a), meanwhile, seem to vary according to the flow regimes. In the frictional and toroidal regime (impeller speeds 50-250 rpm or Fr : 0.02-0.50), the blade maintains a continuous contact with the bed, resulting in relatively smaller fluctuation amplitudes or relative standard deviations (Figure 7.13a-iii). Subsequently in the fluidised regime (≥ 300 rpm, Fr : 0.71) the stresses fluctuate considerably, as evidenced by the increased relative standard deviations in Figure 7.13a-iii, which indicates the fluctuating motion of the bed at the blade region in this regime. Previously, runs at different speeds without any granules have shown that that the stress signals do not fluctuate significantly (Chapter 3: Section 3.2.2.3), therefore also ruling out vibratory noise effects or circuitry problems. The low

sampling frequency, i.e. measurement every 0.5 seconds or 2 Hz, of the stress however, deters further analysis of the measurements to determine any recurring fluctuations and corresponding frequencies. These will instead be studied from the DEM simulations with an output interval of 0.005 seconds, as described in Chapter 6: Section 6.4.

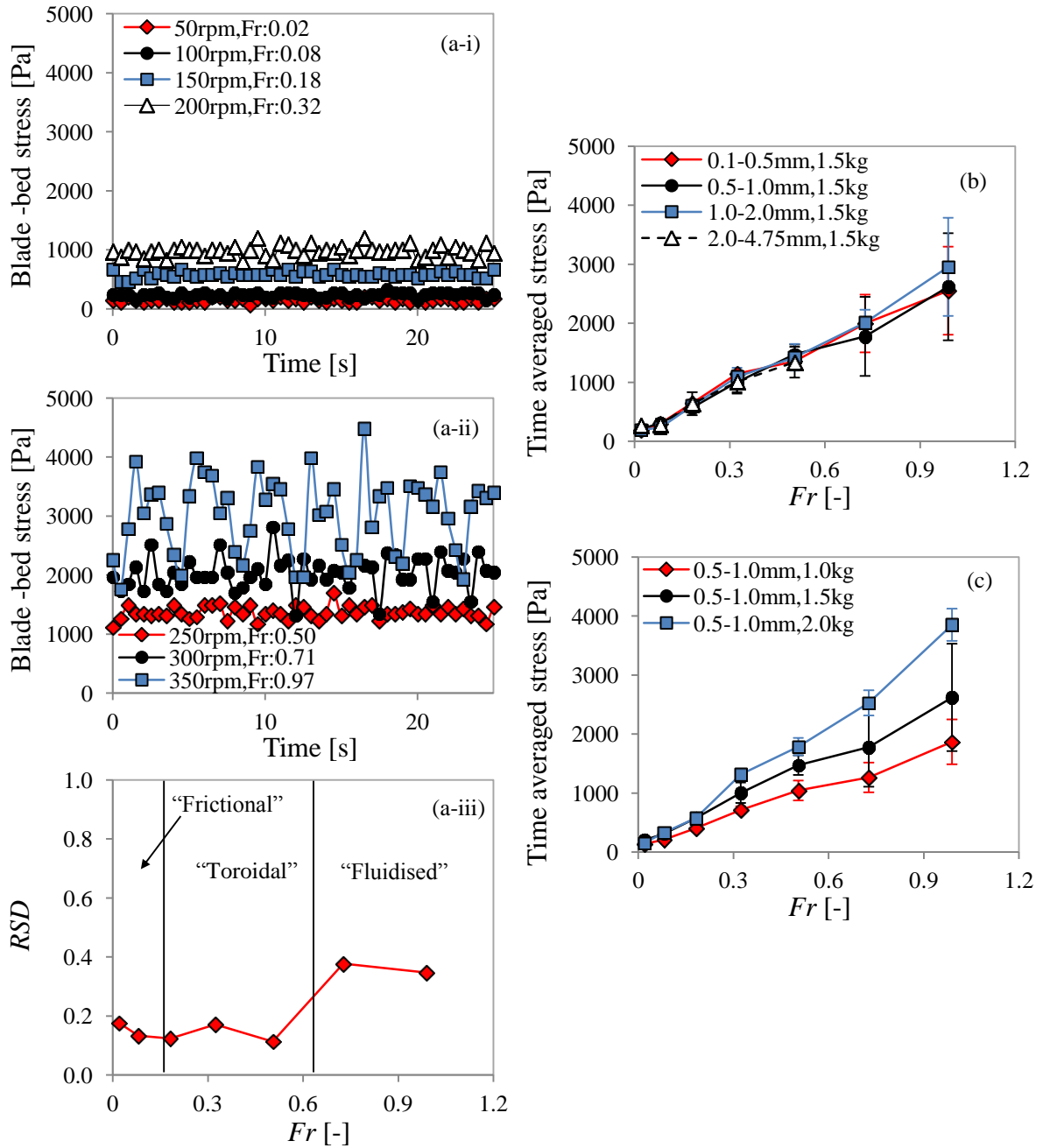


Figure 7.13: Experimental blade–granule bed stress results: (a) temporal values and RSD (relative standard deviation) for 0.5-1.0 mm, 1.5 kg granule bed (b) time-averaged values for different sieve sizes (c) time-averaged values for different bed loads.

7.6.2 Simulated bed-blade stress

The simulated temporal blade-bed stresses for the 1.5 kg bed of 3.5 mm diameter particles are presented in Figure 7.14a. These are also previously compared and validated with the experimental results in Chapter 6: Section 6.5. The results in Figure 7.14 also include smaller intervals of impeller speeds up to 1400 rpm (Fr : 15.54), as compared to those presented in Chapter 6. Like the experimental results, it can be seen that in the frictional and toroidal flow regime (50-250 rpm, Fr : 0.02-0.50), the amplitude of the stress fluctuations is low (Figure 7.14a) due to continuous contact of the particle bed with the blade. The amplitude then increases in the fluidised regime. Interestingly, there is a range of impeller speeds where periodic stress fluctuations are observed (~300-450 rpm, Fr : 0.71-1.61), indicating that the particle bed is lifted up and down steadily. This periodicity however, ceases beyond these impeller speeds. FFT analyses conducted on these fluctuations return frequencies slightly higher than the frequency of three blade passes or one impeller rotation (Figure 7.14b) in all cases, i.e. the bottom of the particle bed lifts up and down almost every three blade passes or one impeller rotation. At higher impeller speeds, due to the high blade frequencies, it could be reasoned that there is insufficient time for the particle bed to lift up and down steadily from the blade to give any periodic blade-bed stress fluctuations.

The fluctuation amplitude and periodicity of the blade-granule bed stress was also studied for other particle/particle bed properties, impeller geometries and granulator scale simulated in Chapter 6. Figure 7.15 presents results for the different particle sizes and bed loads at 350 rpm impeller speed (Fr : 0.97), which is the only simulated impeller speed for the rest of cases/parameters which falls into the periodic blade-bed stress fluctuation range of ~300-450 rpm (Fr : 0.71-1.61) obtained previously in Figure 7.14. At the other simulated impeller speeds for the different bed particle size and bed load cases (i.e. 50, 150, 250 and 700 rpm), it was confirmed that there are no periodic fluctuations. The amplitude of the fluctuations are larger with the 2.0 mm particle bed which fluctuates at the same frequency as the 3.5 mm particles (Figure 7.15a). The fluctuation periodicities then cease in the 5.0 mm and 10.0 mm particle beds. Increasing the bed load increases both the fluctuation amplitude and frequency (Figure 7.15b).

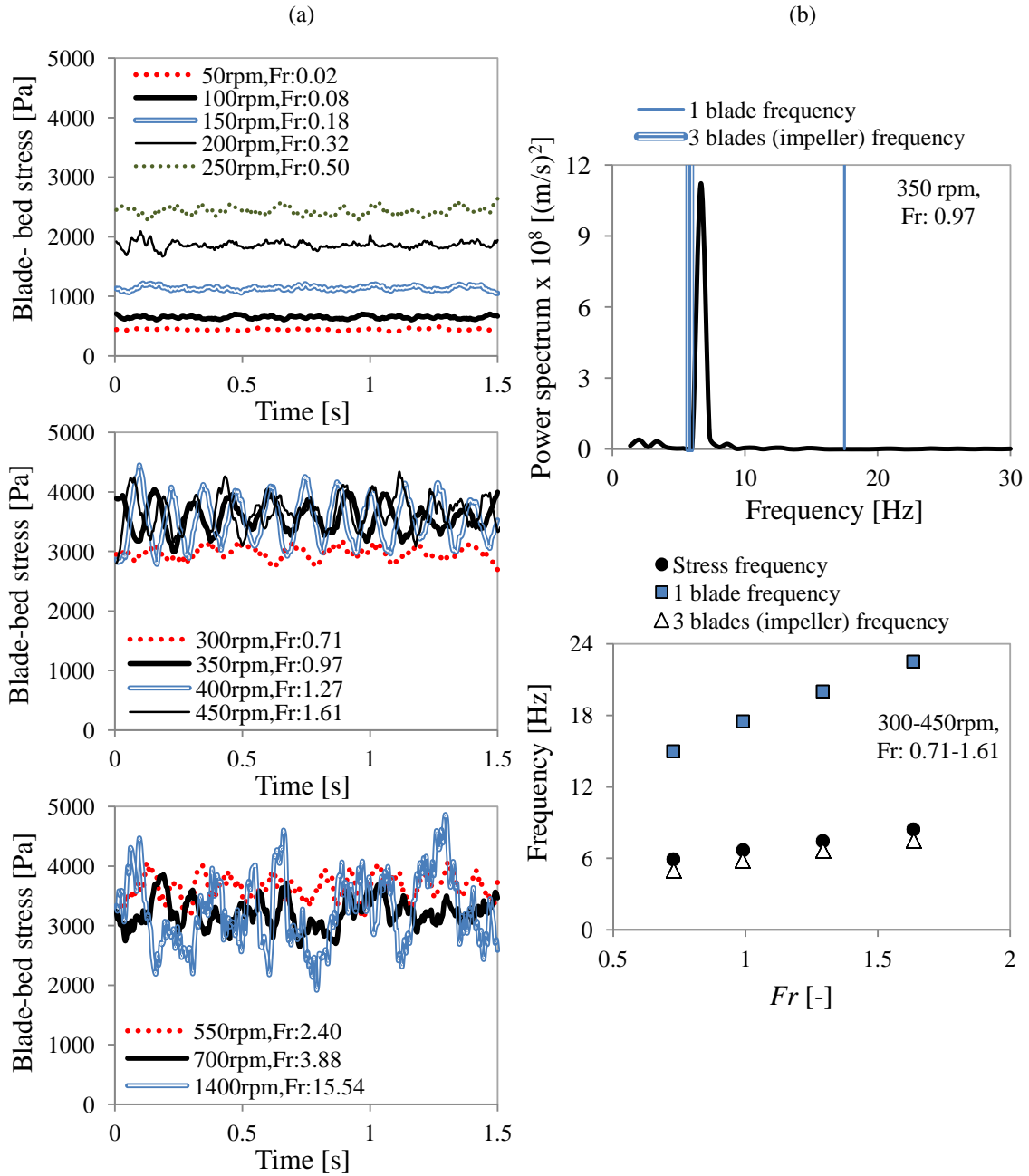


Figure 7.14: Simulated blade-bed stress results for 3.5 mm, 1.5 kg bed of particles (a) temporal blade-bed stress and (b) FFT analysis.

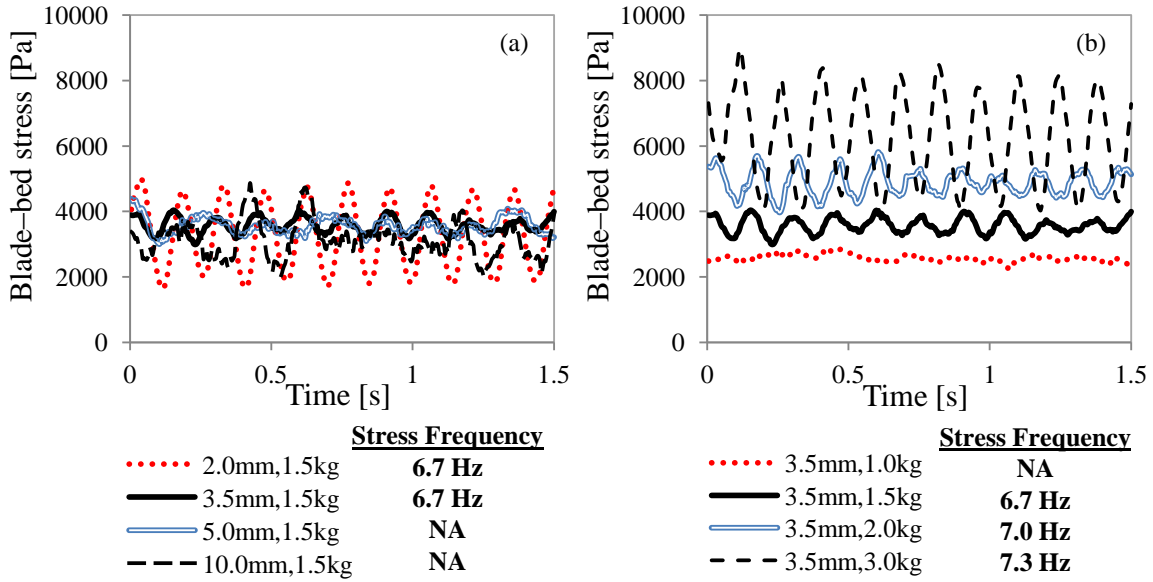


Figure 7.15: Simulated temporal blade-bed stress at 350 rpm ($Fr: 0.97$) for (a) different particle sizes and (b) different bed loads.

The blade-bed stress periodicity results for the particle size, bed load and other parameters are summarised in Table 7.3 and Table 7.4. Both the blade-bed stress fluctuation frequency and fluctuation amplitude (given by the relative standard deviation, RSD values) are reported. The results are again reported for only the 350 rpm impeller speed case (or $Fr: 0.97$ for different granulator scales). Again, it was observed that there are no periodic fluctuations of the blade-bed stress at the other simulated impeller speeds and Froude number (i.e. 50, 150, 250 and 700 rpm or $Fr: 0.02, 0.18, 0.50$ and 3.88) for all the studied parameters.

The cells shaded in gray indicate conditions where no periodic fluctuations are observed. The bed load, particle density (Table 7.3) and blade width (Table 7.4) results show that periodic fluctuations of the blade-bed stress are only obtained above a certain fill level compared to the blade height, represented by the undisturbed bed height to blade inclined height ratio, H_{g0}/h_I , which is ≥ 1.7 for the range studied in this work. The fluctuation amplitudes also increase with increasing H_{g0}/h_I for the studied range.

Table 7.3: Summary of the blade-bed stress fluctuation properties for different particle/particle bed properties at Fr : 0.97 (350 rpm in the 11.1 L granulator) from simulation.

Particle/ particle bed properties	H_{g0}/h_1	Blade-bed stress		Impeller frequency [Hz]	Blade frequency [Hz]	
		RSD [-]	Frequency [Hz]			
Bed load	1.0 kg	1.5	0.081	NA	5.83	17.5
	1.5 kg	2.1	0.087	6.7		
	2.0 kg	2.6	0.096	7		
	3.0 kg	3.7	0.227	7.3		
Particle size	2.0 mm	2.1	0.318	6.7		
	3.5 mm		0.087	6.7		
	5.0 mm		0.072	NA		
	10.0 mm		0.182	NA		
Particle density	600 kg/m ³	4.3	0.205	6.7		
	1230 kg/m ³	2.1	0.087	6.7		
	2500 kg/m ³	1.3	0.068	NA		
Interparticle sliding friction coefficient	0.02	2.1	0.055	6.7		
	0.1		0.089	6.7		
	0.3		0.087	6.7		
	0.5		0.090	6.7		
	0.9		0.077	6.7		
Restitution coefficient	0.1	2.1	0.069	NA		
	0.3		0.087	6.7		
	0.5		0.126	6.7		
	0.7		0.136	6.7		
	0.9		0.134	6.7		
Young's modulus	0.1 MPa	2.1	0.105	3.5		
	1 MPa		0.071	6.7		
	100 MPa		0.077	6.7		
	160 MPa		0.087	6.7		
	1000 MPa		0.125	NA		

For different interparticle sliding friction coefficients (Table 7.3), periodic blade-bed stress fluctuations are detected for all studied coefficients at the same frequency. There is also no detected periodic fluctuations at a low restitution coefficient (i.e. 0.1) and the fluctuation amplitudes increase with the restitution coefficient. For the Young's modulus (Table 7.3), the "soft" particles with 0.1 MPa Young's modulus exhibit a smaller blade-bed stress fluctuation frequency at 3.5 Hz, almost half of that for the higher Young's modulus. No periodic fluctuations are detected, however, when the Young's modulus is 1000 MPa.

Table 7.4: Summary of the blade-bed stress fluctuation properties for different impeller geometries and granulator scale at Fr : 0.97 from simulation.

Impeller geometries & granulator scale	H_{g0}/h_I	Blade-bed stress		Impeller frequency [Hz]	Blade frequency [Hz]
		RSD [-]	Frequency [Hz]		
Blade width (blade inclined height)	20(10.6) mm	3.6	0.270	6.7	5.83
	35(18.5) mm	2.1	0.087	6.7	
	50(26.5) mm	1.7	0.044	NA	
	65(34.4) mm	1.4	0.045	NA	
Blade angle	20°	3.2	0.453	6.7	17.5
	32°	2.1	0.087	6.7	
	45°	1.8	0.028	NA	
	65°	1.5	0.064	3.5	
	90°	1.4	0.063	3.5	
Number of blades	2		0.452	4.5	11.67
	3	2.1	0.087	6.7	17.5
	4		0.038	NA	23.33
Granulator scale	0.173 L		0.041	NA	11.67
	1.39 L		0.064	9.5	8.25
	11.1 L	2.1	0.087	6.7	5.83
	88.7 L		0.220	5	4.12

Results for small blade inclined angles at 20° and 32° show periodic blade-stress fluctuations at the same frequency, with the 20° having a much higher fluctuation amplitude due to the larger H_{g0}/h_I (Table 7.4). At 45°, the periodicity ceases conforming to other results of similar H_{g0}/h_I . The fluctuation amplitude is also the minimum at this angle. The periodic fluctuations recur at 65 and 90°, with a smaller frequency of 3.5 Hz.

A smaller blade-bed stress frequency from the 2-bladed impeller, i.e. 4.5 Hz, is obtained as compared to the 3-bladed impeller, which can be explained by the smaller blade frequency of the 2-bladed impeller (Table 7.4). Additionally, a loss of blade-bed periodicity is observed when a 4-bladed impeller is used. This implies that the high blade frequency achieved by the 4-bladed impeller (also shown in Table 7.4) deters the steady lifting and falling of the particle bed on the blade, such as that observed at high blade frequencies for the 3-bladed impeller shown in Figure 7.14. A similar behaviour is obtained for the different granulator scales, where the smallest scale studied, i.e. 0.173 L, does not show periodic blade-bed stress fluctuations due to the high blade frequency. For the other granulator scales, the blade-bed stress frequencies are also found to be slightly higher than the respective impeller frequencies.

7.7 Chapter summary and conclusions

This chapter focuses on the variability/fluctuations of the temporal values for the steady-state measurements (i.e. bed surface velocity, bed height and blade-bed stress) reported in the previous chapters, from both the experimental and DEM simulation results. More importantly, the results are studied and linked to the different identified flow regimes of the granule/particle beds in the studied granulator configuration, i.e. frictional, toroidal and fluidised. Also, from the above flow regimes, the fluidised flow is distinguished for the first time in this thesis. Transitions between the flow regimes for most cases are found to occur at Froude numbers of 0.08-0.18 and 0.50-0.71 respectively. The main findings of the variability studies in the each flow regime are summarised as follows:

- In the frictional flow regime, the time-averaged bed surface velocity and height increased steadily with the Froude number. Large amplitudes of velocity and height fluctuation are observed initially due to the deflection of the bed every time a blade passed through. Frequencies of the fluctuations correspond to the frequencies of each blade pass. The above behaviours hold true for both the dry and wet beds, although with increasing water content for the wet beds, increasingly “noisy” fluctuations are noted (also at other flow regimes). The time-averaged blade-bed stress increases with the Froude number and the amplitude of stress fluctuations are low due to continuous contact with the blade. No periodic blade-bed stress fluctuations are detected;
- In the toroidal flow regime, the time-averaged bed surface velocity and bed height increase less significantly with the Froude number compared to the frictional regime. The bed surface becomes more unsteady and at the same time, less sensitive to the blade motion. This behaviour is observed for the dry beds and the majority of the wet beds. At 200-250 rpm (Fr : 0.32-0.50), the frequencies of the surface velocity and height fluctuations correspond to every two blade passes for the dry beds. This periodicity behaviour is observed for the first time in this thesis. For wet beds, a combination of both the “2 blade passes” and irregular fluctuations are obtained. The time-averaged blade-bed stress increases steadily with the Froude number while small fluctuation amplitudes of the blade-bed stress are still obtained.
- In the fluidised regime, the time-averaged bed surface velocity and height becomes constant or reduces with increasing Froude number, and the periodicity of the fluctuations

diminishes for the dry beds. For the wet beds, although the fluctuation amplitude reduces significantly in this regime, periodic surface velocity fluctuations corresponding to the single blade frequency are still exhibited due to the bed cohesion. Larger amplitude of blade-bed stress fluctuations implies a more fluctuating motion of the particle bed at the blade region. Periodic stress fluctuations mostly at frequencies slightly higher than one impeller rotation or three blade passes are observed at a certain Froude number range (Fr : 0.71-1.61). Existence of these periodic fluctuations is also dependent on other studied parameters: (i) above a certain bed height to blade inclined height ratio (H_{g0}/h_l) of 1.7 for the studied H_{g0}/h_l range (except for the 65° and 90° inclined blades) (ii) below a certain particle size relative to the granulator diameter ($D/d \leq 80$) (iii) particle restitution coefficient ≥ 0.3 (iv) particle Young's modulus ≤ 160 MPa and (v) if the blade frequency is not too high as observed in the 4-bladed impeller and 0.173 L granulator cases.

Chapter 8

Overall conclusions and future work

8.1 Thesis conclusions

This thesis has focused on understanding and characterising the external stress exerted on the granule bed in a vertical axis, cylindrical high shear granulator (i.e. impeller blade-bed stress), a fundamental parameter which affects the granule growth behavior. Firstly, a novel, custom-built telemetric impeller stress sensor is developed for direct and online measurement of the blade-bed stress.

The work encompasses the characterisation of the blade-bed stress from the measurements and by using Discrete Element Method (DEM) simulations, a study of the blade-bed stress change during the wet granulation process and finally further insight into the variability of the blade-bed stress and bed surface behaviour in different identified flow regimes. Additionally, for the blade-bed stress characterisation, the bed surface velocity and bed height are also studied.

8.1.1 Dry granule/particle bed characterisation (Chapter 4)

The main achievements/findings in this section are listed below:

- A blade-granule bed stress equation for the high shear granulator is derived based on the imparted inertial force on a continuous bed (Equation 4.8). From the equation, the blade-bed stress at a particular radial position is dependent on the granule bed properties (i.e. bed height, bed bulk density and bed velocity) and the blade properties (blade width, blade angle and blade velocity). The bed surface velocity and bed height at the wall are chosen as the equation parameters;
- Steady-state measurements of the blade-bed stress are carried out using the novel telemetric impeller stress sensor. The steady-state bed surface velocity and bed height are also measured using high speed recording. The impeller speed is varied from 50 to 350 rpm (Froude number, Fr : 0.02-0.97) where the granule/particle bed transits through several flow regimes. From parameter studies (i.e. bed load, granule/particle sieve size, granule/particle

bed density) using prepared, dry granule/particle beds, the time-averaged blade-bed stress increases consistently with the impeller speed up to 350 rpm due to the larger imparted inertial force by the blade (e.g. Figure 4.8a). The average bed surface velocities and bed height increase significantly at the low impeller speeds and then become constant or reduce due to flow regime transition (e.g. Figure 4.8b&c); and

- The proposed blade-bed stress from theory gives over-predictions for impeller speeds around 150 rpm (Froude number: 0.18). Interestingly, results from DEM simulation also demonstrate the reduction of bed velocity with bed height for impeller speeds above 150 rpm (Figure 4.11). A correction factor B_I which is applied to the blade-bed stress equation to account for the increasing “fluidisation” of the bed and the use of surface velocity, is taken to be proportional to the inverse of the relative velocities, $B_I = K_I/v_{rel}$. The corrected blade-bed stress equation gives a much improved prediction of the blade-bed stress at the high impeller speeds. Fitting of the experimental data gives a fitted constant, K_I , of ~ 1 for all conditions studied in this section, i.e. impeller speed, bed load, granule/particle sieve size and granule/particle bed density (Figure 4.12).

8.1.2 Wet granule/particle bed characterisation (Chapter 5)

The following are the main achievements/findings in this section:

- For study of steady-state wet beds at different liquid saturation states, addition of increasing amounts of liquid does not change the blade-bed stress significantly with a constant bed load, except when the bed is in the capillary liquid saturation state. At this state, it is found that the bed behaves unsteadily due to large clumps of wetted polypropylene balls moving in the granulator, as evidenced by the large fluctuations of the blade-bed stress and bed surface velocity (Figure 5.3). Reduced surface velocities and increased heap formation or bed porosity of the wet beds are obtained;
- Fitting of the experimental data to the blade-bed stress equation with correction factor B_I gives K_I value of ~ 1 for the studied liquid types and liquid content (Figure 5.7), the same as that obtained for the dry granule/particle beds. The corrected blade-bed stress equation reasonably predicts the average stress, provided the bed is not in the capillary liquid saturation state; and

- Blade-bed stress measurements during the granulation process with varying water to powder ratios show the following general behaviours (Figure 5.9, Figure 5.11 and Figure 5.13): an initial steep increase during the binder addition stage and a subsequent plateau region with a small increase when the granules are growing steadily or undergoing densification/consolidation. Large fluctuations are obtained when predominantly oversized granules or pasty lumps are being formed. The exhibited blade-bed stress behaviour seems to follow the general impeller torque or power consumption curves during wet granulation.

8.1.3 Further dry bed characterisation using DEM simulations (Chapter 6)

The main achievements/findings in this section are described as follows:

- With the employed DEM contact models, the simulations are successfully validated with the experimental results in Chapter 4 in terms of the temporal characteristics and time-averaged values of the blade-bed stress, bed surface velocity and bed height. Additionally, these are validated for impeller speeds up to 350 rpm (maximum achievable in the experiments). The simulations are, therefore, subsequently applied to study higher impeller speeds (i.e. up to 700 rpm or $Fr: 3.88$) and other parameters (i.e. particle/particle bed properties, impeller geometries and granulator scales) for steady-state beds;
- From the simulations, the blade-bed stress, bed surface velocity and bed height along the radial position are studied. It is shown that the blade-bed stress variation along the radial position is very much affected by the bed height profile of the particle bed (Figure 6.19 and Figure 6.20). The variation of the surface velocity along the radial position is also found to be strongly dependent on the flow regime (Figure 6.21);
- It is previously shown from the experiments (Chapter 4 and Chapter 5) that the average blade-bed stress at the sensor region increases steadily with impeller speed up to 350 rpm ($Fr: 3.88$). The simulation results show that the blade-bed stress at the sensor region could be constant/reduce with a further increase in impeller speed up to 700 rpm ($Fr: 3.88$), such as for low bed fill level cases (i.e. smaller bed load, Figure 6.27a or larger particle density, Figure 6.30a), due to the steep decrease of bed height from the wall to the sensor region. Consequently, the sensor region-averaged bed height reduces at 700 rpm for the

aforementioned cases (Figure 6.27c and Figure 6.30c). The average bed surface velocity, meanwhile, does not change much after 350 rpm for most cases;

- Similar flow behaviours can be obtained at different granulator scales by keeping the Froude number constant when the mixer diameter to particle diameter ratio (D/d_p) is ≥ 40 . The average blade-bed stress, bed surface velocity and bed height can also be scaled with the bed bulk pressure, impeller linear velocity and blade inclined height respectively for $D/d_p \geq 40$;
- Fitting of the simulation results to the blade-bed stress equation with the correction factor B_1 proposed in Chapter 4 gives a K_I value of 1.1 (Figure 6.44a), close to the $K_I \approx 1$ from the experimental data fittings. Despite that, the use of the corrected bed height, i.e. sensor-averaged bed height, instead of the bed height at the wall used previously in the experiments, is crucial for blade-bed stress predictions > 350 rpm ($Fr: 0.97$) (Figure 6.45);
- A modified correction parameter, $B_2 = K_2 \frac{1}{Fr_{rel}^{0.5}} \left(\frac{h_w}{R}\right)^{0.3}$, i.e. related to the inverse of the relative Froude number and the blade width to impeller radius ratio to account for different granulator scales and blade widths, gave improved fitting constants, K_2 , for all studied cases except for the blade angle (Table 6.7 summarises the fitting constants for different cases). A power law relationship between K_2 and the blade angle is obtained (Figure 6.51); and
- Comparison of blade-bed stress predictions using the bed surface velocity or bed height-averaged velocities conclude that the usage of the bed surface velocity is not the dominant factor for the stress over-prediction with increasing impeller speeds (Figure 6.52), i.e. the increasing bed “fluidisation” is the dominant factor.

8.1.4 Variability studies across flow regimes (Chapter 7)

The following describe the main achievements/findings in this section:

- For the different flow regimes that the granule/particle bed transits with increment of the impeller speed or Froude number (Figure 7.1), the “fluidised” flow regime is distinguished for the first time in this thesis. This is when the bed becomes increasingly lifted up from the bottom of the granulator and also when the surface shape is independent of the blade motion underneath. Transitions between the regimes (i.e. “frictional to toroidal” and

“toroidal to fluidised”) for most cases occur at Froude numbers of 0.08-0.18 and 0.50-0.71 respectively;

- Study of the variability/fluctuation of the temporal values and time-averaged values of the blade-bed stress, bed surface velocity and bed height from both experiments and simulations show that the results can be linked to the flow regimes, as summarised in Chapter 7: Section 7.7;
- While previous works have noted frequencies of the bed surface velocity fluctuations corresponding to the blade frequencies, a different fluctuation periodicity behaviour, i.e. bed surface velocity frequency corresponding to two blade passes, is observed for the first time in this work (Table 7.1). This occurs at 200-250 rpm (Fr : 0.32-0.50) in the toroidal flow regime before the bed transits into the fluidised regime where a loss of surface velocity periodicity is then observed; and
- From DEM simulations which enable a smaller output interval of the blade-bed stress, interestingly, periodic blade-bed stress fluctuations are obtained when the bed transits into the fluidised regime (300 rpm, Fr : 0.71) with frequencies slightly higher than one impeller rotation or three blade passes (Figure 7.14). This suggests the steady lifting and falling of the particle bed on the impeller blade. The periodicity then ceases at high impeller speeds or Froude number when the blade frequency becomes too high. The existence of these periodic fluctuations and the fluctuation amplitude are also dependent on other studied parameters as listed in Table 7.3 and Table 7.4.

8.2 Future work

The potential work avenues following this research work are discussed as follows:

In this work, the impeller blade-bed stress equation from the imparted inertial force is successfully applied to the dynamic granule or particle beds in a vertical axis, cylindrical high shear granulator, by implementing certain correction factors. A similar characterisation method can also be extended to study other vertical axis granulator configurations, particularly for high volume, production scale granulators. Additionally, since this thesis does not aim to improve the granulation process, the characterised blade-bed stress will be very useful for granule growth kinetics, growth behaviour and granulation regime mapping studies as reviewed in Chapter 2. Implementation of the blade-bed stress equation to the Stokes deformation number

will now provide a better representation of the external stress in a high shear granulator. The characterised blade-bed stress can also be applied in scaling-up of high shear granulators, i.e. keeping the same blade-bed stress in different scales.

This work also introduced a novel, telemetric impeller stress sensor to measure the instantaneous blade-bed stress. Study of the blade-bed stress changes during the granulation process highlights the potential use of the system for granulation monitoring. Moreover, the blade-bed stress profile seems to show similar trends during granulation as that generally observed from impeller torque or power consumption curves, which are commonly used monitoring measurements. Employing the blade-bed stress measurements instead of torque or power can be advantageous as it gives direct knowledge on the stress experienced by the granule bed which can be used for granule growth kinetics or growth behaviour studies. The sensor can also be further developed to enhance the sampling rate capability for variability/fluctuation studies. Due to the incapability of the high shear granulator used in this thesis's work in measuring the impeller torque, another interesting area of study will be the correlation between the blade-bed stress and impeller torque.

In this thesis, characterisation of the wet beds is carried out for different liquid contents using water and a more viscous HPC solution. It will be of interest to investigate the effect of very viscous liquids on the bed flow and on the blade-bed stress characterisation. In addition, the wet beds can also be characterised in terms of bed cohesion and frictional properties from shear cell measurements, especially for wet granule/powder beds with liquid filled pores. DEM simulations for cohesive beds can also be applied for further insight on the bed flow and blade-bed stress characterisation for different liquid properties, where such existing models have incorporated liquid bridges into the particle bed (pendular state only) (Murugama et al., 2000; Radl et al., 2010; Washino, 2011).

References

- Adams, M.J., Edmondson, B., 1987. Forces between particles in continuous and discrete liquid media, in: Briscoe, B.J., Adams, M.J. (Eds.), *Tribology in Particulate Technology*, Adams Hilger, Bristol, pp. 154-172.
- Adams, M.J., Mullier, M.A., Seville, J.P.K., 1994. Agglomerate strength measurement using a uniaxial confined compression test, *Powder Technology*, 78, 5-13.
- Adrian, R.J., 1991. Particle-imaging techniques for experimental fluid mechanics, *Annual Review of Fluid Mechanics*, 23, 261-304.
- Bagster, D.F., Bridgwater, J., 1967. The measurement of the force needed to move blades through a bed of cohesionless granules, *Powder Technology*, 1, 189-198.
- Bagster, D.F., Bridgwater, J., 1969. The flow of granular material over a moving blade, *Powder Technology*, 3, 323-338.
- Bashaiwoldu, A.B., Podczeczek, F., Newton, J.M., 2004. Application of dynamic mechanical analysis (DMA) to determine the mechanical properties of pellets, *International Journal of Pharmaceutics*, 269, 329-342.
- Beer, F.P., Johnson, E.R., 1976. *Mechanics for Engineers - Statics and Dynamics*. McGraw Hill, New York.
- Bika, D.G., Gentzler, M., Michaels, J.N., 2001. Mechanical properties of agglomerates, *Powder Technology*, 117, 98-112.
- Blake, G.R., Hartge, K.H., 1986. Particle density, in: Klute, A. (Ed.), *Methods of soil analysis. Part 1. Physical and mineralogical methods*, 2nd edition ed, American Society of Agronomy, Inc., Madison, Wisconsin, pp. 377-382.
- Campbell, C.S., 2006. Granular material flows - An overview, *Powder Technology*, 162, 208-229.
- Cavinato, M., Bresciani, M., Machin, M., Bellazzi, G., Canu, P., Santomaso, A.C., 2010. Formulation design for optimal high-shear wet granulation using on-line torque measurements, *International Journal of Pharmaceutics*, 387, 48-55.
- Chalmers, G.F., 1982. Part I: Electrical Resistance Strain Gauges. Materials, Construction, Performance and Characteristics, in: Window, A.L., Holister, G.S. (Eds.), *Strain Gauge Technology*, Applied Science Publisher, Essex, England, pp. 1-38.
- Chandratilleke, G.R., Yu, A.B., Stewart, R.L., Bridgwater, J., 2009. Effects of blade rake angle and gap on particle mixing in a cylindrical mixer, *Powder Technology*, 103, 303-311.
- Cheong, Y.S., Adams, M.J., Hounslow, M.J., Salman, A.D., 2005. Mechanical behaviour of dry binderless polystyrene granules, *Chemical Engineering Research and Design*, 83, 1276-1282.
- Chitu, T.M., Oulahna, D., Hemati, M., 2011. Wet granulation in laboratory-scale high shear mixers: Effect of chopper presence, design and impeller speed, *Powder Technology*, 206, 34-43.

- Cliff, M.J., 1990. Granulation end point and automated process control: Part 1, *Pharmaceutical Technology*, 14, 112-132.
- Conway, S.L., Lekhal, A., Khinast, J.G., Glasser, B.J., 2005. Granular flow and segregation in a four-bladed mixer, *Chemical Engineering Science*, 60, 7091-7107.
- Corvari, V., Fry, W.C., Seibert, W.L., Augsburger, L., 1992. Instrumentation of a high-shear mixer: evaluation and comparison of a new capacitive sensor, a watt meter, and a strain-gage torque sensor for wet granulation monitoring, *Pharmaceutical Research*, 9, 1525-1533.
- Coury, J.R., Aguiar, M.L., 1995. Rupture of dry agglomerates, *Powder Technology*, 85, 37-43.
- Cundall, P.A., Strack, O.D.L., 1979. A discrete numerical model for granular assemblies, *Geotechnique*, 29, 47-65.
- Darelius, A., Lennartsson, E., Rasmuson, A., Bjorn, I.N., Folestad, S., 2007. Measurement of the velocity field and frictional properties of wet masses in a high shear mixer, *Chemical Engineering Science*, 62, 2366-2374.
- Darelius, A., Rasmuson, A., van Wachem, B., Bjorn, I.N., Folestad, S., 2008. CFD simulation of the high shear mixing process using kinetic theory of granular flow and frictional stress models, *Chemical Engineering Science*, 63, 2188-2197.
- Dorvlo, S., 2009. Agglomeration of food powders, Department of Chemical and Process Engineering, University of Sheffield, UK, PhD Thesis.
- Eliassen, H., Kristensen, H.G., Schaefer, T., 1999. Growth mechanisms in melt agglomeration with a low viscosity binder, *International Journal of Pharmaceutics*, 186, 149-159.
- Eliassen, H., Schaefer, T., Kristensen, H.G., 1998. Effects of binder rheology on melt agglomeration in a high shear mixer, *International Journal of Pharmaceutics*, 176, 73-83.
- Ennis, B.J., Litster, J.D., 1997. Particle Size Enlargement, in: Perry, R.H., Green, D.W. (Eds.), *Perry's Chemical Engineers' Handbook*, 7th ed, McGraw-Hill, New York, pp. 56-89.
- Ennis, B.J., Tardos, G., Pfeffer, R., 1991. A microlevel-based characterization of granulation phenomena, *Powder Technology*, 65, 257-272.
- Fu, J., 2006. Impact deformation, rebounding and breakage of high quality wet granules, Department of Chemical and Process Engineering, University of Sheffield, UK, PhD Thesis.
- Fu, J., Chan, E.L., Song, T., Gilmour, C.M., Hounslow, M.J., Salman, A.D., 2009. Characterisation and measurement of impeller stress in high shear granulation, 9th International Symposium on Agglomeration, Sheffield, UK.
- Fu, J., Reynolds, G.K., Adams, M.J., Hounslow, M.J., Salman, A.D., 2005. An experimental study of the impact breakage of wet granules, *Chemical Engineering Science*, 60, 4005-4018.
- Fu, J., Tan, H.S., Dodd, M., 2011. Fundamentals of product makeup in high shear mixer, 5th International Granulation Workshop, Lausanne, Switzerland, Paper No. 91.
- FujifilmCorporation, 2012a. Prescale: Overview, Available from: <http://www.fujifilm.com/products/prescale/prescalefilm/>.
- FujifilmCorporation, 2012b. Prescale: Specifications, Available from: <http://www.fujifilm.com/products/prescale/prescalefilm/specifications/>.

- Gabbott, I., 2007. Designer granules: Beating the trade-off between granule strength and dissolution time, Department of Chemical and Process Engineering, University of Sheffield, UK, PhD Thesis.
- Ganderton, D., Hunter, B.M., 1971. A comparison of granules prepared by pan granulation and by massing and screening, *Journal of Pharmacy and Pharmacology*, 23, 1-10.
- Ghanta, S.R., Srinivas, R., Rhodes, C.T., 1984. Use of mixer-torque measurements as an aid to optimizing wet granulation process, *Drug Development and Industrial Pharmacy*, 10, 305-311.
- Green, D.W., Perry, R.H., 2008. *Perry's Chemical Engineers' Handbook*, 8th ed., McGraw-Hill Publishing.
- Gui, L.C., Merzkirch, W., 1996. A method for tracking ensembles of particle images, *Experiments in Fluids*, 21, 465-468.
- Hapgood, K.P., Iveson, S.M., Litster, J.D., Liu, L.X., 2007. Granulation Rate Processes, in: Salman, A.D., Hounslow, M.J., Seville, J.P.K. (Eds.), *Handbook of Powder Technology: Granulation*, Elsevier Science, Amsterdam, pp. 897-978.
- Heckel, R.W., 1961. Density pressure relationship in powder compaction, *Transactions of the Metallurgical Society of AIME*, 221, 671-675.
- Heckmann, W., Hilgers, S., Merzkirch, W., Schluter, T., 1994. Automatic evaluation of double-exposed PIV records by an autocorrelation, *Optical methods and data processing in heat and fluid flow II*. Institute of Mechanical Engineers, London, pp. 5-8.
- Heiskanen, J., 1992. Comparison of three methods for determining the particle density of soil with liquid pycnometers, *Communications in Soil Science and Plant Analysis*, 23, 841-846.
- Hiramatsu, Y., Oka, Y., 1966. Determination of the tensile strength of rock by a compression test of an irregular test piece, *International Journal of Rock Mechanics and Mining Sciences & Geomechanics Abstracts*, 3, 89-99.
- Holm, P., Bonde, M., Wigmore, T., 1996. Pelletization by Granulation in a Roto-Processor RP-2. Part I: Effects of Process and Product Variables on Granule Growth, *Pharmaceutical Technology Europe*, 8, 22-37.
- Holm, P., Jungersen, O., Schaefer, T., 1984. Granulation in high speed mixers: Part 2. Effects of process variables during kneading, *Pharmazeutische Industrie*, 46, 97-101.
- Holm, P., Jungersen, O., Schaefer, T., Kristensen, H.G., 1983. Granulation in high speed mixers: Part 1: Effects of process variables during kneading, *Pharmazeutische Industrie*, 45, 806-811.
- Holm, P., Schaefer, T., Kristensen, H.G., 1985a. Granulation in high-speed mixers Part V. Power consumption and temperature changes during granulation, *Powder Technology*, 43, 213-223.
- Holm, P., Schaefer, T., Kristensen, H.G., 1985b. Granulation in high-speed mixers Part VI. Effects of process conditions on power consumption and granule growth, *Powder Technology*, 43, 225-233.
- Hoomans, B.P.B., Kuipers, J.A.M., Briels, W.J., Swaaij van, W.P.M., 1996. Discrete particle simulation of bubble and slug formation in a two-dimensional gas-fluidised bed: A hard-sphere approach, *Chemical Engineering Science*, 51, 99-118.

- Hoornaert, F., Wauters, P.A.L., Meesters, G.M.H., Pratsinis, S.E., Scarlett, B., 1998. Agglomeration behaviour of powders in a Lodige mixer granulator, *Powder Technology*, 96, 116-128.
- Horsthuis, G.J.B., van Laarhoven, J.A.H., van Rooij, R.C.B.M., Vromans, H., 1993. Studies on upscaling parameters of the Gral high shear granulation process, *International Journal of Pharmaceutics*, 92, 143-150.
- IMAPharma, 2012a. Roto Cube - High shear granulator dryer, Available from: http://www.ima-pharma.com/Product/EN/Products-F575/Solid_Dose_Processing_%2f_Manufacturing-S591/Granulation-T601/High_shear_mixer_granulators-Q603/Roto_Cube___High_shear_granulator_dryer-M3.html.
- IMAPharma, 2012b. Roto Mix – High shear mixers for wet granulation, Available from: http://www.ima-pharma.com/Product/EN/Products-F575/Solid_Dose_Processing_%2f_Manufacturing-S591/Granulation-T601/High_shear_mixer_granulators-Q603/Roto_Mix_%E2%80%93_High_shear_mixers_for_wet_granulation-M4.html.
- Iveson, S.M., Beathe, J.A., Page, N.W., 2002. The dynamic strength of partially saturated powder compacts: The effect of liquid properties, *Powder Technology*, 127, 149-161.
- Iveson, S.M., Litster, J.D., 1998a. Fundamental studies of granule consolidation Part 2: Quantifying the effects of particle and binder properties, *Powder Technology*, 99, 243-250.
- Iveson, S.M., Litster, J.D., 1998b. Growth regime map for liquid-bound granules, *AIChE Journal*, 44, 1510-1518.
- Iveson, S.M., Litster, J.D., 1998c. Liquid-bound granule impact deformation and coefficient of restitution, *Powder Technology*, 99, 234-242.
- Iveson, S.M., Litster, J.D., Ennis, B.J., 1996. Fundamental studies of granule consolidation Part 1. Effects of binder content and binder viscosity, *Powder Technology*, 88, 15-20.
- Iveson, S.M., Litster, J.D., Hapgood, K., Ennis, B.J., 2001a. Nucleation, growth and breakage phenomena in agitated wet granulation processes: A review, *Powder Technology*, 117, 3-39.
- Iveson, S.M., Wauters, P.A.L., Forrest, S., Litster, J.D., Meesters, G.M.H., Scarlett, B., 2001b. Growth regime map for liquid-bound granules: Further development and experimental validation, *Powder Technology*, 117, 83-97.
- Johnson, K.L., 1985. *Contact Mechanics*. Cambridge University Press, Cambridge, UK.
- Jumikis, A.R., 1962. Active and passive earth pressure coefficient tables. Bureau of Engineering Research, New Jersey.
- Kawakita, K., Ludde, K., 1971. Some considerations on powder compression equations, *Powder Technology*, 4, 61-68.
- Keane, R.D., Adrian, R.J., 1990. Optimization of particle image velocimeters. Part I: Double pulsed systems, *Measurement Science and Technology*, 1, 1202-1215.
- Keningley, S.T., Knight, P.C., Marson, A.D., 1997. An investigation into the effects of binder viscosity on agglomeration behaviour, *Powder Technology*, 91, 95-103.

- Knight, P.C., 1993. An investigation of the kinetics of granulation using a high-shear mixer, *Powder Technology*, 77, 159-169.
- Knight, P.C., Johansen, A., Kristensen, H.G., Schaefer, T., Seville, J.P.K., 2000. An investigation of the effects on agglomeration of changing the speed of a mechanical mixer, *Powder Technology*, 110, 204-209.
- Knight, P.C., Seville, J.P.K., Wellm, A.B., Instone, T., 2001. Prediction of impeller torque in high shear powder mixers, *Chemical Engineering Science*, 56, 4457-4471.
- Kopcha, M., Roland, E., Bubb, G., Vadino, W.A., 1992. Monitoring the granulation process in a high shear mixer/granulator: An evaluation of three approaches to instrumentation, *Drug Development and Industrial Pharmacy*, 18, 1945-1968.
- Kristensen, H.G., Schaefer, T., 1987. Granulation: a review on pharmaceutical wet-granulation, *Drug Development and Industrial Pharmacy*, 13, 803-872.
- Kuo, H.P., Knight, P.C., Parker, D.J., Tsuji, Y., Adams, M.J., Seville, J.P.K., 2002. The influence of DEM simulation parameters on the particle behaviour in a V-mixer, *Chemical Engineering Science*, 57, 3621-3638.
- Lekhal, A., Conway, S.L., Glasser, B.J., Khinast, J.G., 2006. Characterization of granular flow of wet solids in a bladed mixer, *AIChE Journal*, 52, 2757-2766.
- Leuenberger, H., 1982. Granulation, new techniques., *Pharmaceutica Acta Helvetica*, 57, 72-82.
- Leuenberger, H., Luy, B., Studer, J., 1990. New development in the control of a moist agglomeration and pelletization process, *STP Pharma Sciences*, 6, 303-309.
- Levin, M., 2007. Wet Granulation: End-point Determination and Scale-up, in: Swarbrick, J. (Ed.), *Encyclopedia of Pharmaceutical Technology*, 3rd ed, Informa Healthcare, New York, USA, pp. 4078-4098.
- Lindberg, N.O., Leander, L., Nilsson, P.G., Reenstierna, B., 1977. Studies on granulation in a small planetary mixer. I. Instrumentation, *Acta Pharmaceutica Suecica*, 14, 191-196.
- Litster, J.D., Ennis, B.J., 2004. *The Science and Engineering of Granulation Processes*, 1st ed., Kluwer Academic Publishers.
- Litster, J.D., Hapgood, K.P., Michaels, J.N., Sims, A., Roberts, M., Kameneni, S.K., 2002. Scale-up of mixer granulators for effective liquid distribution, *Powder Technology*, 124, 272-280.
- Liu, L.X., Litster, J.D., Iveson, S.M., Ennis, B.J., 2000. Coalescence of deformable granules in wet granulation processes, *AIChE Journal*, 46, 529-539.
- Liu, L.X., Smith, R., Litster, J.D., 2009. Wet granule breakage in a breakage only high-shear mixer: Effect of formulation properties on breakage behaviour, *Powder Technology*, 189, 158-164.
- Mackaplow, M.B., Rosen, L.A., Michaels, J.N., 2000. Effect of primary particle size on granule growth and endpoint determination in high-shear wet granulation, *Powder Technology*, 108, 32-45.

- Makishima, S., Shirai, T., 1968. Experimental study on the power requirements for agitating beds of solid particles, and proposal of a new model, *Journal of Chemical Engineering of Japan*, 1, 168-174.
- Mangwandi, C., Adams, M.J., Hounslow, M.J., Salman, A.D., 2011. Effect of batch size on mechanical properties of granules in high shear granulation, *Powder Technology*, 206, 44-52.
- Mangwandi, C., Cheong, Y.S., Adams, M.J., Hounslow, M.J., Salman, A.D., 2007. The coefficient of restitution of different representative types of granules, *Chemical Engineering Science*, 62, 437-450.
- Marzouk, Y.M., Hart, D.P., 1998. Assymmetric autocorrelation function to resolve ambiguity in PIV images, *Experiments in Fluids*, 25, 401-408.
- McGeary, R.K., 1961. Mechanical packing of spherical particles, *Journal of the American Ceramic Society*, 44, 513-522.
- Mindlin, R.D., 1949. Compliance of elastic bodies in contact, *Journal of Applied Mechanics*, 71, 259-268.
- Mori, N., Chang, K.-A., 2009. Introduction to MPIV - PIV toolbox in MATLAB, Available from: http://www.oceanwave.jp/software/mpiv_doc/index.html.
- Mort, P.R., 2005. Scale-up of binder agglomeration processes, *Powder Technology*, 150, 86-103.
- Mort, P.R., 2009. Scale-up and control of binder agglomeration processes - Flow and stress fields, *Powder Technology*, 189, 313-317.
- Murugama, Y., Tanaka, T., Tsuji, Y., 2000. Numerical simulation of particulate flow with liquid bridge between particles (simulation of centrifugal tumbling granulator), *Powder Technology*, 109, 49-57.
- Nedderman, R.M., 1992. *Statics and Kinematics of Granular Materials*. Cambridge University Press, Cambridge.
- Newitt, D.M., Conway-Jones, J.M., 1958. A contribution to the theory and practice of granulation, *Transactions of the Institution of Chemical Engineers*, 36, 422-441.
- Nilpawar, A.M., Reynolds, G.K., Salman, A.D., Hounslow, M.J., 2006. Surface velocity measurement in a high shear mixer, *Chemical Engineering Science*, 61, 4172-4178.
- Ohike, A., Ashihara, K., Ibuki, R., 1999. Granulation monitoring by fast fourier transform technique, *Chemical & Pharmaceutical Bulletin*, 47, 1734-1739.
- Ohno, I., Hasegawa, S., Yada, S., Kusai, A., Moribe, K., Yamamoto, K., 2007. Importance of evaluating the consolidation of granules manufactured by high shear mixer, *International Journal of Pharmaceutics*, 338, 79-86.
- Ouchiyama, N., Tanaka, T., 1975. Probability of coalescence in granulation kinetics, *Industrial & Engineering Chemistry Process Design and Development*, 14, 286-289.
- Ouchiyama, N., Tanaka, T., 1980. Stochastic model for compaction of pellets in granulation, *Industrial & Engineering Chemistry Process Design and Development*, 19, 555-560.
- Oulahna, D., Cordier, F., Galet, L., Dodds, J.A., 2003. Wet granulation: The effect of shear on granule properties, *Powder Technology*, 130, 238-246.

- Pepin, X., Simons, S.J.R., Blanchon, S., Rossetti, D., Couarraze, G., 2001. Hardness of moist agglomerates in relation to interparticle friction, granule liquid content and nature, *Powder Technology*, 117, 123-138.
- Picker-Freyer, K.M., Dürig, T., 2007. Physical mechanical and tablet formation properties of hydroxypropylcellulose: In pure form and in mixtures, *AAPS PharmSciTech*, 8, E1-E9.
- Pitchumani, R., Zhupanska, O., Meesters, G.M.H., Scarlett, B., 2004. Measurement and characterization of particle strength using a new robotic compression tester, *Powder Technology*, 143-144, 56-64.
- Plank, R., Diehl, B., Grinstead, H., Zega, J., 2003. Quantifying liquid coverage and powder flux in high-shear granulators, *Powder Technology*, 134, 223-234.
- Radl, S., Kalvoda, E., Glasser, B.J., Khinast, J.G., 2010. Mixing characteristics of wet granular matter in a bladed mixer, *Powder Technology*, 200, 171-189.
- Ramaker, J.S., Jelgersma, M.A., Vonk, P., Kossen, N.W.F., 1998. Scale-down of a high-shear pelletisation process: Flow profile and growth kinetics, *International Journal of Pharmaceutics*, 166, 89-97.
- Ramirez, A., Nielsen, J., Ayuga, F., 2010. On the use of plate-type normal pressure cells in silos. Part 1: Calibration and evaluation, *Computers & Electronics in Agriculture*, 71, 71-76.
- Realpe, A., Velazquez, C., 2008. Growth kinetics and mechanism of wet granulation in a laboratory-scale high shear mixer: Effect of initial polydispersity of particle size, *Chemical Engineering Science*, 63, 1602-1611.
- Redding, T.E., Hannam, K.D., Quideau, S.A., Devito, K.J., 2005. Particle density of aspen, spruce, and pine forest floors in Alberta, Canada, *Soil Science Society of America Journal*, 69, 1503-1506.
- Remy, B., Canty, T.M., Khinast, J.G., Glasser, B.J., 2010. Experiments and simulations of cohesionless particles with varying roughness in a bladed mixer, *Chemical Engineering Science*, 65, 4557-4571.
- Remy, B., Glasser, B.J., 2010. The effect of mixer properties and fill level on granular flow in a bladed mixer, *AIChE Journal*, 56, 336-353.
- Remy, B., Khinast, J.G., Glasser, B.J., 2009. Discrete element simulation of free flowing grains in a four-bladed mixer, *AIChE Journal*, 55, 2035-2048.
- Reynolds, G.K., Phung, K.L., Nilpawar, A.M., 2007. High Shear Granulation, in: Salman, A.D., Hounslow, M.J., Seville, J.P.K. (Eds.), *Handbook of Particle Technology: Granulation*, Elsevier Science, Amsterdam, pp. 3-21.
- Ritala, M., Holm, P., Schaefer, T., Kristensen, H.G., 1988. Influence of liquid bonding strength on power consumption during granulation in a high shear mixer, *Drug Development and Industrial Pharmacy*, 14, 1041-1060.
- Rondet, E., Denavaut, M., Mandato, S., Duri, A., Ruiz, T., Cuq, B., 2012. Power consumption profile analysis during wet agglomeration process: Energy approach of wheat powder agglomeration, *Powder Technology*, 229, 214-221.
- Rumpf, H., 1962. The strength of granules and agglomerates, in: Knepper, W.A. (Ed.), *Agglomeration*, Wiley/Interscience, New York, pp. 379-418.

- Saito, Y., Fan, X., Ingram, A., Seville, J.P.K., 2011. A new approach to high-shear mixer granulation using positron emission particle tracking, *Chemical Engineering Science*, 66, 563-569.
- Samimi, A., Hassanpour, A., Ghadiri, M., 2005. Single and bulk compressions of soft granules: Experimental study and DEM evaluation, *Chemical Engineering Science*, 60, 3993-4004.
- Sastry, K.V.S., Fuerstenau, D.W., 1973. Mechanisms of agglomerate growth in green pelletization, *Powder Technology*, 7, 97-105.
- Schaefer, T., 1995. Melt pelletization in a high shear mixer VI. Agglomeration of a cohesive powder *International Journal of Pharmaceutics*, 132, 221-230.
- Schaefer, T., 2001. Growth mechanisms in melt agglomeration in high shear mixers, *Powder Technology*, 117, 68-82.
- Schaefer, T., Holm, P., Kristensen, H.G., 1986. Comparison between granule growth in a horizontal and a vertical high speed mixer: I. Granulation of dicalcium phosphate, *Archiv for Pharmaci og Chemi Scientific Edition*, 14, 209-224.
- Schaefer, T., Holm, P., Kristensen, H.G., 1990. Melt granulation in a laboratory scale high shear mixer, *Drug Development and Industrial Pharmacy*, 16, 1249-1277.
- Schaefer, T., Holm, P., Kristensen, H.G., 1992. Melt pelletization in a high shear mixer. II. Power consumption and granule growth, *Acta Pharmaceutica Nordica*, 4, 141-148.
- Schaefer, T., Mathiesen, C., 1996. Melt pelletization in a high shear mixer. VIII. Effects of binder viscosity, *International Journal of Pharmaceutics*, 139, 125-138.
- Schaefer, T., Taagegaard, B., Thomsen, L., Kristensen, H., 1993. Melt pelletization in a high shear mixer. V. Effects of apparatus variables, *European Journal of Pharmaceutical Science*, 1, 133-141.
- Schubert, H.G., 1975. Tensile-strength of agglomerates, *Powder Technology*, 11, 107-119.
- Scott, A.C., Hounslow, M.J., Instone, T., 2000. Direct evidence of heterogeneity during high-shear granulation, *Powder Technology*, 113, 205-213.
- Seo, A., Schaefer, T., 2001. Melt agglomeration with polyethylene glycol beads at a low impeller speed in a high shear mixer, *European Journal of Pharmaceutics and Biopharmaceutics*, 52, 315-325.
- Sherrington, P.J., 1981. *Granulation (Monographs in Powder Science and Technology)*. Heyden and Son Ltd, UK.
- Simons, S.J.R., Pepin, X., 2003. Hardness of moist agglomerates in relation to interparticle friction, capillary and viscous forces, *Powder Technology*, 138, 57-62.
- Snow, R.H., Allen, T., Ennis, B.J., Litster, J.D., 1997. Size Reduction and Size Enlargement, in: Perry, R.H., Green, D.W. (Eds.), *Perry's Chemical Engineers' Handbook*, McGraw-Hill, USA.
- Staniforth, J.N., Quincey, S.M., 1986. Granulation monitoring in a planetary mixer using a probe vibration analysis technique, *International Journal of Pharmaceutics*, 32, 177-185.
- Staniforth, J.N., Walker, S., Flanders, P., 1986. Granulation monitoring in a high-speed mixer processor using a probe vibration analysis technique, *International Journal of Pharmaceutics*, 31, 277-280.

- Stewart, R.L., Bridgwater, J., Zhou, Y.C., Yu, A.B., 2001. Simulated and measured flow of granules in a bladed mixer - a detailed comparison, *Chemical Engineering Science*, 56, 5457-5471.
- Talu, I., Tardos, G.I., Ruud Van Ommen, J., 2001. Use of stress fluctuations to monitor wet granulation of powders, *Powder Technology*, 117, 149-162.
- Tan, H.S., Salman, A.D., Hounslow, M.J., 2006. Kinetics of fluidised fed melt granulation 1-effect of process variables, *Chemical Engineering Science*, 61, 1585-1601.
- Tardos, G.I., Hapgood, K.P., Ipadeola, O.O., Michaels, J.N., 2004. Stress measurements in high-shear granulators using calibrated test particles: Application to scale-up, *Powder Technology*, 140, 217-227.
- Tardos, G.I., Khan, M.I., Mort, P.R., 1997. Critical parameters and limiting conditions in binder granulation of fine powders, *Powder Technology*, 94, 245-258.
- Terashita, K., Kato, M., Ohike, A., 1990a. Analysis of end-point with power consumption in high speed mixer, *Chemical & Pharmaceutical Bulletin*, 38, 1977-1982.
- Terashita, K., Watano, S., Miyanami, K., 1990b. Determination of end-point by frequency analysis of power consumption in agitation granulation, *Chemical & Pharmaceutical Bulletin*, 38, 3120-3123.
- Terzaghi, K., 1966. *Theoretical Soil Mechanics*. Wiley, New York.
- Theis, R., Kleinebudde, K., 1999. Melt pelletisation of a hygroscopic drug in a high shear mixer: Part 1. Influence of process variables, *International Journal of Pharmaceutics*, 188, 131-143.
- Tory, E.M., Church, B.H., Tam, M.K., Ratner, M., 1973. Simulated random packing of equal spheres, *Canadian Journal of Chemical Engineering*, 51, 484-493.
- Tsuji, Y., Tanaka, T., Ishida, T., 1992. Lagrangian numerical simulation of plug flow of cohesionless particles in a horizontal pipe, *Powder Technology*, 1992, 239-250.
- Tu, W.D., 2008. An investigation into the high shear wet granulation behaviours and the regime map development, Department of Mechanical Engineering, National Central University, Zhongli, Taiwan, PhD Thesis.
- Tu, W.D., Ingram, A., Seville, J., Hsiao, S.S., 2009. Exploring the regime map for high-shear mixer granulation, *Chemical Engineering Journal*, 145, 505-513.
- Van Den Dries, K., De Vegt, O.M., Girard, V., Vromans, H., 2003. Granule breakage phenomena in a high shear mixer; influence of process and formulation variables and consequences on granule homogeneity, *Powder Technology*, 133, 228-236.
- Van Den Dries, K., Vromans, H., 2002. Relationship between inhomogeneity phenomena and granule growth mechanisms in a high-shear mixer, *International Journal of Pharmaceutics*, 247, 167-177.
- Vonk, P., Guillaume, C.P.F., Ramaker, J.S., Vromans, H., Kossen, N.W.F., 1997. Growth mechanisms of high-shear pelletisation, *International Journal of Pharmaceutics*, 157, 93-102.
- Vromans, H., Poels-Janssen, H.G.M., Egermann, H., 1999. Effects of high-shear granulation on granulate homogeneity, *Pharmaceutical Development and Technology*, 4, 297-303.

- Walker, G.M., Andrews, G., Jones, D., 2006. Effect of process parameters on the melt granulation of pharmaceutical powders, *Powder Technology*, 165, 161-166.
- Washino, K., 2011. Multiscale modelling of nucleation processes in wet granulation using discrete element method and constrained interpolation profile, Department of Chemical and Biological Engineering, University of Sheffield, UK, PhD Thesis.
- Watano, S., Okamoto, T., Sato, Y., Osako, Y., 2005. Scale-up of high shear granulation based on the internal stress measurement, *Chemical & Pharmaceutical Bulletin*, 53, 351-354.
- Watano, S., Tanaka, T., Miyanami, K., 1995. A method for process monitoring and determination of operational end-point by frequency analysis of power consumption in agitation granulation, *Advanced Powder Technology*, 6, 91-102.
- Wellm, A.B., 1997. Investigation of a high shear mixer/agglomerate, University of Birmingham, UK, PhD Thesis.
- Willert, C.E., Gharib, M., 1991. Digital particle image velocimetry, *Experiments in Fluids*, 10, 181-193.
- Wynnyckyj, J.R., 1985. The correlation between the strength factor and the true tensile strength of agglomerate spheres, *The Canadian Journal of Chemical Engineering*, 63, 591-597.
- Zhou, Y.C., Wright, B.D., Yang, R.Y., Xu, B.H., Yu, A.B., 1999. Rolling friction in the dynamic simulation of sandpile formation, *Physica A: Statistical Mechanics and its Applications*, 269, 536-553.
- Zhou, Y.C., Yu, A.B., Stewart, R.L., Bridgwater, J., 2004. Microdynamic analysis of the particle flow in a cylindrical bladed mixer, *Chemical Engineering Science*, 59, 1343-1364.

Appendix A

Blade-bed stress measurements using pressure colouring films

A.1 Film description

The pressure colouring films (model name: Prescale) are manufactured by FujiFilm, Japan and (FujifilmCorporation, 2012a). The polyester-based films typically consist of two types of sheets: the A-film and C-film, each 100 μm in thickness. The A-film is coated with micro-capsules which contain colour-forming material, while the C-film is coated with colour-developing material. For measurement, the two coated sides of both sheets are brought into contact with each other and upon pressure, the micro-capsules on the A-film burst and release the colour-forming material which reacts with the colour-developing material on the C-film, thus producing coloured (red) patches. Certain grades of the film only have a single sheet which has both the colour-forming and colour-developing substances. The density of these patches varies according to the intensity of pressure applied. Figure A.1 shows a schematic diagram of the film. The manufacturer supplies different grades of the films, each with different pressure ranges from 0.05 MPa up to 300 MPa (Table A.1).

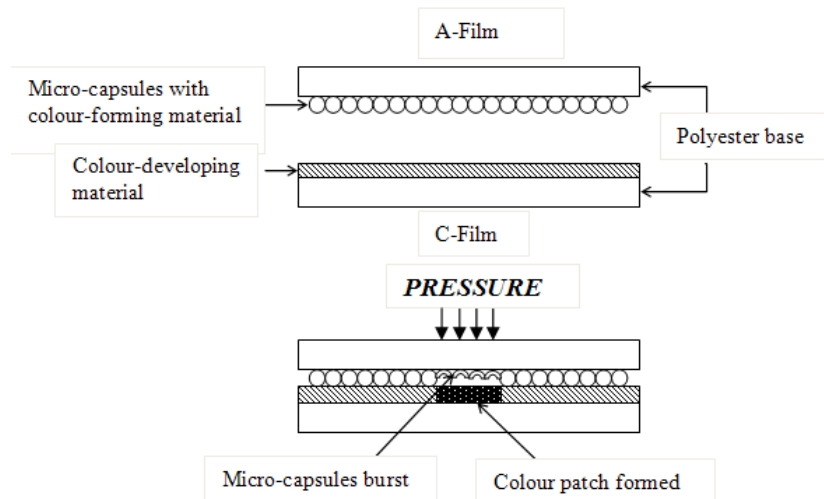


Figure A.1: Schematic diagram of the pressure colouring film.

Table A.1: Grades of the pressure films (FujiFilm Corporation, 2009a)

<i>Grade</i>	<i>Pressure range (MPa)</i>	<i>Type</i>
4LW (extreme low pressure)	0.05-0.2	Two sheet
3LW (ultra super low pressure)	0.2-0.6	Two sheet
2LW (super low pressure)	0.5-2.5	Two sheet
LW (low pressure)	2.5-10	Two sheet
MW (medium pressure)	10-50	Two sheet
MS (medium pressure)	10-50	Single sheet
HS (high pressure)	50-130	Single sheet
HHS (super high pressure)	130-300	Single sheet

Prior to actual stress measurements in the high shear granulator, some trial runs using the different grades of films were carried out to determine the suitable grade or grades of films. The trial runs showed that the 4LW and 3LW films gave reasonable colour patches while higher grades films (2LW, LW and MW) did not give rise to noticeable colour formation.

A.2 Film calibration

Pressure charts for the films are provided by the manufacturer. Figure A.2 shows a standard chart for the low pressure (LW) film (2.5 to 10 MPa). The different curves, A to D, represent different temperature and humidity conditions. To determine the corresponding pressure, the colour formed on the films is compared with those on the charts to estimate the colour density. Determination of the exact colour density visually is difficult using the provided charts. Instead, calibration of the film was carried out under the lab's ambient conditions for the colour density-pressure conversion. Using a Zwick/Roell Z0.5 compression machine (Figure 3.17 in Chapter 3), known values of pressures were applied on the film by the compression punch (diameter: 6 mm). Figure A.3 shows an example of coloured patches on a 4LW film compressed at a pressure of 0.15 MPa.

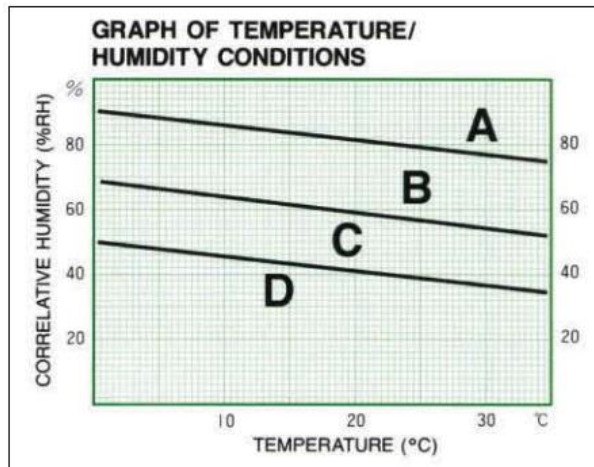
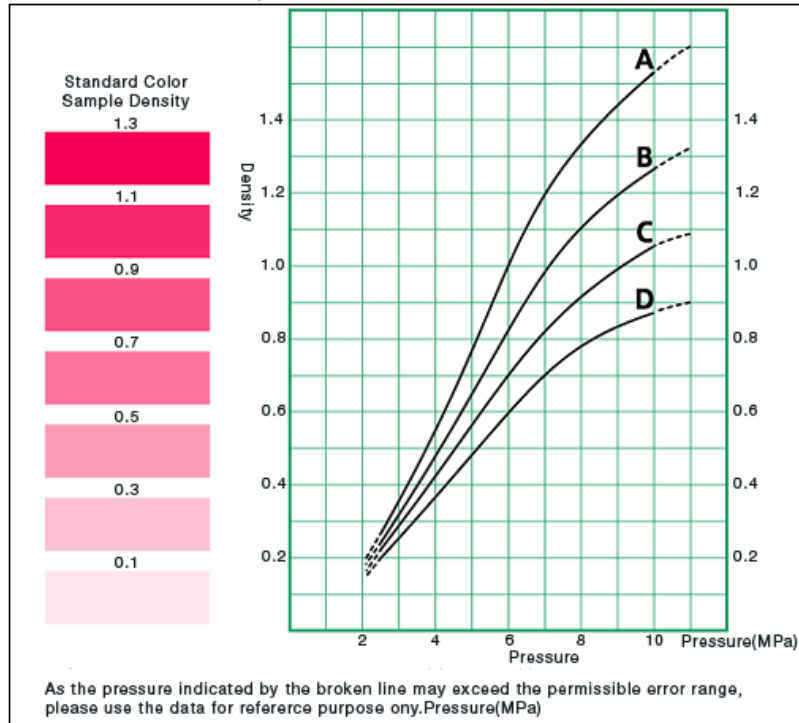


Figure A.2: Pressure chart for LW (low pressure) film (FujifilmCorporation, 2012b).

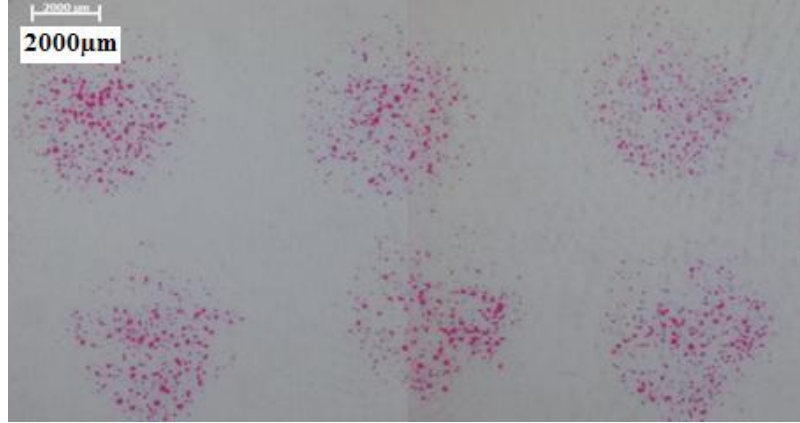


Figure A.3: Calibration image for a 4LW film: coloured patches from six compressions.

Using an image analysis software (AxioVision Rel 4.5), the coloured areas were segmented using a suitable pixel value thresholding and calculated. The colour density, ρ_c , is given in Equation A.1.

$$\rho_c = \frac{\text{Coloured area}}{\text{Total area}}$$

Equation A.1

Figure A.4 presents the calibration data for the 3LW and 4LW films and the resulting polynomial expressions. The ranges of pressures tested for each film were according to the ranges given by manufacturer as presented in Table A.1.

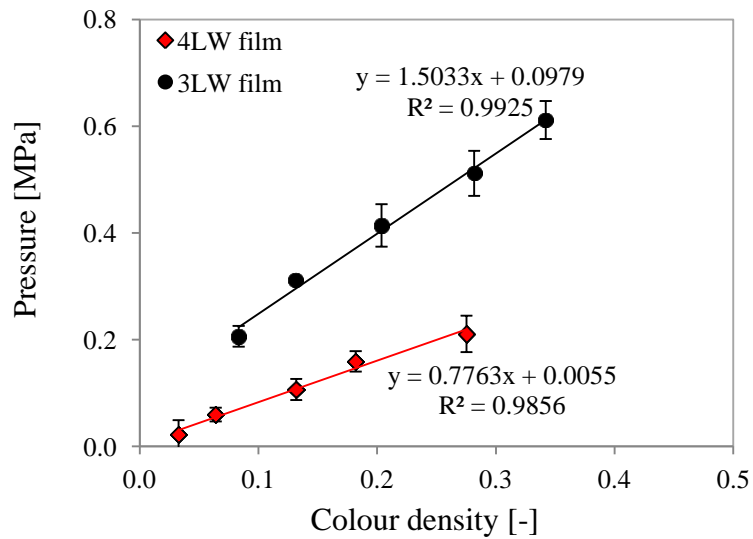


Figure A.4: Pressure calibration plots for 3LW and 4LW films.

A.3 Application for blade-granule bed stress measurements

For the blade-granule bed normal stress (pressure) measurements, the films were cut into strips of 3.0 x 0.5 cm and affixed onto the tip of each impeller blade using thin cellophane tape (Figure A.5a). Special care was taken when sticking to minimise the pressing of the films when the colour forming and colour developing surface are in contact. The impeller was placed in the granulator, followed by a typical granulation run: The powder formulation was loaded and pre-mixed (~1 min at 100 rpm) before water was sprayed. For the spraying, the 0.71 mm orifice, atomising spray nozzle (1/4" LNN SS Atomizing from Spraying Systems Limited) with a spraying pressure of 0.8 bar was used. This gave a spraying rate of ~65 g/min for water. The films were removed after a wet massing time of 5 minutes (i.e. 5 minutes after water addition finishes) for analysis. A typical coloured film after granulation is shown in Figure A.5b. Images of the films (under a suitable magnification) were then taken using a Carl Zeiss Stereo microscope and the coloured areas were segmented (Figure A.6) and computed with AxioVision and the colour density was calculated from Equation A.1. The colour density values were converted to normal stress (pressure values) using the polynomial expressions in Figure A.4.

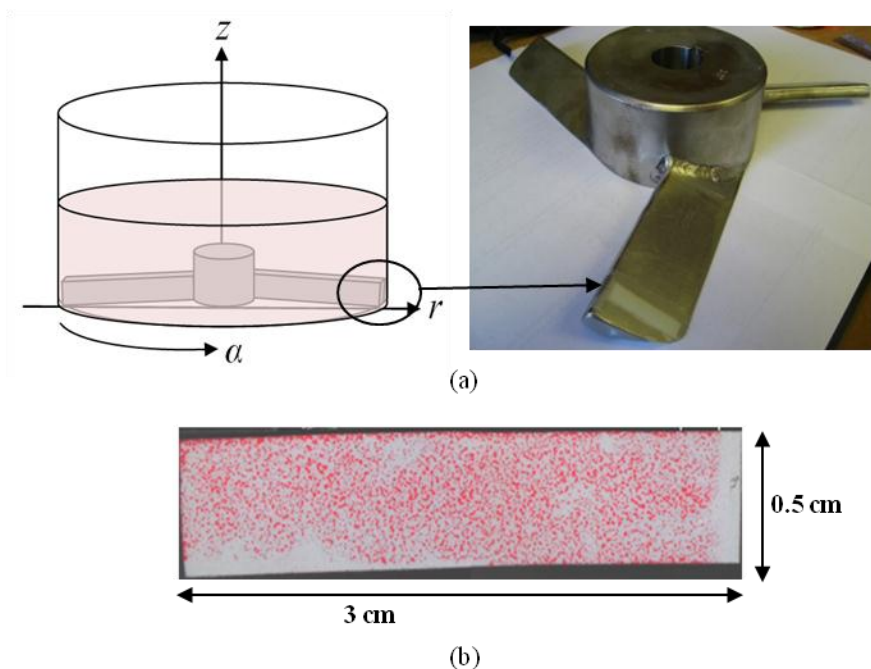


Figure A.5: Measurement using pressure films in the high shear granulator (a) film strip on the blade (b) film strip (C-film) after measurement.

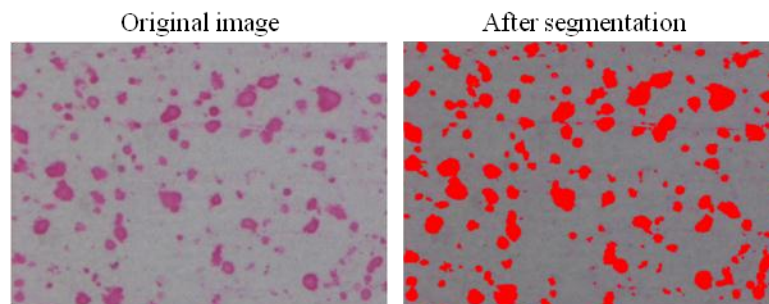


Figure A.6: Segmented areas (indicated by the bright red patches) of the film for area determination (x37.5 magnification - 2.3 mm x 1.6 mm).

Measurements using the films were carried out for wet granule beds using lactose monohydrate (Pharmatose 450 M) and hydroxypropyl methylcellulose, HPMC (Pharmacoat 603), both which are a common pharmaceutical excipient and binder respectively. Water was spray added into the powder to hydrate the HPMC for binding effect. Table A.2 presents the formulation, powder size data (measured using a Malvern mastersizer described in Chapter 3: Section 3.4.1) and granulation conditions. In addition to the impeller speed and bed load, the films were also used on impellers with different blade inclined angles.

Table A.2: Formulation and granulation conditions for pressure film measurements.

<i>Ingredients</i>	<i>% (w/w)</i>	<i>Particle size distribution</i>				
		<i>x₁₀ (μm)</i>	<i>x₅₀ (μm)</i>	<i>x₉₀ (μm)</i>	<i>Span</i>	<i>SSA* (m²/g)</i>
<i>α-lactose monohydrate (Pharmatose 450M)</i>	95	3.74	21.1	53.4	2.36	0.73
<i>HPMC (Pharmacoat 603)</i>	5	37.0	83.1	322.2	3.43	0.07
<i>*SSA – Specific surface area</i>						
<i>Parameters</i>	<i>Varying impeller speed</i>		<i>Varying impeller angle</i>		<i>Varying bed load</i>	
<i>Bed load, kg</i>	2.0		2.0		1.5, 2, 2.5, 3.0	
<i>Liquid to solid ratio (w/w)</i>	0.12		0.12		0.12	
<i>Impeller speed, rpm</i>	200, 300, 400, 500		400		400	
<i>Impeller angle, °</i>	32		27, 32, 38, 45		32	

Figure A.7 presents the blade-granule bed stress results using the pressure film method for all the granulation conditions listed in Table A.2. The bed surface velocity and height results are also included. Stress measurements were taken (film removed for analysis) after 5 minutes of wet massing time where granules were formed and growing steadily. From the results, the blade-bed stress ranges from ~50,000 to 400,000 Pa, at least a magnitude higher than those

measured using the impeller stress sensor system and the simulated stresses in Chapter 4, Chapter 6 and Chapter 5 for both dry and wet granule beds. Expected trends are still observed, i.e. the blade-bed stress increases with impeller speed, angle and bed load as obtained in Chapter 4 and Chapter 6's results.

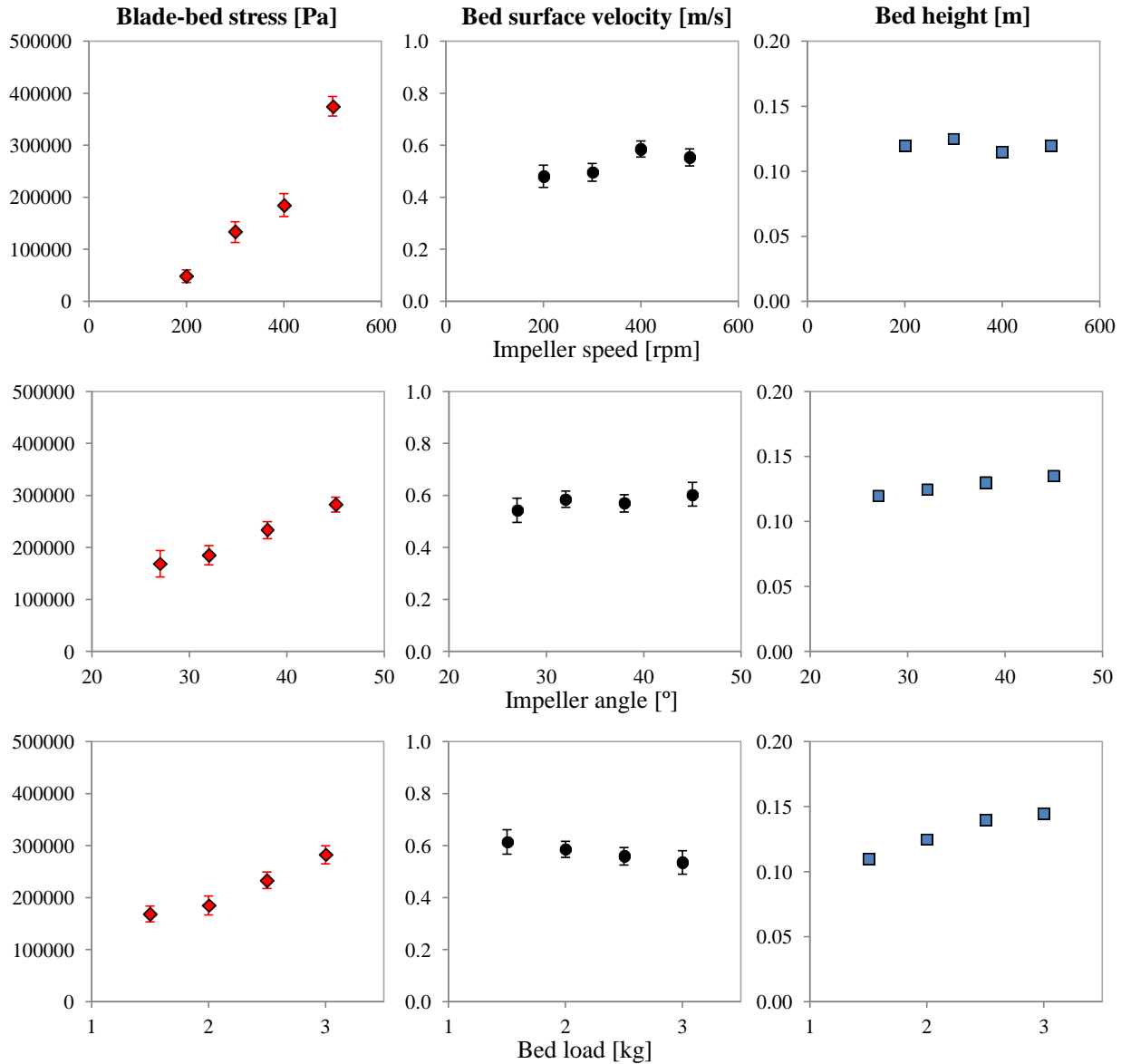


Figure A.7: Results for varying impeller speed, angle and bed load cases (pressure film method).

The blade-bed stresses were also calculated using the blade-bed stress equation introduced in Chapter 4 (Equation 4.8) without any correction factor. Values for the blade inclined height, h_I , are 0.015 m, 0.018 m, 0.021 m and 0.024 m for the 27°, 32°, 38° and 45° angled blades respectively. The bed bulk densities of granule beds were also measured at the time of the films' removal and are 0.6 to 0.7 kg/m³.

$$\sigma_{i(r)} = \frac{\rho_b H_{g,r} (v_I - v_g)^2 r^2 (1 - \cos\theta_I)}{h_I}$$

From: Equation 4.8

Figure A.8 displays the blade-bed stress measured with films plotted against the calculated values from Equation 4.8. A linear correlation was obtained and the proportionality constant is ~8 (i.e. the measured stress is 8 times larger than the calculated values even without correction factor). When the correction factor of $B_I = K_I/v_{rel}$ is applied to the blade-bed stress equation to account for the increasing bed “fluidisation” with impeller speed (which gives Equation 4.12) with the K_I value taken to be 1, the proportionality constant increases to ~50.

$$\sigma_{i(r)cor} = \frac{K_I \rho_b H_{g,r} (v_I - v_g) (1 - \cos\theta_I)}{h_I}$$

From: Equation 4.12

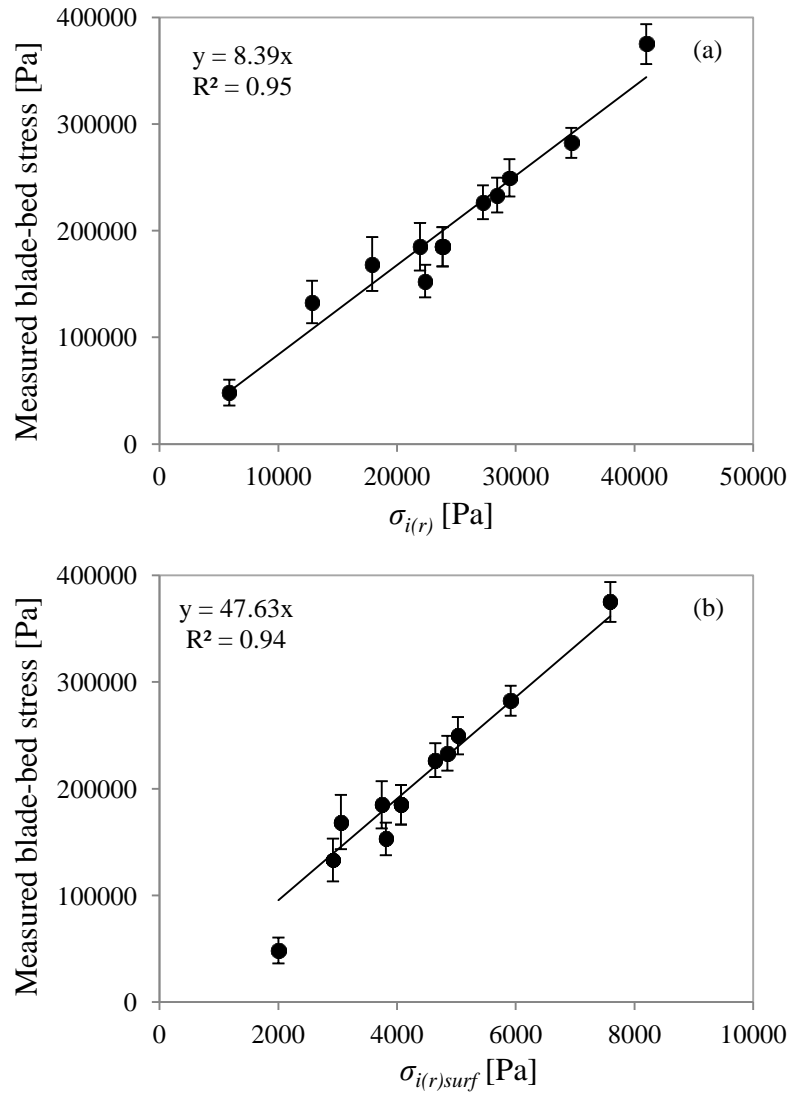


Figure A.8: Plotted measured blade-bed stress using the pressure films with (a) blade-bed stress equation (no correction factor, Equation 4.8) and (b) blade-bed stress model with correction factor $B_I = K_I/v_{rel}$ (Equation 4.12).

These results highlight that whilst the pressure films gave reasonable comparative blade-bed stresses for the different granulation conditions studied, the stress values with this method are evidently higher than the actual values. The films were removed after water spraying and 5 minutes of wet massing time and gave a build-up stress value over this time period, which was found to 1-2 magnitudes higher than the measured (impeller stress sensor), simulated and model-predicted values. Additional investigation on the effect of the measurement time on the film measurements is detailed in the following section.

A.4 Comparison with impeller stress sensor and time effect

For direct comparison of the film and sensor methods, the measurements using the pressure film with dimensions (22×22 mm) and at location identical to the impeller stress sensor (Figure A.9a) were carried out for the dry mannitol granule bed (1.5 kg, 0.5-1.0 mm sieve size). The films (4LW grade) were carefully attached on each blade, followed by the loading of the granules into the granulator and rotation of the impeller. The films were removed after a certain impeller rotation or measurement time. The above steps were repeated for several measurement times up to 60 seconds. Figure A.9a displays an example of the pressure film after a measurement. Observably, the colour distribution on the film shows a higher colour density and hence, stress towards the blade tip and bottom of the blade.

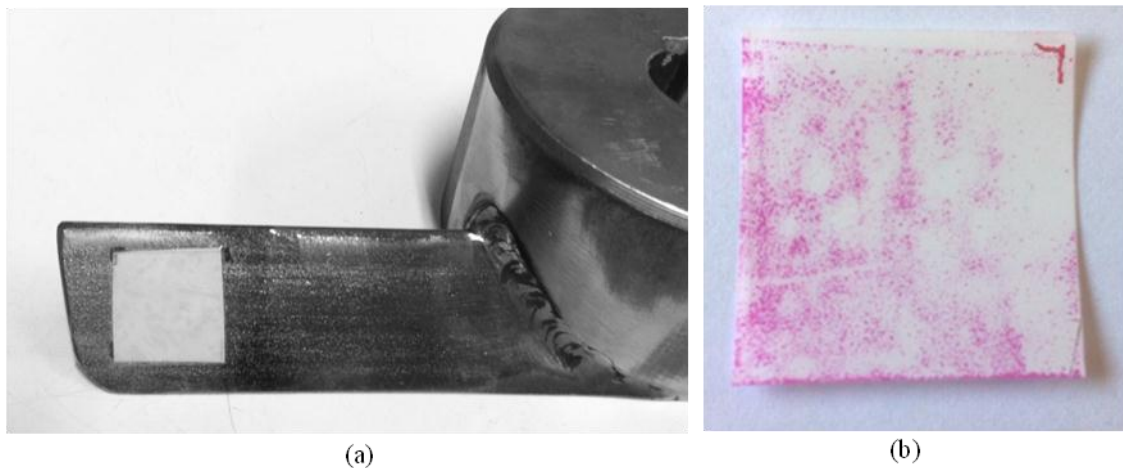


Figure A.9: Comparison with the impeller stress sensor (a) pressure film affixed onto the blade (b) pressure film (C-film) after measurement.

Figure A.10 presents the blade-bed stress data from both the film and sensor methods for 150 and 350 rpm impeller speeds. The dashed lines indicate the time-averaged stresses measured using the impeller sensor. Clearly, the results show a consistent increase of the blade-bed stress measured using the film with the measurement time. The film stresses are also higher than the sensor's after 10 seconds measurement time. This is the smallest measurement time achievable since very little colour is formed on the films for reliable analysis otherwise. After 60 seconds, the film stresses are found to be more than a magnitude higher than the sensor measurements. From the structure of the film and its working principle, this means that an increasing number of colour-containing micro-capsules on the A-film are being broken upon

contact with the granules with time, leading to more colour formation on the C-film. Figure A.11 shows images of the micro-capsules on a 4LW grade A-film taken with a Carl Zeiss Stereo microscope at different magnification rates where the size of the micro-capsules are smaller than $\sim 170 \mu\text{m}$. In the granulator, the blade and pressure film is continuously impacted by the granule bed when the impeller rotates. Consequently, different areas and micro-capsules on the film will be in contact with the granules continuously, resulting in a build-up of colour over time.

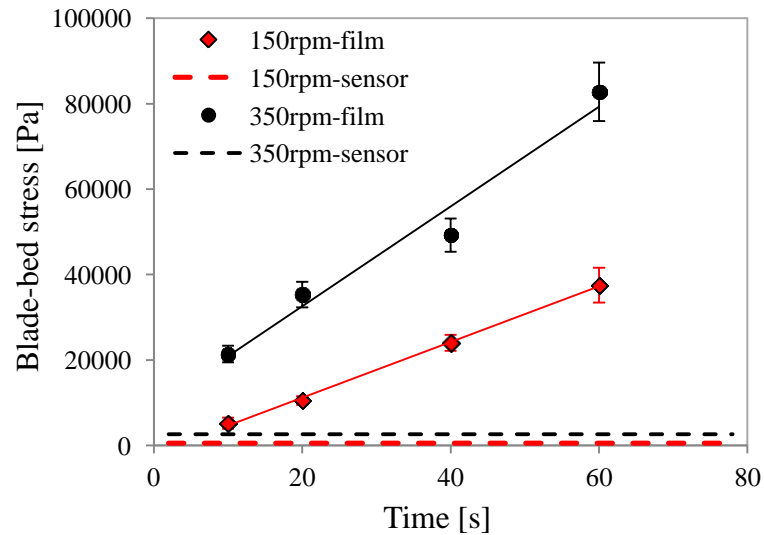


Figure A.10: Measured blade-bed stress using the impeller stress sensor and pressure film for 0.5-1.0 sieve size dry mannitol granules, 1.5kg bed load. Dashed lines represent the time-averaged values from the sensor measurements.

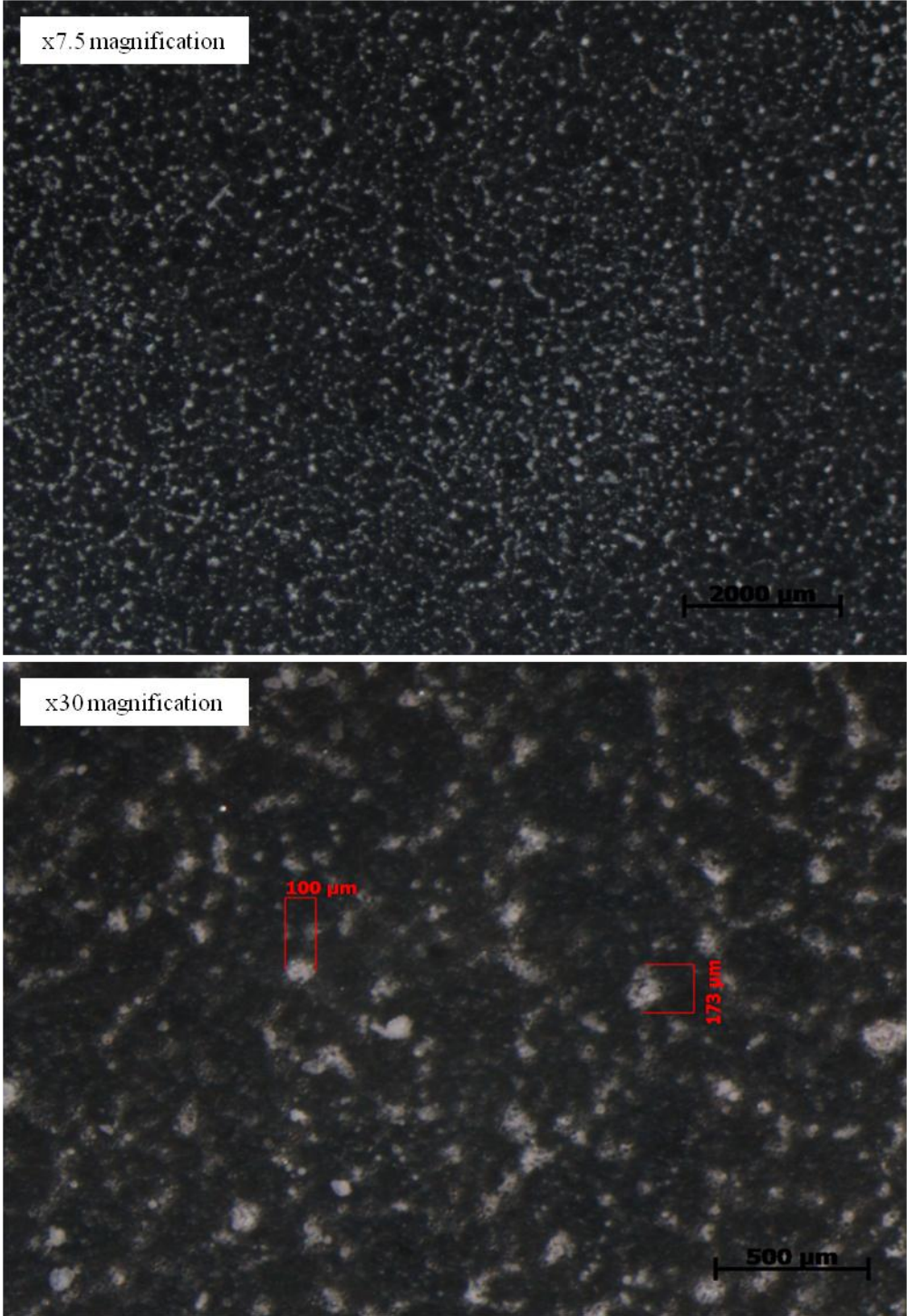


Figure A.11: Micro-capsules containing colour-forming material on the A-film (4LW grade).

Appendix B

Particle Imaging Velocimetry (PIV): further details

B.1 Overview of PIV algorithms

B.1.1 Auto-correlation algorithm

Applied for only multiple exposure images, e.g. double pulsed illumination using a pulsed laser method, the auto-correlation method (Adrian, 1991; Heckmann et al., 1994; Keane and Adrian, 1990; Marzouk and Hart, 1998) correlates interrogation areas within the same image (Figure B.1). The auto-correlation function (Marzouk and Hart, 1998) is given in Equation B.1, where Co is the correlation number in a particular interrogation area. The function is also normalised with the mean and standard deviation of the pixel values for that interrogation area. Therefore, Co values of 1 or 0 denote perfect or no correlation respectively. When Co is max (maximum correlation), then Δx and Δy are taken as the displacements. Directions of the velocity vectors, however, are ambiguous using this method as 2 displacement peaks are obtained (positive and negative).

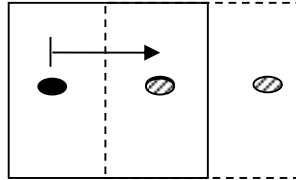


Figure B.1: Schematic of a multiple exposure image (arrow indicates the displacement vector).

$$Co(\Delta x, \Delta y) = \frac{\sum_{i=1}^N \sum_{j=1}^N [f_1(x_i, y_j) - \bar{f}_1][f_1(x_i + \Delta x, y_j + \Delta y) - \bar{f}_1]}{\sqrt{\sum_{i=1}^N \sum_{j=1}^N [f_1(x_i, y_j) - \bar{f}_1]^2} \sqrt{\sum_{i=1}^N \sum_{j=1}^N [f_1(x_i + \Delta x, y_j + \Delta y) - \bar{f}_1]^2}}$$

Equation B.1

B.1.2 Cross-correlation (COR) algorithm

For single exposure images with a fixed time interval, Δt , the PIV COR algorithm (Mori and Chang, 2009; Willert and Gharib, 1991) correlates interrogation areas of successive images. The COR equation, taken from Mori and Chang, is given in Equation B.2. Like the auto-correlation function, Co is the correlation number of a certain interrogation area and the function is also normalised with the mean and standard deviation of the pixel values in that interrogation area. Δx and Δy are taken as the displacements when Co is max. To reduce the influence of noise and eliminate invalid vectors, some additional specifications are set, i.e. the ratio between the maximum and second highest peak and the ratio between the maximum and rms (root mean square) error from noise signal is larger than critical values.

$$Co(\Delta x, \Delta y) = \frac{\sum_{i=1}^N \sum_{j=1}^N [f_1(x_i, y_j) - \bar{f}_1][f_2(x_i + \Delta x, y_j + \Delta y) - \bar{f}_2]}{\sqrt{\sum_{i=1}^N \sum_{j=1}^N [f_1(x_i, y_j) - \bar{f}_1]^2} \sqrt{\sum_{i=1}^N \sum_{j=1}^N [f_2(x_i + \Delta x, y_j + \Delta y) - \bar{f}_2]^2}}$$

Equation B.2

B.1.3 Minimum quadratic difference (MQD) algorithm

As described in Chapter 3: Section 3.2.2.3, the MQD algorithm (Gui and Merzkirch, 1996; Mori and Chang, 2009), which is used in this thesis, determines the displacements, Δx and Δy , from the minimum of the quadratic difference in pixel values of search areas between successive images (P in Equation B.3). This is analogous to the statistical least square method. The criteria to retain the velocity vector is the same as the COR algorithm.

$$P(\Delta x, \Delta y) = \min \left[\sum_{i=1}^{N_x} \sum_{j=1}^{N_y} \left| f_1(x_i, y_j) - f_2(x_i + \Delta x, y_j + \Delta y) \right| \right]$$

Equation B.3

B.2 Pixel-distance calibration

The top view of the granule bed in the high shear granulator was recorded using a high speed camera for the surface velocity analysis as previously described in Chapter 3: Section 3.3.1, and the pixel-distance calibration was carried out at different heights in the mixer. Figure B.2 shows the plot of the pixel-distance value with increasing height. The camera (Photron Fastcam 1024-PCI) with a Nikon 24-85mm f/2.8-4 AF-D macro lens was directed vertically downwards on the granule bed at the near wall region (Figure 3.13 in Chapter 3) and with a distance between the end of the lens to the top of the granulator of ~50 mm.

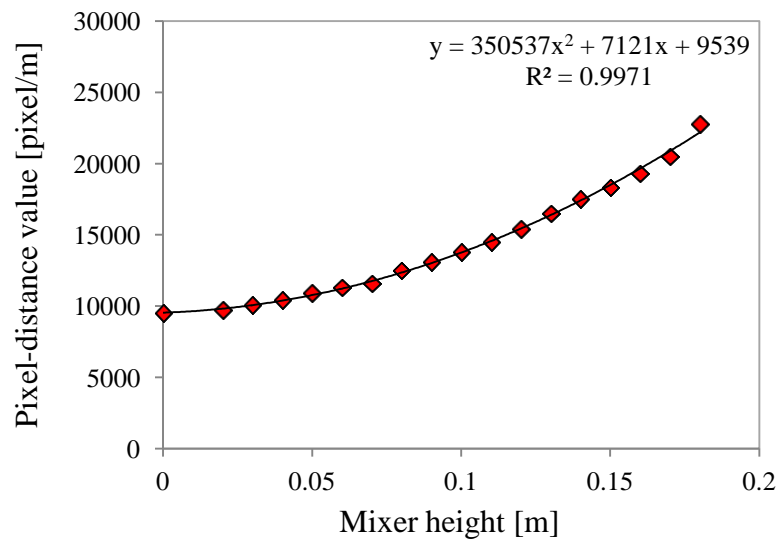


Figure B.2: Pixel-distance values at different mixer heights.

B.3 Size of interrogation area

The size of the interrogation area for the PIV analyses of the bed surface velocity using the MQD algorithm is varied for dry mannitol granules of different sieve sizes; 0.1-0.5 mm, 0.5-1.0 mm, 1.0-2.0 mm and 2.0-4.75 mm used in Chapter 4. Figure B.3, Figure B.4, Figure B.5 and Figure B.6 show the temporal data of the total bed surface velocity (averaged spatially across the analysed region in Chapter 3: Figure 3.14) for these different sieve sizes. The total resolution of the analysed region in the recorded image (Figure 3.14) is about 512×256 pixels. Therefore, changing the interrogation area size from 8×8 pixels to 128×128 pixels gives about 2048 to 8 interrogation areas and, therefore, velocity vectors respectively. In addition, the average pixels per particle diameter are about 2, 7, 18 and 40 for the 0.1-0.5 mm, 0.5-1.0 mm, 1.0-2.0 mm and 2.0-4.75 mm granule sieve sizes respectively. From the figures, it can be seen that surface velocity fluctuations averaged over the analysed region differ slightly at either 8×8 or 128×128 pixels interrogation area sizes for all granule sieve sizes. However, there isn't any significant noise of the velocity fluctuations and a clear periodicity can still be observed. Since the surface velocity is averaged over the analysed region for this thesis, the size of this region, i.e. 512×256 pixels, is sufficient to obtain a clear texture of the bed surface for all the studied sieve sizes and the individual interrogation area size does not affect the result significantly.

Figure B.7 presents the time-averaged surface velocity from the temporal data for the different granule sieve sizes. The time-averaged values stabilise around the 32×32 and 64×64 pixels interrogation area sizes. Therefore, in order to also minimise the processing times, a 64×64 pixels interrogation area size is used for the different mannitol granule sieve sizes. This size is also used for the other granule beds reported in Chapter 4, i.e. polypropylene balls with a sieve size of 1.0-2.0 mm and for the different granule types (lactose, MCC and calcium carbonate) with a sieve size of 0.1-2.0 mm.

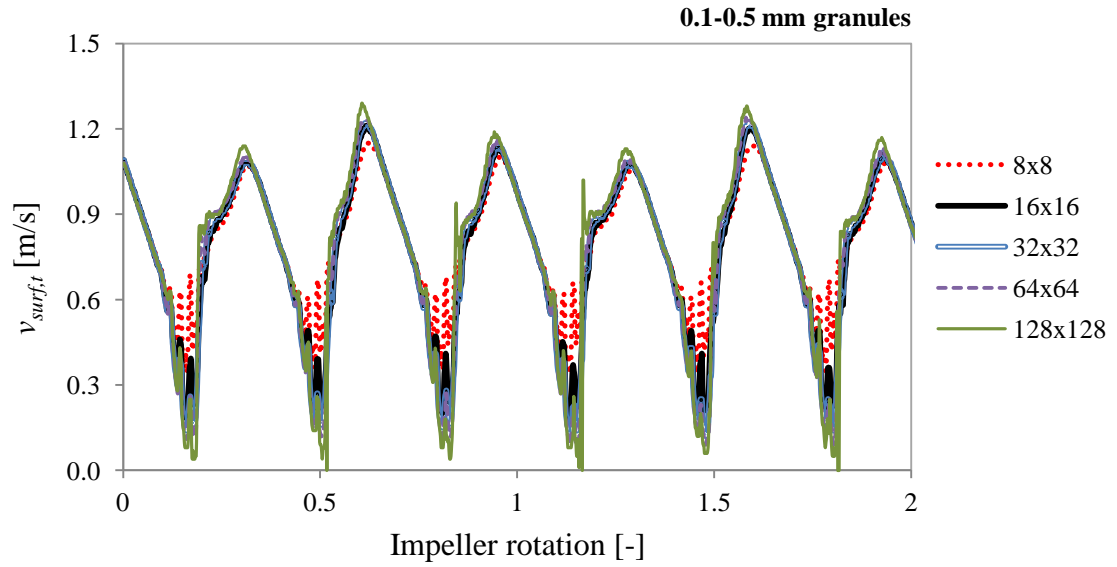


Figure B.3: Temporal bed surface velocity (circumferential+radial components), $v_{surf,t}$ for 0.1-0.5 mm mannitol granules at 150 rpm impeller speed for different interrogation area sizes.

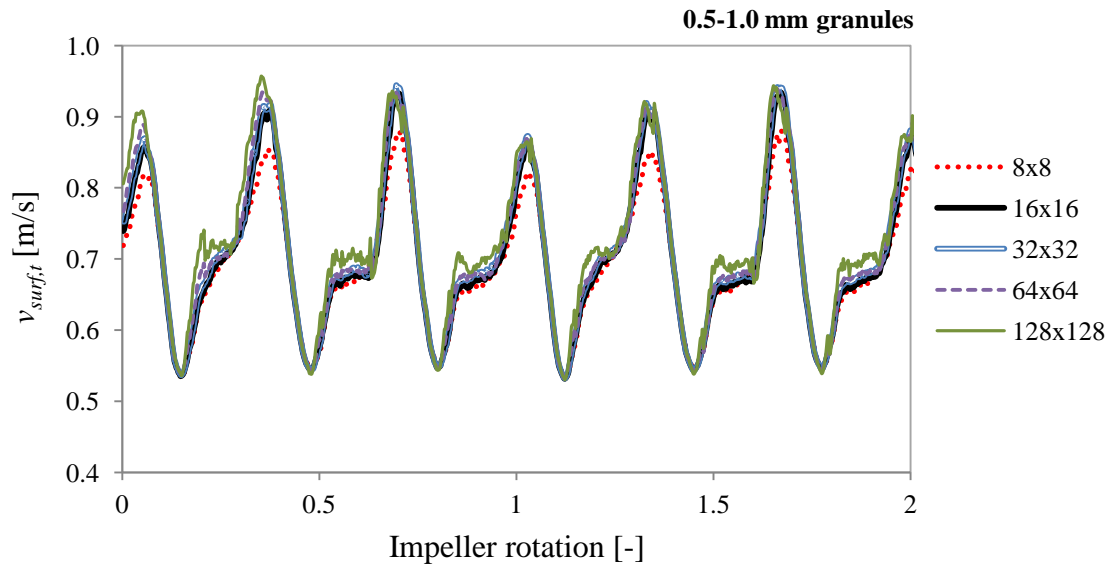


Figure B.4: Temporal bed surface velocity (circumferential+radial components), $v_{surf,t}$ for 0.5-1.0 mm mannitol granules at 150 rpm impeller speed for different interrogation area sizes.

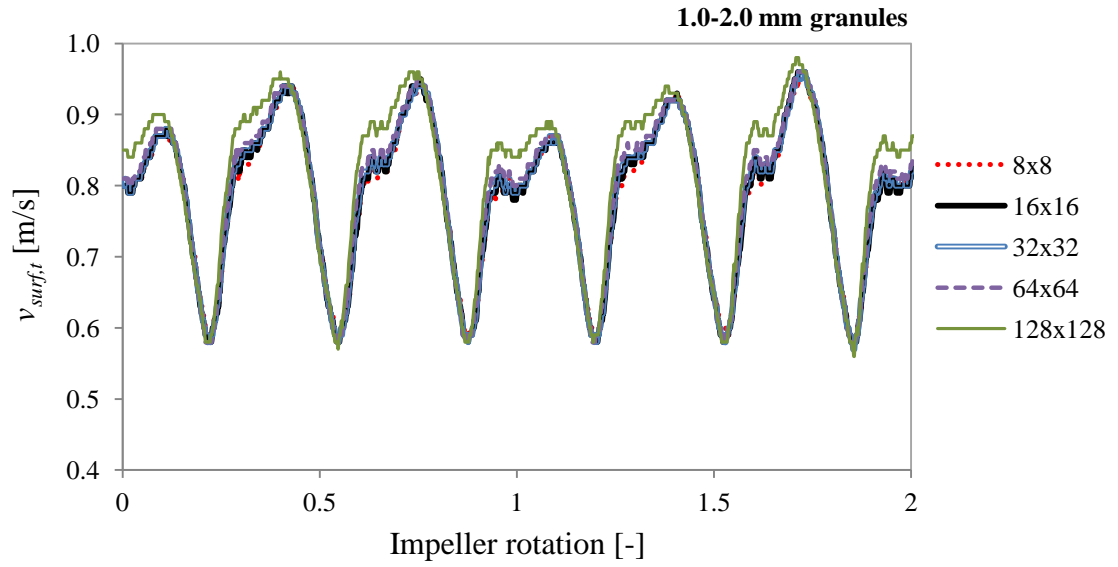


Figure B.5: Temporal bed surface velocity (circumferential+radial components), $v_{surf,t}$ for 1.0-2.0 mm mannitol granules at 150 rpm impeller speed for different interrogation area sizes.

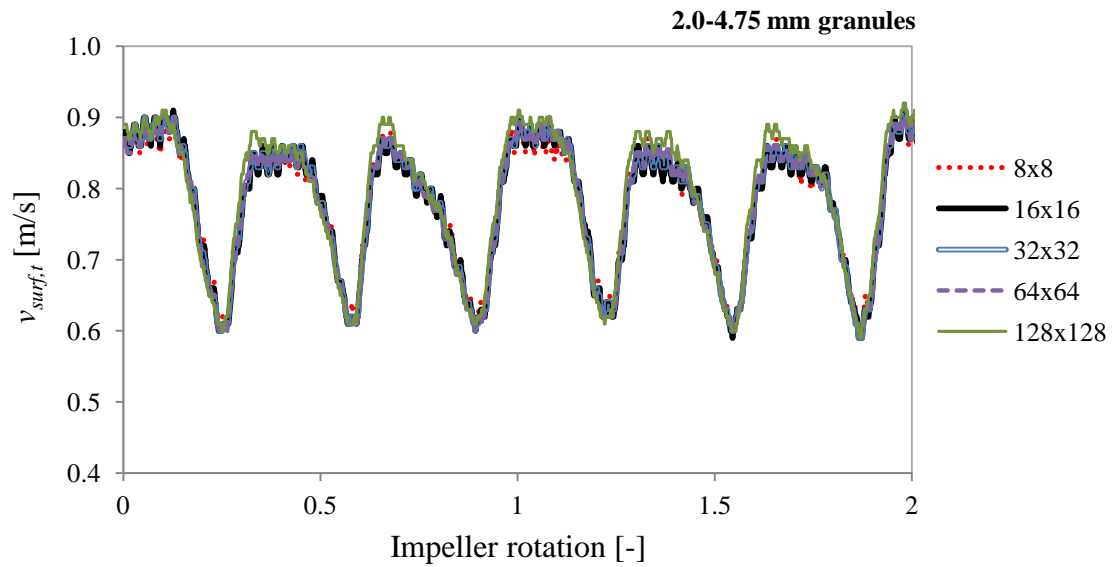


Figure B.6: Temporal bed surface velocity (circumferential+radial components), $v_{surf,t}$ for 2.0-4.75 mm mannitol granules at 150 rpm impeller speed for different interrogation area sizes.

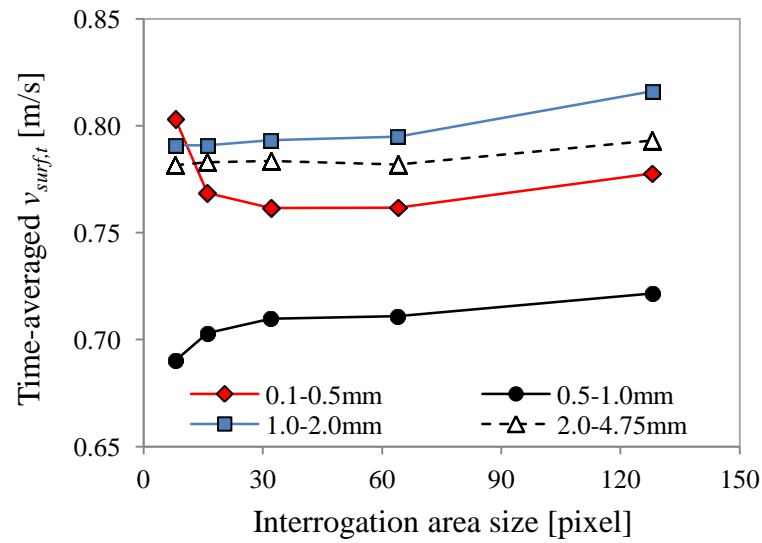


Figure B.7: Time-averaged bed surface velocity (circumferential+radial components), $v_{surf,t}$, at different interrogation area sizes for different mannitol granule sieve sizes.

Appendix C

Granulation: binder spray system calibration

Figure C.1 shows the spray rate data at different air pressures for the binder spray system attached to the ~10 L Roto Junior high shear granulator. Atomising spray nozzles (Model: 1/4" LNN SS Atomizing) from Spraying Systems Limited with three different nozzle sizes (0.41 mm, 0.71 mm and 1.1 mm diameters) were calibrated.

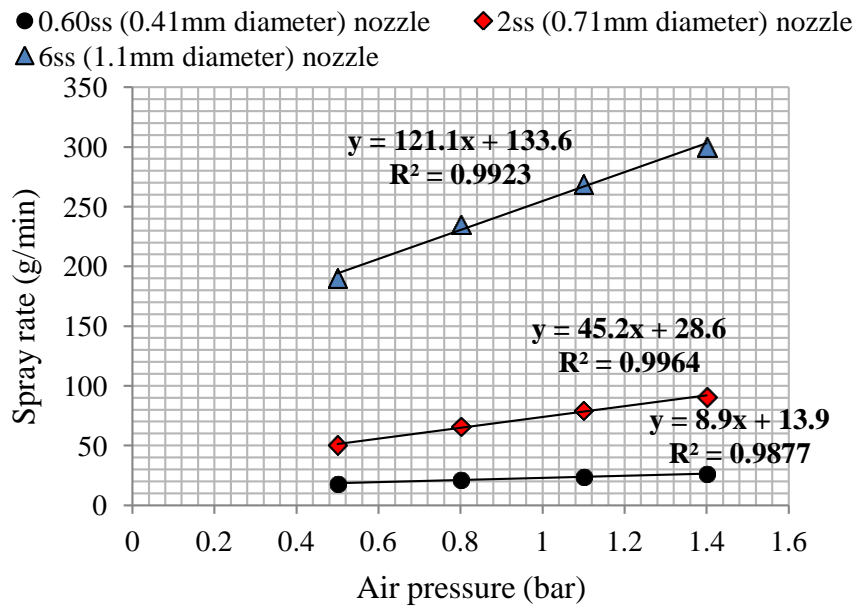


Figure C.1: Spray rate calibration with different nozzle sizes for water.

Appendix D

DEM simulations: particle bed flow images and further details

D.1 Particle bed/particle properties

D.1.1 Bed load

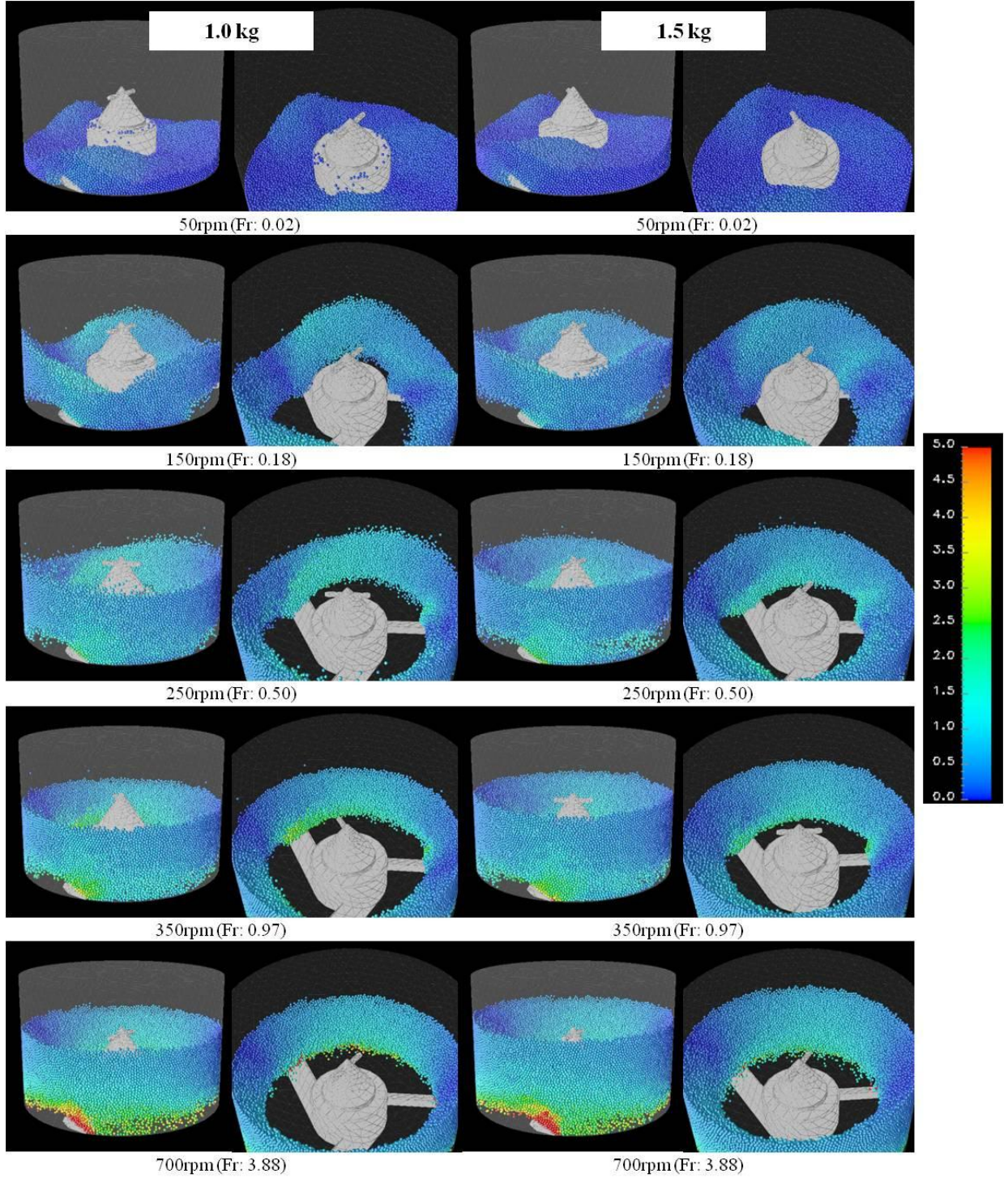


Figure D.1: Particle bed image for 1.0 kg (left column) and 1.5 kg (right column) bed loads. The colour bar indicates the particle total velocity in m/s (and also for subsequent figures in Appendix D).

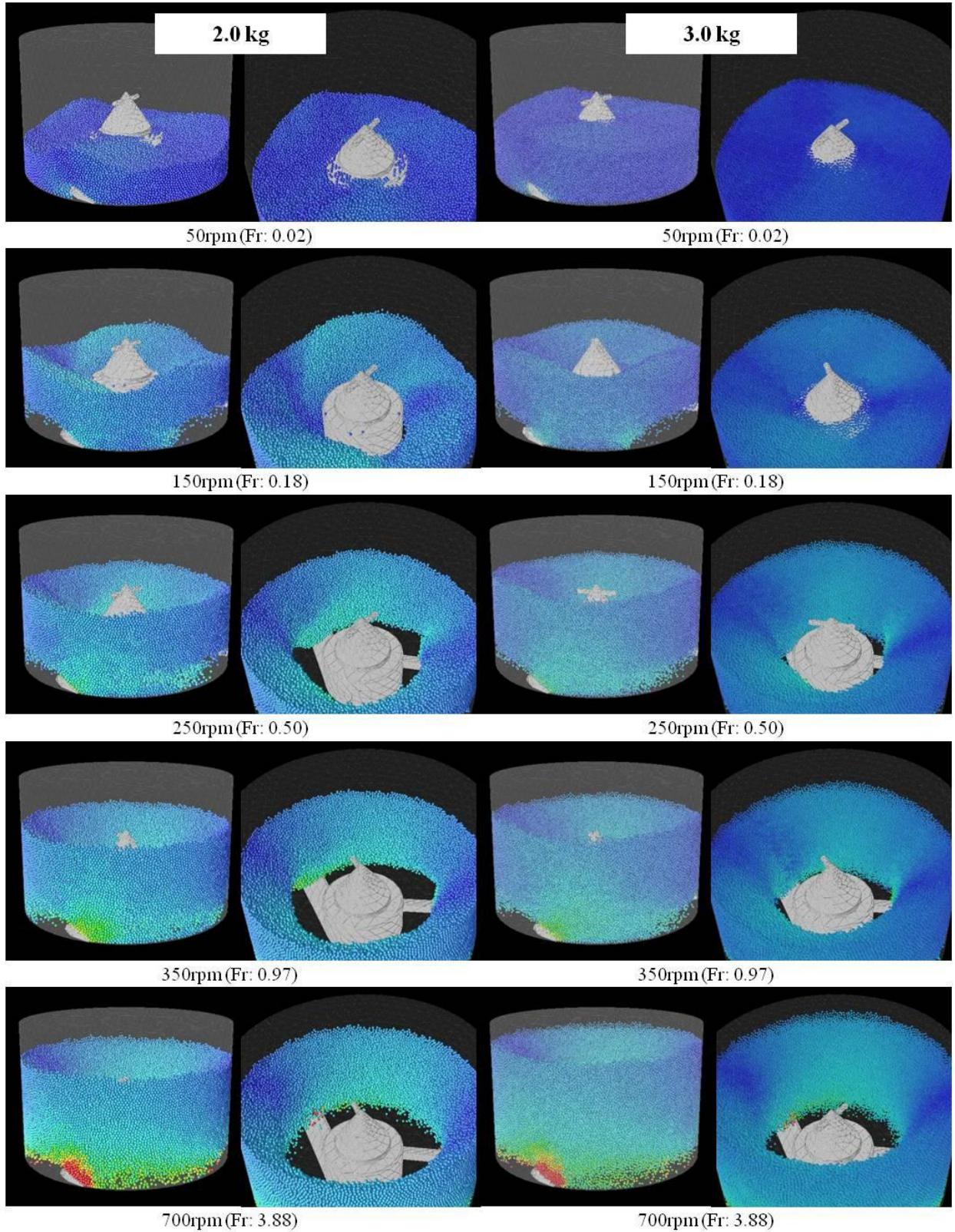


Figure D.2: Particle bed images for 2.0 kg (left column) and 3.0 kg (right column) bed loads.

D.1.2 Particle size

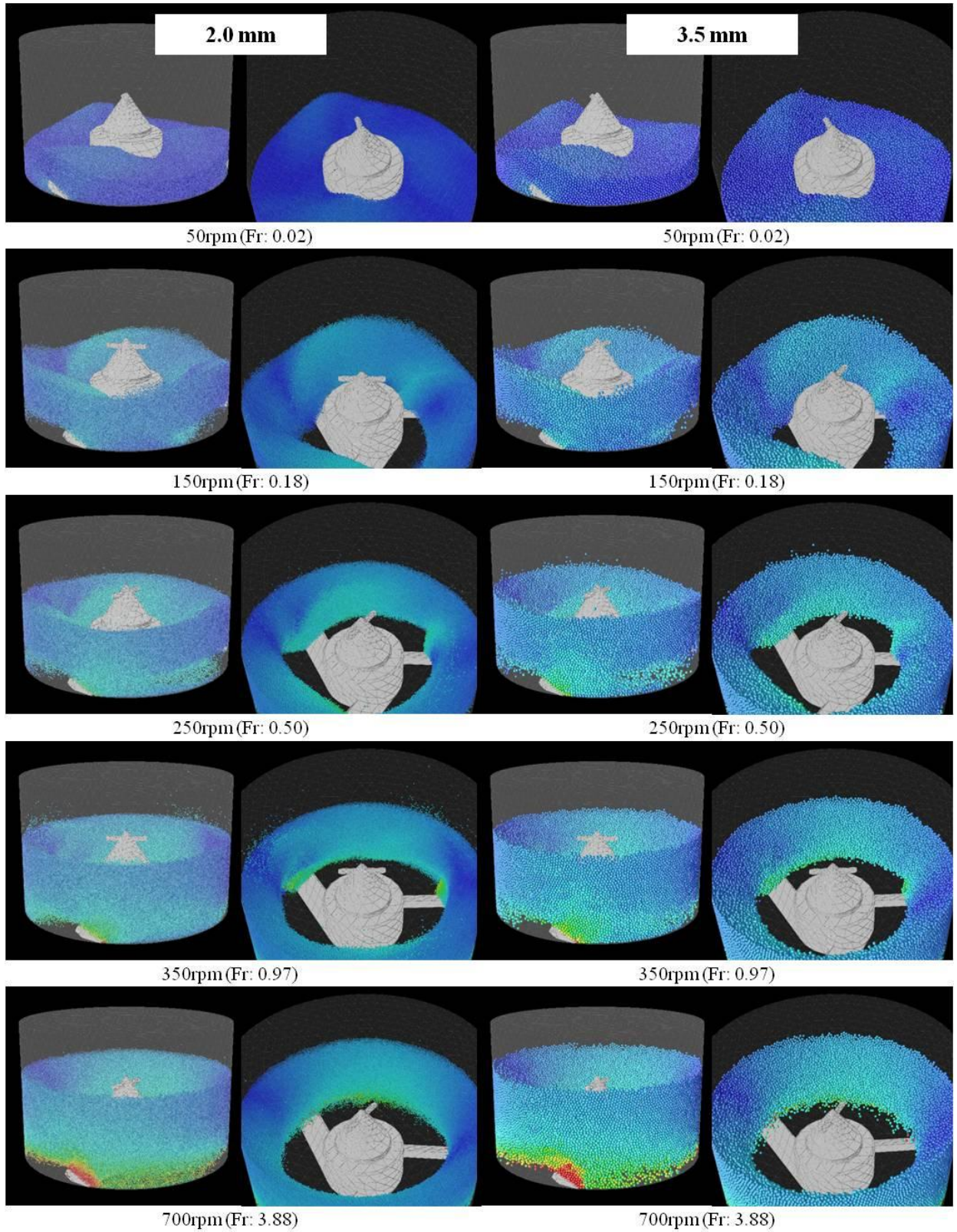


Figure D.3: Particle bed images for 2.0 mm (left column) and 3.5 mm (right column) particles.

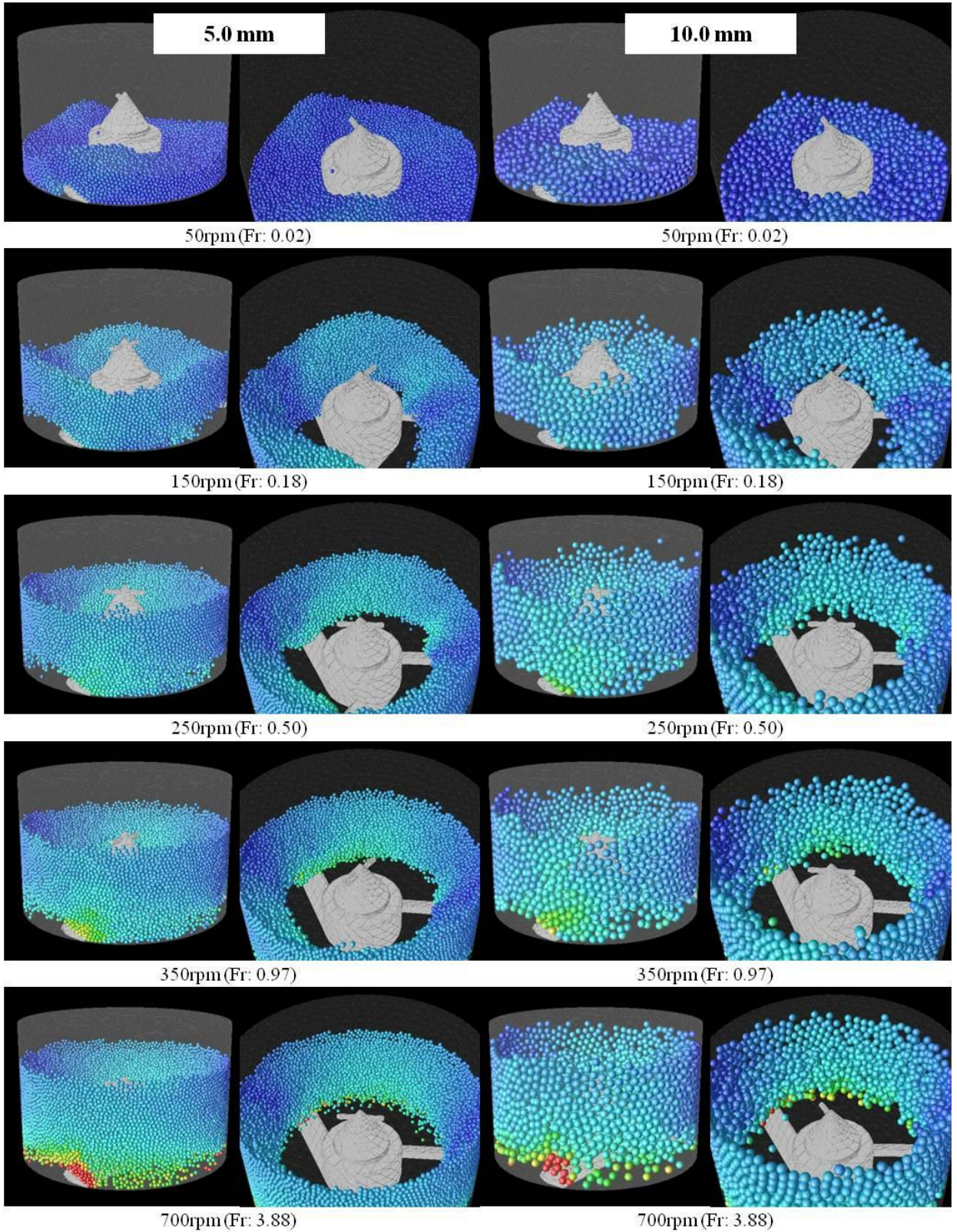


Figure D.4: Particle bed images for 5.0 mm (left column) and 10.0 mm (right column) particles.

D.1.3 Particle density

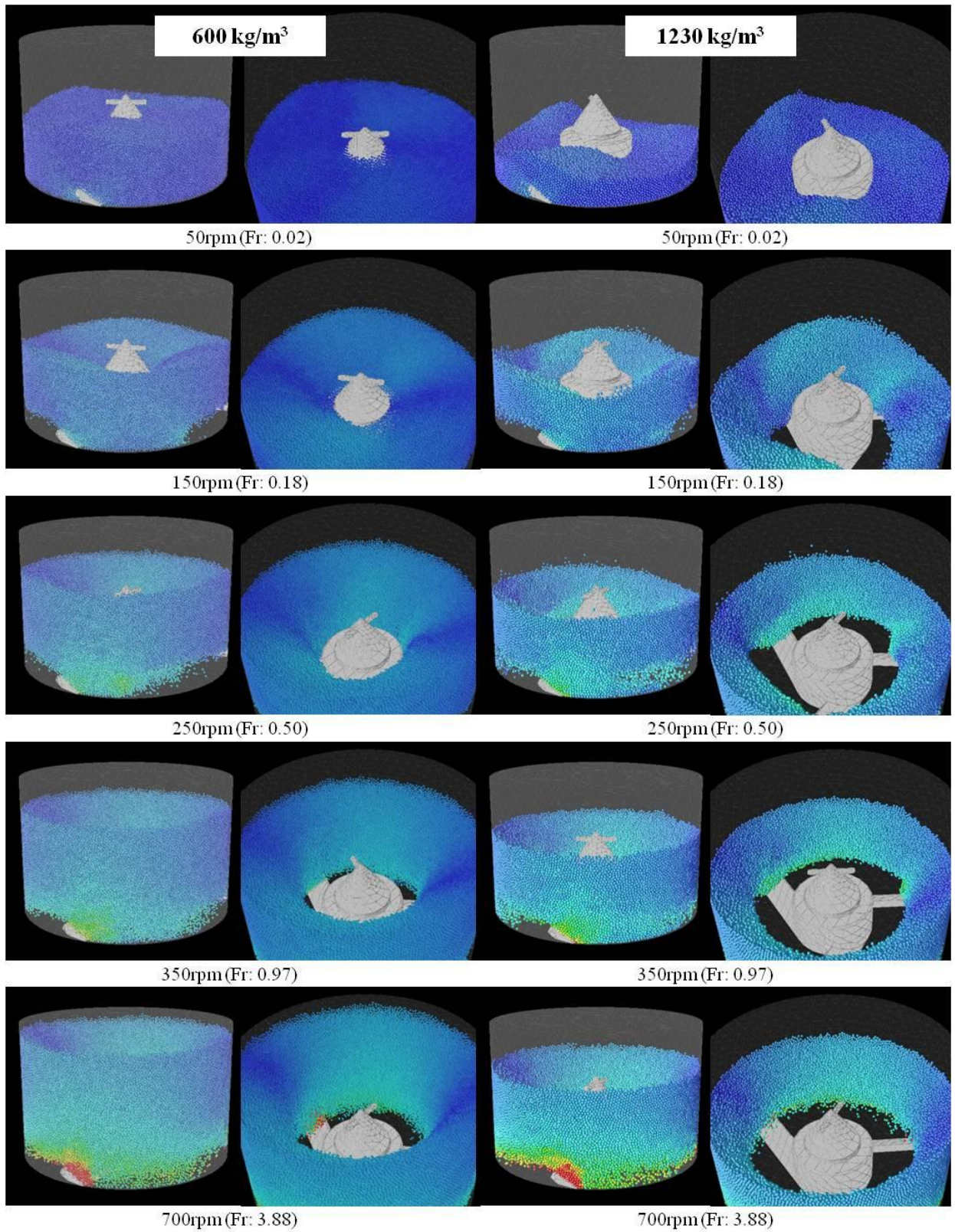


Figure D.5: Particle bed images for 600 kg/m^3 (left column) and 1230 kg/m^3 (right column) particles.

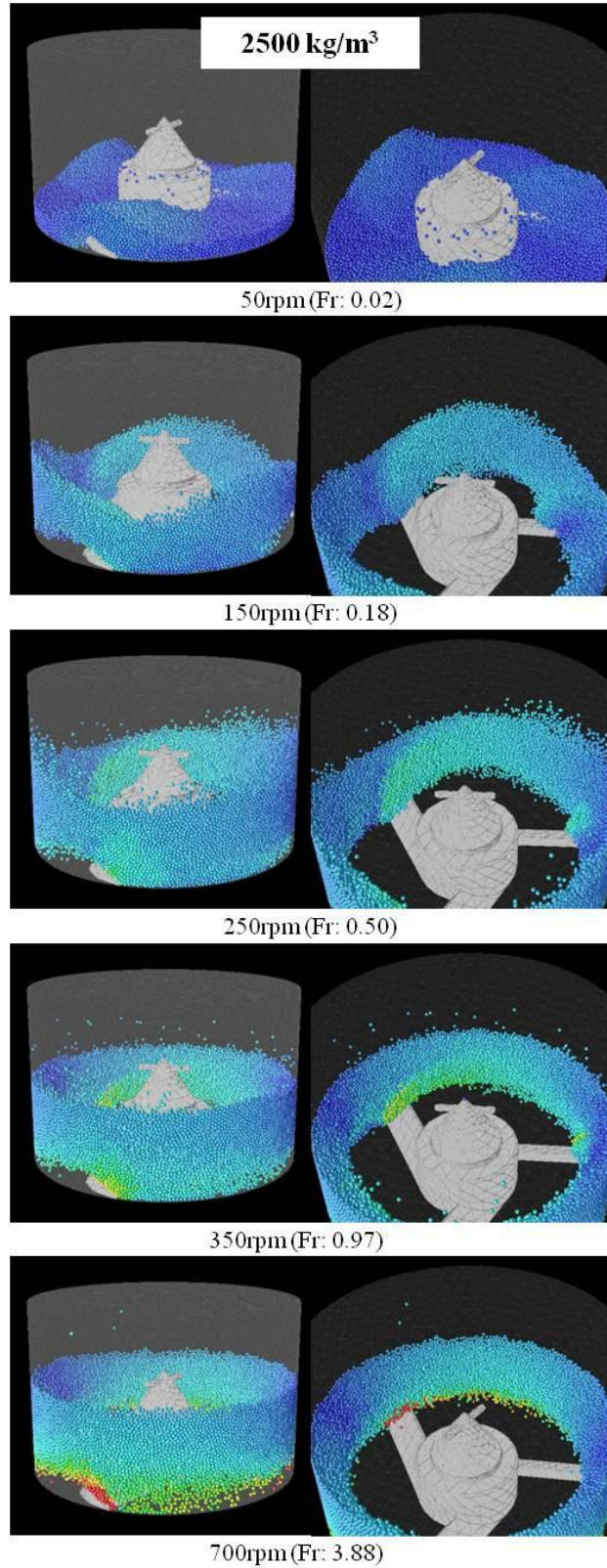


Figure D.6: Particle bed images for 2500 kg/m³ particles.

D.1.4 Interparticle sliding friction coefficient

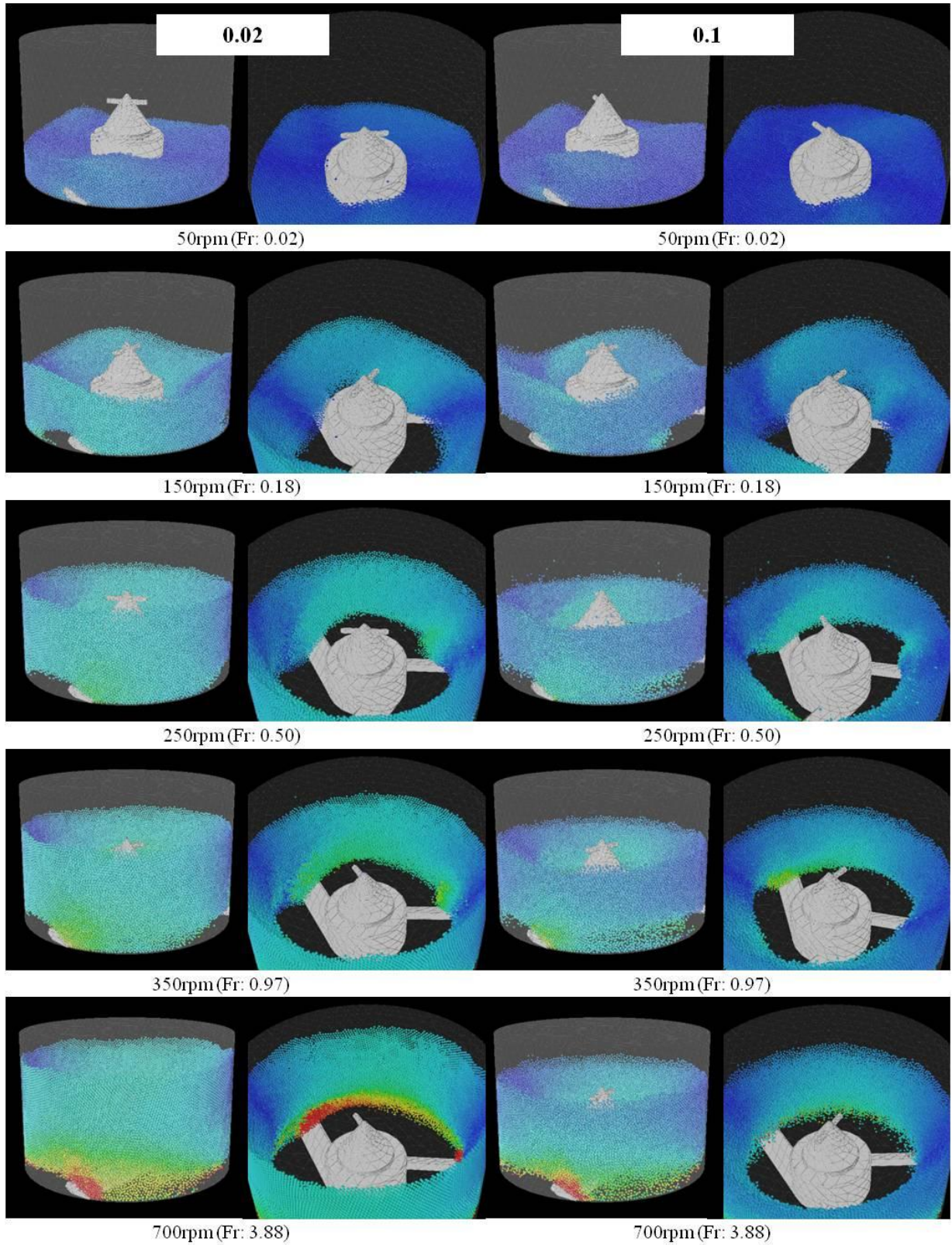


Figure D.7: Particle bed images for $\mu_f = 0.02$ (left column) and $\mu_f = 0.1$ (right column).

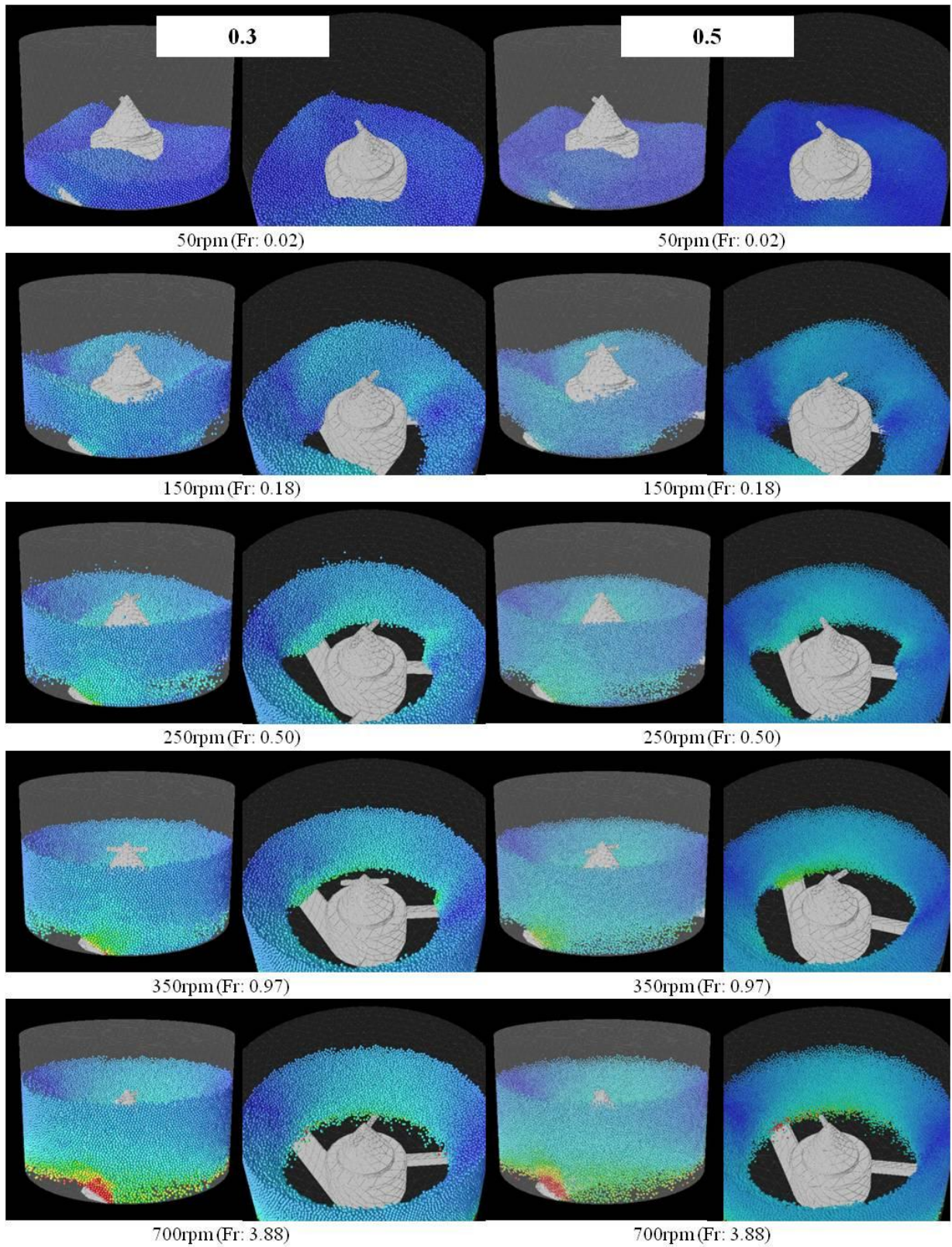


Figure D.8: Particle bed images for $\mu_f = 0.3$ (left column) and $\mu_f = 0.5$ (right column).

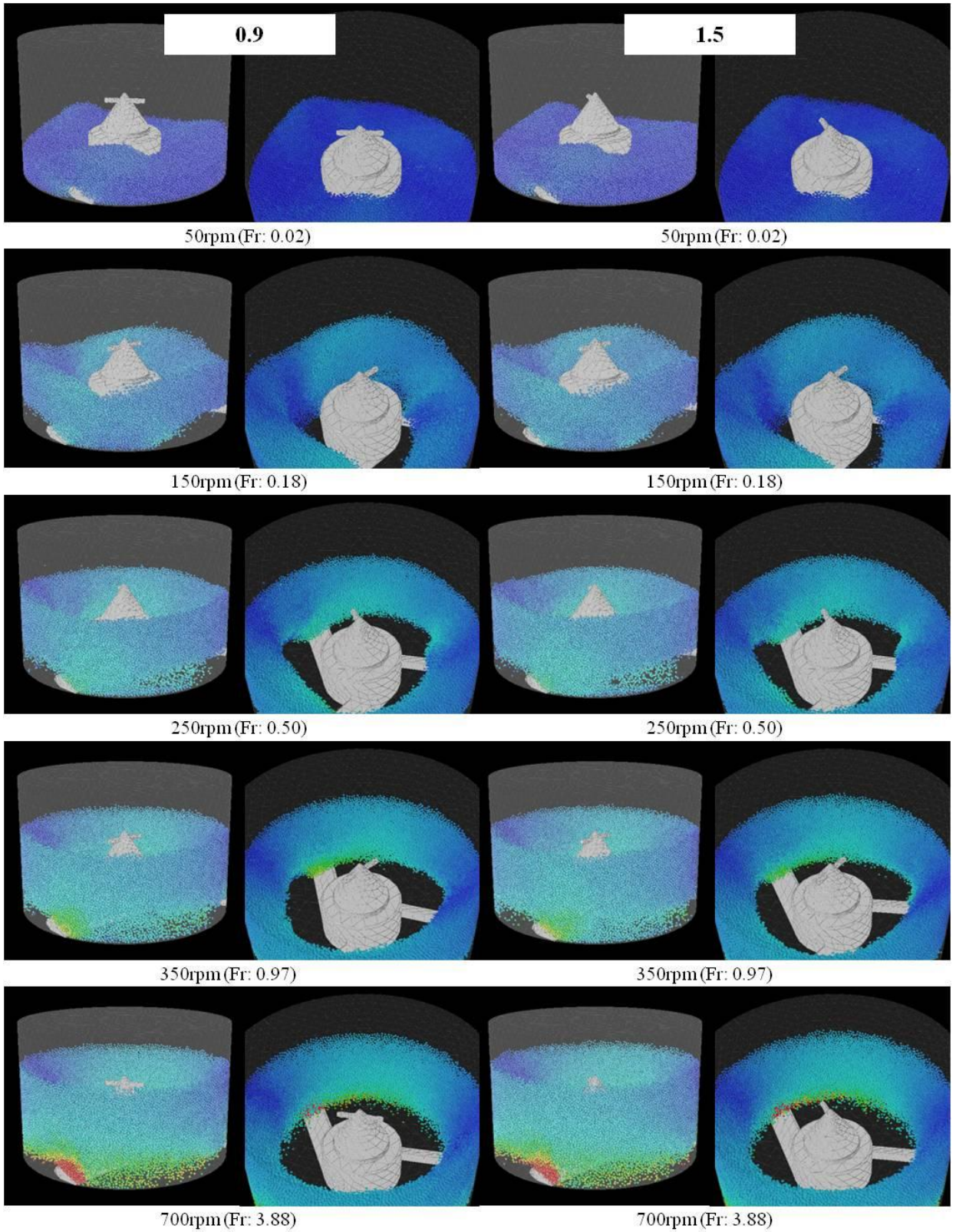


Figure D.9: Particle bed images for $\mu_f = 0.9$ (left column) and $\mu_f = 1.5$ (right column).

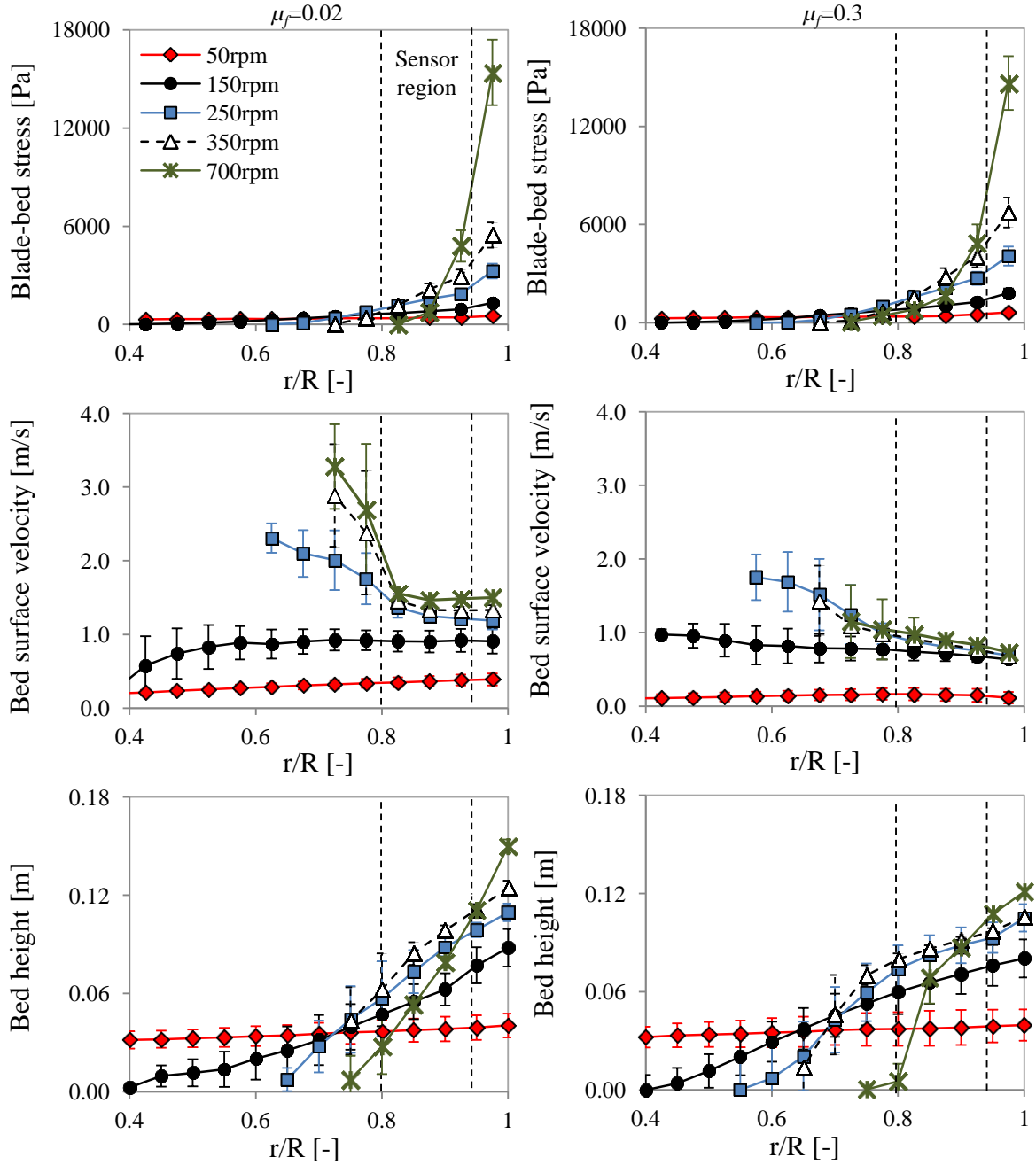


Figure D.10: Simulated time-averaged blade-bed stress, bed surface circumferential velocity and bed height along the radial position for $\mu_f = 0.02$ (left column) and $\mu_f = 0.3$ (right column).

D.1.5 Restitution coefficient

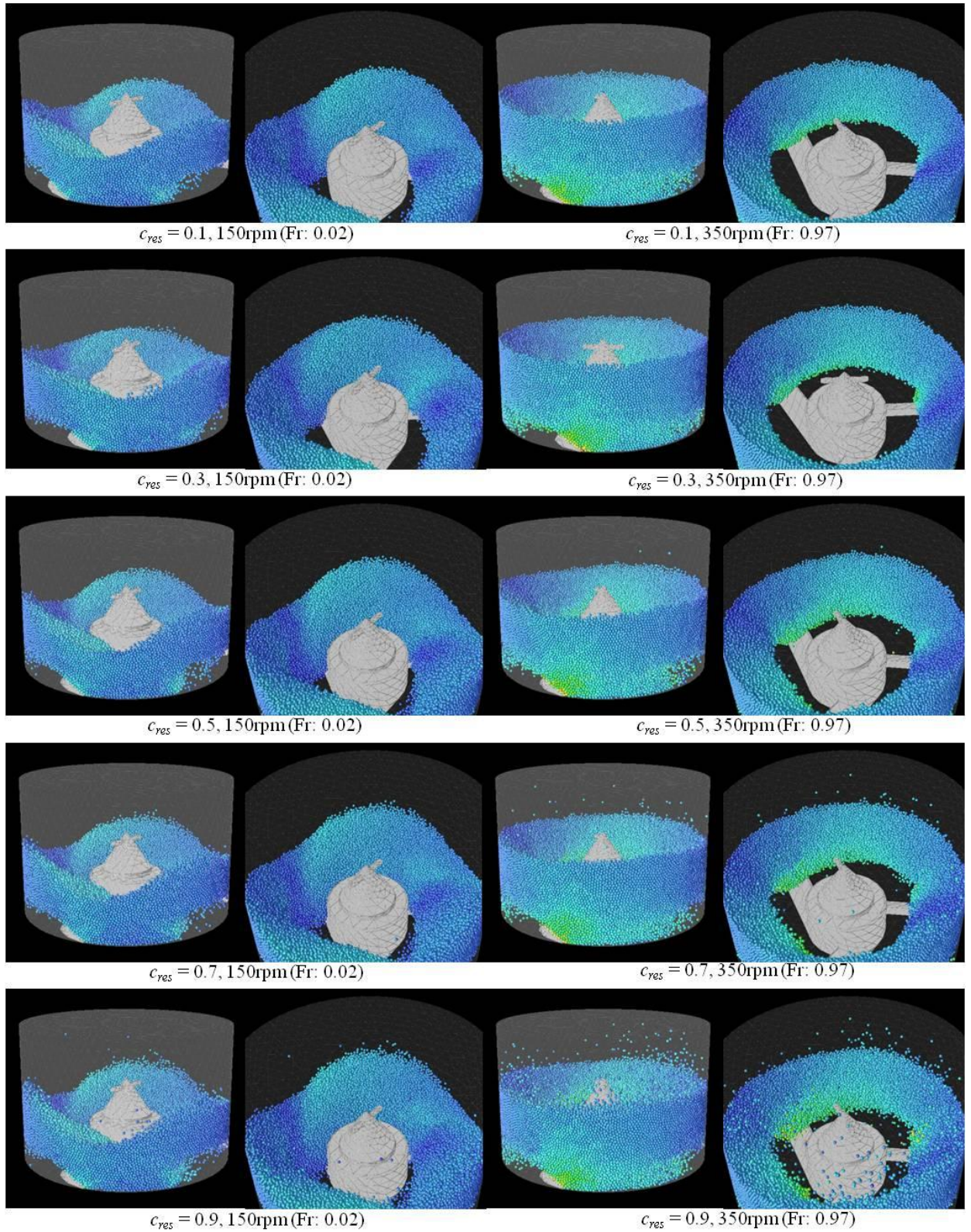


Figure D.11: Particle bed images for different restitution coefficients. Left: 150 rpm, Right: 350 rpm.

D.1.6 Young's modulus

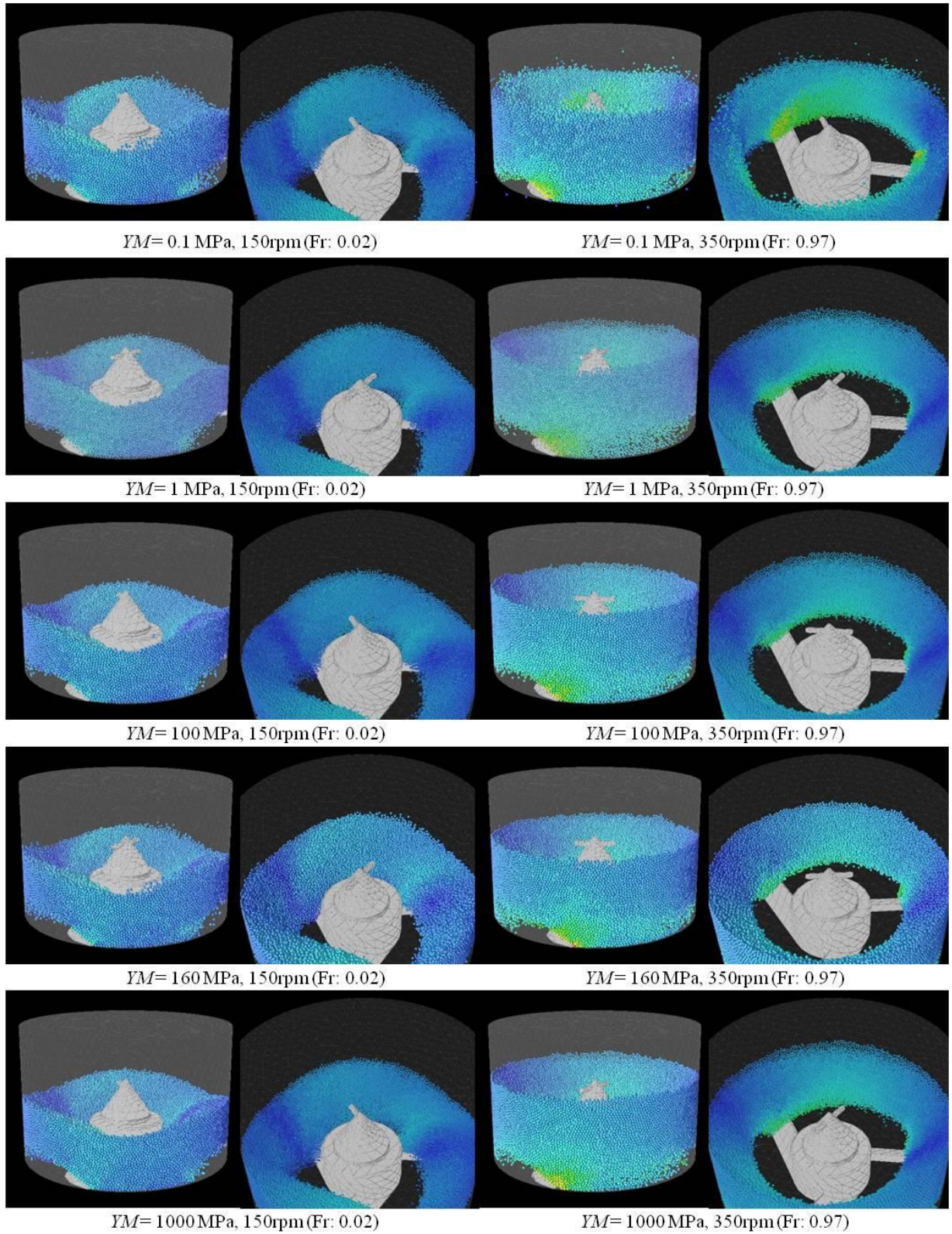


Figure D.12: Particle bed images for different Young's modulus. Left: 150 rpm, Right: 350 rpm.

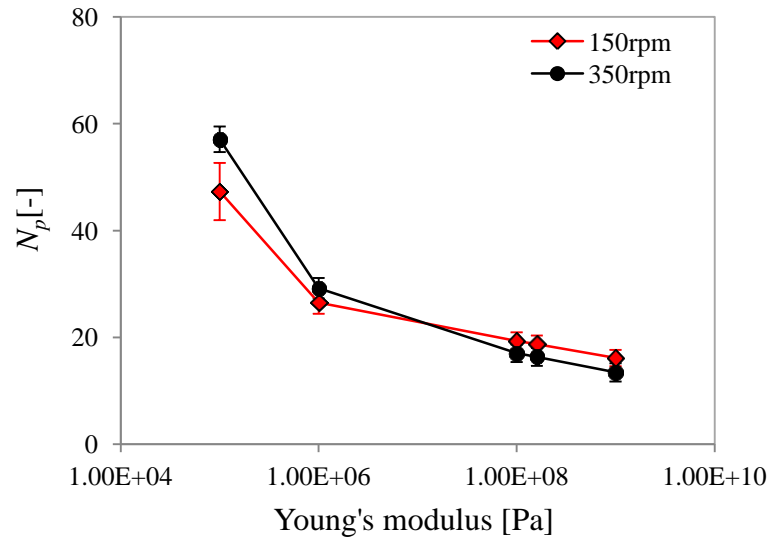


Figure D.13: Simulated time-averaged number of particles in contact with the blade at the sensor region, N_p , for different Young's modulus.

D.2 Impeller geometries

D.2.1 Blade width

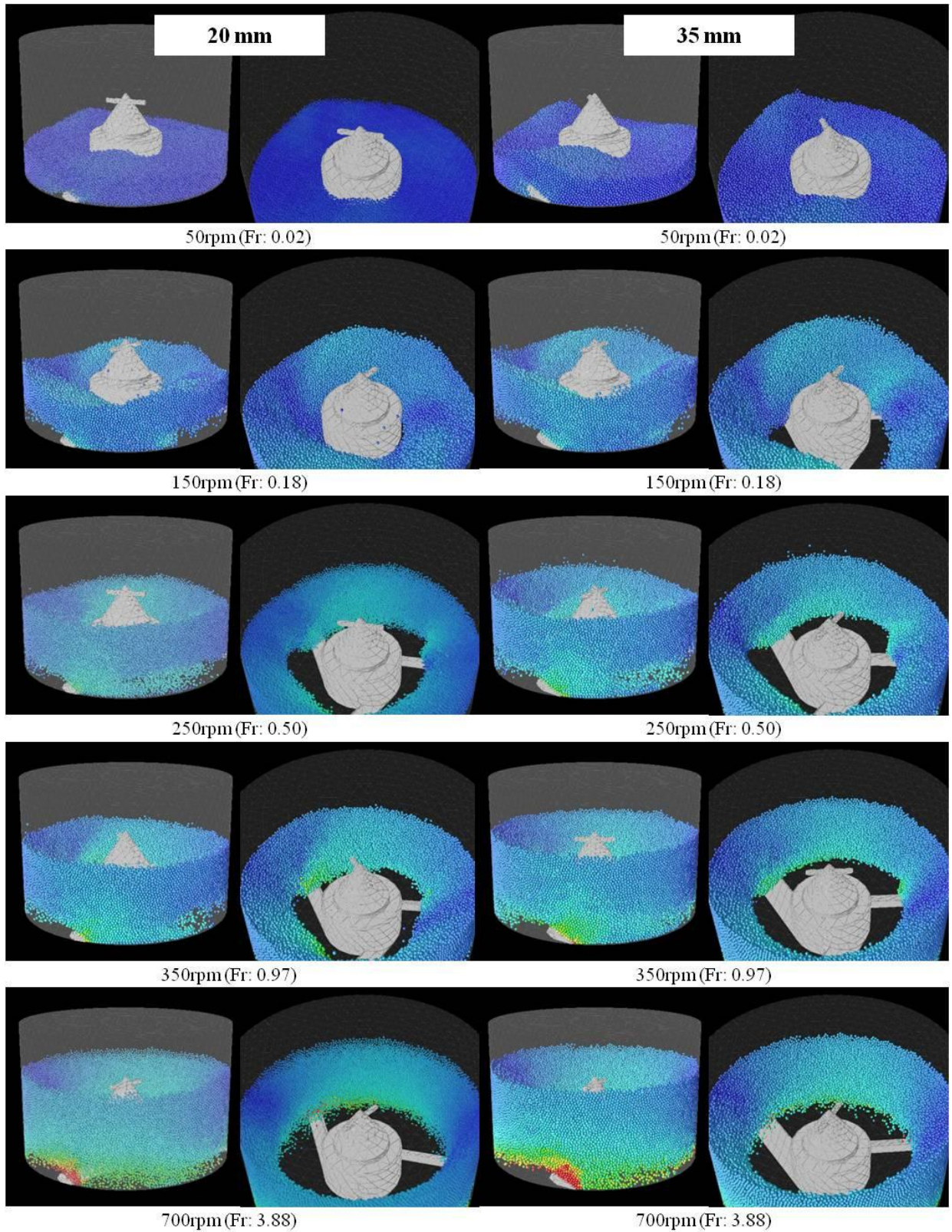


Figure D.14: Particle bed images for $h_w = 20$ mm (left column) and $h_w = 35$ mm (right column).

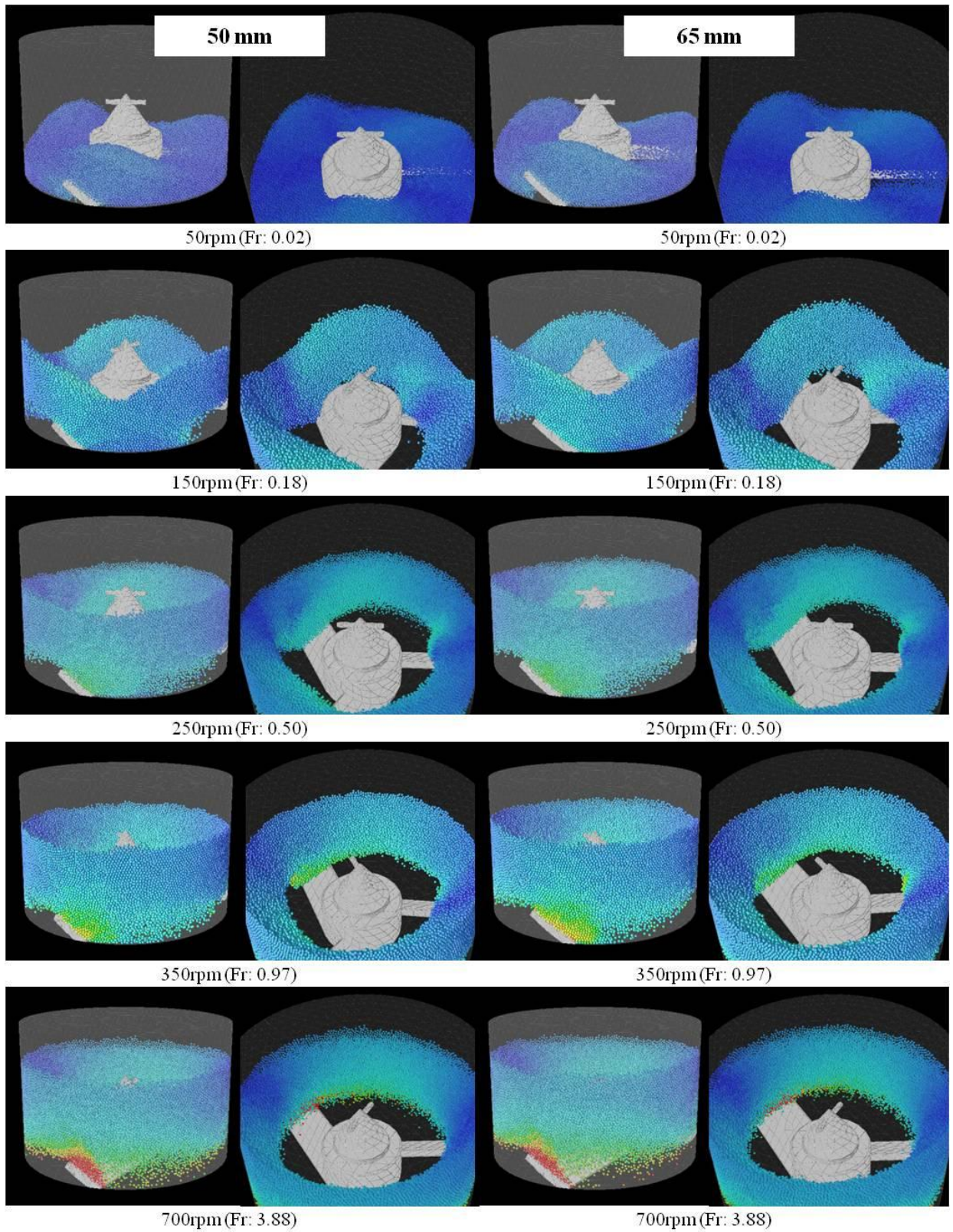


Figure D.15: Particle bed images for $h_w = 50$ mm (left column) and $h_w = 65$ mm (right column).

From Chapter 6: Section 6.8.2, the blade-bed stress equation with correction parameter B_2 is given as follows:

$$\sigma_{i(r)cor} = \frac{B_2 \rho_b H_{g,r} v_{rel}^2 (1 - \cos\theta_l)}{h_l}$$

From: Equation 6.25

$$B_2 = K_2 \frac{1}{Fr_{rel}^{0.5}} \left(\frac{2h_w}{D} \right)^n$$

From: Equation 6.26

To find n in Equation 6.26, the equation is rearranged and taking the log on both sides gives Equation D.1. Plotting $\log(B_2 Fr_{rel}^{0.5})$ against $\log(2h_w/D)$ for the different blade width cases as shown in Figure D.16 gives a straight line where the slope of the line is n .

$$\log(B_2 Fr_{rel}^{0.5}) = \log K_2 + n \log \left(\frac{2h_w}{D} \right)$$

Equation D.1

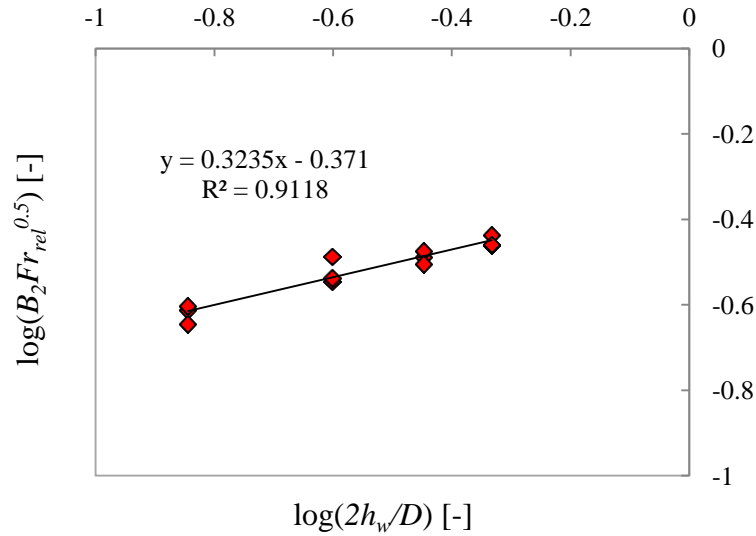


Figure D.16: Plot of $\log(B_2 Fr_{rel}^{0.5})$ against $\log(2h_w/D)$ for different blade width cases from simulation.

D.2.2 Blade angle

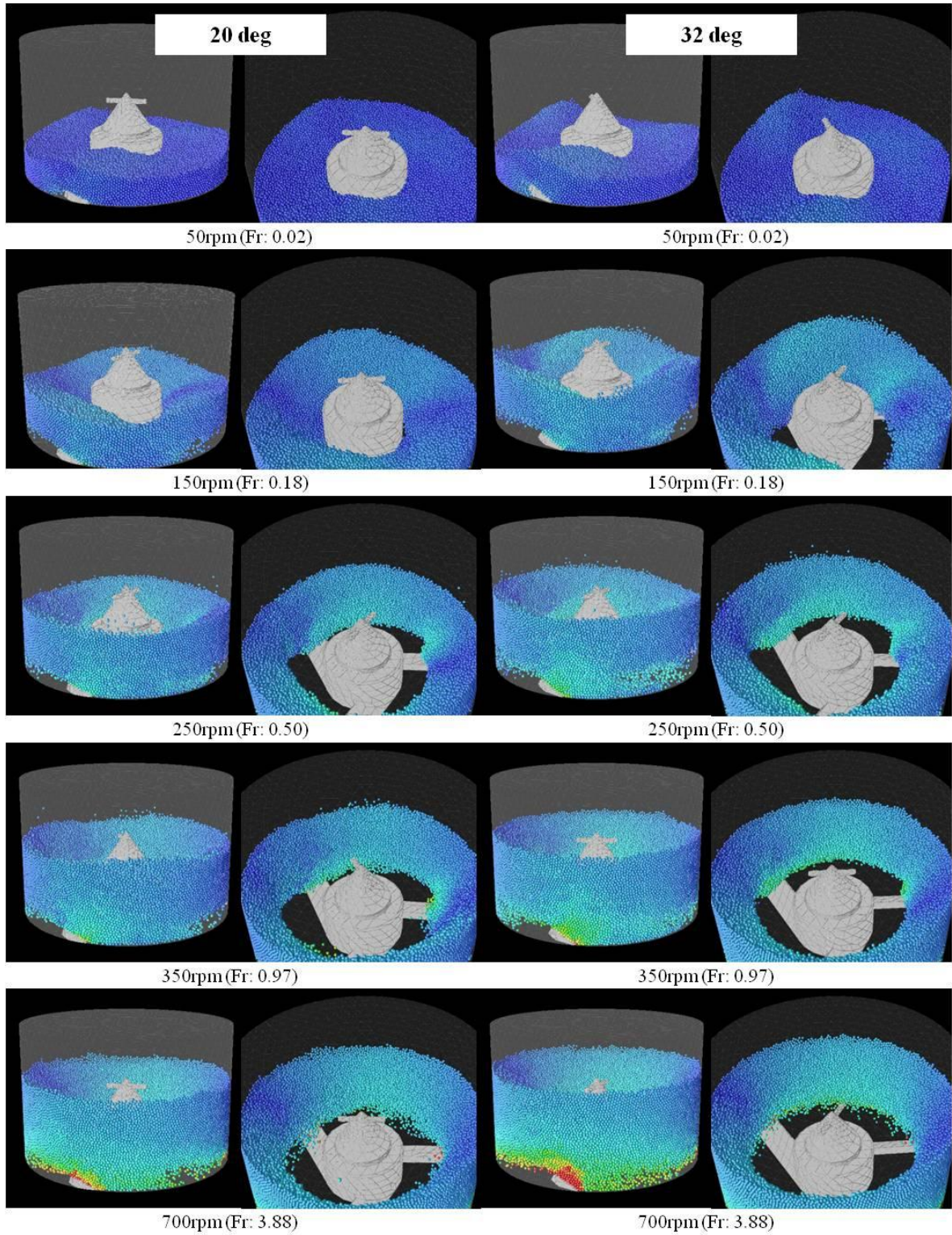


Figure D.17: Particle bed images for 20° (left column) and 32° (right column) inclined blades.

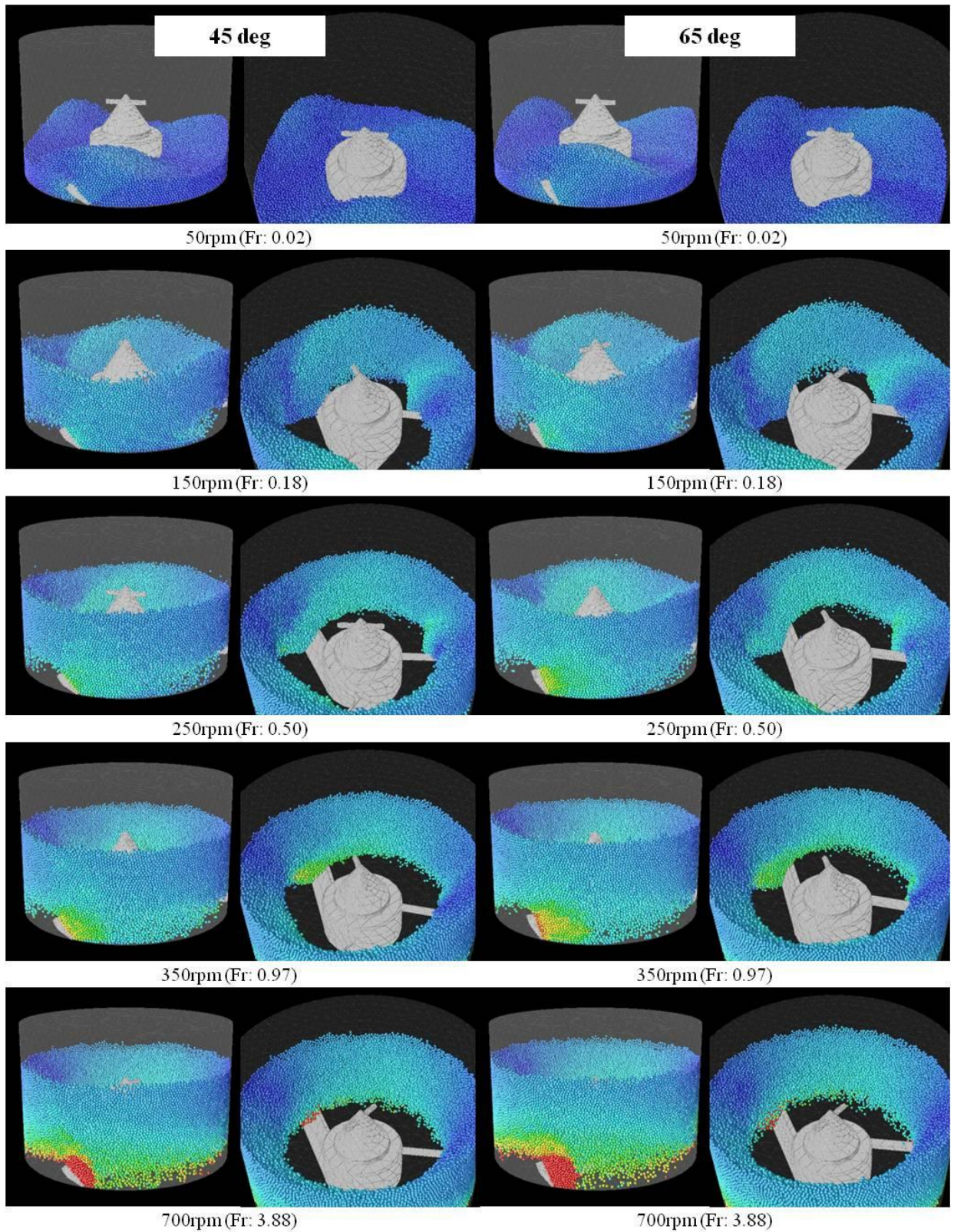


Figure D.18: Particle bed images for 45° (left column) and 65° (right column) inclined blades.

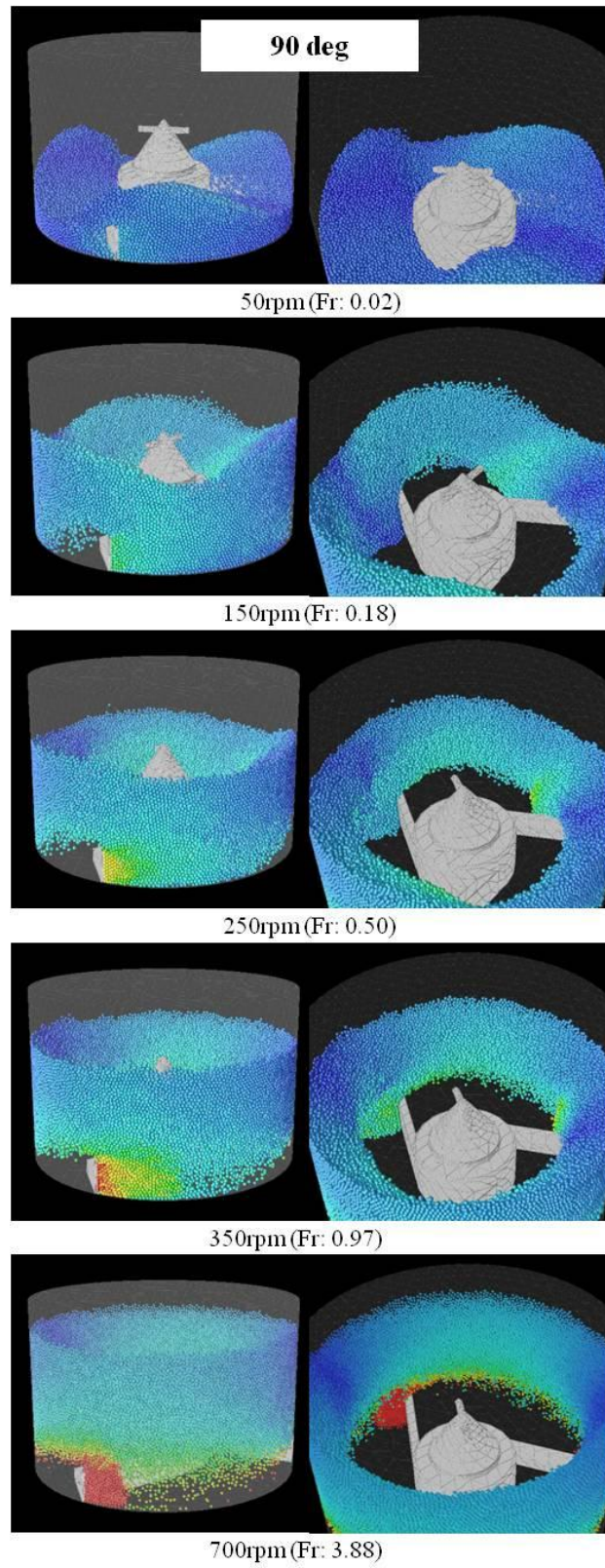


Figure D.19: Particle bed images for 90° inclined blades.

D.2.3 Number of blades

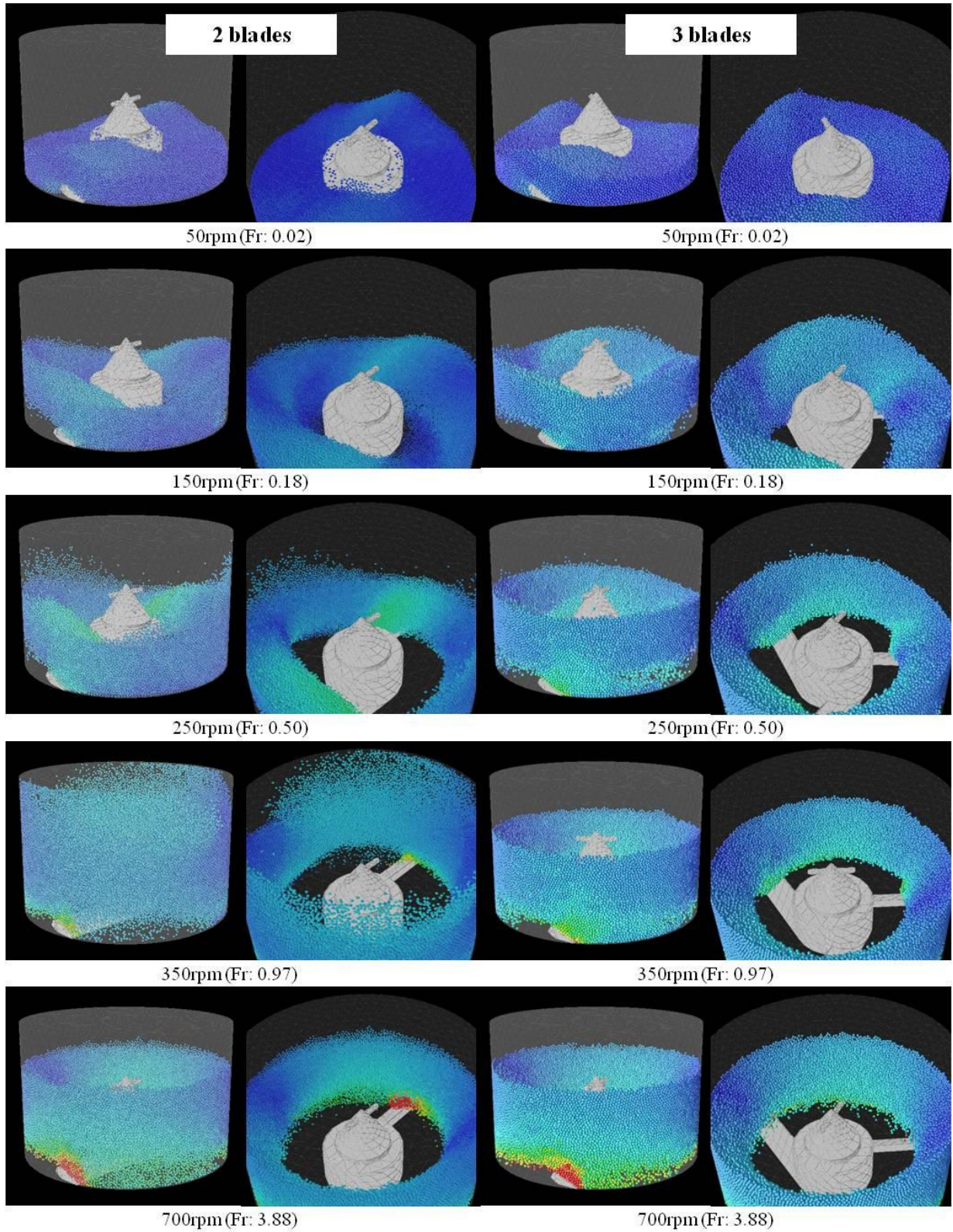


Figure D.20: Particle bed images for the 2-bladed (left column) and 3-bladed (right column) impellers.

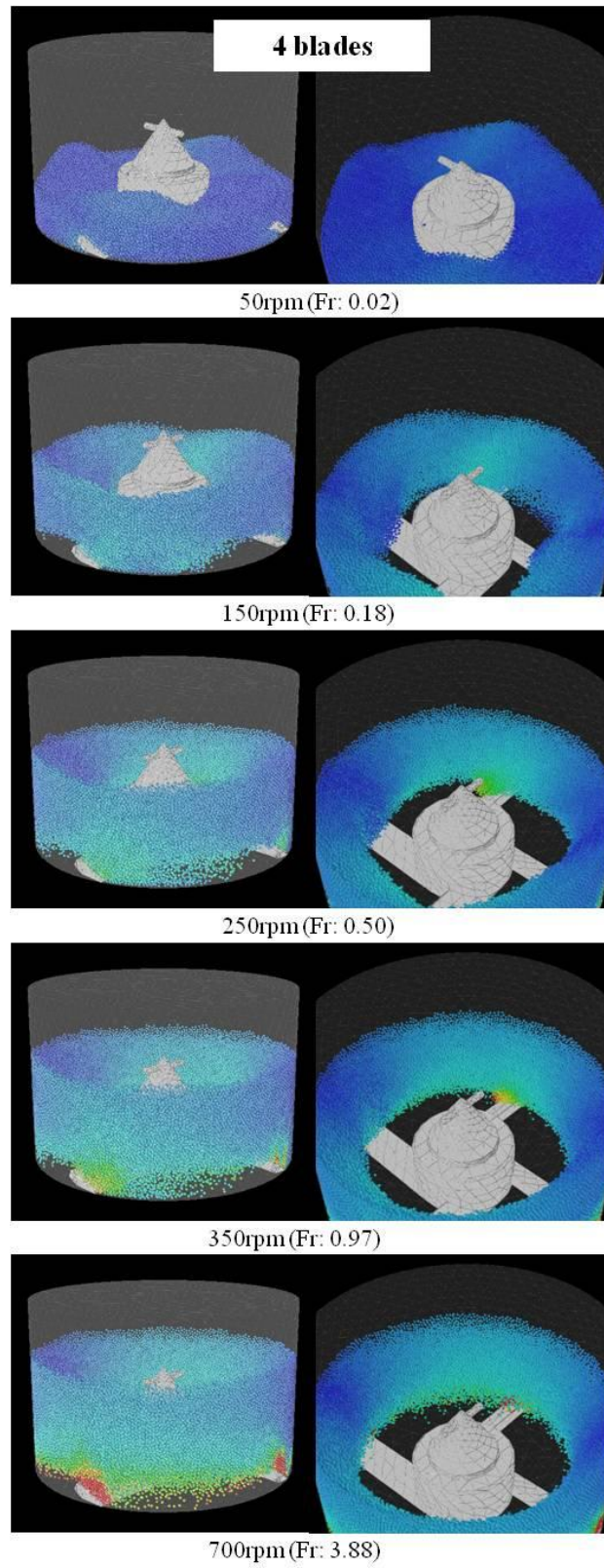


Figure D.21: Particle bed images for the 4-bladed impellers.

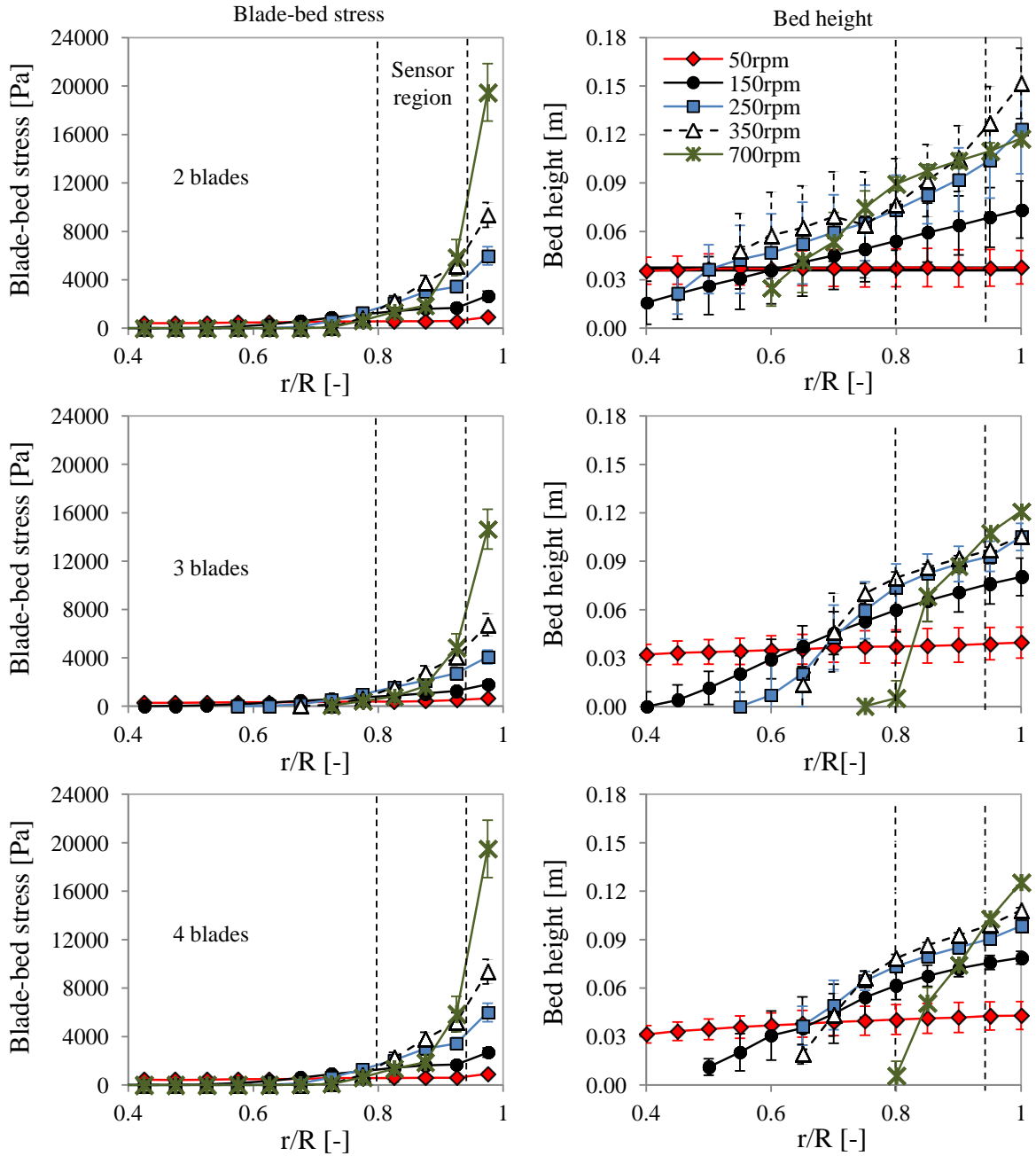


Figure D.22: Simulated time-averaged blade-bed stress (left column) and bed height (right column) along the radial position for different number of blades.

D.3 Granulator scale

D.3.1 Same particle diameter ($D/d_p = 20-160$)

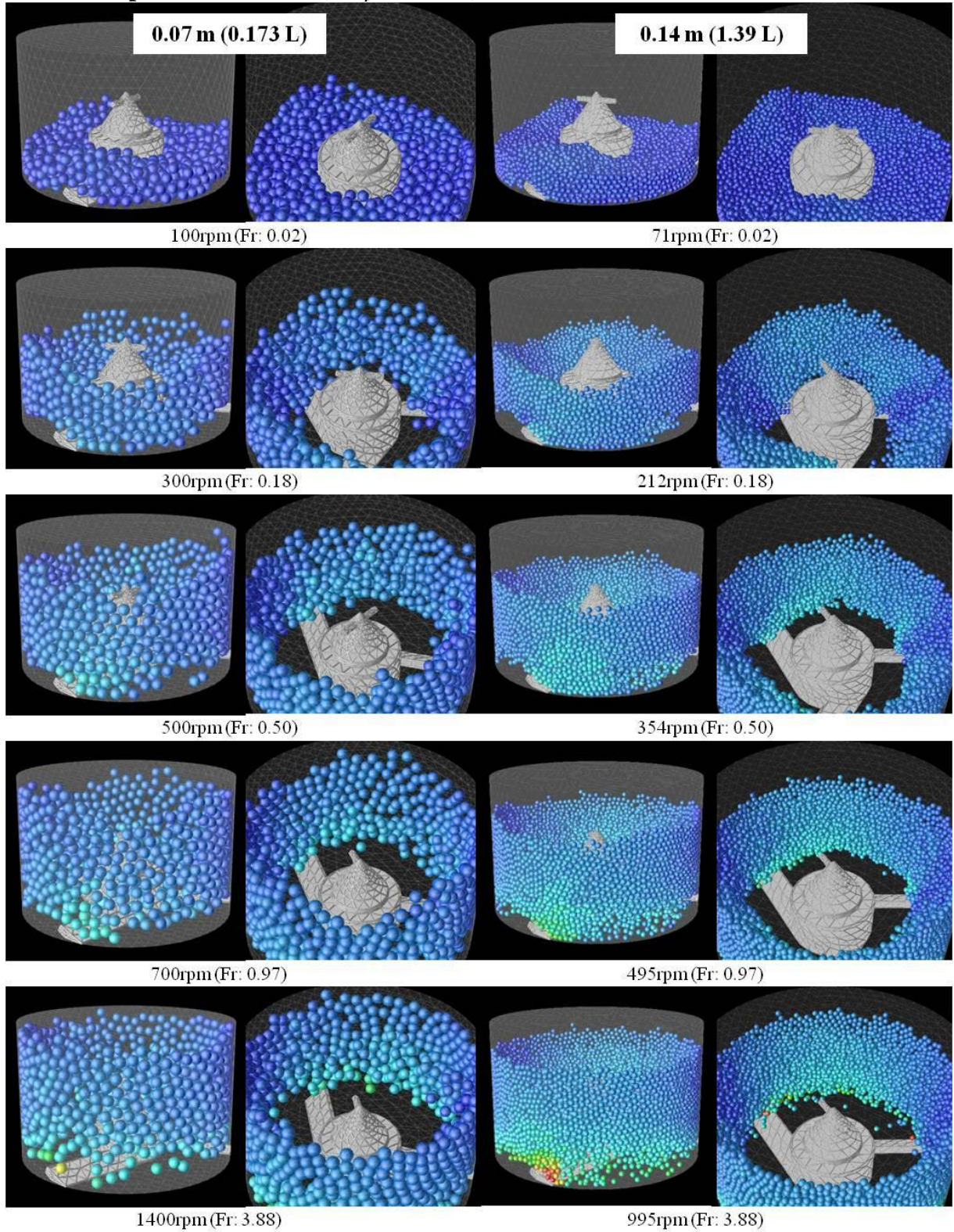


Figure D.23: Particle bed images for the 0.173 L, $D/d_p = 20$ (left column) and 1.39 L, $D/d_p = 40$ (right column) granulators.

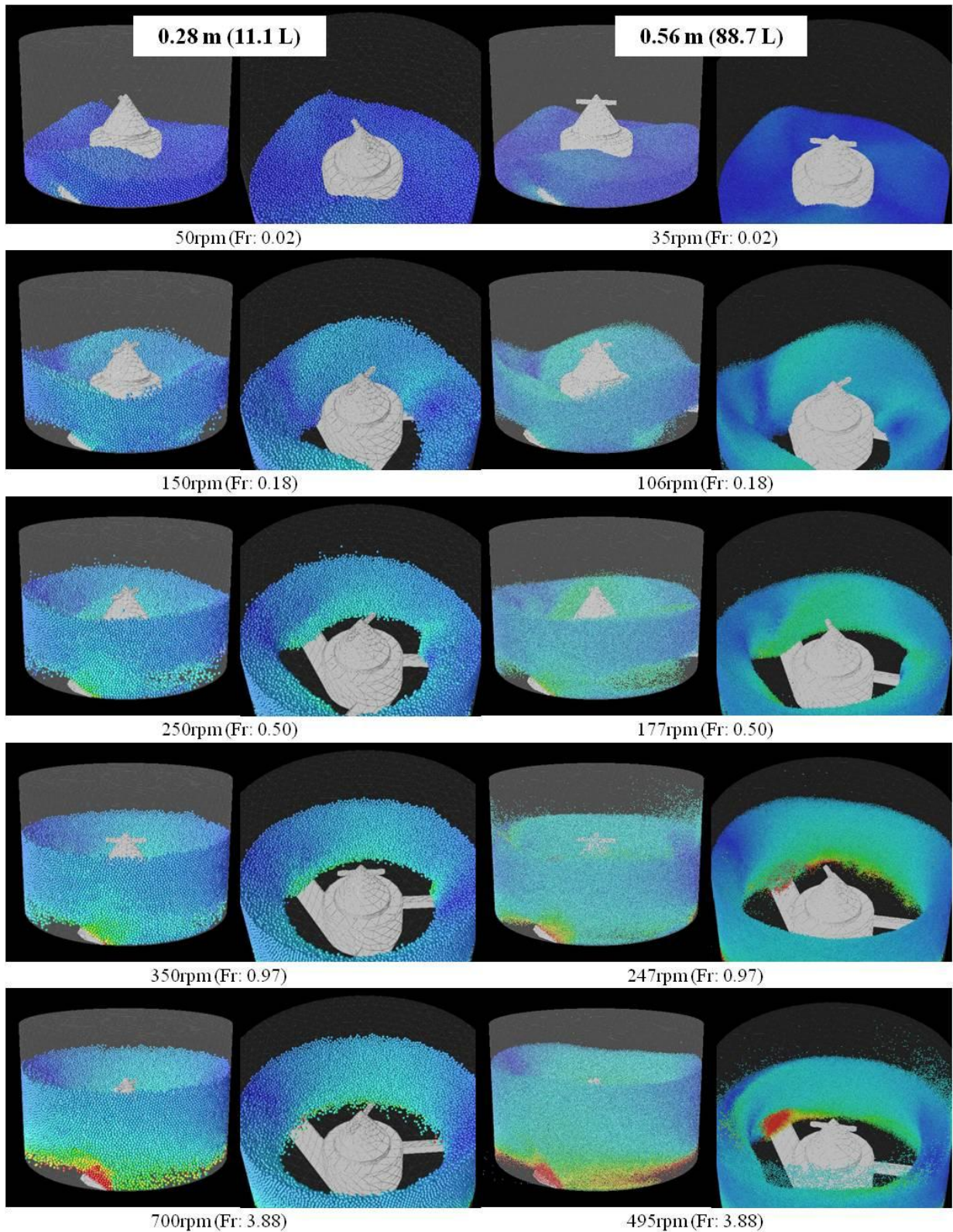


Figure D.24: Particle bed images for the 11.1 L, $D/d_p = 80$ (left column) and 88.7 L, $D/d_p = 160$ (right column) granulators.

D.3.2 Same particle diameter to granulator diameter ratio ($D/d_p = 80$)

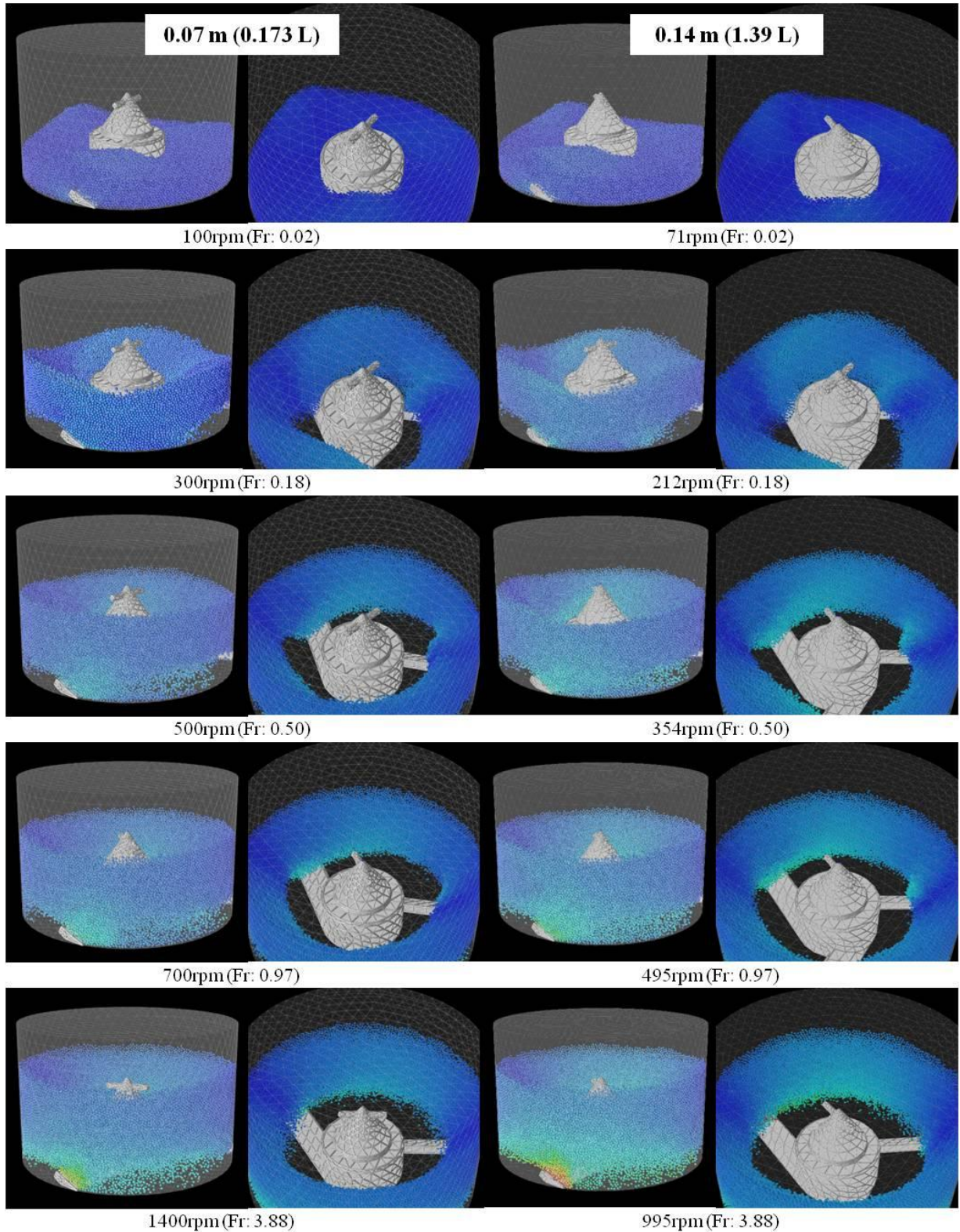


Figure D.25: Particle bed images for the 0.173 L (left column) and 1.39 L (right column) granulators ($D/d_p = 80$).

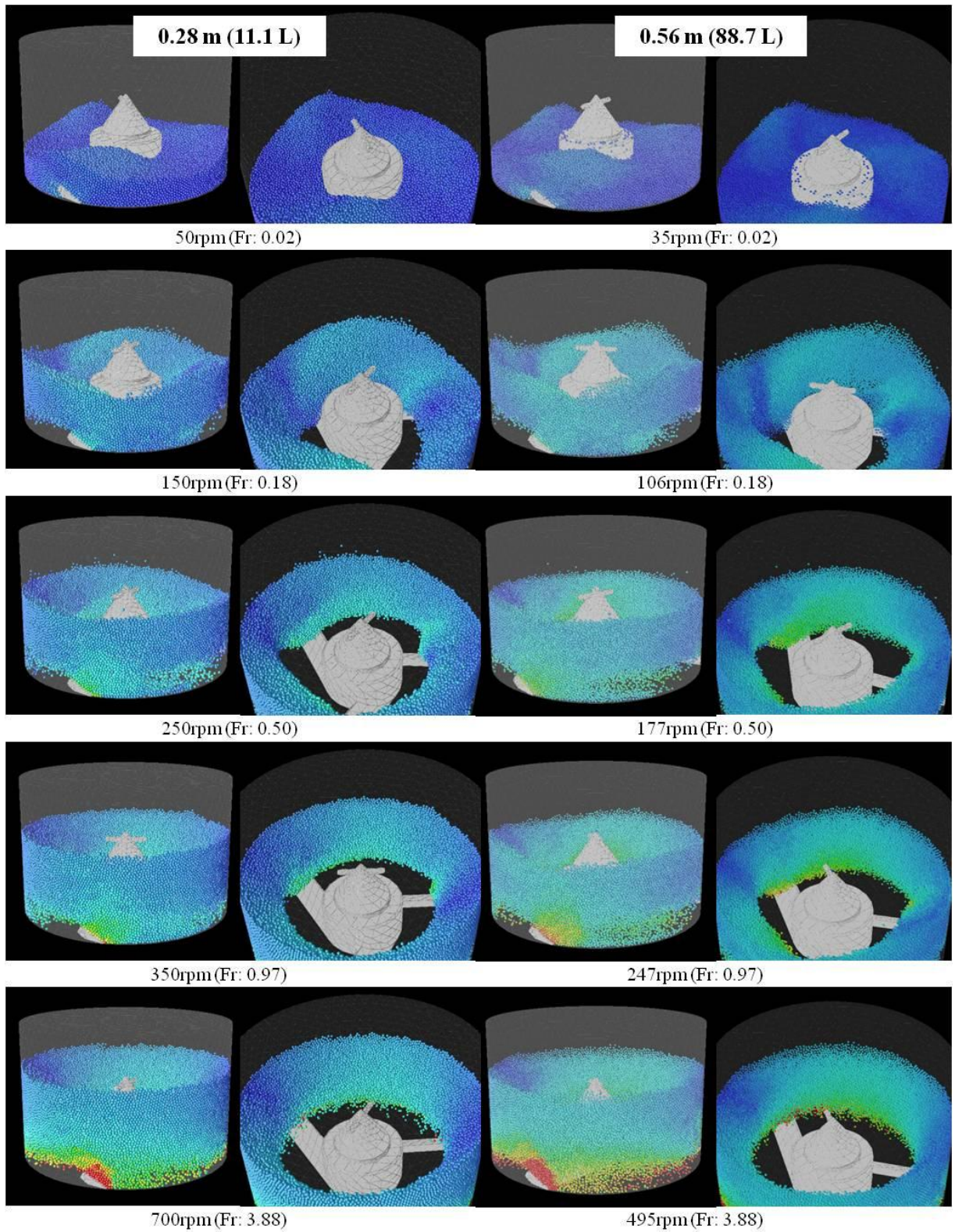


Figure D.26: Particle bed images for the 11.1 L (left column) and 88.7 L (right column) granulators ($D/d_p = 80$).